



**Università
degli Studi
di Palermo**

AREA QUALITÀ, PROGRAMMAZIONE E SUPPORTO STRATEGICO
SETTORE STRATEGIA PER LA RICERCA
USO DOTTORATO
UNIVERSITÀ SIGILLATA DI PALERMO

UNIVERSITÀ DEGLI STUDI DI PALERMO

Dottorato di Ricerca in Scienze Fisiche e Chimiche

Dipartimento di Fisica e Chimica – Emilio Segrè

Settore Scientifico Disciplinare CHIM/03

**Computational Studies of Materials for Energy Technology:
CO₂ Methanation, and Halloysite Carbon-Coating**

IL DOTTORE
MARCO BERTINI

Marco Bertini

IL COORDINATORE
MARCO CANNAS

Marco Cannas

IL TUTOR
DARIO DUCA

D.D.

IL CO TUTOR
FRANCESCO FERRANTE

Francesco Ferrante

CICLO XXXV
ANNO CONSEGUIMENTO TITOLO 2022

Computational Studies of
Materials for Energy Technology:
CO₂ Methanation, and
Halloysite Carbon-Coating

Marco Bertini

December 5, 2022

Contents

Preface	3
1 Empathes	5
1.1 Introduction	5
1.2 Nudged Elastic Band	6
1.2.1 Climbing Image NEB	8
1.3 Overview of Empathes Modules	9
1.4 Workflow	10
1.5 Generating Images	13
1.5.1 Linear Interpolation	13
1.5.2 Image Dependent Pair Potential	13
1.6 Elastic Band Optimization	15
1.7 Parallelization	17
1.8 Usage Examples	18
1.9 Performance	21
1.10 Extending the Interface	22
1.11 Conclusion	27
2 CO₂ Methanation	29
2.1 Introduction	29
2.2 Computational Details	30
2.3 Reactions, Hopping Processes and Migrations	33
2.4 CO ₂ Methanation on Pristine Ni (111)	34
2.5 CO ₂ Methanation on Ru-Decorated Ni (111)	64
2.6 CO ₂ Methanation on Fe-Decorated Ni (111)	95
2.7 Influence of an External Electric Field	125
2.8 Enumerating all Reaction Paths	126
2.9 The Simplified Christiansen Method	132
2.10 Searching the Best Reaction Path	134
2.11 Conclusion	141

3 Halloysite Carbon-Coating	144
3.1 Introduction	144
3.1.1 Li–O ₂ Batteries	144
3.1.2 HNTs Applied to Electrochemical Systems	145
3.1.3 Purpose of the Study	146
3.2 Computational Details	147
3.3 Pristine Halloysite Surface	151
3.4 Substituted Halloysite Surface	159
3.5 Si-vacant Halloysite Surface	169
3.6 Density of States Analysis	179
3.7 Conclusion	180
3.8 Acknowledgment	184
Afterwords	185
A Tables	187
B Listings	197
C H₂ Transformations on Graphene Supported Palladium Cluster	203
Bibliography	214

Preface

It goes without saying how dependent the contemporary human society is on energy. It is used in every area, from basic to medical services, transport, communication, research, production. The machine is in motion, and has already acquired such an inertia that stopping it and changing its course can no longer be done, although the nefarious effects of the excessive and short-sighted use of natural resources have been under the gaze of public opinion for decades. The ecological transition is therefore a physiologically slow process, both because it requires the dismantling of current energy production structures, no longer sustainable, that need to be substituted with different ones; and because it requires new technologies that can at least compete with the tremendous energy demand.

This dissertation, in its small and contained way, is a part of this vast mosaic. Here the models and theories of quantum chemistry, mainly those within the density functional theory framework, are applied in order to study some materials of interest in the field of energy technology, in order to understand their behaviors and verify their suitability for eventual applications.

This thesis is divided into three chapters, which incidentally follow the chronological order of the activities carried out during my PhD course. The first chapter discusses the Empathes software, a Fortran code written mainly during my first year. It implements the CI-NEB method, used to search for transition states in a chemical reaction. The chapter illustrates the theory behind this method, as well as all the contour algorithms necessary for its application, such as interpolation methods and optimizers. A section of this chapter discusses the parallelization strategy and the resulting performances, while another one explains how to extend the Empathes interface to use it with other condensed matter or quantum chemistry software beyond those supported by default.

The second chapter is entirely devoted to the study of the methanation reaction of carbon dioxide. Three different catalysts were investigated, all based on the nickel (111) surface. On each of them, 16 different chemical species (the possible intermediates of methanation reaction) have been

investigated, finding a total of 28 different elementary steps (and relative transition states) that can take place. Some of these elementary steps have also been studied by applying an external electric field to the system, in order to see how this affects the kinetics of the reaction. Finally, the activation energies obtained were used in a kinetic analysis that combines graph theory with the *Simplified Christiansen Method*.

The third chapter concerns the study of the carbon-coating process of halloysite (HNT), a natural clay with a nanotubular structure. Halloysite is an electrical insulator, therefore not usable as is within an electrochemical cell. The carbon-coating process solves this issue, as many experimental papers point out. The context is the applicability of carbon-coated HNT as a cathode material for Li–O₂ cells, specifically exploiting the nanotube lumen to confine the growth of lithium oxides, the discharge products. However, since computational studies related to the carbon-coating process itself are lacking in the scientific literature, it was chosen to study this phenomenon instead. The chapter describes the approach used to reproduce the carbon accretion on three different models of halloysite surface (a pristine, and two defective ones). The final part shows the DOS and carbon-PDOS for these systems, that were calculated to check if the computational results obtained at the chosen level of theory are in agreement with the experimental ones.

Lastly, at the end of this dissertation, there are some appendices that contain additional data and images which did not find place within the main chapters without interfering too much with the reading experience. Furthermore, one of the appendices is dedicated to a paper on the transformations of H₂ on a Pd₄ cluster supported on a graphene sheet. Part of this article reports some hopping processes of hydrogen atoms obtained by means of the Empathes code, investigated to unravel the spillover mechanism of hydrogen atoms from Pd to graphene. That was the first time that Empathes was used for the production of new data.

Chapter 1

Empathes

1.1 Introduction

This chapter is about the implementation of the *Nudged Elastic Band* method (NEB) and its *Climbing Image* variant (CI-NEB) in a computer software called *Empathes* (for **E**x^tensible **M**inimum **P**ath **E**stimator). This computational method is a numerical procedure used to determine the transition state of a chemical reaction when an analytical formula for atomic forces is not available, as in the case of solid state physics software packages that work with *periodic boundary conditions* (PBC). The Empathes code is designed to be easy to modify in order to be associated with the user's preferred calculation software, even with those that implement composite approaches. In particular, the interfaces to both the Gaussian and Siesta packages will be discussed in details, being the former mainly used for testing purpose, while the latter has been productively employed for transition states search, as will be shown in the next chapter.

The search for the structure of transition states through computational methods, essentially based on *Density Functional Theory* (DFT), is of overwhelming importance for the determination of the elementary steps forming a reaction mechanism. Allowing to develop basic knowledge, these investigations can be used to experimentalists towards a more efficient realization of synthesis processes of chemical compounds. In cases where it is necessary to describe the reactive system through periodic calculations, which is very common in heterogeneous catalysis, this research must be done through the use of non-analytical methods.

The NEB approach is, together with its variants, one of the most used for this purpose. In accordance with the NEB algorithm, a chain of geometric structures, generated by interpolation between the reactant and product ge-

ometries, are joined by fictitious springs and then relaxed on the *Minimum Energy Path* (MEP), allowing the association of the transition state to the maximum along this path. The NEB method involves the determination of molecular energies and forces acting on the nuclei of the system, which is generally carried out through a program for electronic structure calculation. Empathes is thus like a manager: it chooses which molecular geometry needs a single point calculation, and then uses the obtained data (i.e. final energy and atomic forces) to optimize each image of the elastic band. It will repeat this operation until a predefined threshold is reached, and the whole process can be considered convergent.

Although some commercial quantum chemistry software capable of applying the NEB procedure already exist (e.g. VASP [1]), this implementation of the method is general enough to be easily interfaced with virtually any program capable to compute energy and atomic forces of a chemical system. At present, Empathes can interface both Gaussian [2, 3] and Siesta.[4] The former was chosen for testing purpose, since it has an implicit analytical method for TS discovery with which the TS found by the numerical NEB method can be compared. Siesta was, instead, the main target, since when I started to develop Empathes Siesta lacked a NEB procedure. Now the developers implemented it directly in the Siesta code. Nevertheless, Empathes is still useful because of its parallel implementation, capable of performing single point calculation on all images at once, a difficult task to perform when a NEB calculation is execute inside the Siesta code.

1.2 Nudged Elastic Band

The NEB is a numerical method used for the discovery of the MEP connecting two molecular geometries, generally the reactant and the product of a chemical reaction, along the *Potential Energy Surface* (PES). This method is largely used to study transposition or migration processes, although it can be applied, at least in principle, to any kind of reaction. Knowledge of the MEP gives useful information about *transition states* (TS) and possible *reaction intermediates*. By knowing the TS structure, useful energetic and kinetic information, like activation barriers and reaction rates, can be extrapolated.

The logic behind this method is pretty straightforward. Given the molecular geometries of reactant and product, an arbitrary number of intermediate structures, called images, are interpolated between them. Those images are virtually connected one another by some fictitious springs, thus an *elastic band* of geometries is obtained, which will be gently *nudged* on the PES. This is done by an iterative calculation of some appropriate forces acting on

the images, that are used to optimize their geometries. The numerical process ends when the norms of the forces are below a given convergence threshold. If this threshold is chosen wisely, then the band will be an accurate estimation of the real MEP.

In the NEB method, as described in the work of Henkelman et al.,[5] each image i is optimized with respect to the total forces \mathbf{F}_i^{tot}

$$\mathbf{F}_i^{tot} = \mathbf{F}_{i\perp}^{PES} + \mathbf{F}_{i\parallel}^{el} \quad (1.1)$$

where $\mathbf{F}_{i\perp}^{PES}$ is the perpendicular component of the real atomic forces \mathbf{F}_i^{PES} acting on the system, calculated by any computational chemistry software, and $\mathbf{F}_{i\parallel}^{el}$ is the parallel component of the elastic forces, computed by the Hooke's law. These forces are projected along the normalized tangent, $\hat{\boldsymbol{\tau}}_i = \boldsymbol{\tau}_i / \|\boldsymbol{\tau}_i\|$, on image i , with $\boldsymbol{\tau}_i$ computed as

$$\boldsymbol{\tau}_i = \begin{cases} \boldsymbol{\tau}_i^+ & \text{if } E_{i+1} > E_i > E_{i-1} \\ \boldsymbol{\tau}_i^- & \text{if } E_{i+1} < E_i < E_{i-1} \end{cases} \quad (1.2)$$

where E_i is the calculated energy of the image i , while $\boldsymbol{\tau}_i^+$ and $\boldsymbol{\tau}_i^-$ are defined as

$$\boldsymbol{\tau}_i^+ = \mathbf{R}_{i+1} - \mathbf{R}_i, \quad \text{and} \quad \boldsymbol{\tau}_i^- = \mathbf{R}_i - \mathbf{R}_{i-1} \quad (1.3)$$

being \mathbf{R}_i the molecular geometry of the image i . If i is related to either an energy minimum or a maximum, the following alternative equation is used to compute $\boldsymbol{\tau}_i$

$$\boldsymbol{\tau}_i = \begin{cases} \boldsymbol{\tau}_i^+ \Delta E_i^{max} + \boldsymbol{\tau}_i^- \Delta E_i^{min} & \text{if } E_{i+1} > E_{i-1} \\ \boldsymbol{\tau}_i^+ \Delta E_i^{min} + \boldsymbol{\tau}_i^- \Delta E_i^{max} & \text{if } E_{i+1} < E_{i-1} \end{cases} \quad (1.4)$$

where

$$\begin{aligned} \Delta E_i^{max} &= \max(|E_{i+1} - E_i|, |E_{i-1} - E_i|) \\ \Delta E_i^{min} &= \min(|E_{i+1} - E_i|, |E_{i-1} - E_i|) \end{aligned} \quad (1.5)$$

Once determined $\hat{\boldsymbol{\tau}}_i$, the components of \mathbf{F}_i^{tot} can be computed as

$$\mathbf{F}_{i\parallel}^{el} = k(\|\mathbf{R}_{i+1} - \mathbf{R}_i\| - \|\mathbf{R}_i - \mathbf{R}_{i-1}\|)\hat{\boldsymbol{\tau}}_i \quad (1.6)$$

$$\mathbf{F}_{i\perp}^{PES} = \mathbf{F}_i^{PES} - (\mathbf{F}_i^{PES} \cdot \hat{\boldsymbol{\tau}}_i)\hat{\boldsymbol{\tau}}_i \quad (1.7)$$

1.2.1 Climbing Image NEB

The Climbing Image is a slight variation of the original NEB method.[6] Essentially it finds the same MEP as the regular NEB, but here the maximum along the MEP is rigorously converged to a saddle point, thus giving a real transition state. This is obtained by the application of the following equation to calculate the total forces acting on exactly one image, the energy maximum (as denoted by the TS subscript).

$$\mathbf{F}_{TS}^{tot} = \mathbf{F}_{TS}^{PES} - 2(\mathbf{F}_{TS}^{PES} \cdot \hat{\boldsymbol{\tau}}_{TS})\hat{\boldsymbol{\tau}}_{TS} \quad (1.8)$$

This equation is pretty intuitive, it states that the total forces acting on TS are the ones obtained from the electronic structure calculation (\mathbf{F}_{TS}^{PES}), but with a flipped parallel component. This can be clearly seen by the relations:

$$\begin{aligned} \mathbf{F}^{PES} &= \mathbf{F}_{\perp}^{PES} + \mathbf{F}_{\parallel}^{PES} \\ \mathbf{F}_{TS}^{tot} &= \mathbf{F}_{TS}^{PES} - 2\mathbf{F}_{TS\parallel}^{PES} = \\ &= \mathbf{F}_{TS\perp}^{PES} - \mathbf{F}_{TS\parallel}^{PES} \end{aligned} \quad (1.9)$$

The resulting effect is that TS, when relaxed using this forces, will move along the MEP tangent towards the nearest saddle point, far away from the closest energy minimum.

Another further improvement to the algorithm, generally adopted along with the Climbing Image variant, is the use of dynamic spring constants in the evaluation of parallel elastic forces. This means that the images are no longer kept together by similar springs, and that stronger springs can be used in the high portion of the MEP, thus improving the resolution around the transition state (i.e. more images are now close to the maximum, the region of interest). Dynamic spring constants generally reduce the computational time of a CI-NEB by leading to a faster convergence. They are computed using the following formula:

$$k'_i = \begin{cases} k_{\max} - \Delta k \left(\frac{E_{\max} - E_i}{E_{\max} - E_{\text{ref}}} \right) & \text{if } E_i > E_{\text{ref}} \\ k_{\max} - \Delta k & \text{if } E_i < E_{\text{ref}} \end{cases} \quad (1.10)$$

where $E_i = \max(E_i, E_{i-1})$ is the higher energy of two images connected by a spring, E_{\max} is the higher value of E_i for the whole elastic band, and E_{ref} is the energy of the higher energy endpoint of the MEP. This way all the spring constants are scaled between the two values of $k_{\max} - \Delta k$ (for the lowest energy images) and k_{\max} (for the highest energy images).

1.3 Overview of Empathes Modules

The design behind this program involves communication between modules based on protected global variables, i.e. accessible in read-only mode. When it is necessary to set one of these variables, this is done through a call to the appropriate subroutine. This prevents unintentional changes to their content. A brief presentation of the modules follows:

`mod_input.f90`: deals with reading the input file, and also checks that all the mandatory arguments have been specified and are consistent.

`mod_geometry.f90`: contains information about the geometry of the images, as well as the linear interpolation procedure necessary to initialize them.

`mod_idpp.f90`: implement the logic of the *Image Dependent Pair Potential* method (IDPP) [7], that can be used as an initial estimation of the reaction path, and is an excellent alternative to the simpler linear interpolation. Within this module the subroutines that determine the value of the IDPP object function and its derivatives are defined, ready to be used with any minimization method.

`mod_elastic.f90`: is the heart of the NEB method. This module collects the subroutines for the calculation of the tangents $\hat{\tau}_i$ between images, as well as those for the decomposition of PES and elastic forces into $\mathbf{F}_{i\perp}^{PES}$ and $\mathbf{F}_{i\parallel}^{el}$, and for the determination of the total forces \mathbf{F}_i^{tot} acting on each image.

`mod_pes.f90`: here are specified the subroutines that interface to computational chemistry software, necessary to get the energy E_i of the images and the atomic forces \mathbf{F}_i^{PES} acting on them. These calculations can also be performed in parallel thanks to a specific subroutine that uses the MPI library.[8]

`mod_pes_data.f90`: set additional information for external calculations, such as the maximum number and convergence threshold of SCF cycles, as well as the names of auxiliary files.

`mod_pes_input_template.f90`: the data written inside the input blocks will be stored in specific structures defined here. This module defines subroutines to store the read data in the appropriate location, and to write it where necessary during the composition of input files for the external electronic structure program.

`mod_climbing.f90`: contains the procedures to perform the Climbing Image (CI) [6] and the Descending Image (DI) methods, which is an analogue of the previous one that applies to the energy minima.

`mod_optimization.f90`: within this module are collected the subroutines that solve the minimization problem using the values of a function and its first derivatives in a given point (e.g. energies and PES forces, or the analogous quantities of the IDPP method). The Steepest Descent, the Fast Inertial Relaxation Engine (FIRE), the Broyden–Fletcher–Goldfarb–Shanno (BFGS) and the limited-memory BFGS (L-BFGS) are currently implemented, being the latter the default method thanks to its effectiveness.

`mod_output.f90`: all the subroutines that print information, such as geometries, forces, energy barriers, etc. are grouped here.

`mod_slave.f90`: defines a subroutine to put MPI slave processes in an idle state, waiting for the master to assign them a task.

`mod_utility.f90`: all global parameters and generic utility functions are collected in this module. The `get_field` subroutine is located here; how it is used to read the output of external programs will be detailed later.

`mod_c_utility.f90`: defines some Fortran subroutines that interface the C code contained in `c_utility.c`. This C module is intended to collect operating system specific functionalities (e.g. changing the execution directory) in a portable way using standard OS libraries, making it possible, at least in principle, to compile this program on any Linux system regardless of the compiler used.

1.4 Workflow

The flowcharts outlining how Empathes works are reported in Figure 1.1 and 1.2. Once read the input file, the geometries of the images that make up the elastic band are generated. This is done either through an interpolation technique, or through a direct reading of these geometries from a file. The latter case occurs mostly when a calculation needs to be restarted, but this feature can also be exploited to pass some handcrafted geometries to the program.

The NEB method is now applied. As equation (1.1) shows, the total forces are computed from the real PES forces. Obtaining \mathbf{F}_i^{PES} and E_i is therefore the first step, as well as the critical part of the program and the one that takes almost all of the execution time. The present code can be seen

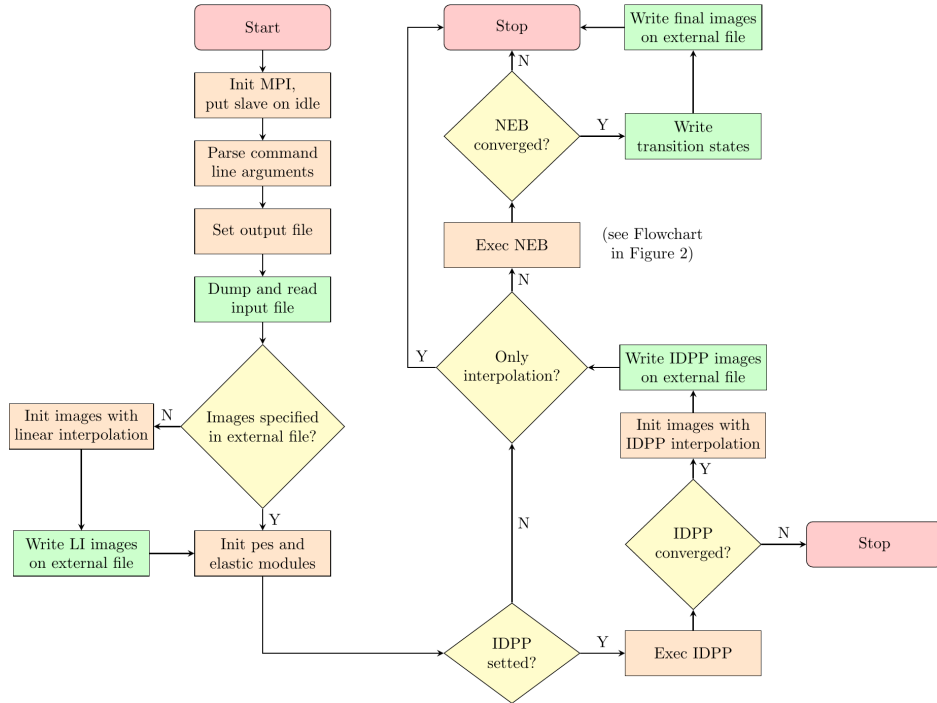


Figure 1.1: Flowchart of the Empathes code.

as an automation of the NEB method in order to make it available with any computational chemistry program, interacting with it by writing its input, executing it, and reading its output. If the calculation has converged all the necessary information is read and stored, otherwise, if desired, the SCF convergence threshold is automatically increased up to a certain limit value, and the calculation is launched again.

The second step is the construction of \mathbf{F}_i^{tot} from the information obtained above, using the equations of the NEB method. The third and last step is the optimization of the images with respect to their energy and \mathbf{F}_i^{tot} . This minimization problem has been solved in countless ways, and many algorithms are reported in the literature. For this task, one of the optimizers currently available can be chosen: Steepest Descent, FIRE, BFGS or L-BFGS.

These three steps are repeated iteratively until the norm of \mathbf{F}_i^{tot} is below a certain threshold for each i . Its value depends on the optimizer employed, but can also be set by the user. If at the end all images converge, then a file containing the relaxed geometries is written, and the activation barriers for each transition state that has been found are printed in the Empathes output file.

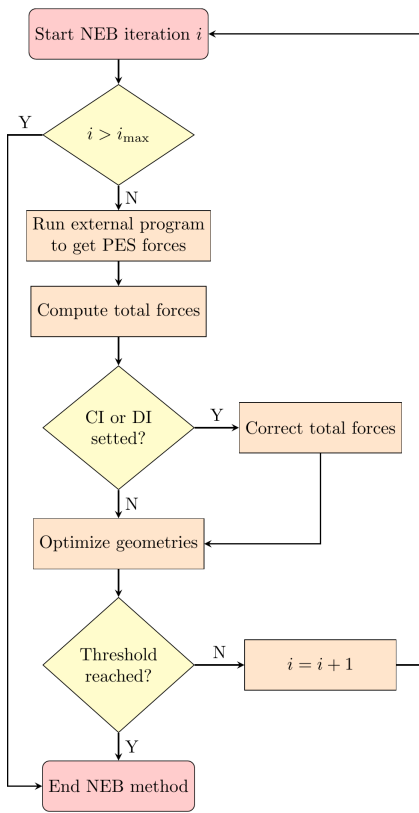


Figure 1.2: Flowchart detailing the NEB algorithm.

1.5 Generating Images

1.5.1 Linear Interpolation

Linear interpolation is the simplest interpolation technique: knowing the initial and final positions of an object, the displacement between the two is assumed as a straight line. In this way, a number of points can be chosen in the segment connecting the two endpoints, and the position of the original object in each of the points can be computed.

Dealing with molecular geometries each atom is a point that have to be interpolated, so instead of dealing with a single coordinate the mathematical objects are vectors, but the principle stays the same. First thing to do is to quantify the amount of displacement ($\Delta\mathbf{R}$) between the reactant (\mathbf{R}_r) and the product (\mathbf{R}_p) geometries.

$$\Delta\mathbf{R} = \mathbf{R}_p - \mathbf{R}_r \quad (1.11)$$

Then, having N different images between reactant and product, indicated by the letter i ($1 \leq i \leq N$), the geometries (\mathbf{R}_i) of each one of these can be calculated as:

$$\mathbf{R}_i = \mathbf{R}_r + \frac{i}{N+1} \Delta\mathbf{R} \quad (1.12)$$

Unfortunately, it happens most of the times that the structures of the NEB images generated by linear interpolation are flawed because two (or more) atoms are too close one another. However, despite this flaw, they are not completely useless, since they can be employed as a starting point for the more refined IDPP interpolation technique that will be shown in the following section.

1.5.2 Image Dependent Pair Potential

The idea behind the Image Dependent Pair Potential approach is the generation of NEB images through linear interpolation on interatomic distances. This technique has a double advantage over the common linear interpolation performed on the coordinates. The first one is that the geometries of the images estimated this way follow a smoother path going from reactant to product. The second and most important one is that it never produces geometries with atoms too close one another (a quite frequent case with linear interpolation), a situation that can make it hard for the external program to run successfully on that given image.

Since, given N atomic nuclei, there are generally more interatomic distances, $((N-1)N/2)$, than atomic coordinates, $(3N)$, the IDPP method

cannot be applied as easily as the linear interpolation. The solution is to find the minimum of a properly defined objective function, S_i^{IDPP} ; this problem is quite similar to the one solved by the NEB, with S_i^{IDPP} used in place of E_i and its derivatives instead of \mathbf{F}_i^{PES} , being the elastic part of the forces calculated exactly in the same way.

The equation set employed in the present implementation showed to define an efficient frame allowing to avoid waste of system resources. Let's denote by d_{ij}^I and d_{ij}^F the interatomic distances between the i and j nuclei of the initial and final geometry, respectively. For each image k , the ideal interatomic distances can therefore be defined as

$$d_{ij}^k = d_{ij}^I + k(d_{ij}^F - d_{ij}^I)/(p+1) \quad (1.13)$$

where p is the total number of images. So, starting from an initial guess on the images geometries (generally by standard linear interpolation), a set of coordinates that produces interatomic distances d_{ij} as close as possible to d_{ij}^k is obtained. For this purpose, given that each image k contains N atoms, the IDPP objective function is defined as

$$S_k^{IDPP}(\mathbf{r}) = \sum_i^N \sum_{j>i}^N \omega(d_{ij}) (d_{ij}^k - d_{ij})^2 \quad (1.14)$$

where $\mathbf{r} \equiv \{x_1, y_1, z_1, \dots, z_N\}$ is the set of all the spatial coordinates, d_{ij} is the actual interatomic distance between i and j , and $\omega(d_{ij})$ is a weight function that prevents two nuclei from being too close each other

$$\omega(d_{ij}) = (d_{ij})^{-4} \quad (1.15)$$

By contracting all terms after the summations in (1.14) into a single term s_{ij}^k

$$s_{ij}^k = \omega(d_{ij}) (d_{ij}^k - d_{ij})^2 \quad (1.16)$$

the forces acting on atom l , obtained by taking the negative derivative of S_k^{IDPP} , can be written as

$$\mathbf{F}_l^k = -\nabla_l S_k^{IDPP} = -\nabla_l \sum_i^N \sum_{j>i}^N s_{ij}^k \quad (1.17)$$

where only the s_{ij}^k terms having either i or j equal to l give non vanishing contributions. If a generic s_{ij}^k is derived with respect to a certain spatial variable α_r ($\alpha = x, y, z$; $r = i, j$), we get

$$\frac{\partial}{\partial \alpha_r} s_{ij}^k = -4t \frac{(d_{ij}^k - d_{ij})^2}{(d_{ij})^6} - 2t \frac{(d_{ij}^k - d_{ij})}{(d_{ij})^5} \quad (1.18)$$

where

$$t = \begin{cases} +(x_i - x_j) & \text{if } \alpha_r = x_i \\ -(x_i - x_j) & \text{if } \alpha_r = x_j \\ +(y_i - y_j) & \text{if } \alpha_r = y_i \\ -(y_i - y_j) & \text{if } \alpha_r = y_j \\ +(z_i - z_j) & \text{if } \alpha_r = z_i \\ -(z_i - z_j) & \text{if } \alpha_r = z_j \end{cases} \quad (1.19)$$

Therefore, for a given atom l , the force component along α is given by the general equation

$$F_{l,\alpha}^k = \sum_{i=1}^{l-1} \frac{\partial}{\partial \alpha_i} s_{il}^k - \sum_{j=l+1}^N \frac{\partial}{\partial \alpha_l} s_{lj}^k \quad (1.20)$$

If these components are calculated sequentially starting from $l = 1$, then it can be argued that for a generic l the terms inside the first summation have already been calculated. In this way all the forces can be composed without wasting computing resources and system memory, that is by calculating once all the three spatial derivatives of all s_{ij}^k , and adding them in the right place in the final matrix that will contain the IDPP forces.

1.6 Elastic Band Optimization

The core of the NEB procedure is the iterative optimization of the image structures with respect to \mathbf{F}_i^{tot} acting on them. This is a minimization problem in which each image must have the lowest possible energy, that thus can be seen as the objective function whose variables are the atomic coordinates. Moreover, to perform this task its (not strictly speaking) derivatives are the only information available one can work with.

The first method that was implemented to solve this problem was the simple *Steepest Descent*. At each optimization step, the image structures are relaxed by moving their nuclei in the direction of the force (i.e. the negative of the gradient) acting on them, changing their position by a quantity that depends on the slope of the gradient in that region of the hypersurface. This means that nuclear positions change more and more slowly as they approach a minimum. The end result is that the whole CI-NEB calculation is painfully slow for small-size systems, and totally inapplicable even for medium-size ones.

Another optimization method implemented in Empathes is the *Fast Inertial Relaxation Engine* (FIRE).[9, 10] This is a so called molecular dynamics method, in the sense that the geometry being optimized can gain or lose

“momentum” at each FIRE iteration, depending on whether it keeps moving towards a minimum or it has just found a rise in the hypersurface, respectively. Internally, the FIRE algorithm works with two dynamic parameters that change their value depending on the situation: α , that blends together the total forces acting on that particular geometry and the momentum already acquired by it; and Δt , the time step, which has an influence on the spatial step with which the nuclei will be moved in the direction of the momentum. These parameters start with some default values that can improve if good conditions are met (i.e. the geometry keeps moving towards a minimum), or can be reset if an upward portion of the hypersurface is suddenly encountered, in which case even the momentum accumulated so far is lost. This optimization technique is way more efficient than the Steepest Descent. Moreover, it is the main one used in the calculations of chapter 2.

The last two optimizers implemented were BFGS (from the names of its discoverers Broyden, Fletcher, Goldfarb and Shanno), and the limited-memory version of BFGS (L-BFGS).[11] These are two of the most popular quasi-Newton methods available. Just like Steepest Descent and FIRE, they only require the gradients of the objective function to work, the difference being that they compute the changes in gradients, thus effectively building an estimation of the Hessian matrix that will then be used to speed up the search of the minimum. There could be some problems with BFGS, for example if the system extension is too large, then the storage of the entire approximate Hessian in memory could be too demanding or even impossible to perform. The L-BFGS method solves this problem by storing just a few vectors of length n (the gradients of the latest m optimization iterations, where m can be chosen arbitrarily) from which the $n \times n$ approximate Hessian matrix can be inferred. In Empathes, both methods are implemented in order to optimize all the image geometries at once, as suggested by Sheppard et al.[12]

Finally, a quantitative example to demonstrate the behavior of these optimizers. To locate the transition state of the keto-enol tautomerism of formaldehyde, the iteration steps required by the various optimizers are: Steepest Descent more than 1200; FIRE 90; BFGS 24; and L-BFGS, with a memory of the last seven steps, 24. This simple test seems to show that quasi-Newton methods have a noticeable advantage over the others, and this is the reason why L-BFGS has been selected as the default optimizer in Empathes. However, for more complex scenarios, such as the surface reactions that will be investigated in chapter 2, the L-BFGS method was not as useful as FIRE. In general, it has been observed that, by choosing a loose convergence threshold, L-BFGS finds the minimum faster than FIRE. However, using tight thresholds, L-BFGS diverges hopelessly, while FIRE manages, patiently and consistently, to get to the minimum.

1.7 Parallelization

As previously said most of the time is spent waiting for the external program to finish its calculations on the images. Since these computations are totally independent from each other, this is an embarrassingly parallel problem. It was therefore decided to make the code parallel using the MPI library, in order to support its use on computer clusters. However, the use of conditional compilation techniques also allows to build a serial executable suited for smaller systems.

Master and slaves is the parallelization paradigm employed, where the master performs almost all operations alone, with the exception of the calculations of PES energies and forces in which all processes contribute. Since the master is the only one who reads the Empathes input file, it must also initialize the slaves by broadcasting those information to them, so that they will be able to write the input files for the external program.

In order to carry out the PES computations in parallel, firstly the master broadcasts the images to the slaves since it is the only process that has the updated geometries. Then each process independently determines whether a given image belongs to it, and runs the PES computations on those that do. This determination does not require communication: it is as simple as taking the module between the image number and the number of processes, and comparing it to the process ID. Once each process executed all its PES computations, the inter-process communication begin. Slaves send the energies to the master via point to point communication. After that, master and slaves meet at the only MPI barrier present in the code, and finally also the forces are sent from slaves to master via point to point. It's worth to be noted that, with a single call to the `MPI_Send` subroutine, two information can be passed: one is either the energy or the force array itself, the other one is the image number to which those values refer, stored in the `tag` argument.

It is possible to run Empathes in parallel with any number of processes, although the best situation is achieved by setting it equal to the number of images used or a submultiple, so that each process has roughly the same workload.

Finally, at the present moment Empathes can be executed in parallel (via MPI) and it can exploit the parallel capabilities of an external quantum chemistry software if this one makes no use of MPI (OpenMP is fine). This is due to the difficulties encountered while interfacing two programs both linked to MPI. Specifically, an external MPI program can not be called through the `mpirun` command inside another MPI program using the intrinsic Fortran subroutine `execute_command_line()` if the caller was itself executed through `mpirun`. The correct way to perform this operation would be through the

MPI subroutine `MPI_Comm_spawn()`, the problem being that this one, as opposed to `execute_command_line()`, returns immediately the control to the caller, without waiting for the called external program to end its task. The workaround seems to be a manual check on the status of the called program before trying to process its output, but this is not implemented yet.

1.8 Usage Examples

By executing Empathes with the “-h” option, usage instructions and more command line arguments will be printed. Some of them generate a template for the input file, that is a good starting point for the user since it lists and describes all the keyword that can be used to set the Empathes runtime behavior. Some keywords are mandatory, some are optional, and some are even mutually exclusive. They can be specified in any order, but an error message will follow if the same keyword is set more than once. Any keywords begin with a “#” character and could be followed by one or more arguments depending on its kind. A “!” at the beginning of the line, instead, states a comment that will be ignored by the program.

One of the main tasks of Empathes is to write the input files for the quantum chemistry software that will compute energy and atomic forces on images. From the Empathes point of view, these input files can be conceptually divided into two parts: one that varies from one image to another, and another that remains the same. Information to be written in the variable part must be somehow known by Empathes, so that it can adapt and write them appropriately. Among these information there are the geometries of the images, which change from one iteration to another; the SCF convergence threshold, so that Empathes can automatically lower it up to a limit value if the calculation does not reach it; and the maximum number of SCF cycles that will be performed by the external program, necessary to determine the convergence when using Empathes with some older versions of Siesta. These information must be specified by some appropriate keywords, like `#START` and `#END` for the starting and ending geometries, `#SCFCOV` and `#SCFCYCLE` for the SCF convergence threshold and maximum number of cycles, respectively. As for the part of the input that does not vary, this generally includes all the information related to the calculations that is intended to be performed on the various images. In this case, Empathes does not need to “understand” what will be written in this section of the input, but it will simply copy and paste these information, which are specified by means of the `#PESINPUTTEMPLATE` blocks.

The input files built by Empathes for Gaussian and Siesta are respectively

shown in the listings (B.1) and (B.2) reported in the appendix. The first two characters of every line are here reported for explanatory reason, they are not printed in the real file. The first character indicates who prints that section of the input: a number means that it has been specified in the relative `#PESINPUTTEMPLATE` block, while an “E” indicates that Empathes itself prints it in that exact format. The second character “|”, instead, is only a graphic separator, and is followed by what is actually written in the file. If Gaussian is used as the external program, the user may want to specify something after the geometry block, like a basis set or a pseudopotential. This can be done by specifying a “`#PESINPUTTEMPLATE 3`” block. If, instead, Siesta is used, more than two `#PESINPUTTEMPLATE` blocks are never needed, as it uses a free format for the input. In this case, however, it is worth noting that the geometry block written by Empathes must not contain chemical elements that refer to coordinates, but labels. For this reason, using Siesta, it is necessary to specify these labels by putting them as the fifth column in both the `#START` and `#END` geometries.

The following three examples of input files for Empathes will show how to execute a NEB calculation with Gaussian and with Siesta, as well as how to restart a NEB calculation if something wrong occurs.

Example 1 - Gaussian

Listing (B.3) shows an Empathes input file of use with Gaussian. Below the `#START` and `#END` keywords are specified, respectively, the coordinates of reactant and product in the *xyz* format. It has to be noticed that it is up to the user to ensure the consistency of the two geometries, since Empathes can only verify that the elements are inserted in the same order in the initial and final geometries, but it cannot do anything in the event that two lines referring to the same element have been accidentally swapped. The energies of those structures, needed to compute the tangents $\hat{\tau}_i$, are given by `#STARTENERGY` and `#ENDENERGY`. Then the keywords that define the NEB computation itself begin: `#OPTCYCLE` specifies the maximum number of NEB iteration (a negative value indicates “until convergence is achieved”), `#OPTCONV` sets the threshold on the total force, `#IDPP` specifies that the IDPP interpolation must be used, `#IMAGES` tells the program how many images have to be generated, and “`#CLIMBING 1`” means that the CI-NEB will be performed only on “one” image that is an energy maximum. It is to say that, in the general case, “`#CLIMBING n`” will apply climbing up to the *n* highest energy maxima. The final part contains info on the PES calculation: `#PESPROGRAM` specifies the kind of program is

intended to use, `#PESEXEC` contains the actual name of the executable, and the two `#PESINPUTTEMPLATE` blocks contain information to write in the input files for Gaussian.

Example 2 - Siesta

Listing (B.4) shows an Empathes input file of use with the Siesta code. Although the system in this example is the same as the previous one, the input file required to execute this NEB calculation is longer than that used for Gaussian, mostly due to the larger `#PESINPUTTEMPLATE` blocks. The first difference is a fifth additional column in the specification of both initial and final geometries. These numbers (but they can be anything, since they are stored as strings) are the labels related to every atom of the geometry. It's mandatory that the labels appear in the same order in both geometries, just like the atomic nuclei. The next new keyword is `#PESPROC`, used to specify the number of processors on which the external program will run. This information is needed because a parallel run of Siesta is obtained via MPI. The `#SCFCYCLE` sets the number of SCF cycles that the external program will perform. `#AUXINPUTFILES` is used to specify how many and what auxiliary input files the external program needs. In this case only one file is needed, that is `*.psml`. Here the asterisk has the same function as in regular expressions, so all the files ending with `.psml` will be copied from the master directory into the working directories. The `#AUXOUTPUTFILES` keyword has a similar behavior as the previous one. It can be used to specify how many and what auxiliary output files are to be stored, in order to reuse them in the next optimization iteration. Here the density matrix files are requested to be saved, that is all the files ending with `.DM`, since using them as the starting point for the next optimization iteration is a tremendous improvement in terms of computational time.

Example 3 - Restarting a Calculation

Suppose that the NEB calculation in listing (B.3) is launched and that for some reason it didn't end well. In the master directory there is a file called `lastgeom.bkp` containing, in order, the *xyz* molecular geometries of reactant, images and product, computed in the last well-ended optimization iteration. These can be used as the restarting point. In such a circumstance, it is preferable to copy `lastgeom.bkp` into another file, let's say `geometries.in`, and tell the program that the geometries it needs are located in this file.

Listing (B.5) shows an Empathes input file to restart a calculation. The

#GEOMETRIESFILE keyword is followed by the name of the file that stores the geometries. The first geometry is associated with the reactant, the last one with the product, and all the intermediate geometries will be the corresponding images. When this keyword is specified, in order to avoid mistakes, the #START, #END, #IMAGES, and #IDPP keywords must not be present in the input file. The remaining of the input file is the same except for the new #CLIMBINGQUICKSTART keyword, that is used to apply the Climbing Image method from the very first iteration.

1.9 Performance

All the tests here reported has been executed using Gaussian09 as external program, so that the TS obtained from the NEB method could be directly compared with those coming from its analytic method. Parallel performances were also investigated on a homogeneous cluster, where each node has two Intel Xeon E5-2690 processors for a total of 16 physical CPUs. Being the Intel Hyper-Threading technology enabled during the tests, there were 32 logical CPUs available on each node.

The first reaction studied was the simple CH2O —> CHOH tautomerism. This system has been analyzed with the DFT B3LYP/cc-pVDZ method, 6 images were generated by IDPP interpolation, and the CI-NEB method was applied on one of them. Dynamic spring constants were used, and the FIRE optimization algorithm with a convergence threshold of $1.0 \cdot 10^{-3}$ $E_h/\text{\AA}$ was set. Following this setting, convergence was achieved after 90 iterations. The TS found showed an energy of -114.370339 E_h , that is the same result obtained with the Gaussian09 analytic method. The running times related to parallel executions are reported in table (1.1). This table also contains a timing relative to an OpenMP run. This was the first form of parallelization implemented, but, being suitable only for computations on small systems, it has been removed, also considering the identical performance with MPI. In these runs, Gaussian was executed with 2 threads. The theoretical performance in this case is 1/6 of the serial time (i.e. 16.67%), that can be achieved only if each Gaussian calculation on each of the 6 images lasts exactly the same amount of time. Here a pretty close result of 19.03% is achieved in the best MPI run.

The second test was the acetone – propen-2-ol tautomerism. Once again the hydrogen hopping is involved, but this time in a slightly larger system. The calculation was carried out using the same conditions as in the previous case. The energies obtained for the TS from NEB and Gaussian09 computations were, respectively, -193.058873 E_h and -193.058869 E_h , so there is

Table 1.1: H migration on formaldehyde.

Type ^a	<i>c</i>	<i>N</i>	<i>c/N</i>	<i>U</i> ^b	Time	% ^c
Serial	1	1	1	2	11m 56.282s	100.00
OpenMP	6	1	6	12	2m 16.541s	19.06
MPI	6	1	6	12	2m 16.317s	19.03
MPI	6	3	2	4	2m 25.274s	20.28
MPI	6	6	1	2	2m 49.560s	23.67
Theoretical best time					1m 59.404s	16.67

^a Gaussian09 executed with $t=2$ threads. Empathes executed with c processes on N nodes.

^b Total number of CPUs used per node: $t \cdot c/N$.

^c $\% = 100 \cdot \text{Time}/\text{Time}_{\text{Serial}}$.

virtually no difference between the two results.

The last test was performed on a phosphoro-thionate cation, where the $\text{CH}_3-\text{PO}-\text{SCH}_3^+ \longrightarrow \text{CH}_3-\text{PS}-\text{OCH}_3^+$ reaction involves the hopping of a methyl group from S to O.[13] This time B3LYP/6-311+G calculation was performed, and the NEB was set to use 8 images. Once again the analytic calculation and the estimation by NEB of the TS are in agreement, being the energies, respectively, -894.207182 E_h and -894.207170 E_h. Table (1.2) contains the computing times related to the parallel runs. For these tests the B3LYP/cc-pVDZ method was used, and Gaussian was executed with 4 threads. There being 8 images, the theoretical best time in this case is 12.50% of serial time, and in the best MPI run a very close 14.17% is obtained.

1.10 Extending the Interface

The interface of Empathes can be extended to other chemistry software. To do this, the user must edit the `mod_pes.f90` module only. Here he has to accomplish two tasks:

A) to write at the end of the module three new subroutines that must:

1. write the input file for the external program
2. run it
3. read its output to get energy and atomic forces

Table 1.2: CH₃ migration on phosphoro-thionate cation.

Type ^a	<i>c</i>	<i>N</i>	<i>c/N</i>	<i>U</i> ^b	Time		% ^c
Serial	1	1	1	4	2h	19m 13.107s	100.00
MPI	8	1	8	32	33m	38.119s	24.16
MPI	8	2	4	16	21m	48.204s	15.66
MPI	8	4	2	8	19m	43.837s	14.17
Theoretical best time					17m	24.138s	12.50

^a Gaussian09 executed with *t*=4 threads. Empathes executed with *c* processes on *N* nodes.

^b Total number of CPUs used per node: *t* · *c/N*.

^c % = 100 · Time/Time_{Serial}.

B) to modify the `get_pes_force` subroutine in three points, which can be find by searching the “@end_user” string:

1. setting a maximum SCF convergence threshold for the new program
2. inserting a check between the actual SCF threshold (stored in `conv_threshold`) and the maximum one
3. inserting the calls to the three previously written subroutines (at point A), in that order.

The points B.2 and B.3 require to specify a new `case` statement with the name of the new program, in which to insert the said logic.

The `get_pes_force` subroutine is used to obtain energy and atomic forces of the *i*-image. It sets some variables and then calls the three subroutines whose guidelines will be outlined shortly. It is worth noting that the arguments names are not casual, but are the same as the variables used in `get_pes_force`: in this way the subroutine declarations and their calls are the same. After a successful implementation of an interface, to use Empathes with the new program it is mandatory to specify the `#NEWPESPROGRAM` keyword in its input, that disables some internal checks and makes mandatory the `#SCFCNV` and `#SCFCYCLE` keywords. The keyword `#NEWPESPROGRAM` exists in order to limit possible errors and simplify the implementation of a new interface.

Guideline for `write_progrname_input` Subroutine

Arguments list

```
integer , intent(IN) :: i
real(DBL) , intent(IN) :: conv_threshold
integer , intent(IN) :: fnumb_in
character(*), intent(OUT) :: fname_in
character(*), intent(OUT) :: fname_out
```

`i` is the image on which the computation will be performed; `conv_threshold` is the SCF convergence threshold to use; `fnumb_in` is the integer that must be associated to the input file through the `open` statement; `fname_in` and `fname_out` are respectively the names of the input and output files, that need to be set.

Useful global variables/subroutines/functions

```
integer :: geom_len
real(DBL) :: image_geom(i,j)
character(*) :: element(i)
character(*) :: elabel(i)
integer function :: get_scfcycle()
subroutine :: write_pes_it(fnumb,n)
```

`geom_len` is the geometry length: being N the number of nuclei, `geom_len`= $3N$; `image_geom(i,j)`, where $1 \leq j \leq \text{geom_len}$, is a matrix of real numbers, containing the j -coordinate of the i -image, following the order

$$x_1, y_1, z_1, x_2, y_2, z_2, \dots, x_N, y_N, z_N;$$

the array of strings `element(i)`, where $1 \leq i \leq \text{geom_len}/3$, contains the chemical symbols of the N elements; `elabel(i)`, where $1 \leq i \leq \text{geom_len}/3$, contains the labels specified in the fifth column of the geometry blocks; `get_scfcycle()` function returns the integer specified by `#SCFCYCLE`; `write_pes_it(fnumb,n)` subroutine writes the `#PESINPUTTEMPLATE` block `n` in an opened file associated with `fnumb`.

Subroutine body

Firstly the subroutine must set the names for input and output files. This can be achieved with

```
fname_in = base_name//i_str//in_extension
fname_out = base_name//i_str//out_extension
```

where `base_name` is a global string defined in the current module, `i_str` is the transposition to characters of the integer `i`, and `in_extension` and `out_extension` are the input and output file extensions respectively.

After opening the input file `fname_in`, all the necessary information can be written in the appropriate format. Here the contents of the `#PESIN-PUTTEMPLATE` blocks can be pasted using the `write_pes_it(fnumb,n)` subroutine, while geometry, SCF cycles and SCF convergence threshold must be written manually using the above variables. If it does not do so by default, the keywords needed by the external program to calculate/write the atomic forces should be specified here. Once written, `fname_in` must be closed.

Guideline for `exec_programe` Subroutine

Arguments list

```
character(*), intent(IN) :: fname_in
character(*), intent(IN) :: fname_out !optional
logical,       intent(OUT) :: flag_conv !optional
```

`fname_in` is the input file name, that is generally required as an argument by the external program; `fname_out` is the output file name that is needed sometimes; `flag_conv` is used to store the convergence status: `.true.` if it has been achieved, `.false.` otherwise.

Useful global variables/subroutines/functions

```
character(*) :: pes_exec
integer       :: pes_proc
```

`pes_exec` is the executable name specified in `#PESEXEC`; while the integer `pes_proc` is the number of cores that the program will use, set by `#PESPROC`.

Subroutine body

This subroutine composes the command string to run the external program using the executable name stored in `pes_exec`, the file names, and the number of processors for the parallel run if they must be specified as command line arguments. The resulting string is executed by the operating system by passing it to the `execute_command_line()` subroutine. Sometimes, the exit code returned by the external program can be directly used to determine

if convergence has been achieved or not. If this is the case, the value of `flag_conv` should be set here.

A final note on external programs that use MPI for parallelization. Since Empathes also use MPI, the external program can be launched via `mpirun` only if Empathes is run without `mpirun`. If a parallel run of Empathes is desired, then the external program must be launched using the MPI library subroutine `MPI_Comm_spawn`.

Guideline for `read_programe_output` Subroutine

Arguments list

```
integer,      intent(IN) :: i
integer,      intent(IN) :: fnumb_out
character(*), intent(IN) :: fname_out
logical,      intent(OUT) :: flag_conv !optional
```

`i` is the image on which the computation has been performed; the integer `fnumb_out` must be used to open the output file named `fname_out`; `flag_conv` is used to store the convergence status: `.true.` if it has been achieved, `.false.` otherwise.

Useful global variables/subroutines/functions

```
real(DBL)      :: pes_energy(i)
real(DBL)      :: pes_forces(i,j)
integer function :: get_scfcycle()
subroutine     :: get_field(str,field,n,err_n,err_msg)
```

`pes_energy(i)` is a vector of reals used to store the energy of the i -image; `pes_forces(i,j)`, where $1 \leq j \leq \text{geom_len}$, is a matrix of reals that stores the atomic force j of the i -image, in the order $F_{x_1}, F_{y_1}, F_{z_1}, F_{x_2}, \dots, F_{z_N}$; `get_scfcycle()` function returns the integer specified by `#SCFCYCLE`; `get_field(str,field,n,err_n,err_msg)` subroutine can be used to extract the word `n` from the string `str`, that will be stored into `field`. If an error occurs, a non-zero value is returned in `err_n`, and an error message is set in `err_msg`.

Subroutine body

If the convergence status has been determined in the previous subroutine, the value of `flag_conv` can be used to establish whether the output should be read or not. Otherwise, the convergence status must be inferred by the output file itself, which therefore must be read in any case, and the `flag_conv` value must be set inside this subroutine.

This is the most critical subroutine to write, since the user must tailor its logic based on the format of the output file, which can differ sensibly from one program to another. For this purpose there is a subroutine, defined in the `mod_utility.f90` module, called `get_field()` that extract a specific field from a string of characters. This is a pretty basic subroutine and, at present, the only supported separator between fields is the blank space (one or more characters). This example shows its use

```
str = "Thisuuuisanuuexampleustring"
call get_field(str,field,4,err_n,err_msg)
```

Here the fourth field from the string `str` (i.e. the word “example”) is taken and saved in the `field` variable. It’s a good practice to ensure that `err_n` is zero before using the content of `field`.

If the computation executed by the external program converged, then the user must locate the position of the energy and the atomic forces, and store them inside `pes_energy(i)` and `pes_forces(i,:)`, respectively. It would be advisable to ensure that forces stored in `pes_forces(i,:)` are expressed in $E_h/\text{\AA}$.

1.11 Conclusion

The Nudged Elastic Band method frames a numerical algorithm useful to estimate the minimum energy path connecting pairs of (energy-minimum) molecular structures, belonging to the same potential energy surface. The underneath NEB and CI-NEB theories were here summarized, along with the implementation design of the Empathes code. Some usage examples employing different programs (namely Gaussian and Siesta) with the corresponding input files, as well as the results obtained, were also given.

The main purpose of Empathes was to extend the capabilities of the Siesta package to perform TS search, since at the start of my work this was not directly implemented in it. At the moment of writing, however, Siesta developers implemented the NEB in their code. Nevertheless, an external implementation like Empathes still makes sense because of its capability to perform single point calculations on all images in parallel by calling multiple instances of Siesta, that on the other hand is difficult to implement directly in the Siesta code and, as far as I know, it has not been done yet.

Probably the main value of Empathes is to provide an implementation of the NEB method that is independent from any specific quantum chemistry software. In this way, the end user has the freedom to keep using its software of choice and interface it with the NEB procedure (in the case this is lacking) by writing three simple subroutines.

Empathes is free software distributed under the GPLv3 license. Its source code, along with that of some utilities, can be downloaded from the Github page <https://github.com/marberti/empathes>. The original paper on Empathes appeared on Computer Physics Communications.[14]. The first production application of this code was the investigation of the hydrogen spillover from a Pd₄ cluster to its supporting material, a graphene sheet.[15] The interested reader can find this paper in the appendix.

Chapter 2

CO₂ Methanation

2.1 Introduction

The use of carbon dioxide as a raw material is important not only as a source of carbon, but also to mitigate its environmental impact as a greenhouse gas. Such use includes the direct approach, where CO₂ is not chemically altered, as well as chemical or biological conversion into useful products. Most existing commercial applications involve direct use, including food and beverage manufacturing, metal fabrication, dry cleaning, healthcare, fire extinguishing and the petroleum industry. Although still under development, chemical and biological use has attracted a lot of attention in recent years, in the context of applications that include the synthesis of fuels, chemicals and construction materials. In this respect, one of the most important reactions in the industrial field is the catalyzed transformation of carbon dioxide into methane.

The widely accepted mechanism for CO₂ methanation (Sabatier reaction) involves the combination of an endothermic process (CO₂ + H₂ → CO + H₂O, the reversed water gas shift reaction) with a strongly exothermic one (CO + 3 H₂ → CH₄ + H₂O).[16, 17] For the conversion it is therefore desirable that the catalyst is active at relatively low temperatures and selective towards methane. The catalysts that can be used are noble or non-noble metals, which can be sorted by decreasing activity in the order: Ru>Fe>Ni>Co>Rh>Pd>Pt. In addition to showing maximum activity, ruthenium has other desirable characteristics, such as high selectivity towards methane at low temperatures and high resistance to atmospheric oxidation.[18] There is a large number of computational studies in the literature that target the ruthenium (0001) surface as a catalyst for the methane reforming process.[19, 20, 21, 22] The main disadvantage of using ruthenium concerns its high cost and limited availability, which hinder large-scale in-

dustrial application. For this reason, the most used catalyst so far for CO₂ methanation is nickel supported on oxides, mainly γ -Al₂O₃: it shows indeed a remarkable activity and selectivity combined with an high availability and low cost.[23] However, some limiting and unwanted difficulties are still present: carbon deposition, sintering, the formation of Ni(CO)₄ (the poisonous Mond complex that, in addition to degrading the catalyst, generates a very dangerous by-product that has an high vapor pressure at room temperature) are phenomena that strongly affects the stability and activity of the catalyst. Today's research in the methanation process is therefore mainly related to the modification of the support and the addition of promoters in nickel-based catalytic systems.[24]

The main long-term objective of the computational research in this field is to discover chemical or physical modifications to be implemented on the nickel-based catalysts in order to get a more efficient realization of the conversion reaction of carbon dioxide into methane.[25, 26, 27, 28, 29, 30] Part of this thesis work was focused precisely in this context. In particular, the CO₂ methanation on the pristine nickel (111) surface was analyzed using computational methods based on atom centered basis functions (in contrast to that based on plane waves that are the standard in the literature). Using this investigation as a benchmark, the catalytic properties of two systems, obtained by depositing a single atom of either Ru or Fe on the aforementioned surface, were evaluated. This last study is part of the modern research on the so-called *Single Atom Catalysts* (SACs).[31, 32] From our current knowledge, there are still no studies of Fe/Ni systems as SAC, but only as bimetallic catalysts.[33] In order to achieve this goal, we proceeded by identifying: i) the methanation mechanism on the pure nickel surface using the calculation method of choice; and ii) the critical spots of the reaction, i.e. the highest activation barriers and the points where the mechanism bifurcates to lead to the formation of atomic carbon or other undesirable products.

2.2 Computational Details

In this study, the CO₂ methanation reaction was investigated on three different catalysts, all based on the nickel (111) surface. These are: 1) pristine nickel (111) surface; 2) nickel (111) decorated with a single Ru atom; and 3) nickel (111) decorated with a single Fe atom. The choice for Ru and Fe as small decorations on the main nickel surfaces is based on their activity with respect to the methanation reaction in question. It is publicly known that Ru is a better catalyst than Ni to produce CH₄, but since it is also more expensive, a number of studies tried to combine these two elements together in

many different shapes and ratios, and see the final effect on the methanation process. The same can be said for Fe, with the difference that Ni/Fe systems have not been investigated as thoroughly as the Ni/Ru ones.

Since the catalysts of choice are surfaces, it is best to use a software capable of determining the electronic structure using periodic boundary conditions. For this reason the Siesta software [4] was selected. Siesta has been developed with solid state physics in mind, but in contrast with the majority of other condensed matter codes that work using plane waves, Siesta uses a combination of numerical atomic orbitals (NAOs), pseudopotentials (to replace the core electrons), spacial confinement of the atomic orbitals, and linear scaling techniques.[34] The resulting objects are generally referred to as pseudoatomic orbitals (PAOs), being this approach to solve the electronic structure problem among the fastest to date.

The pristine nickel (111) surface model is constituted by three layers of 16 atoms each, for a total of 48. It is reported in figure 2.1, that also shows the naming convention for the surface sites. The other two catalysts are built from this clean model by adding a Ru and a Fe atom, respectively. Both Ru and Fe are placed in an HCP site, since this resulted to be the most stable position for the hetero atoms in both cases. The theoretical method employed for all calculation was the *density functional theory* (DFT), in which the PBE functional was used along with a double zeta quality basis set with polarization functions (DZP). In all calculations, the total electronic spin was not fixed to a specific value, giving the software the possibility to fit the best spin multiplicity to each system. A mesh cutoff of 450 Ry was used, along with a Monkhorst-Pack grid of $4 \times 4 \times 1$: the former defines the finesse of the integration grid in the real space, while the latter is related to that in the reciprocal space. It is important to note that in no case frequencies were calculated after an optimization due to their prohibitive computational time. This has some implications, like: 1) some of the structures found in the following could not be true energy minima but other kind of stationary points on the potential energy surface; and 2) the *zero point energy* (ZPE) was not computed, and hence the final absolute energy is in all cases is the sole electronic energy.

Since the interest of this study is on the catalytic performance of these three different surfaces, a method is required to locate the transition states for each elementary step involved in the CO₂ methanation reaction. For this purpose, the Empathes code illustrated in chapter 1 was used. The general procedure to investigate an elementary step is: 1) select two good starting structures for both the reactant and the product; 2) perform a geometry optimization of the two aforementioned structures; 3) use the optimized structures as endpoints for the CI-NEB calculation performed by Empathes.

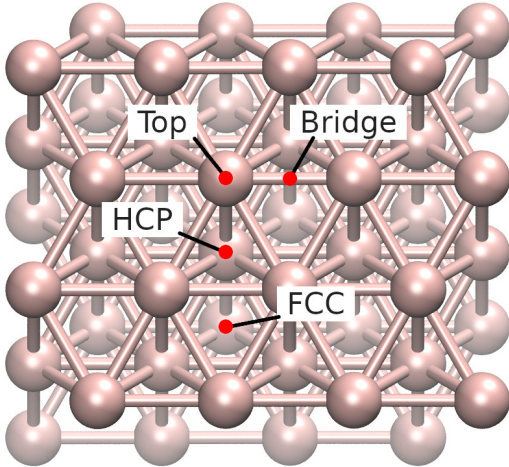


Figure 2.1: Naming convention for the adsorption sites on nickel (111) surface.

Generally, the parameters used for these CI-NEB calculations were: an elastic band composed of six images, generated using the IDPP algorithm and then optimized with FIRE until a value of $3.0 \cdot 10^{-3} E_h/\text{\AA}$ is reached on the force norm of all the images. There were, however, some cases in which the CI-NEB calculations were difficult to converge. When this occurs the relative settings for that specific calculation are provided, otherwise it is implicit that the default values were used.

As a final note, when analyzing the results of the CI-NEB calculations, it was chosen that: when the MEP of a given elementary step locates an intermediate next to the reactant or the product that has a lower energy than them, then ΔE_r and forward and backward activation energies are computed with respect to this intermediate. An advantage of NEB is that it provides a description of the potential energy surface: since Siesta optimization of the reactant and product structures do not necessarily end up in an energy minimum (i.e. it can happen that it stops at another kind of stationary point), the MEP information can be used to understand if the endpoints are indeed minima, or if there is a minimum in their proximity through which the reaction passes. Accordingly, when there are intermediates next to the endpoints of the MEP, their energy is used in the estimation of the energetics of that elementary step, because, even if the intermediates are not rigorous PES minima (they were not optimized in that sense), using them should give results closer to the real ones than not doing so.

2.3 Reactions, Hopping Processes and Migrations

Several preliminary calculations were performed to investigate some phenomena that occur on the nickel (111) surface. The adsorption and desorption energies of some species of interest were computed, such as: CO₂ ($\Delta E_{\text{ads}} = -88.2 \text{ kJ/mol}$); CH₄ ($\Delta E_{\text{des}} = 28.4 \text{ kJ/mol}$); and H₂O ($\Delta E_{\text{des}} = 70.3 \text{ kJ/mol}$). Moreover, a series of CI-NEB calculations were performed to investigate: 1) the dissociation of molecular hydrogen; 2) the hopping processes of the H, C and O atomic species between two different adjacent sites on the surface; and 3) the formation of a water molecule in two steps, i.e. O + H → OH followed by OH + H → H₂O. Table 2.1 reports the reaction energy (ΔE_r) and the forward and backward activation energies ($E_{a\rightarrow}$ and $E_{a\leftarrow}$, respectively) associated with each of them.

The H₂ dissociation was investigated preparing, in the reactant structure, an hydrogen molecule placed vertically above a top site, at a H–Ni optimized distance of 2.246 Å; whereas in the product geometry the two H atoms are on adjacent sites on the surface. This dissociation has an huge ΔE_r of -155.6 kJ/mol, and an activation energy so small (only 1.3 kJ/mol) that one can safely assume that H₂ reacts instantly whenever it comes close enough to the surface.[35]

The hopping processes of the H, C, and O atomic species were all investigated moving from an FCC to an HCP site. First of all, the three ΔE_r associated with them show that H has no preferred site on the surface, C prefers to stay on an HCP site, while O likes FCC more.[36] The activation energies indicate that hydrogen can move more easily on the surface than the other two species, whereas oxygen atoms are the most static. In the following discussion on the methanation process, many elementary steps will involve hydrogen atoms: their high mobility on the surface is used as foundation for the assumption that they are easily available to react with other species in every place at every moment.

The formation of molecular water on the surface was addressed through the investigation of the two steps O + H → OH and OH + H → H₂O. Both of them are moderately endothermic (45.5 and 65.5 kJ/mol, respectively), and in both cases the activation energy is above 115 kJ/mol. It is worth note that the values of the energy barriers for the backwards reactions of the two elementary steps, equal to 71.1 and 60.0 kJ/mol, compare within ∼ 20 kJ/mol with those recently reported by Che et al.[37] These results indicate that, at equilibrium condition, water spontaneously dissociates on the nickel surface. The common setup of the methanation process, however,

Table 2.1: Reactions and hopping processes on pristine Ni (111) surface. All energies expressed in kJ/mol.

Code	Elem. Step	ΔE_r	$E_{a\rightarrow}$	$E_{a\leftarrow}$
ND1	$H_2 \longrightarrow 2 H$	-155.6	1.3	156.9
NW1	$O + H \longrightarrow OH$	45.5	116.7	71.1
NW2	$OH + H \longrightarrow H_2O$	65.5	125.5	60.0
NH1	$H_{FCC} \longrightarrow H_{HCP}$	0.2	12.2	12.1
NH2	$C_{FCC} \longrightarrow C_{HCP}$	-5.6	22.8	28.4
NH3	$O_{FCC} \longrightarrow O_{HCP}$	10.7	47.9	37.2

is given by an hot stream of gasses (a mix of CO_2 and H_2) fluxed over the catalyst: being a very different condition than equilibrium, the water that is produced on the surface is promptly substituted by new molecules from the incoming stream.

Regarding the Ru- and Fe-decorated surface models, they have a decent amount of nickel (111) surface around the decoration site that can be used to study the migration processes of some chemical species between the two environments. This is important because, depending on the ratio between decoration sites and clean surface in a real material, some elementary steps involved in the methanation reaction can occur next to the decoration, while others far away from it. The chemical species taken into account are H, C, CH , CH_2 , and CH_3 .

The results of the CI-NEB calculations, reported in table 2.2, show that: 1) atomic hydrogen prefers by a large amount to stay on the nickel surface rather than next to a decoration of any kind, moreover the activation energies required to move away from them are amazingly low; 2) atomic carbon, on the other hand, prefers to stay close to the decoration (especially if it is Ru), being the activation energies to move away from them the highest; 3) both CH and CH_2 prefer the decoration to the clean nickel surface, moreover both of them like Ru more than Fe; and 4) CH_3 prefers slightly to be close to Fe, but moves away with great ease from Ru.

2.4 CO_2 Methanation on Pristine Ni (111)

A total of 16 chemical species and 28 elementary steps were taken into account to study the $CO_2 + 4 H_2 \longrightarrow CH_4 + 2 H_2O$ reaction on the pristine nickel (111) surface. Figure 2.2 shows the reference scheme about the numbering convention adopted for the elementary steps: in the following discussion, a letter is used as a prefix to these numbers to indicate on which surface

Table 2.2: Migrations from decorated sites to pristine Ni (111) surface. All energies expressed in kJ/mol.

Code	Elem.	Step	ΔE_r	$E_{a\rightarrow}$	$E_{a\leftarrow}$
RM1	H/Ru	\longrightarrow H/Ni	-27.9	0.1	28.0
RM2	C/Ru	\longrightarrow C/Ni	85.1	114.2	29.1
RM3	CH/Ru	\longrightarrow CH/Ni	27.5	59.7	32.2
RM4	CH ₂ /Ru	\longrightarrow CH ₂ /Ni	15.1	23.1	7.9
RM5	CH ₃ /Ru	\longrightarrow CH ₃ /Ni	-31.2	22.2	53.4
FM1	H/Fe	\longrightarrow H/Ni	-71.1	4.2	75.4
FM2	C/Fe	\longrightarrow C/Ni	44.0	64.7	20.7
FM3	CH/Fe	\longrightarrow CH/Ni	8.1	45.6	37.5
FM4	CH ₂ /Fe	\longrightarrow CH ₂ /Ni	4.3	17.4	13.1
FM5	CH ₃ /Fe	\longrightarrow CH ₃ /Ni	8.2	25.6	17.3

model the discussed elementary step refers (it can be N, R or F for pristine nickel, Ru- and Fe-decorated, respectively). Table 2.3 reports ΔE_r and activation energies associated with each of them as investigated on the pristine surface model. It is worth noting that these results are in general agreement with those reported in the literature.[27, 38] A more detailed description of each elementary step follows.

N01: CO₂ \longrightarrow CO + O The first elementary step investigated on the pristine nickel (111) surface is the carbon dioxide dissociation: CO₂ \longrightarrow CO + O. To locate its transition state, a structure was used as reactant where the carbon of CO₂ is placed over a bridge site, while the two oxygens are on two nearby HCP and FCC sites. Here the O–C–O angle is 129.8°, a very distorted geometry for CO₂ as also found by Wang et al.[39] In the product structure, instead, there are an atomic oxygen and a CO molecule both on two neighboring HCP sites (the latter bonded through the carbon).

The smooth minimum energy path, reported in figure 2.3, locates the transition state at image three. The same figure shows also the TS structure, in which the (previously) FCC oxygen, the one that will dissociate, is moving towards the near HCP site. In this geometry the O–C–O angle is 116.9°.

This elementary step has a ΔE_r of -92.9 kJ/mol, while its activation energy is 48.9 kJ/mol. The very exothermic ΔE_r should not surprise considering the very distorted geometry of the adsorbed CO₂ and the high stability of the carbon monoxide species.

N02: CO₂ + H \longrightarrow COOH Another route that carbon dioxide can

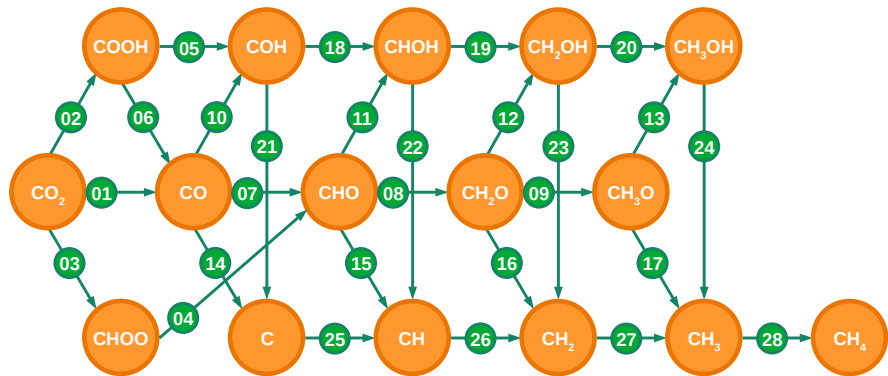


Figure 2.2: Numbering convention for the elementary steps (green arrows) occurring between the chemical species (orange circles) involved in the methanation reaction.

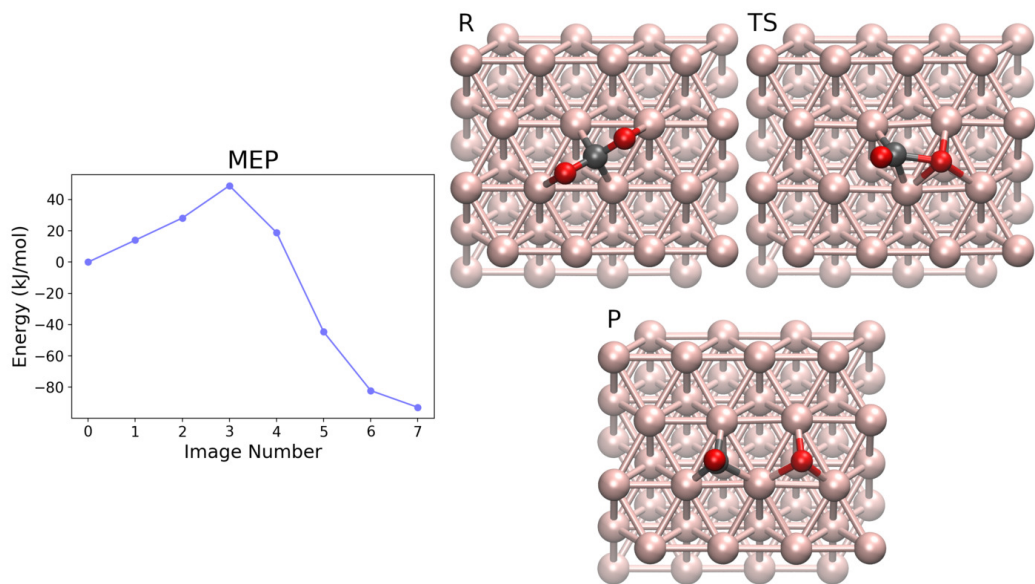


Figure 2.3: MEP and geometries of interest of the N01 elementary step: $\text{CO}_2 \rightarrow \text{CO} + \text{O}$. Reactant, image 0; TS, image 3; Product, image 7. Colors: C black; O red; Ni rose gold.

Table 2.3: Elementary steps on pristine Ni (111) surface. All energies expressed in kJ/mol.

Code	Elem. Step	ΔE_r	$E_{a\rightarrow}$	$E_{a\leftarrow}$
N01	$\text{CO}_2 \longrightarrow \text{CO} + \text{O}$	-92.9	48.9	141.8
N02	$\text{CO}_2 + \text{H} \longrightarrow \text{COOH}$	9.5	75.3	65.8
N03	$\text{CO}_2 + \text{H} \longrightarrow \text{CHOO}$	18.7	72.2	53.5
N04	$\text{CHOO} \longrightarrow \text{CHO} + \text{O}$	18.2	98.0	79.8
N05	$\text{COOH} \longrightarrow \text{COH} + \text{O}$	-17.6	113.7	131.3
N06	$\text{COOH} \longrightarrow \text{CO} + \text{OH}$	-109.2	51.6	160.8
N07	$\text{CO} + \text{H} \longrightarrow \text{CHO}$	138.0	152.4	14.4
N08	$\text{CHO} + \text{H} \longrightarrow \text{CH}_2\text{O}$	63.6	84.3	20.7
N09	$\text{CH}_2\text{O} + \text{H} \longrightarrow \text{CH}_3\text{O}$	41.8	71.5	29.7
N10	$\text{CO} + \text{H} \longrightarrow \text{COH}$	121.9	194.2	72.2
N11	$\text{CHO} + \text{H} \longrightarrow \text{CHOH}$	99.4	126.2	26.8
N12	$\text{CH}_2\text{O} + \text{H} \longrightarrow \text{CH}_2\text{OH}$	80.0	120.0	40.1
N13	$\text{CH}_3\text{O} + \text{H} \longrightarrow \text{CH}_3\text{OH}$	79.6	133.7	54.0
N14	$\text{CO} \longrightarrow \text{C} + \text{O}$	108.2	233.6	125.4
N15	$\text{CHO} \longrightarrow \text{CH} + \text{O}$	-52.7	87.7	140.3
N16	$\text{CH}_2\text{O} \longrightarrow \text{CH}_2 + \text{O}$	-42.6	75.6	118.3
N17	$\text{CH}_3\text{O} \longrightarrow \text{CH}_3 + \text{O}$	-88.2	111.2	199.4
N18	$\text{COH} + \text{H} \longrightarrow \text{CHOH}$	113.5	124.8	11.3
N19	$\text{CHOH} + \text{H} \longrightarrow \text{CH}_2\text{OH}$	33.4	66.5	33.1
N20	$\text{CH}_2\text{OH} + \text{H} \longrightarrow \text{CH}_3\text{OH}$	49.3	95.6	46.3
N21	$\text{COH} \longrightarrow \text{C} + \text{OH}$	34.3	166.4	132.1
N22	$\text{CHOH} \longrightarrow \text{CH} + \text{OH}$	-105.6	42.6	148.2
N23	$\text{CH}_2\text{OH} \longrightarrow \text{CH}_2 + \text{OH}$	-74.8	51.1	126.0
N24	$\text{CH}_3\text{OH} \longrightarrow \text{CH}_3 + \text{OH}$	-73.7	117.4	191.1
N25	$\text{C} + \text{H} \longrightarrow \text{CH}$	-12.2	87.6	99.9
N26	$\text{CH} + \text{H} \longrightarrow \text{CH}_2$	55.8	73.6	17.8
N27	$\text{CH}_2 + \text{H} \longrightarrow \text{CH}_3$	21.6	66.3	44.7
N28	$\text{CH}_3 + \text{H} \longrightarrow \text{CH}_4$	57.3	104.9	47.6

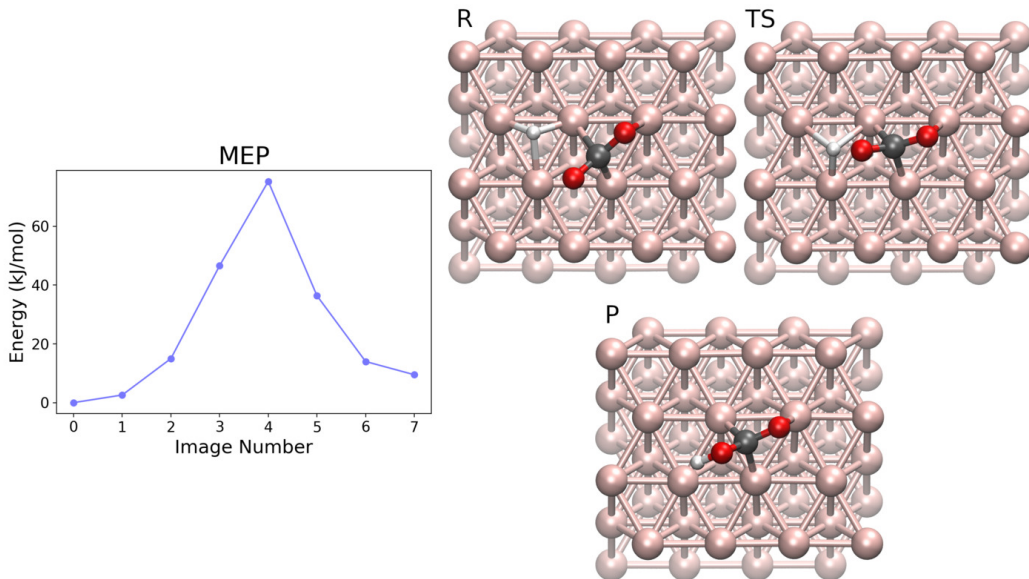


Figure 2.4: MEP and geometries of interest of the N02 elementary step: $\text{CO}_2 + \text{H} \longrightarrow \text{COOH}$. **R**eactant, image 0; **TS**, image 4; **P**roduct, image 7. Colors: H white; C black; O red; Ni rose gold.

follow is an hydrogenation that gives rise to the COOH alcoholic species. To study this elementary step, CO_2 was placed similarly as in N01, but here the HCP oxygen is slightly off center because of the presence of a near FCC atomic hydrogen. In the product structure the said oxygen and hydrogen are bonded together, and the resulting hydroxyl group is pointing to the underlying surface.

As reported in figure 2.4, the MEP presents a peak at image four, the transition state. By inspecting its structure, one can see that the atomic hydrogen is well centered on the FCC site, and that the CO_2 's oxygen moved towards it, the distance between the two being 1.414 Å (while being 2.396 Å in the reactant and 0.994 Å in the product).

The absolute energies of reactant and product do not differ significantly: this elementary step has a small ΔE_r of 9.5 kJ/mol, whereas its activation energy is 75.3 kJ/mol.

N03: $\text{CO}_2 + \text{H} \longrightarrow \text{CHOO}$ This elementary step is another hydrogenation, but this time on carbon. In the reactant, the CO_2 position is the same as in N01: C over a bridge site, the O–C–O angle being 129.8° . Additionally, an atomic hydrogen is placed on a bridge site next to that of C. In the product structure the CHOO species is adsorbed to the nickel surface via the

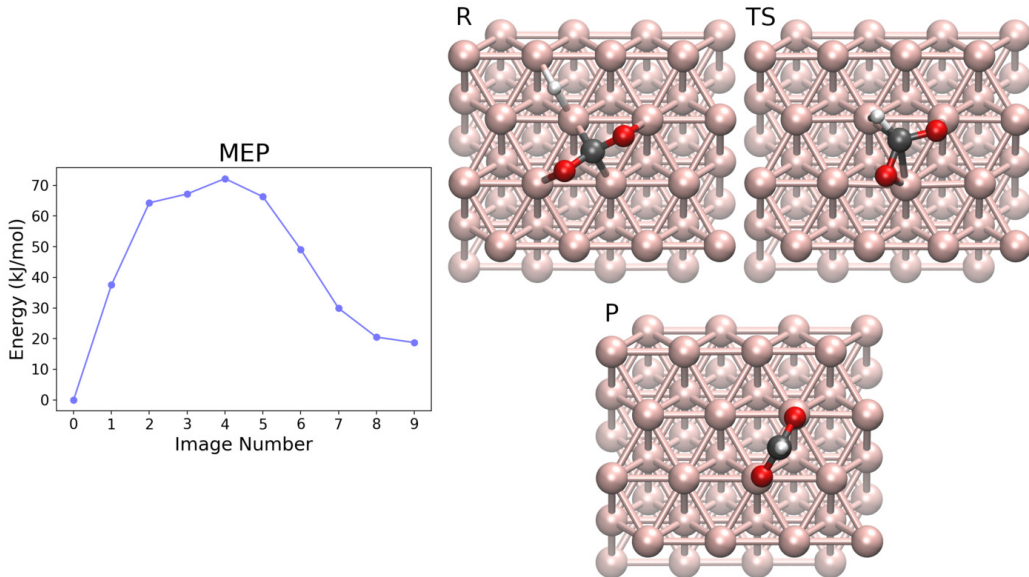


Figure 2.5: MEP and geometries of interest of the N03 elementary step: $\text{CO}_2 + \text{H} \longrightarrow \text{CHOO}$. **R**eactant, image 0; **TS**, image 4; **P**roduct, image 9. Colors: H white; C black; O red; Ni rose gold.

oxygens, both of which are located on top sites, while the CH group points towards the vacuum.

The calculation performed to locate the transition state was not flawless since it was possible to optimize an eight images elastic band only up to $6.6 \cdot 10^{-3} E_h/\text{\AA}$ on all force norms, using the FIRE algorithm. In figure 2.5 both the MEP and the TS (image four) are reported. The transition state structure shows that an oxygen of CO_2 moved towards its final top site, and that the atomic hydrogen is closer to the carbon while also being partially attracted by a top site of the surface.

The ΔE_r and activation energy of this elementary step are 18.7 and 72.2 kJ/mol, respectively. As a final note, the bridged position of the atomic hydrogen in the reactant structure is suspicious to say the least: maybe the carbon in the bridge site nearby has a stabilizing effect on the hydrogen making the whole structure a legit energy minimum, but no calculations were performed to prove it. However, if the real energy minimum were to be the one with the hydrogen in either the HCP or the FCC site, then both the ΔE_r and activation energy should increase by ~ 10 kJ/mol at most.

N04: $\text{CHOO} \longrightarrow \text{CHO} + \text{O}$ The previously seen CHOO species can then dissociate, giving atomic oxygen and CHO. To study this elementary

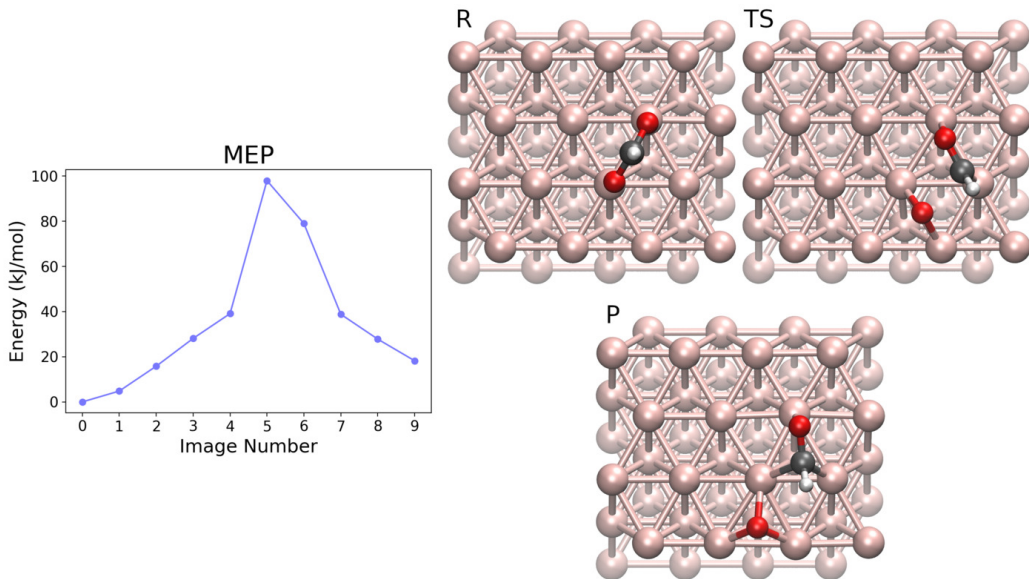


Figure 2.6: MEP and geometries of interest of the N04 elementary step: $\text{CHOO} \longrightarrow \text{CHO} + \text{O}$. Reactant, image 0; TS, image 5; Product, image 9. Colors: H white; C black; O red; Ni rose gold.

step, the geometry of choice for the reactant was the same as the product of N03, in which CHOO is bonded to the surface via the oxygens, both on two different top sites. On the other hand, in the product structure the CHO species is overall on an HCP site: more specifically C is slightly towards a bridge site, whereas O is close to a top site. Finally, the atomic oxygen is on an HCP site close to carbon.

The CI-NEB calculation was performed using eight images, but it was possible to optimize the elastic band only up to $6.4 \cdot 10^{-3} E_h/\text{\AA}$ using the FIRE algorithm. In figure 2.6 the obtained MEP is reported, which is very smooth except for images five (the TS) and six, that have a much higher energy than the rest. Locking at the TS structure, both the atomic oxygen and the CHO species as a whole occupy two different bridge sites. To be more specific, the C–O bond is parallel to the underlying Ni–Ni bond, where both nuclei C and O are positioned almost on two adjacent top sites.

The ΔE_r for this elementary step is 18.2 kJ/mol (very similar to the one of N03), whereas the activation energy is 98.0 kJ/mol.

N05: $\text{COOH} \longrightarrow \text{COH} + \text{O}$ To investigate the $\text{COOH} \longrightarrow \text{COH} + \text{O}$ elementary step, a reactant structure was chosen in which the COOH species is adsorbed on the nickel surface by means of the C–O bond that is placed on

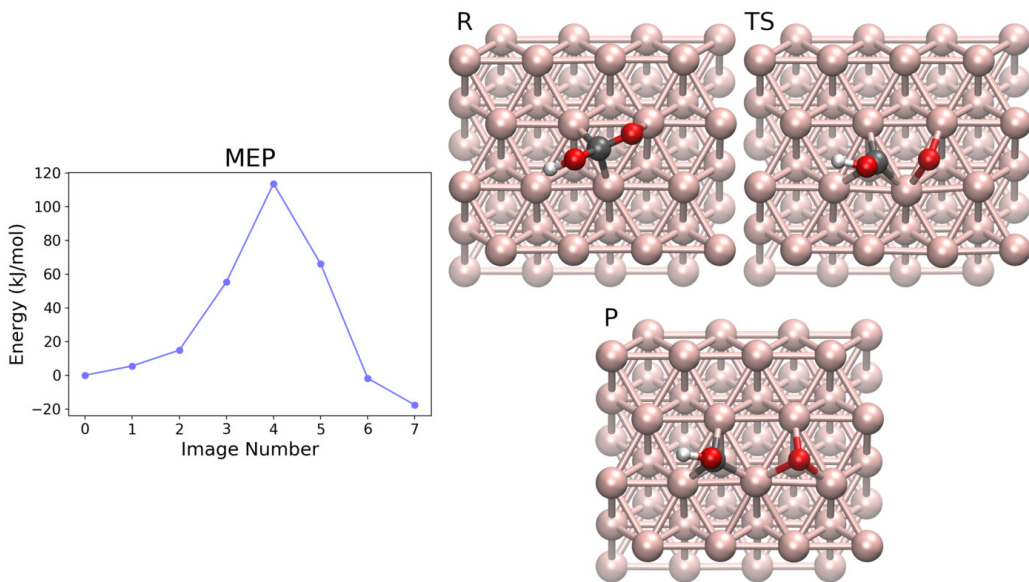


Figure 2.7: MEP and geometries of interest of the N05 elementary step: $\text{COOH} \longrightarrow \text{COH} + \text{O}$. Reactant, image 0; TS, image 4; Product, image 7. Colors: H white; C black; O red; Ni rose gold.

an FCC site. Here the hydroxyl group is lifted up from the surface, with an orientation by which the hydrogen points towards it. Concerning the product geometry, both the atomic oxygen and the COH fragment are placed on two neighboring HCP sites, the latter via its carbon.

The MEP of figure 2.7 shows a single peak at image four. An examination of the transition state geometry reveals a dissociating oxygen on a bridge site, and a COH species slightly shifted towards its final HCP site. Here the C–O distance is 1.828 Å, while in the reactant it was 1.292 Å.

This is a slightly exothermic elementary step with a ΔE_r of -17.6 kJ/mol, and an high activation energy of 113.7 kJ/mol.

N06: $\text{COOH} \longrightarrow \text{CO} + \text{OH}$ The N06 step is about the dissociation of the COOH species into CO and OH. To locate its transition state, a structure was chosen, as reactant, in which the COOH species is adsorbed on the nickel surface through a bridged C and a top O, the C–O bond in question being overall on an FCC site. The oxygen of the hydroxyl group, instead, is not close to the surface, and its hydrogen is pointing upwards. In the product geometry, both the CO molecule and the hydroxyl group are adsorbed on two neighboring FCC sites, the former via C while the latter through O.

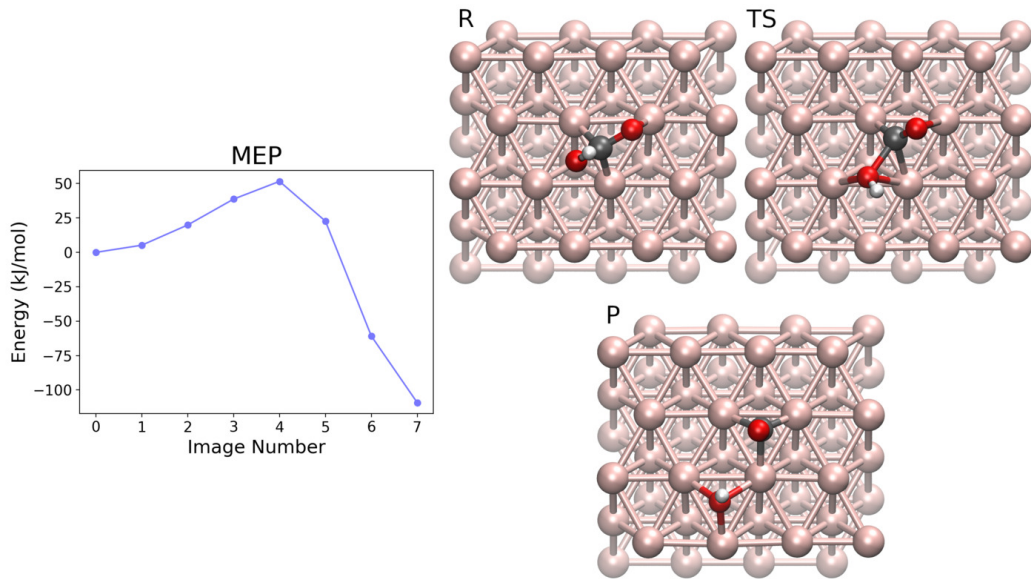


Figure 2.8: MEP and geometries of interest of the N06 elementary step: $\text{COOH} \longrightarrow \text{CO} + \text{OH}$. Reactant, image 0; TS, image 4; Product, image 7. Colors: H white; C black; O red; Ni rose gold.

As shown in figure 2.8, the found MEP is very smooth, with a maximum at image four. The transition state geometry is similar to the one of the reactant, the differences being: 1) the hydroxyl group is close to a bridge site of the nickel surface; and 2) the carbonyl oxygen is slightly lifted from the surface.

The huge difference between the absolute energies of product and reactant gives a ΔE_r of -109.2 kJ/mol, whereas the activation energy is 51.6 kJ/mol.

N07: $\text{CO} + \text{H} \longrightarrow \text{CHO}$ In order to investigate the hydrogenation of carbon dioxide that gives the formyl CHO species, it was chosen, as reactant, a structure where both CO and the atomic H were on two neighboring HCP sites (the former adsorbed via C). In the product, the CHO species is adsorbed with its C–O bond on the FCC site between the two aforementioned HCP sites, with C on a bridge site and O on a top site. In this geometry H is pointing upward, and the resulting O–C–H angle is 114.2° .

To locate the transition state, six images were used in the CI-NEB calculation. The optimization was carried out using the FIRE algorithm. It was possible, however, to optimize the whole elastic band only up to $9.9 \cdot 10^{-3} E_h/\text{\AA}$. Nevertheless, the instability is mainly focused on the first half of the band, where there are a very low energy TS and an intermediate, as shown

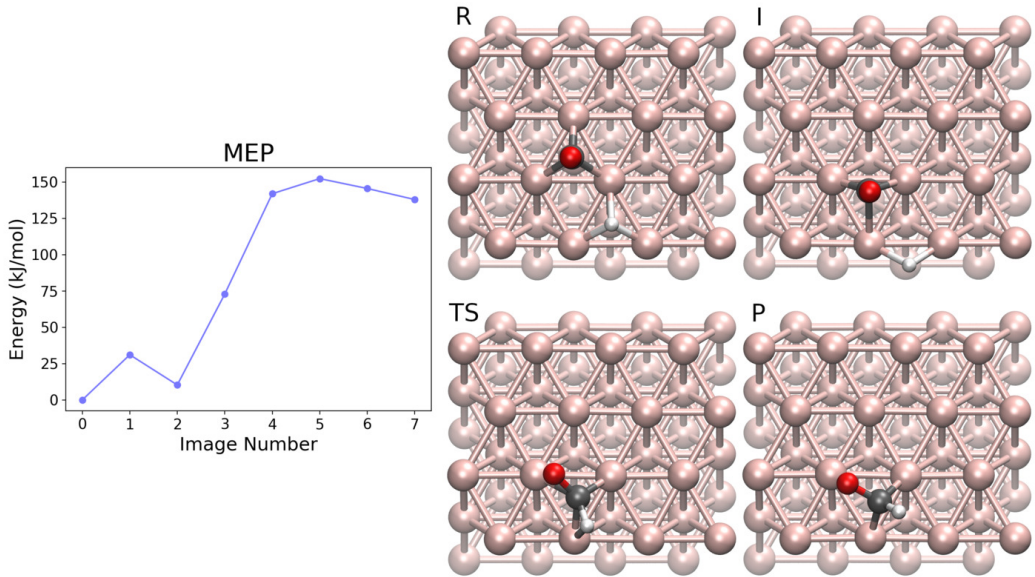


Figure 2.9: MEP and geometries of interest of the N07 elementary step: $\text{CO} + \text{H} \longrightarrow \text{CHO}$. **R**eactant, image 0; **I**ntermediate, image 2; **TS**, image 5; **P**roduct, image 7. Colors: H white; C black; O red; Ni rose gold.

in the MEP of figure 2.9. The last three images of the elastic band are more “relaxed”, being the total force norm below $3.0 \cdot 10^{-3} E_h/\text{\AA}$ for all of them. Thus, it is safe to assume that the global TS is sufficiently optimized to be used for the estimation of the activation energy.

The geometry of the intermediate shows that both CO and H moved towards two FCC sites below their original positions. The reaction then proceeds to the TS at image five, in which the atomic hydrogen is on a top site of the nickel surface, very close to the carbon. The TS geometry is extremely similar to that of the product, the difference being a general, global rotation of the whole CHO species, that in TS is more leaned towards the surface.

As it often happens when there is a CO transformation, this elementary step is extremely endothermic, with a ΔE_r of 138.0 kJ/mol. The activation energy is really high at 152.4 kJ/mol, but since its module is very close to that of ΔE_r , this means that the backward process is hugely favored with an activation energy of 14.4 kJ/mol.

N08: $\text{CHO} + \text{H} \longrightarrow \text{CH}_2\text{O}$ This elementary step was investigated using, as reactant, a geometry where the CHO species is mainly adsorbed over an FCC site, with the carbon slightly shifted towards a bridge site,

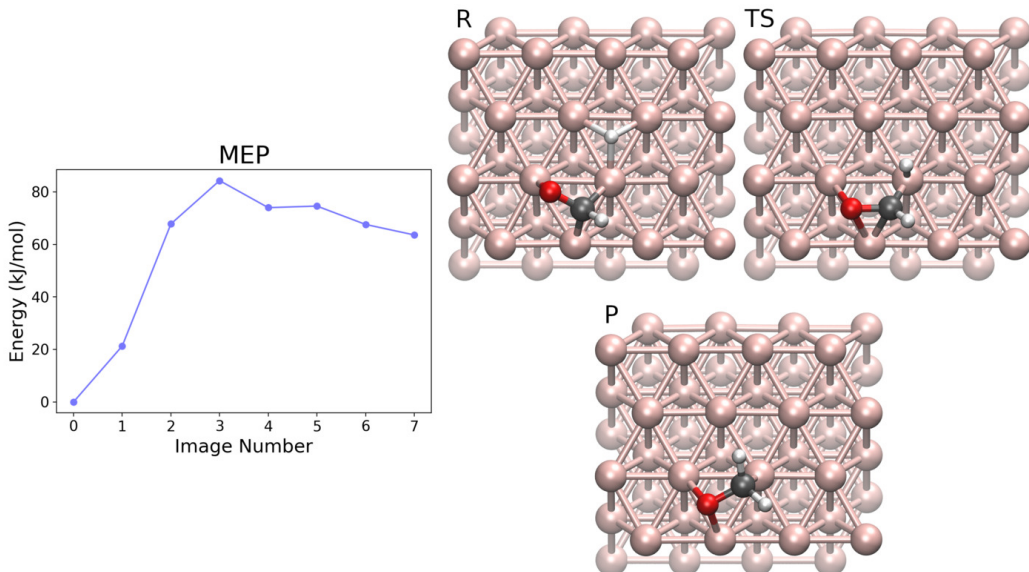


Figure 2.10: MEP and geometries of interest of the N08 elementary step: $\text{CHO} + \text{H} \longrightarrow \text{CH}_2\text{O}$. **R**eactant, image 0; **TS**, image 3; **P**roduct, image 7. Colors: H white; C black; O red; Ni rose gold.

and the oxygen on a top site. The atomic hydrogen is, instead, on an FCC site nearby. In the product structure the CH_2O species is overall still on the original FCC site, but this time the positions are inverted: C is slightly shifted towards a top site, while O is over a bridge site.

Figure 2.10 shows a generally smooth MEP, where the TS is located at image three. Its structure reveals a strange arrangement for the CHO species, which overall is still on the original FCC site, but with both C and O on two different bridge sites. In the meantime, the atomic hydrogen moved to a top site in order to approach the CH group.

This elementary step has a moderate endothermic ΔE_r of 63.6 kJ/mol, its activation energy being 84.3 kJ/mol.

N09: $\text{CH}_2\text{O} + \text{H} \longrightarrow \text{CH}_3\text{O}$ Next there is the CH_2O hydrogenation. The reactant structure was prepared adding to the product of N08 an atomic hydrogen in the HCP site just in front of the CH_2 group, and then optimizing. As a result, the CH_2O species shifted imperceptibly, thus centering the oxygen over the bridge site (compare the reactant of figure 2.11 with the product of figure 2.10), whereas the atomic hydrogen is not perfectly centered on the HCP site but slightly away from the CH_2 group. The product structure, on the other hand, has the CH_3O species adsorbed to the surface

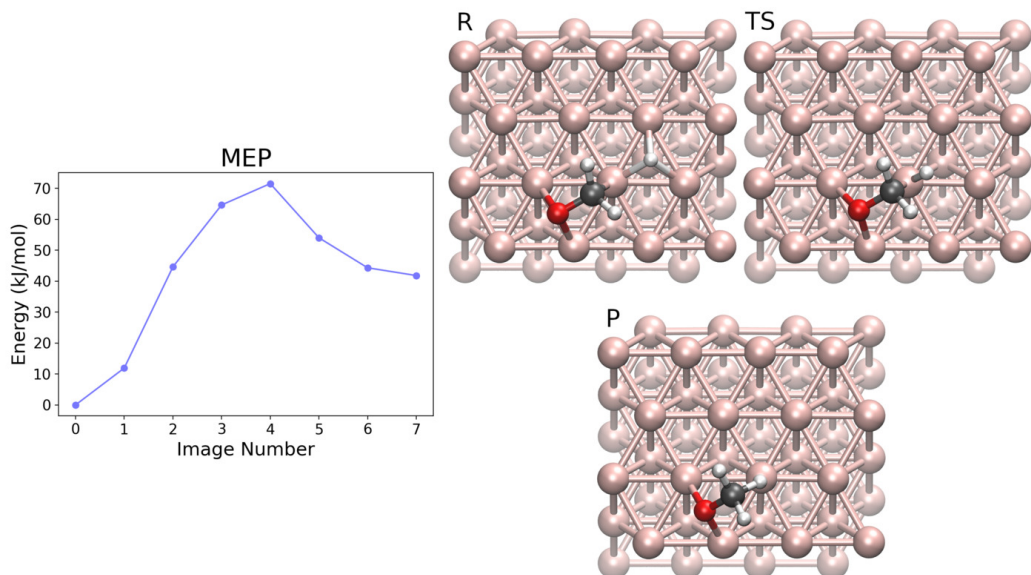


Figure 2.11: MEP and geometries of interest of the N09 elementary step: $\text{CH}_2\text{O} + \text{H} \longrightarrow \text{CH}_3\text{O}$. **R**eactant, image 0; **TS**, image 4; **P**roduct, image 7. Colors: H white; C black; O red; Ni rose gold.

only through its oxygen (that did not move from the original bridge site), while the methyl group points upward, far away from the surface.

Figure 2.11 shows a smooth minimum energy path, whose transition state is located at image four. The TS structure is as expected: the atomic hydrogen approached the CH_2 group, here being almost over the same top site occupied by C. Furthermore, the CH_2O species barely moved as a whole towards the hydrogen, as can be deduced by the off center position of the oxygen with respect to the underlying bridge site.

Even this hydrogenation elementary step has an endothermic ΔE_r of 41.8 kJ/mol, while its activation energy is 71.5 kJ/mol.

N10: $\text{CO} + \text{H} \longrightarrow \text{COH}$ The N10 step investigates the CO hydrogenation on oxygen. It was studied using a reactant structure in which the CO molecule and the atomic hydrogen were placed on two neighboring HCP sites, the former through its carbon. In the product, instead, the CO fragment is pretty much on the same position as in the reactant, the difference being that the hydrogen is no more adsorbed on the nickel surface but bonded to the oxygen.

The MEP has a peak at image four, as shown in figure 2.12. The TS structure is characterized by an inclined CO, whose oxygen is trying to reach

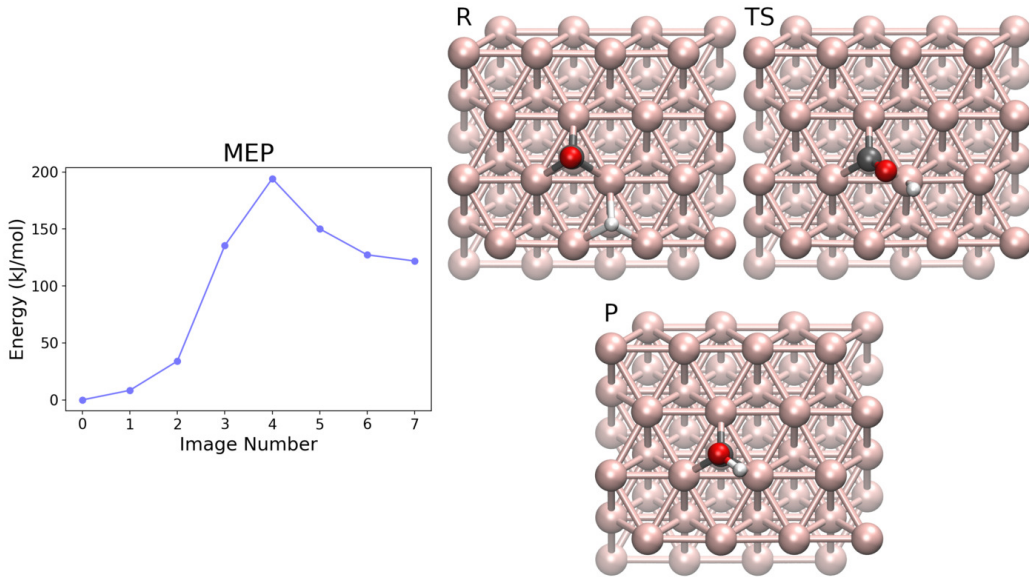


Figure 2.12: MEP and geometries of interest of the N10 elementary step: $\text{CO} + \text{H} \longrightarrow \text{COH}$. Reactant, image 0; **TS**, image 4; Product, image 7. Colors: H white; C black; O red; Ni rose gold.

the atomic hydrogen that in turn moved almost over the near top site.

As it was the case with N07 ($\text{CO} + \text{H} \longrightarrow \text{CHO}$), the ΔE_r of N10 is very endothermic: 121.9 kJ/mol. This time, however, the activation energy is higher, being 194.2 kJ/mol. This means that: 1) the hydrogenation of CO is easiest on the carbon than on the oxygen, but 2) if the COH species happens to be produced, that is more stable than CHO, since the activation energies for the dissociation reactions are 72.2 and 14.4 kJ/mol, respectively.

N11: $\text{CHO} + \text{H} \longrightarrow \text{CHOH}$ To investigate this elementary step, it was chosen a reactant structure in which the CHO species is globally over an FCC site (being C slightly towards a bridge site, and O slightly over a top site), while the atomic hydrogen is on an FCC site next to it. The product structure is very similar to that of N10, the only difference being the position of an hydrogen, here bonded to oxygen instead that to the nickel surface, giving rise to an hydroxyl group.

There were no issues in the CI-NEB calculation, and the MEP reported in figure 2.13 shows a peak at image four. The transition state has an energy not to different from that of the product, while its structure shows that the atomic hydrogen is placed on a bridge site near the oxygen, which in turn moved away slightly from its original top position.

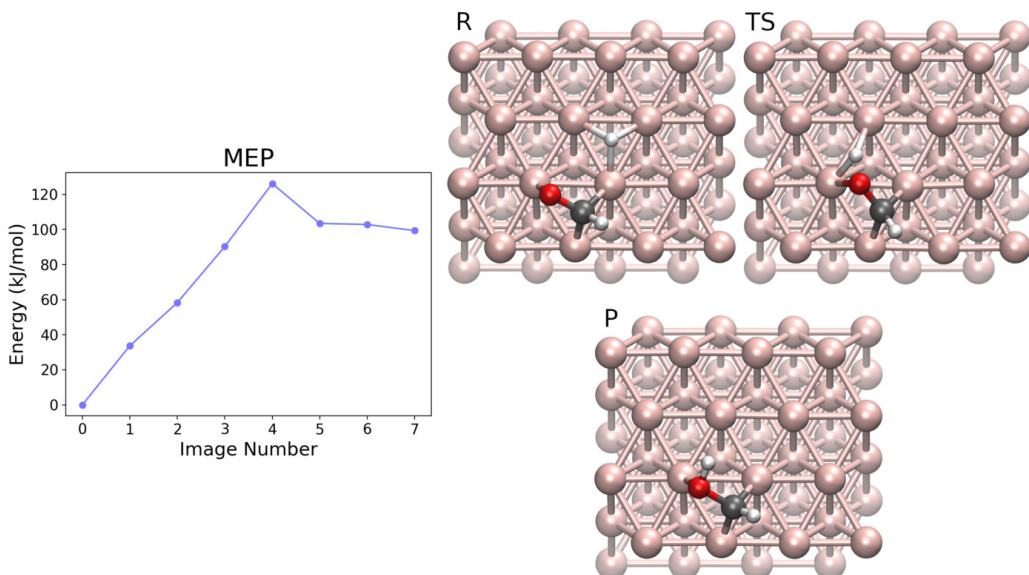


Figure 2.13: MEP and geometries of interest of the N11 elementary step: $\text{CHO} + \text{H} \longrightarrow \text{CHOH}$. **R**eactant, image 0; **TS**, image 4; **P**roduct, image 7. Colors: H white; C black; O red; Ni rose gold.

The ΔE_r and activation energy for this elementary step are 99.4 and 126.2 kJ/mol, respectively. From these values it can be deduced that the activation energy for the backward process is quite low, making the CHOH species prone to dissociate.

N12: $\text{CH}_2\text{O} + \text{H} \longrightarrow \text{CH}_2\text{OH}$ The transition state of the N12 elementary step was located using, as reactant, a structure in which the CH_2O species is overall above an FCC site (more specifically C is near a top site, while O is on a bridge site), whereas the atomic hydrogen is on an HCP site close to the oxygen. The product geometry, on the other hand, is very similar to that of the reactant, the only difference being the position of an hydrogen, here bonded to the bridged oxygen instead that to the nickel surface.

The MEP, reported in figure 2.14, takes a jagged shape starting from the third image. Nevertheless, the FIRE algorithm converged all images up to the usual threshold of $3.0 \cdot 10^{-3} \text{ } E_h/\text{\AA}$. The TS structure (image three) differs from the reactant in two ways: 1) the atomic hydrogen hopped to the HCP site just below the oxygen, 2) which in turn moved from the bridge to a top site. Finally, in the reaction intermediate at image four, the hydrogen leaved the nickel surface to jump on the oxygen (still in the top site). In this structure the C–O bond is parallel to the underlying Ni–Ni bond.

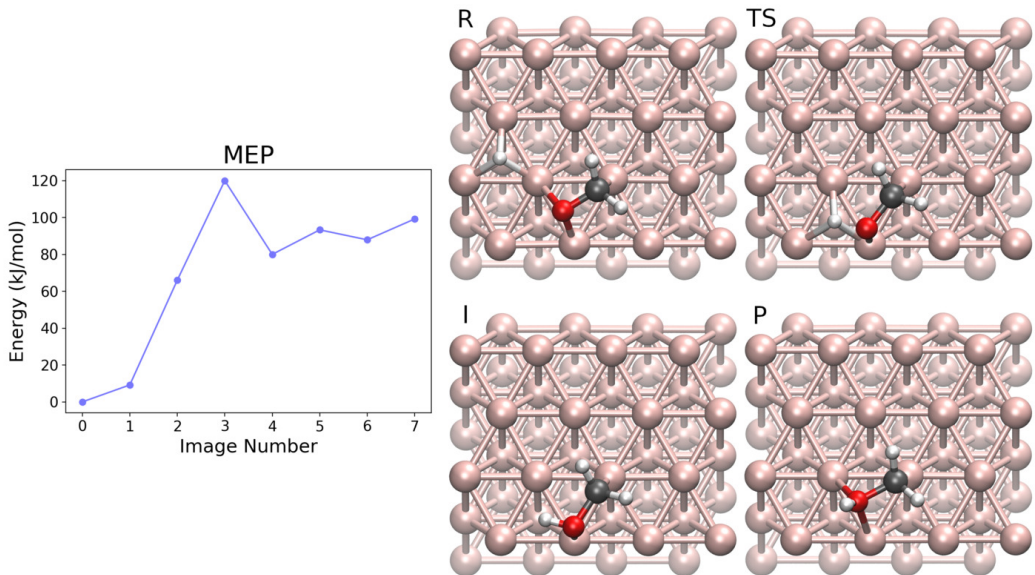


Figure 2.14: MEP and geometries of interest of the N12 elementary step:
 $\text{CH}_2\text{O} + \text{H} \longrightarrow \text{CH}_2\text{OH}$. Reactant, image 0; TS, image 3;
 Intermediate, image 4; Product, image 7. Colors: H white; C black; O red; Ni rose gold.

Since the reaction intermediate has a lower absolute energy than the product, it was used to estimate the ΔE_r of 80.0 kJ/mol. The obtained activation energy for this elementary step is 120.0 kJ/mol.

N13: $\text{CH}_3\text{O} + \text{H} \longrightarrow \text{CH}_3\text{OH}$ This elementary step is about the hydrogenation of the CH_3O species in order to produce a methanol molecule. To locate its TS, a reactant geometry was chosen where both CH_3O and the atomic hydrogen were on two neighboring FCC sites (the former adsorbed via O). In the product structure the CH_3OH species is still adsorbed solely by its oxygen, but now its preferred position is a top site instead of the old FCC one. Since now the oxygen is also coordinated with an extra hydrogen, the C–O bond is no more exactly perpendicular to the nickel surface but at an angle with it.

To converge a five images elastic band, in this CI-NEB calculation a looser convergence threshold of $4.5 \cdot 10^{-3} E_h/\text{\AA}$, along with FIRE, were used. The MEP reported in figure 2.15 has a peak at image four, the transition state. A look at its structure reveals that it is very similar to the one of the product, the difference being that here the O–H bond is not fully formed: the atomic hydrogen is still on a bridge site of the nickel surface, ready to

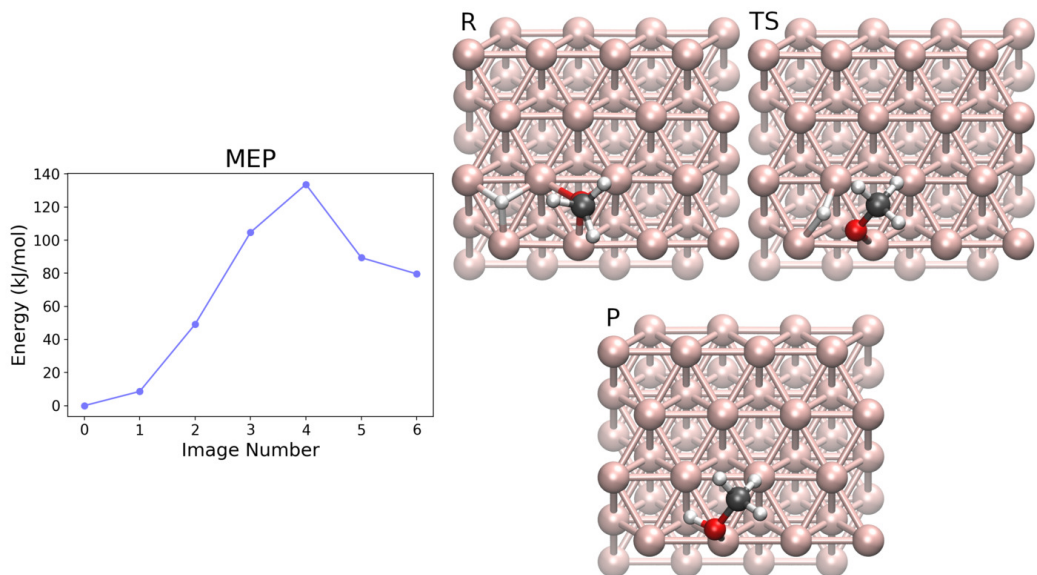


Figure 2.15: MEP and geometries of interest of the N13 elementary step:
 $\text{CH}_3\text{O} + \text{H} \longrightarrow \text{CH}_3\text{OH}$. Reactant, image 0; TS, image 4;
 Product, image 6. Colors: H white; C black; O red; Ni rose gold.

attack the oxygen. The O–H distances are 1.458 and 1.001 Å in TS and product, respectively.

This elementary step is highly endothermic and has a ΔE_r of 79.6 kJ/mol, and an activation energy of 133.7 kJ/mol.

N14: CO \longrightarrow C + O The N14 step is about the dissociation of carbon monoxide on the nickel surface. In the reactant structure there are a CO molecule adsorbed on an HCP site through the carbon, and an atomic oxygen on a HCP site far away from the other species. The atomic oxygen is a product of the CO_2 dissociation. Its presence here is not really necessary, but since it is far away from the reacting molecule, it has no influence on the CO dissociation. In the product geometry, on the other hand, the atomic carbon is still on its original HCP site, while the dissociated oxygen occupies another HCP site next to the carbon.

Figure 2.16 shows that the MEP has a very high peak at image four. The transition state structure has the dissociating C and O placed on two neighboring bridge sites. The C–O axis is parallel to the underlying surface, while in the reactant it was exactly perpendicular to that. Finally, the C–O distance is 1.823 Å in TS and 1.205 Å in the reactant.

This elementary step is strongly endothermic, ΔE_r being 108.2 kJ/mol.

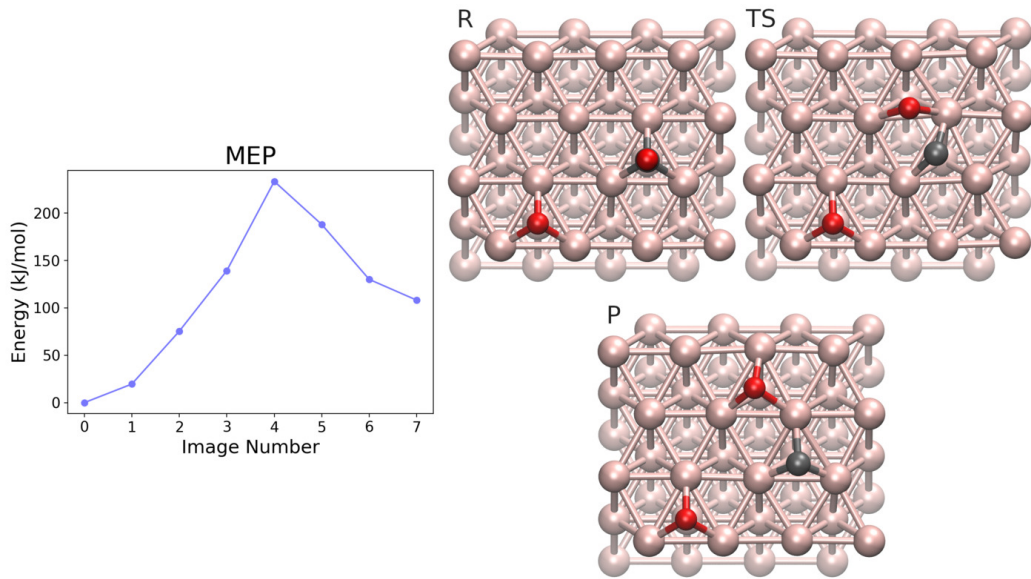


Figure 2.16: MEP and geometries of interest of the N14 elementary step: $\text{CO} \longrightarrow \text{C} + \text{O}$. **R**, Reactant, image 0; **TS**, image 4; **P**, Product, image 7. Colors: C black; O red; Ni rose gold.

Furthermore, it has the highest activation energy (233.6 kJ/mol) among all the steps investigate on the pristine nickel (111) surface.

N15: $\text{CHO} \longrightarrow \text{CH} + \text{O}$ The the breaking of the C–O bond in the CHO species was investigated using, as reactant, a structure where the CHO species is overall on an HCP site, with C leaned over a bridge site and O shifted towards a top site. The product geometry, instead, has both the CH fragment and the atomic oxygen on two FCC sites, both of which were neighbors of the original HCP site.

The MEP reported in figure 2.17 has a peak at image four, the transition state, which structure shows a CH fragment close to its final position on the FCC site, while the atomic oxygen is still on the bridge site between the original HCP site of the reactant and the FCC site that it will occupy in the product.

This reaction is moderately exothermic with a ΔE_r of -52.7 kJ/mol, and an high activation energy of 87.7 kJ/mol.

N16: $\text{CH}_2\text{O} \longrightarrow \text{CH}_2 + \text{O}$ The reactant structure, chosen to study the $\text{CH}_2\text{O} \longrightarrow \text{CH}_2 + \text{O}$ elementary step, has the C–O bond of the CH_2O species over an FCC site, with the carbon more leaned towards a top site,

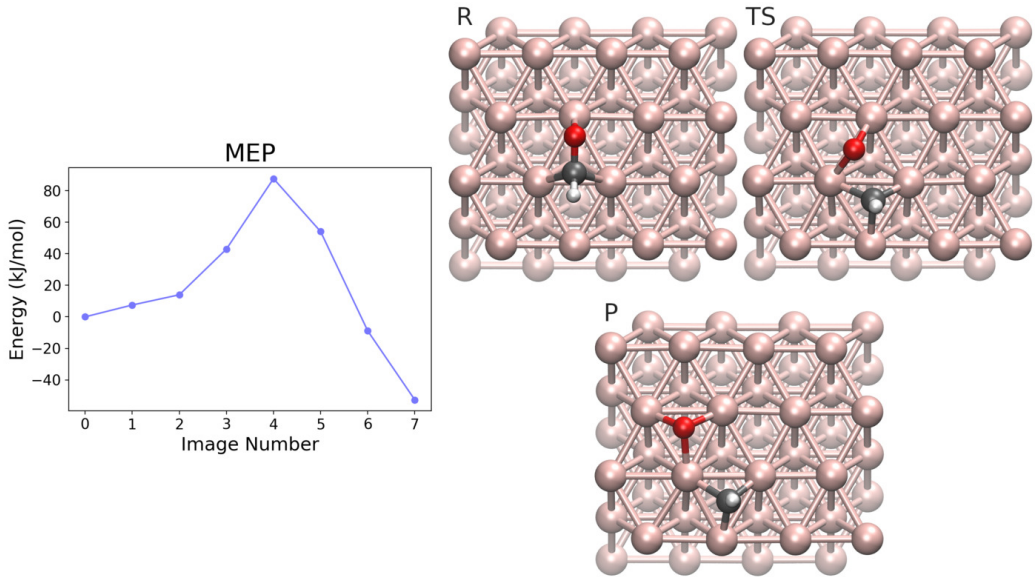


Figure 2.17: MEP and geometries of interest of the N15 elementary step: $\text{CHO} \longrightarrow \text{CH}_3 + \text{O}$. Reactant, image 0; TS, image 4; Product, image 7. Colors: H white; C black; O red; Ni rose gold.

and the oxygen towards a bridge site. On the other hand, in the product structure two HCP sites, between which there is the same FCC site cited in the reactant, are occupied by the atomic oxygen and the CH_2 fragment.

The MEP reported in figure 2.18 is spiky, with sudden jumps in energy between images two and three, and three and five. The TS is located at image three, the structure of which reveals that the CH_2 group moved from the top site to a bridge site. Here the C–O distance is 1.832 Å, whereas in the reactant it was 1.393 Å.

This elementary step has a moderately negative ΔE_r of -42.6 kJ/mol, and an activation energy of 75.6 kJ/mol.

N17: $\text{CH}_3\text{O} \longrightarrow \text{CH}_3 + \text{O}$ The reactant chosen for this step has the CH_3O species adsorbed on the nickel surface by its oxygen, situated on a bridge site. In the product, instead, the atomic oxygen is on the near HCP site, while the methyl group is on an FCC site not to far away.

The CI-NEB for this step was a bit difficult to perform. The TS has been obtained by the optimization of a long elastic band of twelve images with the FIRE algorithm, up to the slightly higher than usual threshold of $3.3 \cdot 10^{-3} E_h/\text{\AA}$. The resulting MEP, reported in figure 2.19, shows a peak at image four, and a little hump (images eight to eleven). Examining the transition

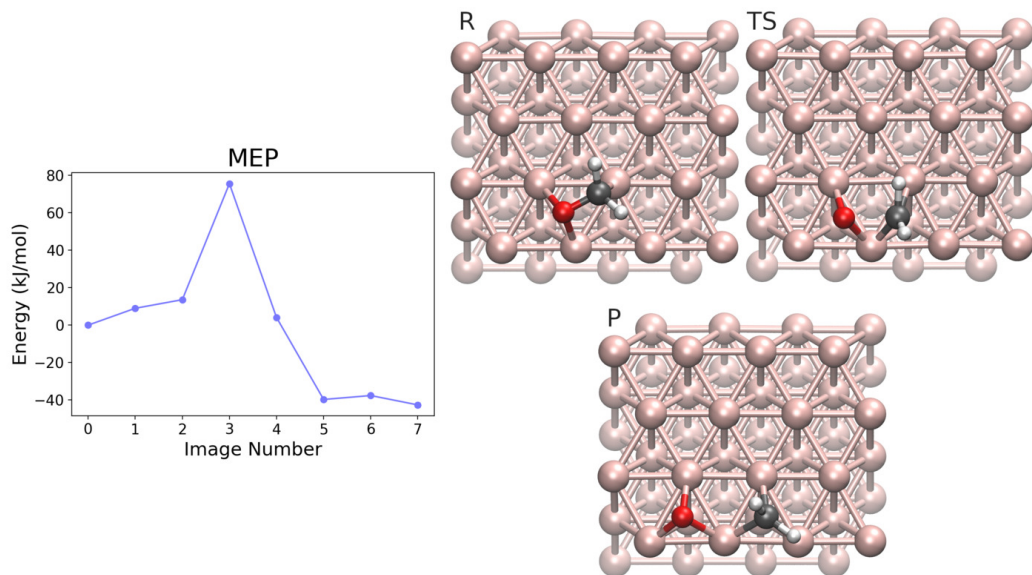


Figure 2.18: MEP and geometries of interest of the N16 elementary step: $\text{CH}_2\text{O} \longrightarrow \text{CH}_2 + \text{O}$. Reactant, image 0; TS, image 3; Product, image 7. Colors: H white; C black; O red; Ni rose gold.

state geometry, the oxygen is midway between the original bridge site and its final HCP site, while the CH_3 fragment is approaching the nearest top site. The C–O distances are 1.426 and 1.861 Å in the reactant and TS structures, respectively. Finally, the little hump is due to an intermediate step of the methyl group on a top site before continuing its journey to the final FCC site.

Despite this is a very exothermic elementary step with a ΔE_r of -88.2 kJ/mol, it has an high activation energy of 111.2 kJ/mol, probably due to reduced interaction capabilities of the fully saturated carbon with the nickel surface.

N18: $\text{COH} + \text{H} \longrightarrow \text{CHOH}$ To study the hydrogenation of the alcoholic species COH that gives rise to CHO_H, it was chosen a reactant in which both COH and H are on two confining FCC sites, the former adsorbed via its carbon, being the C–O bond exactly perpendicular to the surface. In the product structure, the CHO_H species has the C–O bond parallel to the nickel surface, located over the same FCC site of the reactant. More specifically the carbon is more shifted towards a bridge site, whereas the hydroxyl group has its oxygen on a top site.

As can be seen from figure 2.20, the MEP is very smooth, and the TS

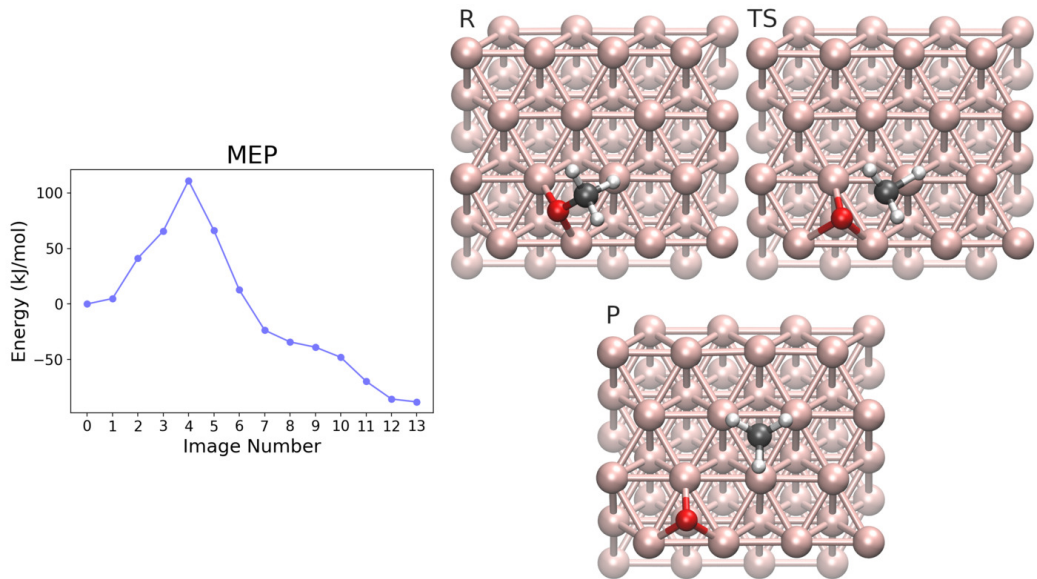


Figure 2.19: MEP and geometries of interest of the N17 elementary step: $\text{CH}_3\text{O} \longrightarrow \text{CH}_3 + \text{O}$. Reactant, image 0; TS, image 4; Product, image 13. Colors: H white; C black; O red; Ni rose gold.

located at image four has an absolute energy close to that of the product, thus making the backward dehydrogenation reaction very easy to occur. Its structure shows that the atomic hydrogen is on an intermediate position between the carbon and a top site of the nickel. The hydroxyl group is here more leaned towards the surface, but not yet over its final top site.

This hydrogenation reaction is very unlikely from a thermodynamic perspective, its ΔE_r being 113.5 kJ/mol. Moreover, the activation energy of 124.8 kJ/mol implies a very low energy barrier for the backward reaction, which in this way turns out to be kinetically fast. All these results depict this hydrogenation step as extremely hard to occur.

N19: $\text{CHOH} + \text{H} \longrightarrow \text{CH}_2\text{OH}$ The further hydrogenation of CHOH that gives the CH_2OH species is investigated in N19. In the reactant geometry, the CHOH species is placed in the same way as it was in the product of N18, with an additional atomic hydrogen on an FCC site next to the carbon. In the product structure, instead, the hydroxyl group of CH_2OH is still on the same top site it occupies in the reactant, but the carbon moved from the bridge to a top site.

As shown in figure 2.21, the MEP has a peak at image two, and a basin centered at image four, a reaction intermediate. The transition state struc-

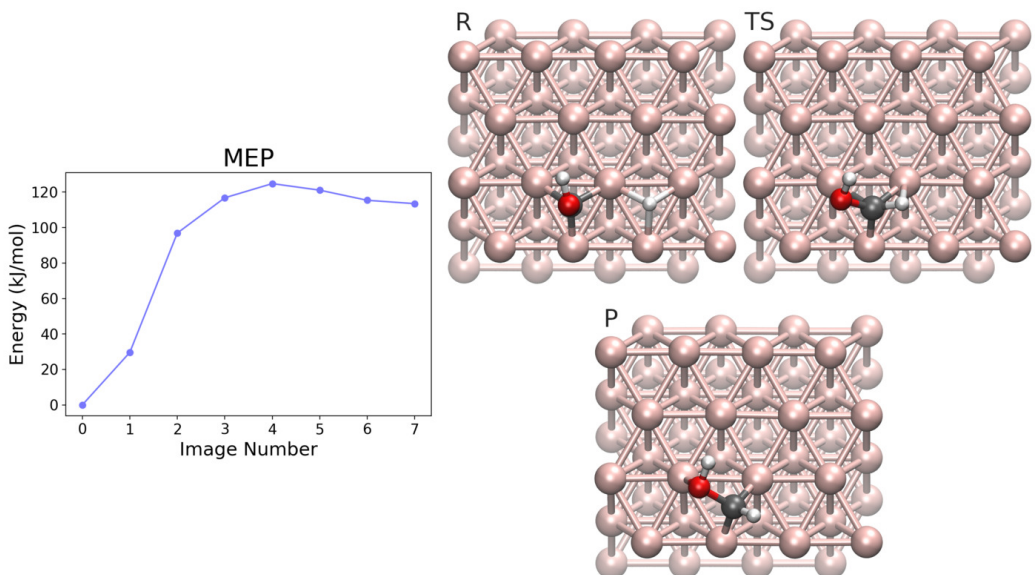


Figure 2.20: MEP and geometries of interest of the N18 elementary step:
 $\text{COH} + \text{H} \longrightarrow \text{CHOH}$. **R**eactant, image 0; **TS**, image 4; **P**roduct, image 7. Colors: H white; C black; O red; Ni rose gold.

ture is almost identical to that of the reactant, the only difference being in the position of the atomic hydrogen, here on a top site at a distance of 1.644 Å from the carbon (it will be 1.122 Å in the product). The reaction intermediate, instead, has the same CH_2OH species of the product, but placed in a different way on the nickel surface. Here the CH_2 group has its carbon on a bridge site, while in the product it is on the near top site.

Since the reaction intermediate is a more stable conformer than the product, the ΔE_r of 33.4 kJ/mol was computed using its absolute energy. The activation energy associated to this elementary step is 66.5 kJ/mol.

N20: $\text{CH}_2\text{OH} + \text{H} \longrightarrow \text{CH}_3\text{OH}$ The last hydrogenation of the CH_2OH species that gives the methanol molecule is discussed in the current paragraph. As reactant, a structure was chosen in which CH_2OH is placed in a similar manner to the intermediate of N19 (with the carbon on a bridge site), where in addition there is an atomic hydrogen on an FCC site near the carbon. In the product, instead, the methanol molecule is adsorbed only through the hydroxyl group, the oxygen of which interacts with a top site, whereas the methyl group points upward far away from the surface.

The MEP of figure 2.22 shows that the first images increase rapidly in energy up to image three (TS), and then start to decrease smoothly up to the

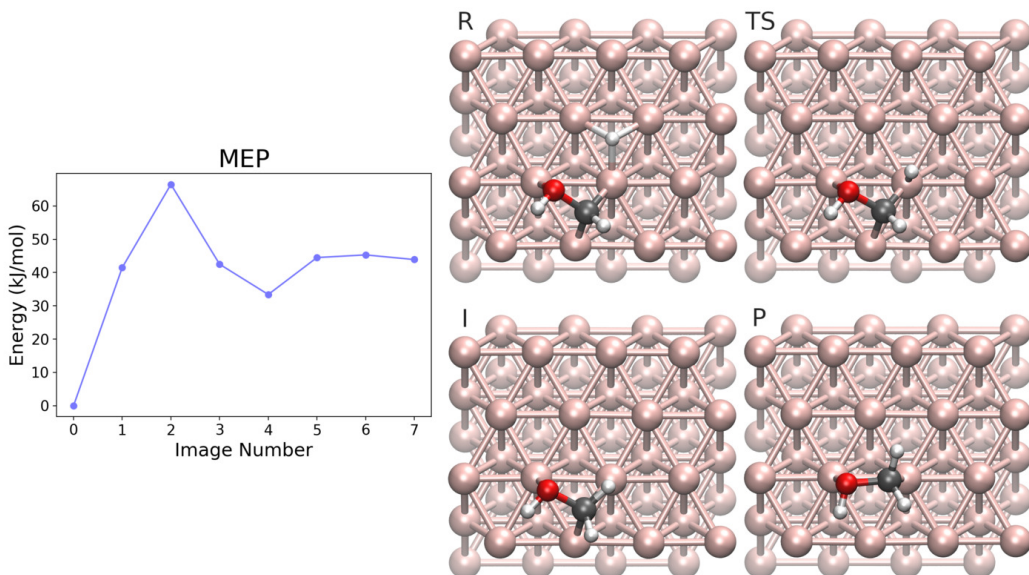


Figure 2.21: MEP and geometries of interest of the N19 elementary step:
 $\text{CHOH} + \text{H} \longrightarrow \text{CH}_2\text{OH}$. Reactant, image 0; TS, image 2;
 Intermediate, image 4; Product, image 7. Colors: H white; C black; O red; Ni rose gold.

product. A look to the TS structure reveals two events: the CH_2 fragment moved on the top site next to the atomic hydrogen, which in turn moved towards the nearest bridge site below the carbon.

This elementary step has a moderately endothermic ΔE_r of 49.3 kJ/mol, and an activation energy of 95.6 kJ/mol.

N21: $\text{COH} \longrightarrow \text{C} + \text{OH}$ This and the next three paragraphs are about the dissociation of the hydroxyl group from alcoholic species, starting from the $\text{COH} \longrightarrow \text{C} + \text{OH}$ elementary step. The chosen reactant structure has the COH species adsorbed on an FCC site through the carbon. Similarly, the product geometry has the atomic carbon on the same FCC site, while the hydroxyl group is adsorbed on another FCC site nearby. From the top view of the product as reported in figure 2.23, it seems that C is slightly off center. This happens because a Ni atom, the one shared between the two FCC sites of C and OH, is a little raised above the surface, thus deforming all the neighboring HCP and FCC sites.

The CI-NEB calculation was a bit difficult to carry out. The best result was the optimization of a six images elastic band up to the looser threshold of $5.2 \cdot 10^{-3} E_h/\text{\AA}$, this time using the L-BFGS algorithm. The MEP is

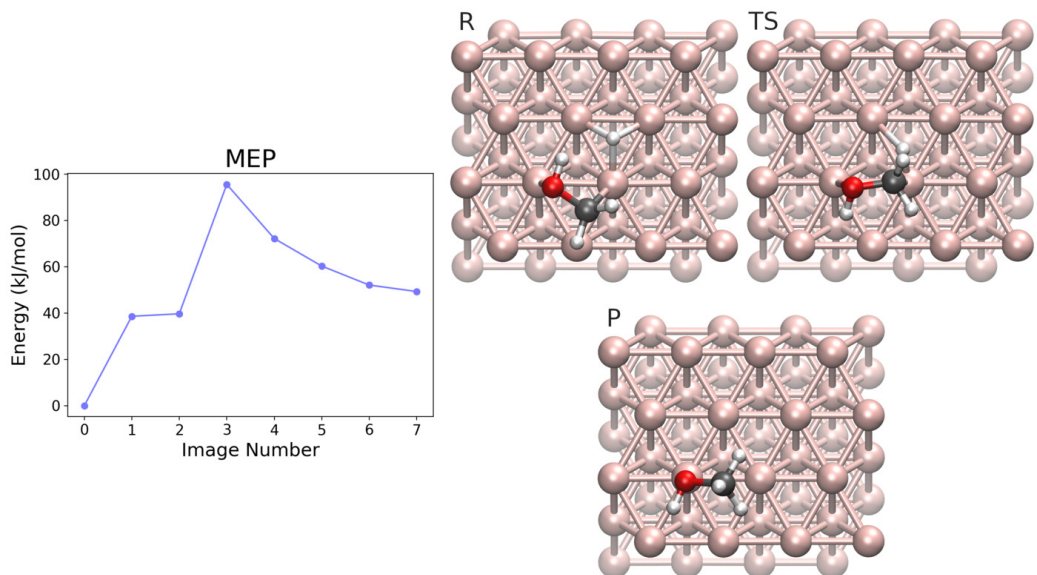


Figure 2.22: MEP and geometries of interest of the N20 elementary step: $\text{CH}_2\text{OH} + \text{H} \longrightarrow \text{CH}_3\text{OH}$. Reactant, image 0; TS, image 3; Product, image 7. Colors: H white; C black; O red; Ni rose gold.

generally smooth, with a maximum at image three. The TS structure shows that the hydroxyl group is placed on a bridge site of the surface, the C–O distance being 1.930 Å (it was 1.346 Å in the reactant).

The elementary step here discussed has a moderately small ΔE_r of 34.3 kJ/mol. Nevertheless, its activation energy is extremely high at 166.4 kJ/mol.

N22: $\text{CHOH} \longrightarrow \text{CH} + \text{OH}$ To investigate the CHOH dissociation, the reactant structure of choice has the CHOH species overall adsorbed over an FCC site, with O being on a top site while C on bridge one. The product geometry selected as the end point for the CI-NEB has both the hydroxyl group and the CH fragment on the two HCP sites next to the original FCC of the reactant.

The MEP, shown in figure 2.24, is anything but smooth with two maxima (image two being the global maximum, i.e. the TS of interest), and two minima. Looking at the TS structure it appears very similar to that of the reactant, the only difference being in the position of the CH fragment, that is still over the same bridge site but here more leaned towards the near HCP site. The C–O distance is 1.905 Å in the TS, whereas in the reactant it was 1.465 Å. The first reaction intermediate (also reported in the aforementioned

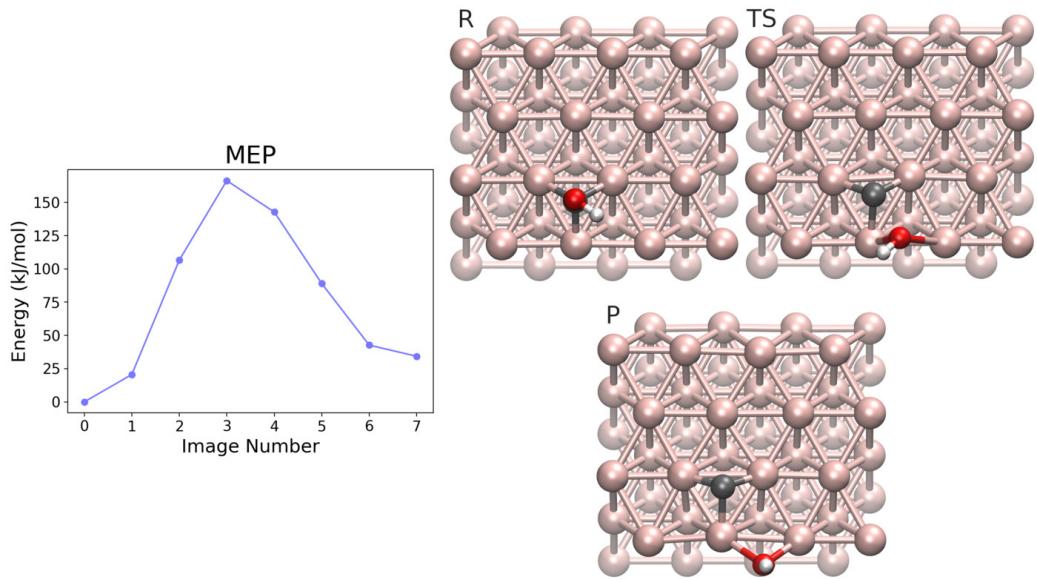


Figure 2.23: MEP and geometries of interest of the N21 elementary step: $\text{COH} \longrightarrow \text{C} + \text{OH}$. **R**, Reactant, image 0; **TS**, image 3; **P**, image 7. Colors: H white; C black; O red; Ni rose gold.

figure) differs from the product about the position of the OH group on the nickel surface, here being on an FCC site. The remaining part of the MEP (from image five to seven) is about the migration of this hydroxyl group in order for it to reach the same HCP site of the product.

Since the intermediate at image four is a more stable structure than the product, its absolute energy was used to compute the ΔE_r of -105.6 kJ/mol associated with this elementary step. Its activation energy, instead, is 42.6 kJ/mol.

N23: $\text{CH}_2\text{OH} \longrightarrow \text{CH}_2 + \text{OH}$ For the investigation of this elementary step a structure was selected, as reactant, where the CH_2OH species has the C–O bond parallel to an underlying Ni–Ni bond, so that both O and C are on two neighboring top sites. The product geometry, on the other hand, has both the hydroxyl group and the CH_2 fragment on two adjacent FCC sites.

As reported in figure 2.25, the MEP seems to consist of three different segments. Image three is a reaction intermediate, even if its energy is very close to that of the reactant, whereas the transition state is located at image four. An analysis of the intermediate geometry shows that it is a different conformation of the CH_2OH species on the surface: here the CH_2 group is on a bridge site while in the reactant it was on a top site. The TS structure is very

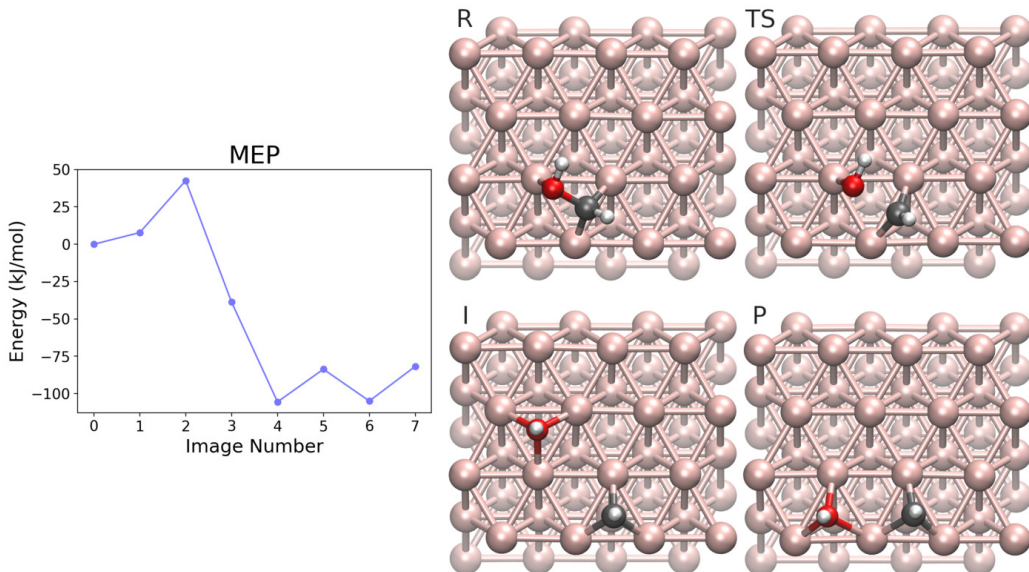


Figure 2.24: MEP and geometries of interest of the N22 elementary step: $\text{CHOH} \longrightarrow \text{CH} + \text{OH}$. Reactant, image 0; TS, image 2; Intermediate, image 4; Product, image 7. Colors: H white; C black; O red; Ni rose gold.

similar to that of the intermediate: the CH_2 fragment is still predominantly on the same bridge site, but here it is slightly shifted towards the near FCC site. The C–O distances are 1.483 and 1.971 Å in the intermediate and in the TS structure, respectively.

Considering that the intermediate is slightly more stable than the reactant, its absolute energy was used to estimate both the ΔE_r and the forward activation energy, these being -74.8 and 51.1 kJ/mol, respectively.

N24: $\text{CH}_3\text{OH} \longrightarrow \text{CH}_3 + \text{OH}$ The last dissociation is that of CH_3OH . In the reactant structure, the methanol molecule is adsorbed on the nickel surface thanks to the weak interaction between the oxygen and a bridge site. The product structure of choice, instead, has the hydroxyl group on an HCP site, while the methyl group is over a top site.

The resulting MEP is smooth, and as can be seen from figure 2.26, the TS structure at image three is very similar to the reactant, the difference being that here the methyl group is closer to the final top site. The C–O distance in TS is 2.070 Å, while it was 1.449 Å in the reactant.

This elementary step has an exothermic ΔE_r of -73.7 kJ/mol, and an activation energy of 117.4 kJ/mol.

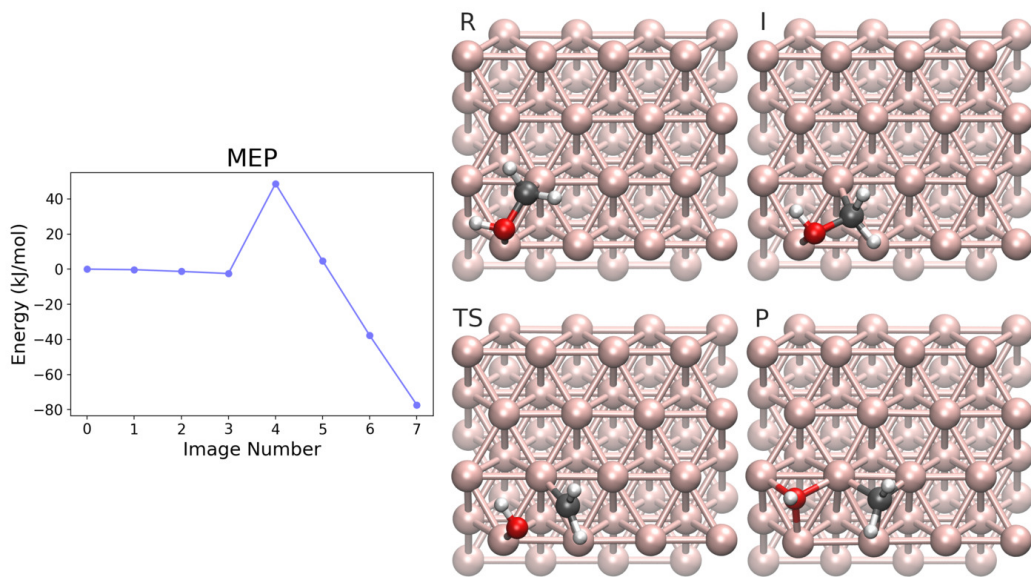


Figure 2.25: MEP and geometries of interest of the N23 elementary step: $\text{CH}_2\text{OH} \longrightarrow \text{CH}_2 + \text{OH}$. Reactant, image 0; Intermediate, image 3; TS, image 4; Product, image 7. Colors: H white; C black; O red; Ni rose gold.

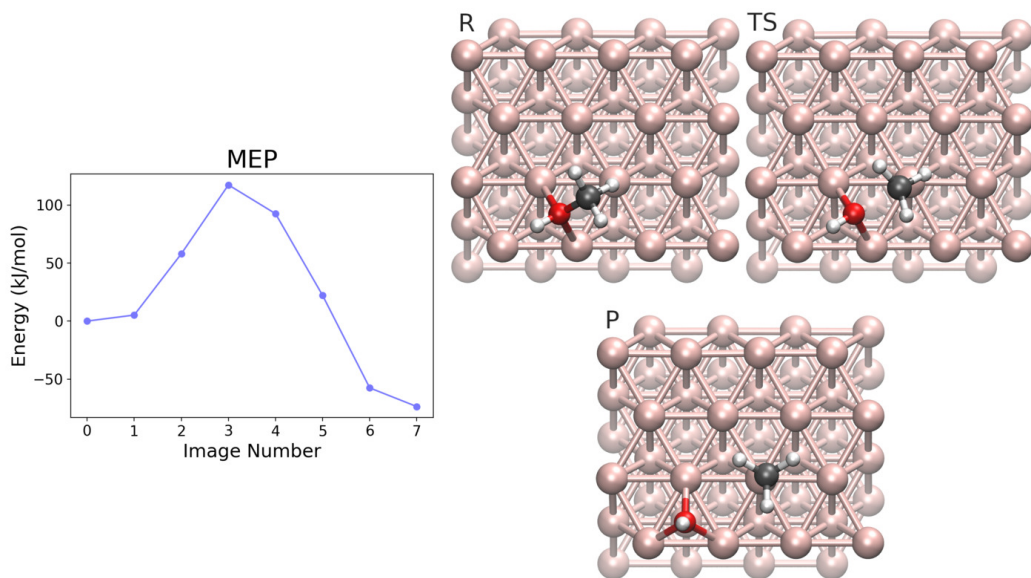


Figure 2.26: MEP and geometries of interest of the N24 elementary step: $\text{CH}_3\text{OH} \longrightarrow \text{CH}_3 + \text{OH}$. Reactant, image 0; TS, image 3; Product, image 7. Colors: H white; C black; O red; Ni rose gold.

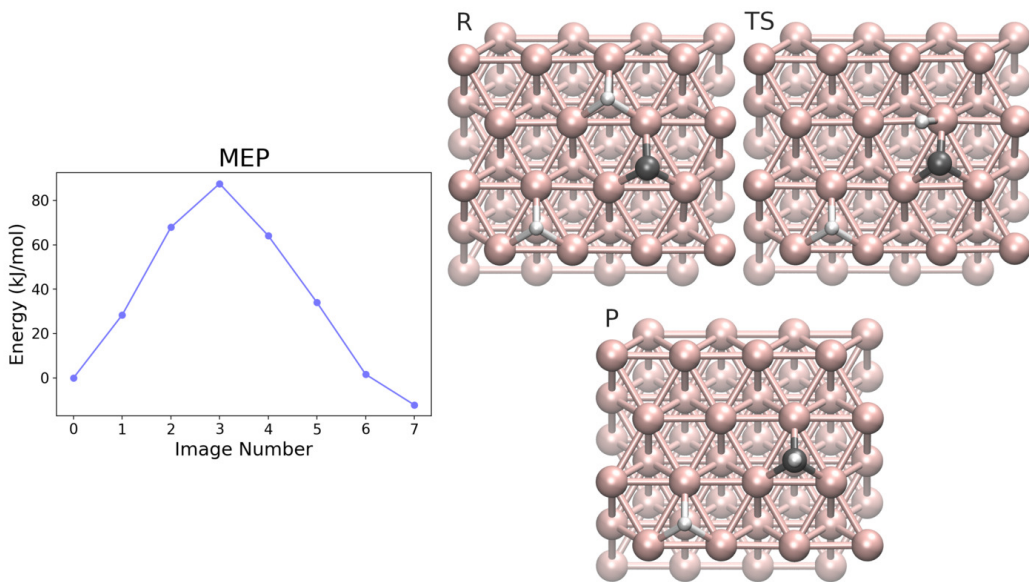


Figure 2.27: MEP and geometries of interest of the N25 elementary step: $\text{C} + \text{H} \longrightarrow \text{CH}$. Reactant, image 0; TS, image 3; Product, image 7. Colors: H white; C black; Ni rose gold.

N25: $\text{C} + \text{H} \longrightarrow \text{CH}$ These four final paragraphs are about the hydrogenation of carbide species. These steps were also investigated by German et al. using a method to predict the activation energies involved.[40, 41, 42] Here the $\text{C} + \text{H} \longrightarrow \text{CH}$ elementary step is discussed. The optimized reactant structure has two atomic hydrogens (derived from the H_2 dissociation on the nickel surface) and an atomic carbon, all three atoms being on different HCP sites. The product structure differs from the reactant only for the position of one hydrogen, here being on top of C, thus giving a CH fragment on a HCP site. The other hydrogen is sufficiently far away to be considered as a mere spectator.

The resulting minimum energy path, reported in figure 2.27, is smooth with a maximum at image three. In the TS geometry there is an hydrogen midway between its original HCP site and the carbon, exploiting an underlying nickel atom for its migration.

This elementary step has a low exothermic ΔE_r of -12.2 kJ/mol, but a quite high activation energy of 87.6 kJ/mol.

N26: $\text{CH} + \text{H} \longrightarrow \text{CH}_2$ The next step to the way of methane is $\text{CH} + \text{H} \longrightarrow \text{CH}_2$. In the reactant structure both the CH fragment and the atomic hydrogen are on two adjacent FCC sites, while in the product the hydrogen

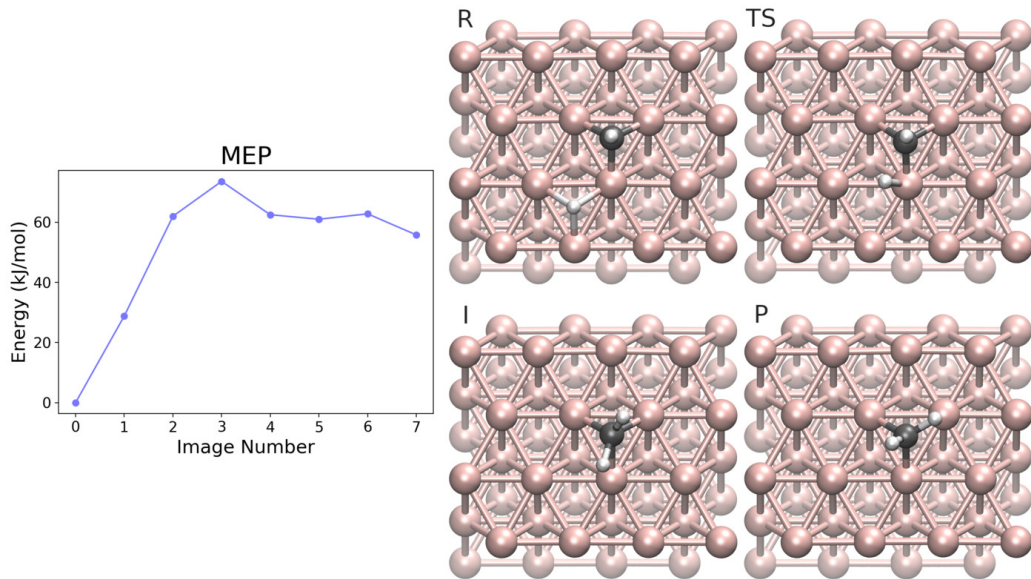


Figure 2.28: MEP and geometries of interest of the N26 elementary step: $\text{CH} + \text{H} \longrightarrow \text{CH}_2$. **R**eactant, image 0; **TS**, image 3; **I**ntermediate, image 5; **P**roduct, image 7. Colors: H white; C black; Ni rose gold.

is now bonded to to C, which in turn did not move from its original position.

Figure 2.28 reports the achieved MEP, that locates the transition state at image three while also locating a very labile reaction intermediate at image five. The TS structure has the atomic hydrogen midway from its original FCC site to the carbon, whereas the intermediate is a conformer of the product, being the CH_2 species oriented in a slightly different way on the surface.

The elementary step here discussed has a moderate ΔE_r of 55.8 kJ/mol, and an activation energy of 73.6 kJ/mol.

N27: $\text{CH}_2 + \text{H} \longrightarrow \text{CH}_3$ To investigate this elementary step, a reactant structure was prepared in which both the CH_2 fragment and the atomic hydrogen are on two neighboring FCC sites. The product geometry is very similar since the carbon did not move from its initial position, the difference being that it is now bonded to a further hydrogen.

The MEP is generally smooth and presents a transition state at image four, as can be seen from figure 2.29. The TS structure shows the atomic hydrogen mainly on a top site, midway between its original FCC site and the carbon.

This elementary step is slightly endothermic with a ΔE_r of 21.6 kJ/mol, it also has a moderate activation energy of 66.3 kJ/mol.

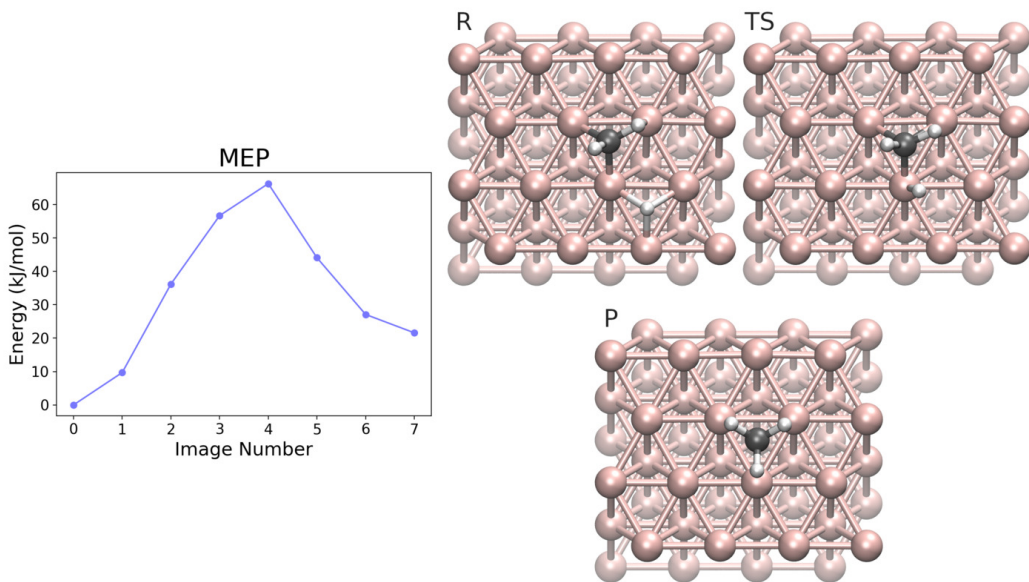


Figure 2.29: MEP and geometries of interest of the N27 elementary step: $\text{CH}_2 + \text{H} \longrightarrow \text{CH}_3$. Reactant, image 0; TS, image 4; Product, image 7. Colors: H white; C black; Ni rose gold.

N28: $\text{CH}_3 + \text{H} \longrightarrow \text{CH}_4$ Finally there is $\text{CH}_3 + \text{H} \longrightarrow \text{CH}_4$, the last elementary step to get to the methane molecule. To locate its TS, a reactant structure was prepared in which an atomic hydrogen and a methyl group are both on two adjacent HCP sites. In the product geometry, instead, there is a CH_4 molecule at interaction distance above the nickel surface due to the lack of meaningful interactions.

The MEP, reported in figure 2.30, increases almost linearly up to the TS at image four, and then starts to decrease smoothly. The transition state structure reveals that the biggest displacement is done by the methyl group, that moves from an HCP to a top site, while the atomic hydrogen shifts towards a bridge site below the carbon. In TS the distance between C and the underlying Ni is 2.057 Å, the same C–Ni distance being 2.124 and 2.998 Å in the reactant and product structures, respectively.

This elementary step is moderately endothermic with a ΔE_r of 57.3 kJ/mol, its activation energy being 104.9 kJ/mol.

Honorable mentions

Some CI-NEB calculations were performed to verify if a nearby atomic hydrogen can help the alcoholic species to lose their hydroxyl group in a concerted

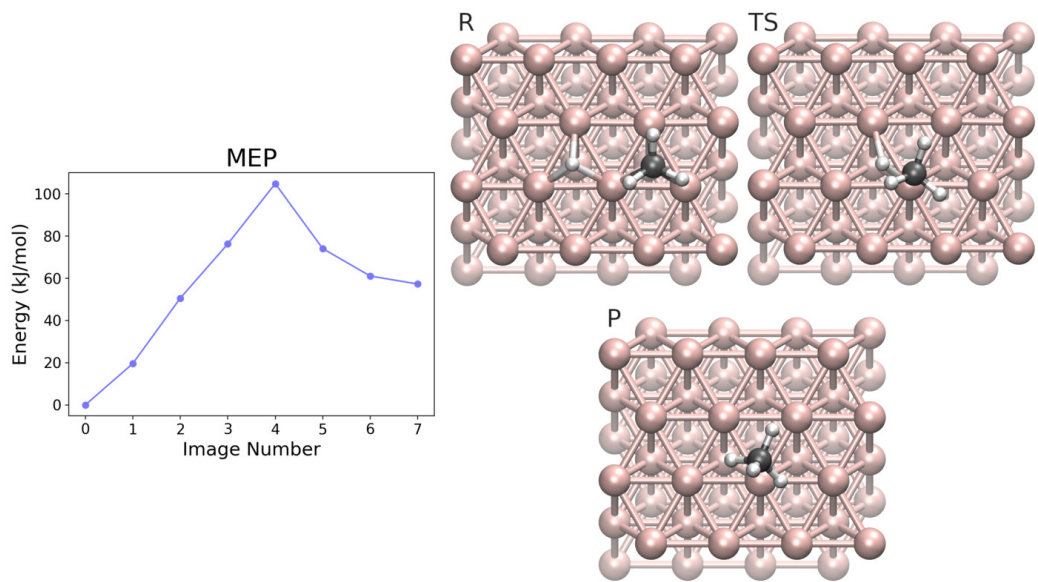


Figure 2.30: MEP and geometries of interest of the N28 elementary step: $\text{CH}_3 + \text{H} \longrightarrow \text{CH}_4$. **R**eactant, image 0; **TS**, image 4; **P**roduct, image 7. Colors: H white; C black; Ni rose gold.

step that involves the production of a water molecule. All attempts resulted in the evidence that the reaction happens in two separate steps (NEBs show two transition states and a reaction intermediate along the reaction path): hydroxyl group dissociation followed by hydrogen attack to give water.

2.5 CO₂ Methanation on Ru-Decorated Ni (111)

It is well known in literature that ruthenium is the most active metal for carbon dioxide methanation. Being an highly expensive element, it is important to design a catalytic material that can exploit its properties without requiring to much of it. For this reason, in this study a nickel (111) surface decorated with a single ruthenium atom was taken into account. The exposed surface is then constituted by a ruthenium site along with Ni (111) sites, a material like this could thus behave like a bifunctional catalyst. The model used to study the methanation reaction has the Ru atom on an HCP site of the nickel (111) surface.

A total of 16 chemical species and 27 elementary steps were taken into account in the study of the reaction CO₂ + 4 H₂ → CH₄ + 2 H₂O on the Ru-decorated surface. Table 2.4 shows them, as well as their reaction and activation energies. It is implicit that all species appearing in the reactions reported in table are adsorbed on the catalytic surface. In order to maintain a general correspondence with the elementary steps investigate on the pristine surface, also in this case the numeration goes from 1 to 28, but the 13th step, CH₃O + H → CH₃OH, is missing due to the difficulties encountered in the CI-NEB calculation. With this catalyst model, elastic bands constituted of six or eight images were generally used. A detailed discussion of each step follows.

R01: CO₂ → CO + O The chosen geometries to study the carbon dioxide decomposition near the ruthenium decoration were: as reactant, a Ru atom on an HCP site, and the CO₂ molecule bonded to Ru through the carbon, with both oxygens interacting with the nickel surface; as product, Ru on a bridge site, CO bonded to ruthenium through its carbon, while the dissociated atomic oxygen being on an HCP site of nickel (111).

Despite the presence of a destabilizing (with respect to the optimization process) reaction intermediate, the calculation managed to converge. As shown in figure 2.31, the transition state is located near the reactant at image two, while an intermediate is at the end of the path at image six, near the product. The TS has a slightly elongated C–O bond: carbon is closer to Ru in TS than in reactant, while the dissociating oxygen seems to center on an FCC site. The reaction intermediate has an absolute energy very close to that of the product, the only difference between the two structures being that the former has the atomic oxygen on an FCC site, while the latter on an HCP site. Regarding the Ru–CO complex, it has pretty much the same

Table 2.4: Elementary steps on Ru-decorated Ni (111) surface. All energies expressed in kJ/mol.

Code	Elem. Step	ΔE_r	$E_{a\rightarrow}$	$E_{a\leftarrow}$
R01	$\text{CO}_2 \longrightarrow \text{CO} + \text{O}$	-91.6	40.6	132.2
R02	$\text{CO}_2 + \text{H} \longrightarrow \text{COOH}$	56.2	102.7	46.5
R03	$\text{CO}_2 + \text{H} \longrightarrow \text{CHOO}$	31.9	126.0	94.1
R04	$\text{CHOO} \longrightarrow \text{CHO} + \text{O}$	-46.3	35.1	81.5
R05	$\text{COOH} \longrightarrow \text{COH} + \text{O}$	-14.2	93.4	107.6
R06	$\text{COOH} \longrightarrow \text{CO} + \text{OH}$	-89.4	37.2	126.6
R07	$\text{CO} + \text{H} \longrightarrow \text{CHO}$	86.8	128.4	41.6
R08	$\text{CHO} + \text{H} \longrightarrow \text{CH}_2\text{O}$	61.3	78.7	17.5
R09	$\text{CH}_2\text{O} + \text{H} \longrightarrow \text{CH}_3\text{O}$	7.4	90.8	83.4
R10	$\text{CO} + \text{H} \longrightarrow \text{COH}$	99.8	135.1	35.3
R11	$\text{CHO} + \text{H} \longrightarrow \text{CHOH}$	100.7	128.8	28.1
R12	$\text{CH}_2\text{O} + \text{H} \longrightarrow \text{CH}_2\text{OH}$	63.6	95.7	32.1
R14	$\text{CO} \longrightarrow \text{C} + \text{O}$	10.4	144.5	134.1
R15	$\text{CHO} \longrightarrow \text{CH} + \text{O}$	-68.8	77.9	146.6
R16	$\text{CH}_2\text{O} \longrightarrow \text{CH}_2 + \text{O}$	-73.2	81.1	154.3
R17	$\text{CH}_3\text{O} \longrightarrow \text{CH}_3 + \text{O}$	-45.4	161.8	207.2
R18	$\text{COH} + \text{H} \longrightarrow \text{CHOH}$	94.9	111.9	17.0
R19	$\text{CHOH} + \text{H} \longrightarrow \text{CH}_2\text{OH}$	50.0	75.3	25.3
R20	$\text{CH}_2\text{OH} + \text{H} \longrightarrow \text{CH}_3\text{OH}$	28.2	62.4	34.2
R21	$\text{COH} \longrightarrow \text{C} + \text{OH}$	-38.8	81.8	120.6
R22	$\text{CHOH} \longrightarrow \text{CH} + \text{OH}$	-112.1	55.2	167.3
R23	$\text{CH}_2\text{OH} \longrightarrow \text{CH}_2 + \text{OH}$	-112.9	24.2	137.1
R24a	$\text{CH}_3\text{OH} \longrightarrow \text{CH}_3 + \text{OH}$	-81.7	80.7	162.4
R24b	$\text{CH}_3\text{OH} \longrightarrow \text{CH}_3 + \text{OH}$	-117.5	121.9	239.3
R25	$\text{C} + \text{H} \longrightarrow \text{CH}$	45.2	86.7	41.5
R26	$\text{CH} + \text{H} \longrightarrow \text{CH}_2$	73.3	96.3	23.0
R27a	$\text{CH}_2 + \text{H} \longrightarrow \text{CH}_3$	56.5	74.9	18.3
R27b	$\text{CH}_2 + \text{H} \longrightarrow \text{CH}_3$	53.4	88.4	35.1
R28	$\text{CH}_3 + \text{H} \longrightarrow \text{CH}_4$	3.7	38.8	35.1

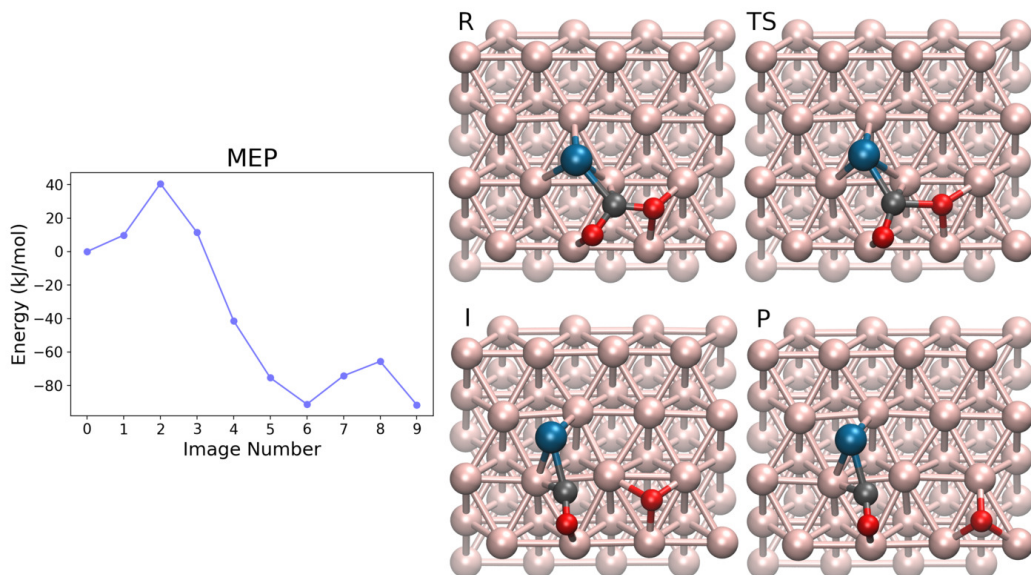


Figure 2.31: MEP and geometries of interest of the R01 elementary step: $\text{CO}_2 \longrightarrow \text{CO} + \text{O}$. Reactant, image 0; TS, image 2; Intermediate, image 6; Product, image 9. Colors: C black; O red; Ni rose gold; Ru blue.

orientation in both the intermediate and the product. The atomic oxygen alone is more stable on an nickel HCP site rather than on an FCC one. The two almost identical absolute energies of intermediate and product in this situation are probably due to the proximity of both carbon and ruthenium to the FCC site, which produces a stabilizing effect on the FCC oxygen.

This highly exothermic reaction has an associated ΔE_r of -91.6 kJ/mol, and an activation energy of 40.6 kJ/mol.

R02: $\text{CO}_2 + \text{H} \longrightarrow \text{COOH}$ This elementary step is about the acquisition of an atomic hydrogen by the adsorbed carbon dioxide that gives the COOH alcohol. In the geometry used for the reactant, the adsorbed CO_2 interacts with an HCP Ru via its carbon, and with the nickel surface through both oxygens, one of which is on a top site while the other is on a bridge site. Meanwhile, the atomic hydrogen is placed in an FCC site nearby. In the product structure, instead, the COOH species interacts with the surface only through the carbon and one of its oxygens. The other oxygen, being now saturated, has lower interaction capabilities with the underlying surface, with the result that the newly formed hydroxyl group is slightly raised from nickel.

Figure 2.32 shows the MEP, as well as some key geometries for this el-

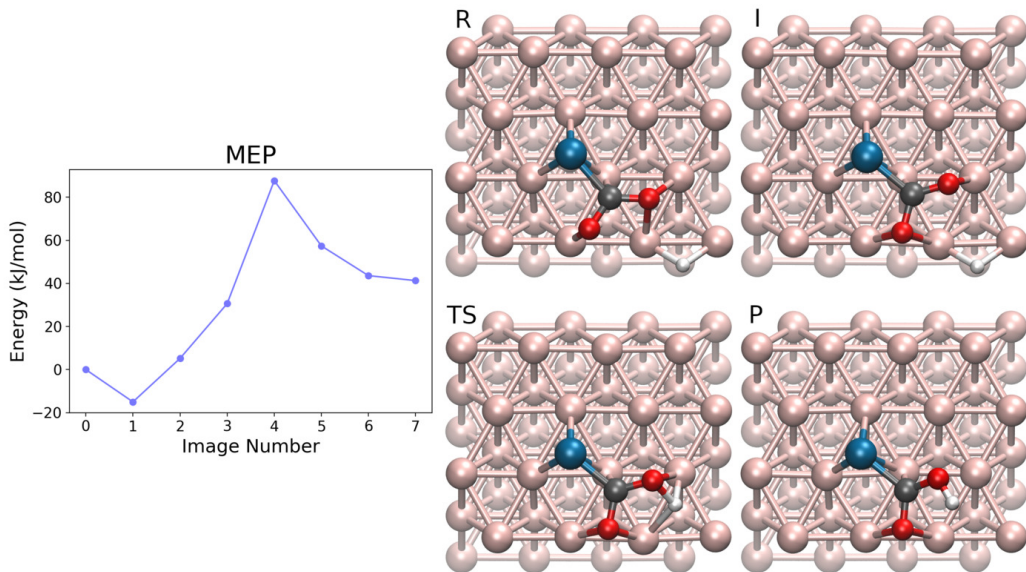


Figure 2.32: MEP and geometries of interest of the R02 elementary step: $\text{CO}_2 + \text{H} \longrightarrow \text{COOH}$. **R**eactant, image 0; **I**ntermediate, image 1; **TS**, image 4; **P**roduct, image 7. Colors: H white; C black; O red; Ni rose gold; Ru blue.

lementary step. The calculation finds a reaction intermediate at image one, which differs from the reactant only for a small rearrangement of the carbon dioxide on the surface, thus making the CO_2 orientation similar to that of the product. The subsequent images increase in energy up to image four, which is the transition state of this reaction. Its structure shows that the atomic hydrogen hopped from an FCC to an HCP site, approaching the oxygen. The latest images of the MEP are related to the hydroxyl group moving away from the nickel surface.

Since the reaction intermediate has a lower absolute energy than the reactant, it was used to estimate both the ΔE_r and the activation energy, the former being 56.2 kJ/mol while the latter 102.7 kJ/mol. The endothermic ΔE_r is probably due to the reduced surface interactions of the COOH species compared to those of CO_2 .

R03: $\text{CO}_2 + \text{H} \longrightarrow \text{CHOO}$ This step was investigated using, as reactant, a structure in which Ru is on a bridge site, bonded to both a bridged atomic hydrogen and a very distorted CO_2 molecule. In the product geometry the ruthenium atom is on the same bridge site, but here it bonds only one oxygen of the CHOO species, whose carbon moved away from both the nickel surface

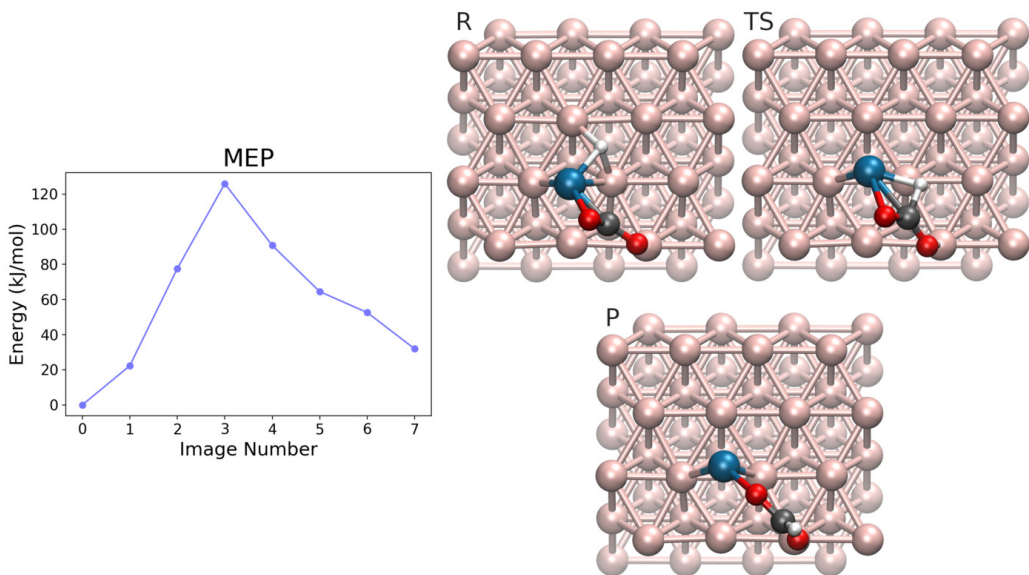


Figure 2.33: MEP and geometries of interest of the R03 elementary step: $\text{CO}_2 + \text{H} \longrightarrow \text{CHOO}$. **R**eactant, image 0; **TS**, image 3; **P**roduct, image 7. Colors: H white; C black; O red; Ni rose gold; Ru blue.

and Ru in order to bond the hydrogen.

Figure 2.33 shows a regular MEP, whose maximum is located at image three. The TS structure shows a rotation of the CO_2 species necessary to move away C from the nickel surface while at the same time bring it closer to the hydrogen, which in turn shifted towards the adjacent top site.

With a ΔE_r of 31.9 kJ/mol, this elementary step is moderately endothermic. It has, however, an high activation energy of 126.0 kJ/mol.

R04: $\text{CHOO} \longrightarrow \text{CHO} + \text{O}$ To investigate this elementary step, a reactant structure was chosen in which the CHOO species interacts with an HCP Ru through both C and O, the other oxygen being on a bridge site of the nickel surface. In the product geometry, instead, Ru is on a bridge site, interacting only with the carbon of CHO. The latter species has both C and O on two adjacent top sites, whereas the atomic oxygen is on an HCP site not to far away from the carbon.

The optimized elastic band shows a MEP in which the highest TS is located at image three, while a reaction intermediate is also present at image five (figure 2.34). The TS structure shows an elongation of the C–O bond (here 1.809 Å, while being 1.348 Å in the reactant), where the dissociating oxygen is over an FCC site, and both C and Ru are slightly moving away

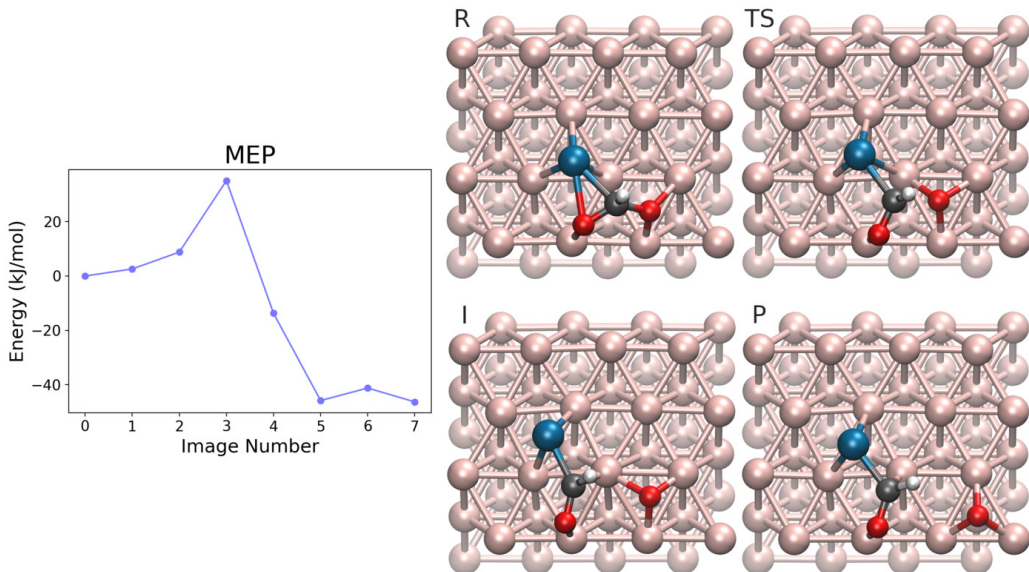


Figure 2.34: MEP and geometries of interest of the R04 elementary step: $\text{CHOO} \longrightarrow \text{CHO} + \text{O}$. Reactant, image 0; TS, image 3; Intermediate, image 5; Product, image 7. Colors: H white; C black; O red; Ni rose gold; Ru blue.

from it. The reaction intermediate has an absolute energy almost identical to that of the product, the differences between the two being: the position of the atomic oxygen (here on the same FCC site as in TS), and the position of the CHO species, here a little more centered (as a whole) over an FCC site.

The discussed elementary step has a moderate exothermic ΔE_r of -46.3 kJ/mol. Moreover, it has a low activation energy of 35.1 kJ/mol.

R05: $\text{COOH} \longrightarrow \text{COH} + \text{O}$ For this elementary step, the structure of choice for the reactant was the same as the product of R02, in which COOH interacts with the nickel surface via a bridged oxygen and the carbon, the latter also being bonded to an HCP Ru. The product geometry, on the other hand, has a COH fragment adsorbed on a top site through the carbon that also interacts with a bridged Ru, whereas the atomic oxygen is located on an FCC site nearby.

The CI-NEB calculation was flawless, and the resulting MEP does not show reaction intermediates. The transition state was located at image three, as shown in figure 2.35. The top view of its geometry shows that the dissociated oxygen is perfectly on a bridge site, on its way to the final FCC site. Regarding the COH fragment, its carbon is approaching a top site of

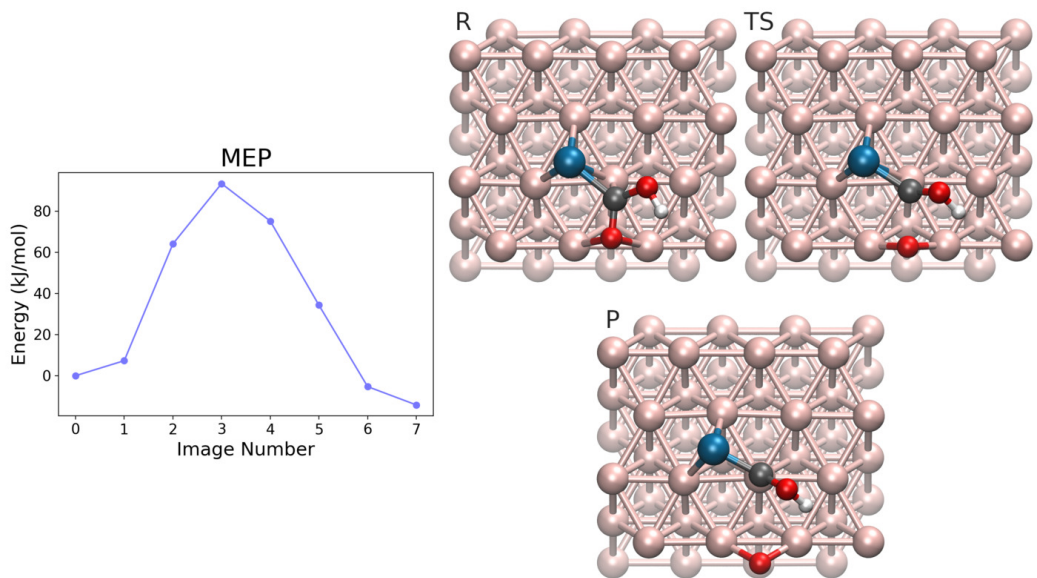


Figure 2.35: MEP and geometries of interest of the R05 elementary step: $\text{COOH} \longrightarrow \text{COH} + \text{O}$. **R**eactant, image 0; **TS**, image 3; **P**roduct, image 7. Colors: H white; C black; O red; Ni rose gold; Ru blue.

the surface, while the hydroxyl group is slightly rotated with respect to its initial position in the reactant structure.

The reaction is slightly exothermic, having a ΔE_r of -14.2 kJ/mol and a pretty high activation energy of 93.4 kJ/mol. Apparently, the interaction of atomic oxygen with an FCC site compensates for the breaking of the C–O bond, making the reaction product slightly favored from a thermodynamic point of view.

R06: $\text{COOH} \longrightarrow \text{CO} + \text{OH}$ The elementary step R06 is similar to the previous one, but instead of the dissociation of an oxygen, this time the COOH species loses its hydroxyl group. The reactant geometry is the same as that of R05. The product structure, instead, has the CO molecule over an HCP site, interacting with a bridged ruthenium through the carbon, meanwhile the lost hydroxyl group is on a FCC site nearby.

Figure 2.36 shows a smooth minimum energy path, with a transition state located at image three. In the TS structure, the hydroxyl group is approaching its nearest Ni atom on the surface, distancing itself from carbon. At the same time, the CO fragment is readjusting its position in order to fit the nearest HCP site. Finally, the ruthenium atom is still on the same HCP site: it has not yet begun its migration to the bridge site it occupies in the

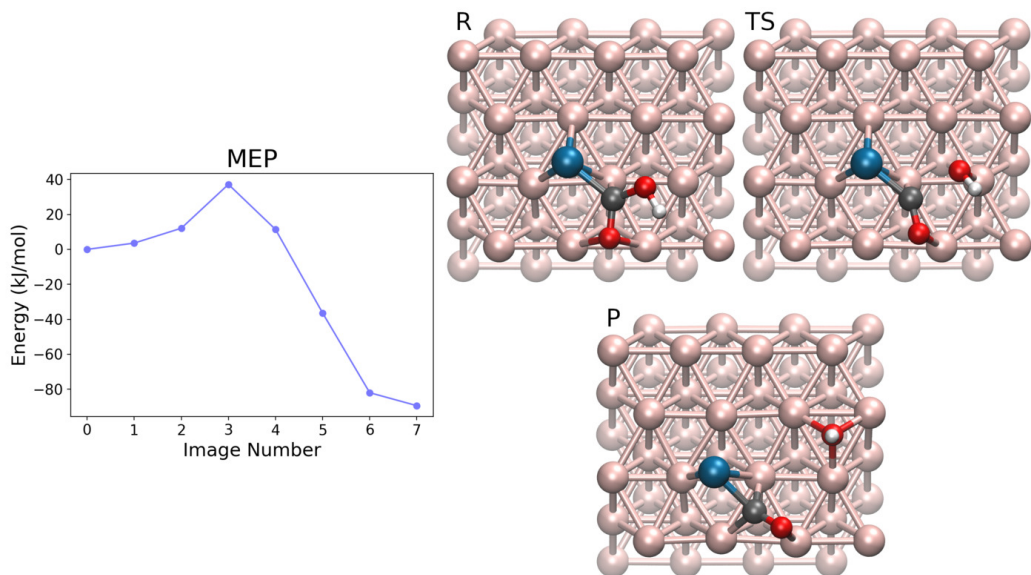


Figure 2.36: MEP and geometries of interest of the R06 elementary step: $\text{COOH} \longrightarrow \text{CO} + \text{OH}$. **R**eactant, image 0; **TS**, image 3; **P**roduct, image 7. Colors: H white; C black; O red; Ni rose gold; Ru blue.

product.

This elementary step has a very exothermic ΔE_r of -89.4 kJ/mol. This can be attributed both to the formation of the very stable CO molecule, as well as to the great interaction of the hydroxyl group with nickel when it is on the FCC site (whereas in the reactant its only interaction was with the carbon). The activation energy for this process is 37.2 kJ/mol.

R07: $\text{CO} + \text{H} \longrightarrow \text{CHO}$ To study the hydrogenation of CO on carbon, the geometry of choice for the reactant has the CO molecule adsorbed on an HCP site via its carbon, the latter also interacting with a bridged Ru, while an atomic hydrogen is located on an HCP site not far away from the carbon. In the product structure, instead, the ruthenium atom is now on an HCP site, still interacting with C. The hydrogen left the surface to bond C, and the oxygen changed its position moving from a top to a bridge site.

Figure 2.37 shows a smooth MEP, in which the only point of interest is the transition state located at image five. The TS structure is more similar to the product than to the reactant: Ru is on an HCP site, O is bridged, and H is very close to the carbon but also oriented towards the surface, resulting in a cluttered environment that is destabilizing for a simple hydrogen.

With a ΔE_r of 86.8 kJ/mol this elementary step is very endothermic,

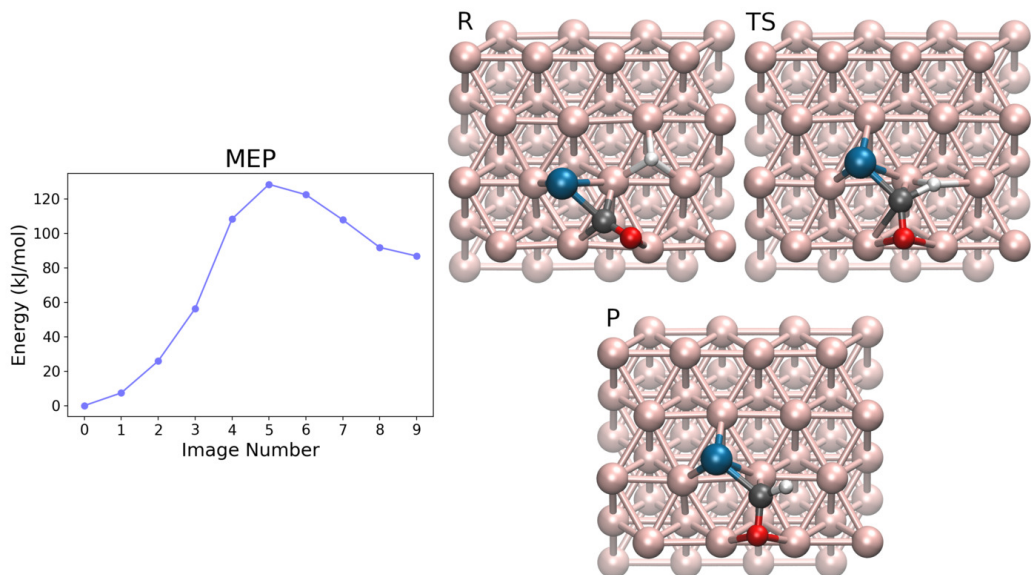


Figure 2.37: MEP and geometries of interest of the R07 elementary step: $\text{CO} + \text{H} \longrightarrow \text{CHO}$. Reactant, image 0; TS, image 5; Product, image 9. Colors: H white; C black; O red; Ni rose gold; Ru blue.

its activation energy being 128.4 kJ/mol. Similarly to R06, the most stable structure (by a large amount) is the one with the CO species, that happen to be the reactant in this case.

R08: $\text{CHO} + \text{H} \longrightarrow \text{CH}_2\text{O}$ The CHO species can further hydrogenate to CH_2O . To investigate this step, in the reactant the CHO geometry and orientation are similar to those of the product of R07, but there is an additional atomic hydrogen very close to Ru, near the less cluttered part of the carbon, ready to jump on it. The idea is to study this reaction by letting the ruthenium atom acting as a pivot for the hydrogen. In the product geometry, the said hydrogen bonds the carbon that in turn is now farther from the nickel surface. In this structure, the anchoring interactions of CH_2O are due to the bridged oxygen, and to the C–Ru bond.

As shown in the MEP of figure 2.38, in the way from reactant to transition state the images keep increasing in energy, but between points three and four the curve flattens out. This could be due to the presence of a reaction intermediate, but the “resolution” of eight images used for this calculation is not enough to find it. The transition state for this reaction is located at image six, the geometry of which is similar to that of the product, but here the carbon is still close to the nickel surface, occurrence that limits its

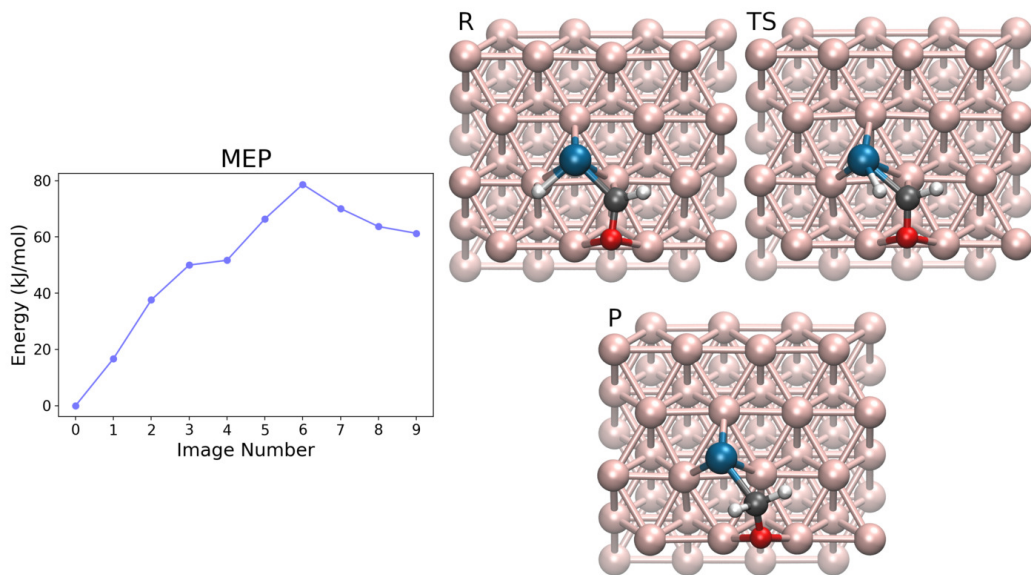


Figure 2.38: MEP and geometries of interest of the R08 elementary step: $\text{CHO} + \text{H} \longrightarrow \text{CH}_2\text{O}$. **R**eactant, image 0; **TS**, image 6; **P**roduct, image 9. Colors: H white; C black; O red; Ni rose gold; Ru blue.

interaction with the now close hydrogen.

Even if less than R07, the R08 elementary step is still endothermic with a ΔE_r of 61.3 kJ/mol, its activation energy being 78.7 kJ/mol.

R09: $\text{CH}_2\text{O} + \text{H} \longrightarrow \text{CH}_3\text{O}$ To discover the transition state for this elementary step, it was used a reactant structure similar to the product of R08, the difference being that here a supplementary hydrogen is placed near the ruthenium, with the consequence that the latter leans towards a bridge site of the nickel surface. In the product structure, instead, Ru is on its favorite position, an HCP site, whereas CH_3O is placed on an FCC site nearby, adsorbed on the surface through its oxygen.

Figure 2.39 shows the result of the CI-NEB calculation. Due to the similar absolute energies of reactant and product, the MEP is pretty symmetrical and the transition state is located in the middle of the elastic band at image four. Its structure shows that the atomic hydrogen is still bonded to Ru, but moved to a top site, being now closer to the carbon. Meanwhile, the CH_2O fragment is more perpendicular to the surface, and its oxygen is also shifted towards the FCC site.

This elementary step is slightly endothermic with a ΔE_r of 7.4 kJ/mol, the activation energy being 90.8 kJ/mol.

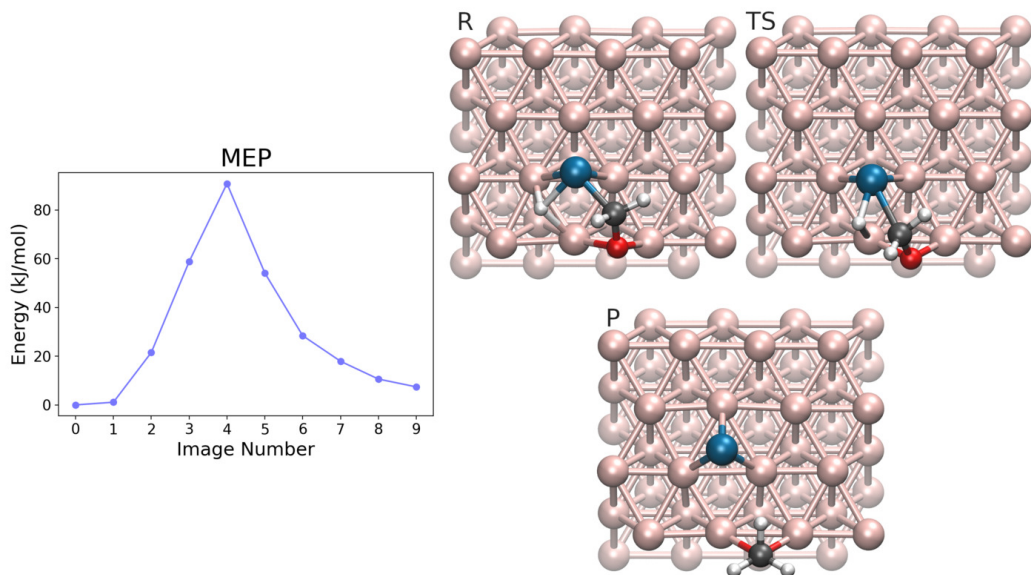


Figure 2.39: MEP and geometries of interest of the R09 elementary step: $\text{CH}_2\text{O} + \text{H} \longrightarrow \text{CH}_3\text{O}$. **R**eactant, image 0; **TS**, image 4; **P**roduct, image 9. Colors: H white; C black; O red; Ni rose gold; Ru blue.

R10: $\text{CO} + \text{H} \longrightarrow \text{COH}$ To investigate the hydrogenation process of carbon monoxide that gives the COH species, a structure was used as reactant in which the CO molecule is overall on an HCP site (with C on a bridge site and O on a top site), where C is also bonded to a bridged Ru. Meanwhile, the atomic hydrogen is placed on a FCC site near the oxygen. In the product geometry, instead, the ruthenium atom is still on the same bridge site, but the carbon of COH is here shifted towards the nearest HCP site thanks to the reduced interaction of the now saturated oxygen with the nickel surface.

The MEP, shown in figure 2.40, is smooth, and the transition state is located on image five. The TS geometry is similar to the one of the product, where the hydrogen is midway to the oxygen but still close enough to the nickel surface: it is using an underlying Ni atom as a pivot for its migration.

In this elementary step the reactant is far more stable than the product, thus giving a strong endothermic ΔE_r of 99.8 kJ/mol. The high activation energy of 135.1 kJ/mol confirms that CO has a low tendency to react.

R11: $\text{CHO} + \text{H} \longrightarrow \text{CHOH}$ In the reactant geometry used to study this elementary step, the CHO species has its carbon near a top site, bonded to an HCP ruthenium, while the oxygen is over a bridge site. Here the atomic

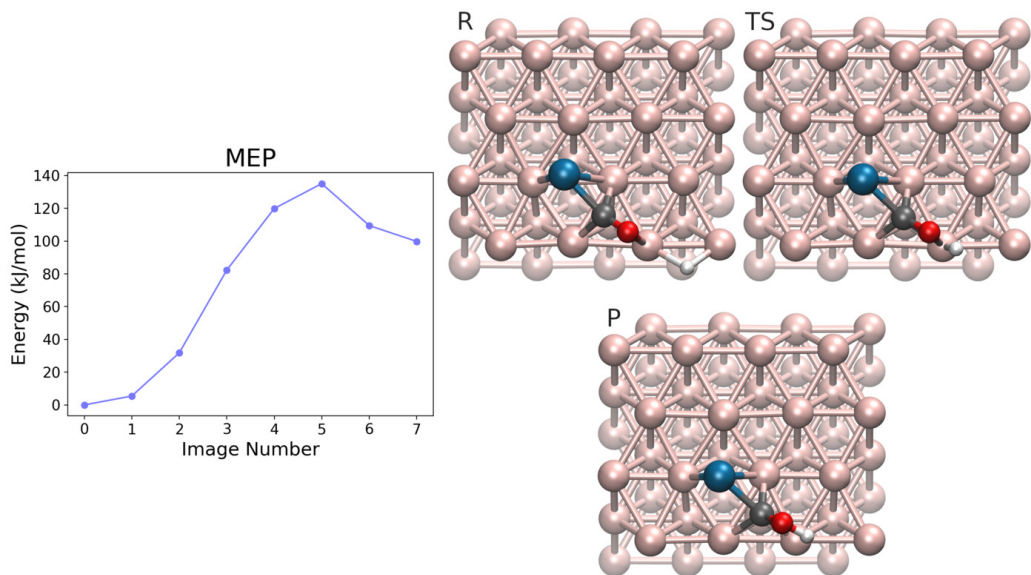


Figure 2.40: MEP and geometries of interest of the R10 elementary step: $\text{CO} + \text{H} \rightarrow \text{COH}$. Reactant, image 0; **TS**, image 5; Product, image 7. Colors: H white; C black; O red; Ni rose gold; Ru blue.

hydrogen is on an FCC site next to the oxygen. In the product structure, on the other hand, the new hydroxyl group is on a top site, thus making the C–O bond of the CHOH species almost parallel to the underlying Ni–Ni bond.

The CI-NEB was performed using a slightly looser threshold of $3.5 \cdot 10^{-3} E_h/\text{\AA}$ on the force norms. Figure 2.41 shows that there is a reaction intermediate along the MEP, located at image two. This is due to the hopping of the atomic hydrogen from the original FCC to a near HCP site. The transition state is then found at image five. Its structure shows that the atomic hydrogen is midway between an FCC site and the oxygen of CHO. Another way to describe its structure is that the hydroxyl group is pointing towards an FCC site of the nickel surface, a destabilizing situation in which the hydrogen is surrounded by too many nuclei.

The ΔE_r of this highly endothermic elementary step is 100.7 kJ/mol, while the activation energy being 128.8 kJ/mol.

R12: $\text{CH}_2\text{O} + \text{H} \rightarrow \text{CH}_2\text{OH}$ To find the transition state of the hydrogenation of the CH_2O species on oxygen, a geometry was used for the reactant where the CH_2O species is bonded to an HCP Ru through C, and to the nickel surface via its oxygen, placed on a bridge site. Finally, the

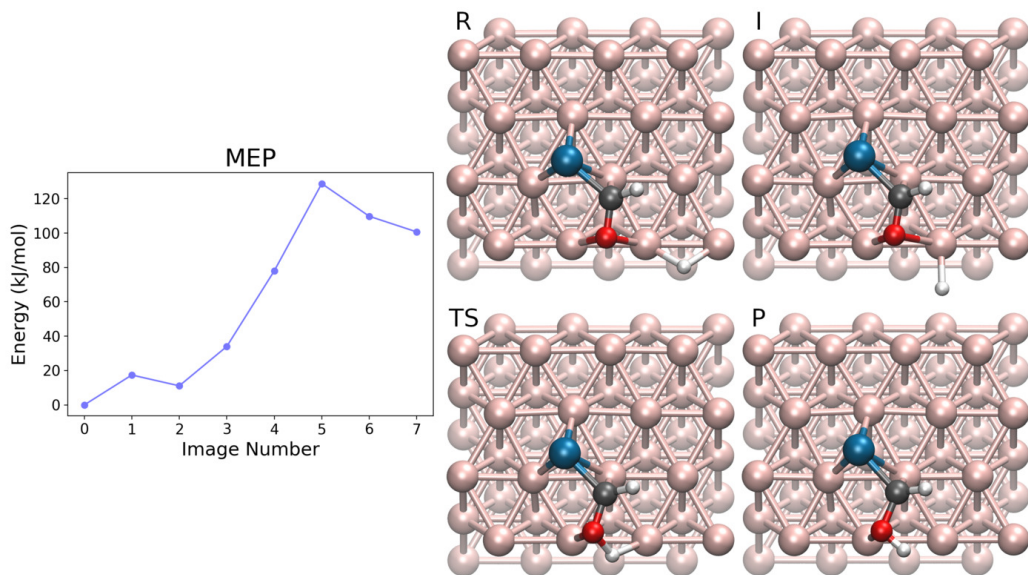


Figure 2.41: MEP and geometries of interest of the R11 elementary step: $\text{CHO} + \text{H} \longrightarrow \text{CHOH}$. **R**eactant, image 0; **I**ntermediate, image 2; **TS**, image 5; **P**roduct, image 7. Colors: H white; C black; O red; Ni rose gold; Ru blue.

atomic hydrogen is near the oxygen on a HCP site. The product structure is pretty similar to the reactant, but here the hydrogen is bonded to the oxygen that maintain its bridged position, with the effect that the resulting hydroxyl group is pointing upward.

The MEP reported in figure 2.42 shows that the transition state is located at image four. Its geometry is quite different from the reactant for several reasons: Ru moved from an HCP to a bridge site, the previously bridged oxygen of CH_2O shifted towards a top site, and finally the atomic hydrogen hopped from the original HCP site to the FCC site located just below the oxygen. Keeping to follow the minimum energy path one can see a reaction intermediate at image six, just before the product geometry. The structure of this intermediate is similar to the one of the product, the difference being the orientation of the hydroxyl group, here pointing in a direction parallel to the underlying surface. This orientation is due to the interaction of the oxygen with a top site, as opposed to its bridged position in the product.

Considering that the reaction intermediate is more stable than the product, its absolute energy was used to compute the ΔE_r of 63.6 kJ/mol, the activation energy for this elementary step being 95.7 kJ/mol.

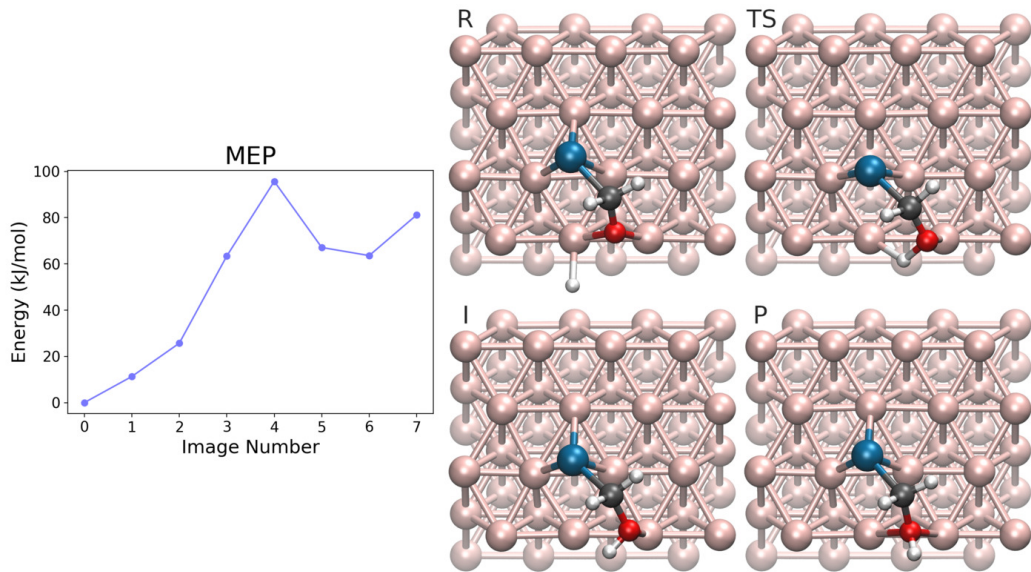


Figure 2.42: MEP and geometries of interest of the R12 elementary step:
 $\text{CH}_2\text{O} + \text{H} \longrightarrow \text{CH}_2\text{OH}$. Reactant, image 0; TS, image 4;
 Intermediate, image 6; Product, image 7. Colors: H white; C black; O red; Ni rose gold; Ru blue.

R14: $\text{CO} \longrightarrow \text{C} + \text{O}$ To study the dissociation of CO into atomic carbon and oxygen, the structure used as reactant has the CO molecule over an HCP site, bonded to a bridged Ru through the carbon, while the oxygen is close to a top site. On the product geometry, Ru is still on the same bridge site bonded to the atomic HCP carbon, whereas the atomic oxygen is on the HCP site next to that of C. Among other things, figure 2.43 shows the product structure: it is hard to notice from its top view, but the nickel atom connecting the two HCP sites occupied by C and O is slightly raised above the surface. This causes a distortion of all the adjacent HCP and FCC sites, and as a consequence both C and O do not appear perfectly centered on their respective HCP sites.

Looking at the MEP of figure 2.43, the TS is located in the middle of the elastic band at image five. As often happens with very symmetrical MEP, the transition state geometry is halfway between those of reactant and product: the oxygen is on the bridge site between the top site it occupies in the reactant and its HCP site in the product, whereas both Ru and C stay pretty much in the same position.

This is a slightly endothermic elementary step with a ΔE_r of 10.4 kJ/mol, which however has an outstandingly high activation energy of 144.5 kJ/mol

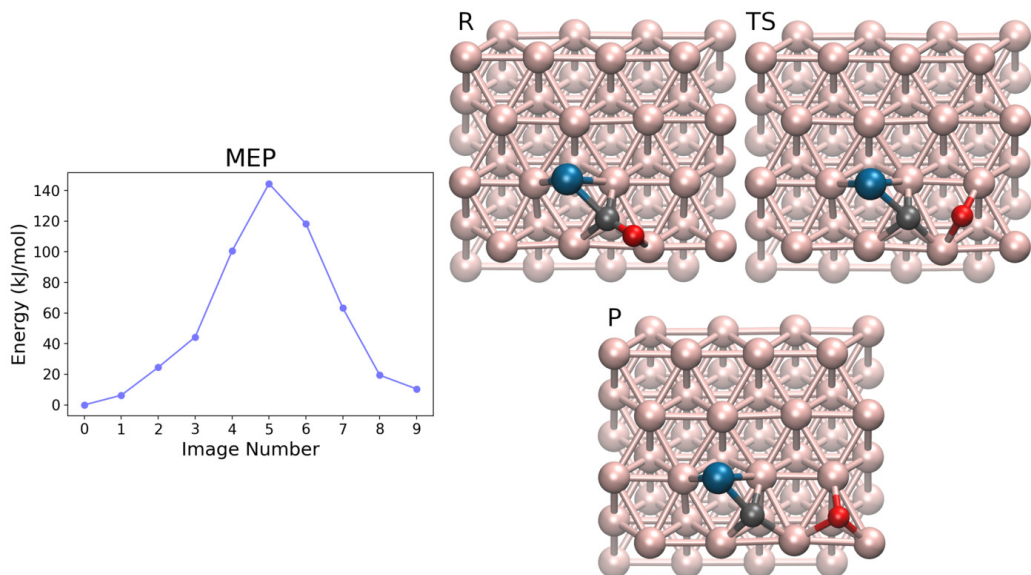


Figure 2.43: MEP and geometries of interest of the R14 elementary step: $\text{CO} \longrightarrow \text{C} + \text{O}$. **R**eactant, image 0; **TS**, image 5; **P**roduct, image 9. Colors: C black; O red; Ni rose gold; Ru blue.

due to the dissociation of a very stable molecule such as CO.

R15: $\text{CHO} \longrightarrow \text{CH} + \text{O}$ To locate the transition state of this elementary step, the reactant structure of choice has the Ru atom on an HCP site, and the CHO species adsorbed on the catalyst through both a C–Ru interaction and a bridged oxygen. In the product geometry, instead, the atomic oxygen is on the FCC site near its starting bridge position, while the Ru–CH complex moved away from O: Ru is on a bridge site and interacts with the CH fragment located on an HCP site.

The CI-NEB calculation was performed using five images due to the small spatial shift the chemical species have to perform going from reactant to product. The minimum energy path, reported in figure 2.44, presents a single peak at image two, the transition state. The TS geometry is a peculiar mix of both elastic band endpoints. The CH fragment is in a similar position as that in the reactant, while the oxygen farther away from C, on the same FCC site it will occupy in the product. The ruthenium position, however, differs from both reactant and product, being on a completely new bridge site.

Despite the pretty exothermic ΔE_r of -68.8 kJ/mol for this elementary step, it has a moderately high activation energy of 77.9 kJ/mol.

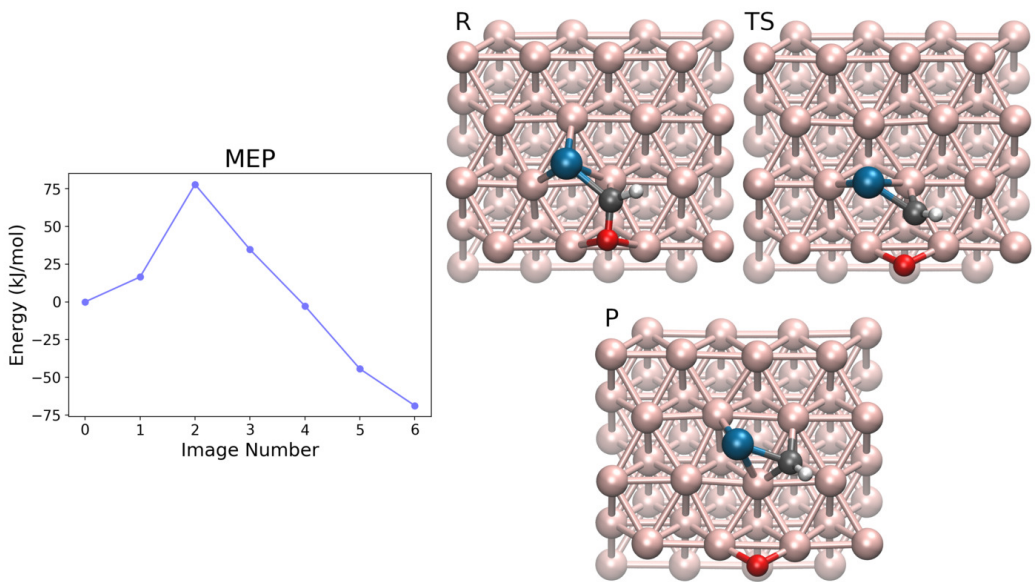


Figure 2.44: MEP and geometries of interest of the R15 elementary step: $\text{CHO} \longrightarrow \text{CH} + \text{O}$. Reactant, image 0; TS, image 2; Product, image 6. Colors: H white; C black; O red; Ni rose gold; Ru blue.

R16: $\text{CH}_2\text{O} \longrightarrow \text{CH}_2 + \text{O}$ This elementary step is about the dissociation of the oxygen from the CH_2O species. To locate its transition state, it was used a reactant structure in which CH_2O is anchored to the surface through a bridged oxygen, while the carbon bonds an HCP Ru. In the product geometry, instead, the atomic oxygen is on the nearest FCC site, while the CH_2 fragment is still bonded to the HCP Ru but drifted away a little with respect to its initial position, now being closer to the nickel surface.

Figure 2.45 shows a fairly regular MEP that presents a steep peak in the first part of the elastic band, with the transition state located at image two. The TS geometry is similar to that of the reactant since in both structures the CH_2 fragment is at the same height from the surface, the difference being that in TS the CH_2 group is slightly rotated and thus a bit spaced from the oxygen.

This elementary step, just like that of R15, is quite exothermic with a ΔE_r of -73.2 kJ/mol, and has an high activation energy of 81.1 kJ/mol.

R17: $\text{CH}_3\text{O} \longrightarrow \text{CH}_3 + \text{O}$ The reactant geometry of choice to study this elementary step has the CH_3O species bonded to the nickel surface through its oxygen, located over an FCC site, while Ru is on an HCP site nearby. In the product structure, on the other hand, the CH_3 group is bonded to the

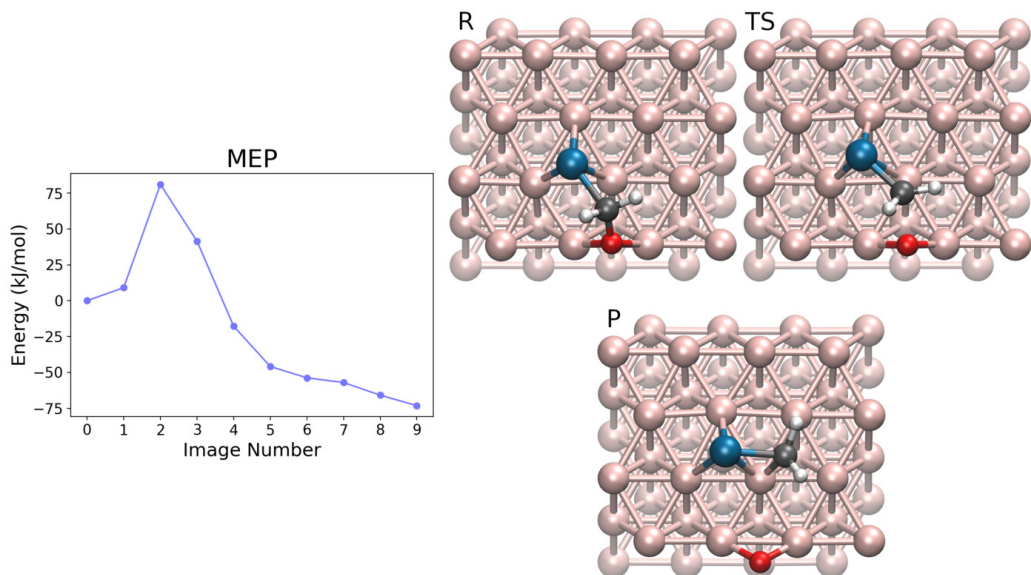


Figure 2.45: MEP and geometries of interest of the R16 elementary step: $\text{CH}_2\text{O} \longrightarrow \text{CH}_2 + \text{O}$. Reactant, image 0; TS, image 2; Product, image 9. Colors: H white; C black; O red; Ni rose gold; Ru blue.

ruthenium atom, while the atomic oxygen remains on the same FCC site. Considering the choice of these initial structures, it is the CH_3 fragment who moves in this reaction (that “jumps” from O to Ru, as it will be shown), but despite all the attempts it was not possible to find a better structure to use as reactant due to the limited interaction capabilities of CH_3O with the catalyst.

The MEP in figure 2.46 shows that the transition state is located at image four. Since this reaction develops in height, it is not simple to see what happens from the top views shown in figure, hence some distances are reported to clarify what is happening. C–O distance: reactant 1.432 Å, TS 2.520 Å, product 3.292 Å. C–Ru distance: reactant 3.988 Å, TS 3.373 Å, product 2.037 Å. In TS, the CH_3 fragment moves away from all the other atomic nuclei (the nearest of which being O and Ru): during this jump, it is isolated and assumes a planar geometry.

The ΔE_r for this elementary step is -45.4 kJ/mol, while the energy barrier being 161.8 kJ/mol. This is the highest forward activation energy found among all elementary steps on the Ru-decorated surface, due to the extreme instability of the isolated CH_3 species in the transition state.

R18: $\text{COH} + \text{H} \longrightarrow \text{CHOH}$ The structure employed as reactant to in-

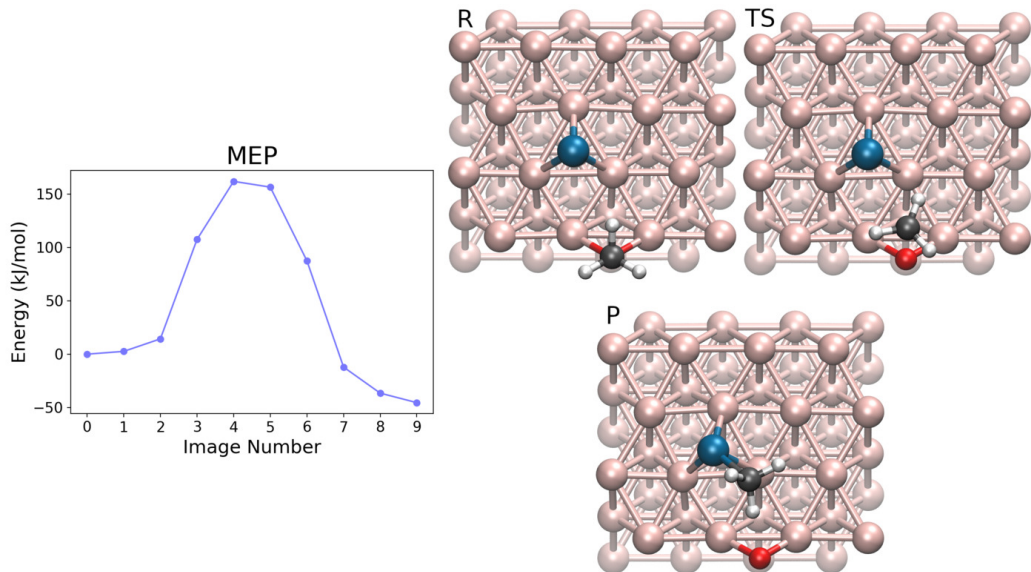


Figure 2.46: MEP and geometries of interest of the R17 elementary step: $\text{CH}_3\text{O} \longrightarrow \text{CH}_3 + \text{O}$. Reactant, image 0; TS, image 4; Product, image 9. Colors: H white; C black; O red; Ni rose gold; Ru blue.

vestigate this elementary step has the COH bonded to a bridged Ru through the carbon, the latter being over an FCC site. Regarding the atomic hydrogen, it is on another FCC site near the ruthenium: the original idea was to exploit Ru as a pivoting center for the hydrogenation reaction. In the product geometry, instead, Ru is slightly shifted towards the near HCP site, the Ru–C interaction being still present, and the CHO fragment lays over a bridge site being the C–O bond parallel to the underlying Ni–Ni one.

As shown in figure 2.47, the MEP presents a reaction intermediate just after the reactant, at image two: its geometry shows that H hopped to the near HCP site, thus excluding the original Ru-pivoting hypothesis for this hydrogenation reaction. The transition state is found at image five. Its geometry shows that Ru is slightly over an FCC site, and the CHO species has the C–O bond centered on another FCC site: the complex Ru–CHO will then shift towards its (very similar) final position in the product geometry, that is not so different in terms of absolute energy.

Since an intermediate was found just after the reactant, its energy was used in place of that of the latter to evaluate both ΔE_r and activation energy, which are 94.9 and 111.9 kJ/mol, respectively.

R19: $\text{CHOH} + \text{H} \longrightarrow \text{CH}_2\text{OH}$ This elementary step is about the

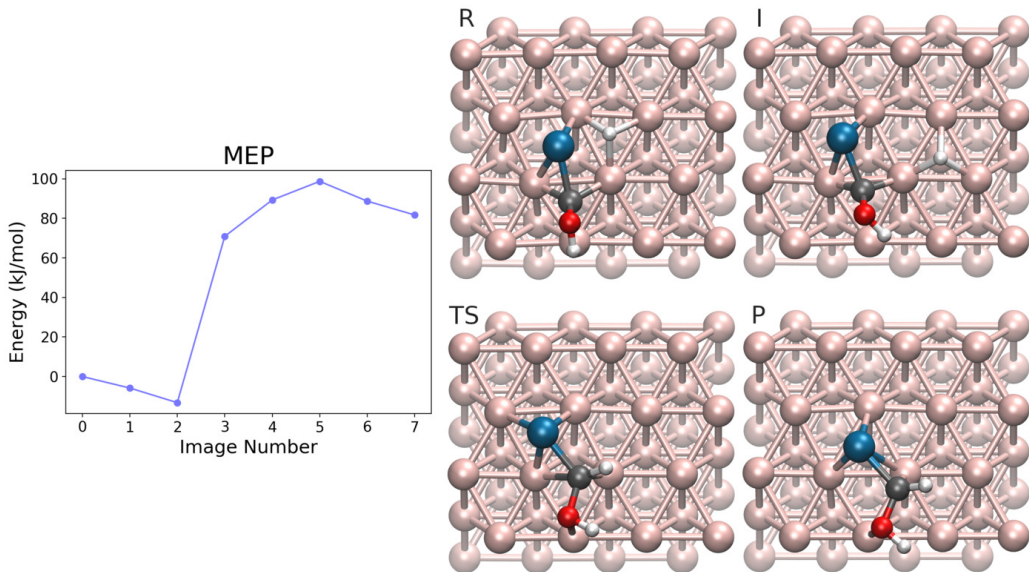


Figure 2.47: MEP and geometries of interest of the R18 elementary step: $\text{COH} + \text{H} \longrightarrow \text{CHOH}$. **R**eactant, image 0; **I**ntermediate, image 2; **TS**, image 5; **P**roduct, image 7. Colors: H white; C black; O red; Ni rose gold; Ru blue.

hydrogenation of CHOH to give the CH_2OH species. To locate the transition state, two geometries were prepared and optimized for reactant and product. In the former, the ruthenium atom is over an HCP site, bonding both the atomic hydrogen and the carbon of CHOH , that in turn has the C–O bond over a bridge site, parallel to the underlying Ni–Ni bond. The position of Ru in the product structure does not change, but this time it bonds only the carbon since the hydrogen moved to give the CH_2 group of CH_2OH . It is important to state that the carbon is close to the nickel surface in the reactant, whereas this is not the case in the product. As in R18, this specific reactant geometry was chosen in order to verify if Ru can act as a pivot.

Figure 2.48 shows that the MEP is mostly smooth, with only a spike going from image three to four, the latter being the transition state. By examining the TS structure, one notices that the hydrogen is approaching the carbon from the top: H is still close to Ru just as C is still close to the nickel surface. Proceeding towards the product, the CH_2 group will move upward, away from the surface.

The considered elementary step has an endothermic ΔE_r of 50.0 kJ/mol, its activation energy being 75.3 kJ/mol.

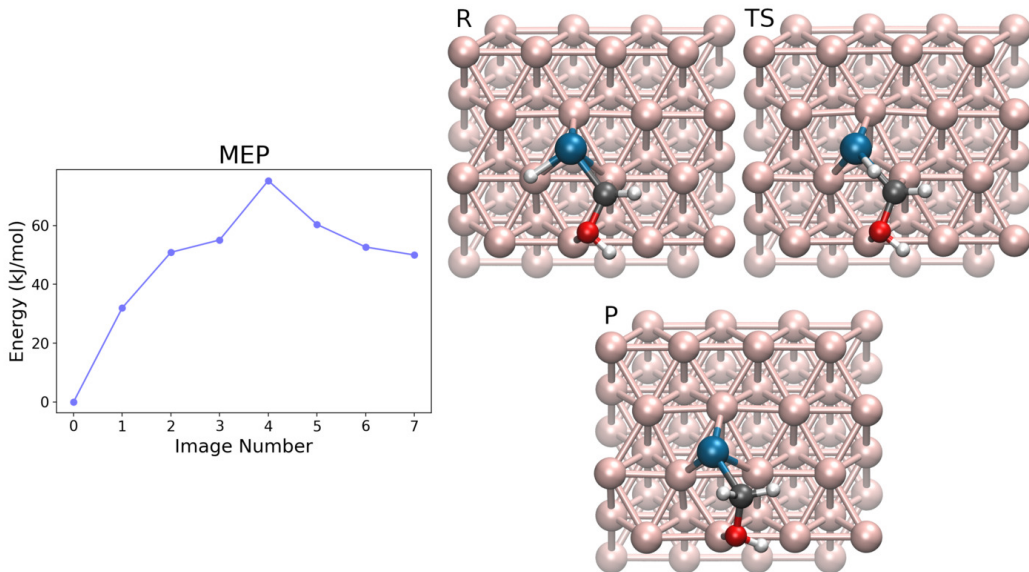


Figure 2.48: MEP and geometries of interest of the R19 elementary step: $\text{CHOH} + \text{H} \longrightarrow \text{CH}_2\text{OH}$. Reactant, image 0; TS, image 4; Product, image 7. Colors: H white; C black; O red; Ni rose gold; Ru blue.

R20: $\text{CH}_2\text{OH} + \text{H} \longrightarrow \text{CH}_3\text{OH}$ In order to investigate the final hydrogenation of CH_2OH , a reactant structure was prepared in which that chemical species is bonded to a bridged Ru through the carbon, while the hydroxyl oxygen interacts with a top site (Ni–O distance being 2.184 Å). The atomic hydrogen is bonded to Ru, willing to pivot around it to reach the CH_2 group. In the product structure, instead, the methanol molecule is adsorbed on the surface thanks to the sole Ni–O interaction (the distance between the two nuclei being 2.333 Å), and the ruthenium atoms occupies an HCP site since it now has no interactions with species other than Ni atoms.

The minimum energy path is reported in figure 2.49, it is spiky around image four, that is the transition state for the reaction. The TS geometry shows that the atomic hydrogen pivoted around Ru in order to approach the CH_2 group from below. Moreover, the hydroxyl group is far away from the surface, at a distance of 3.068 Å from the nearest Ni.

This elementary step is slightly endothermic with a ΔE_r of 28.2 kJ/mol. It also has a not to high activation energy of 62.4 kJ/mol.

R21: $\text{COH} \longrightarrow \text{C} + \text{OH}$ This elementary step is about the dissociation of the COH species into atomic carbon and an adsorbed hydroxyl group.

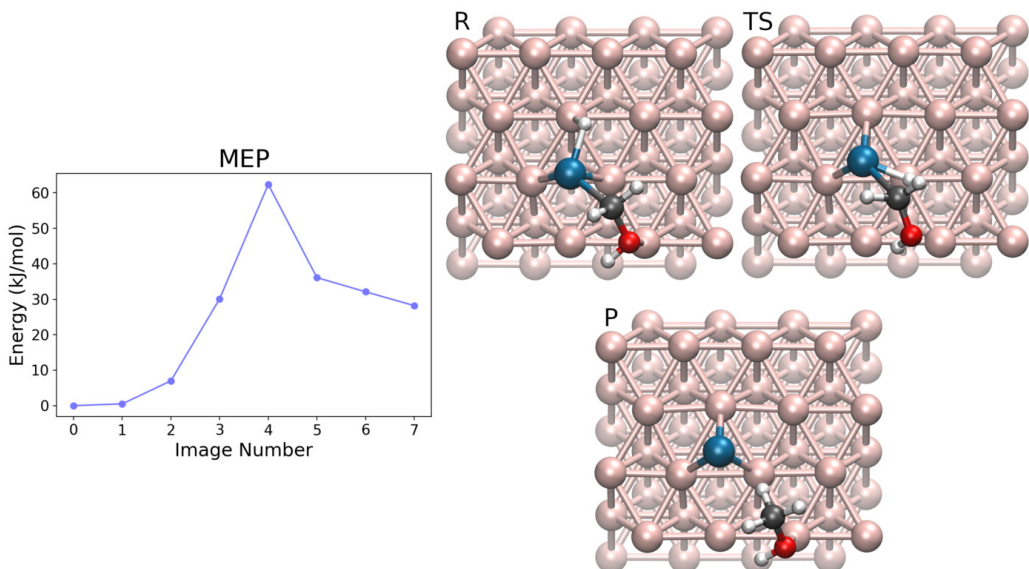


Figure 2.49: MEP and geometries of interest of the R20 elementary step:
 $\text{CH}_2\text{OH} + \text{H} \longrightarrow \text{CH}_3\text{OH}$. Reactant, image 0; TS, image 4;
 Product, image 7. Colors: H white; C black; O red; Ni rose gold;
 Ru blue.

The reactant geometry has the ruthenium on a bridge site, bonded to the an HCP carbon of COH, the hydroxyl group of which has the hydrogen pointing upward. In the product structure both the positions of Ru and C do not change, but now the hydroxyl group is on an HCP site next to that of the carbon. In this structure, the Ni atom shared among the two HCP sites occupied by C and OH protrudes slightly from the rest of the nickel (111) surface: for this reason the top view of the product geometry shows both C and OH a bit off centered from their HCP sites.

The MEP for this reaction shows an intermediate just after the reactant at image two, as reported in figure 2.50. The intermediate geometry differs from that of the reactant for a 180° rotation of the hydroxyl group, the O–H bond here being parallel to the nickel surface. Following the reaction path, the transition state occurs at image five, its geometry shows that the hydroxyl group is over the nearest top site, moving away from C.

The ΔE_r and activation energy were computed using the absolute energy of the intermediate instead of that of the reactant; they are, respectively, -38.8 and 81.8 kJ/mol.

R22: $\text{CHOH} \longrightarrow \text{CH} + \text{OH}$ Concerning this elementary step, the

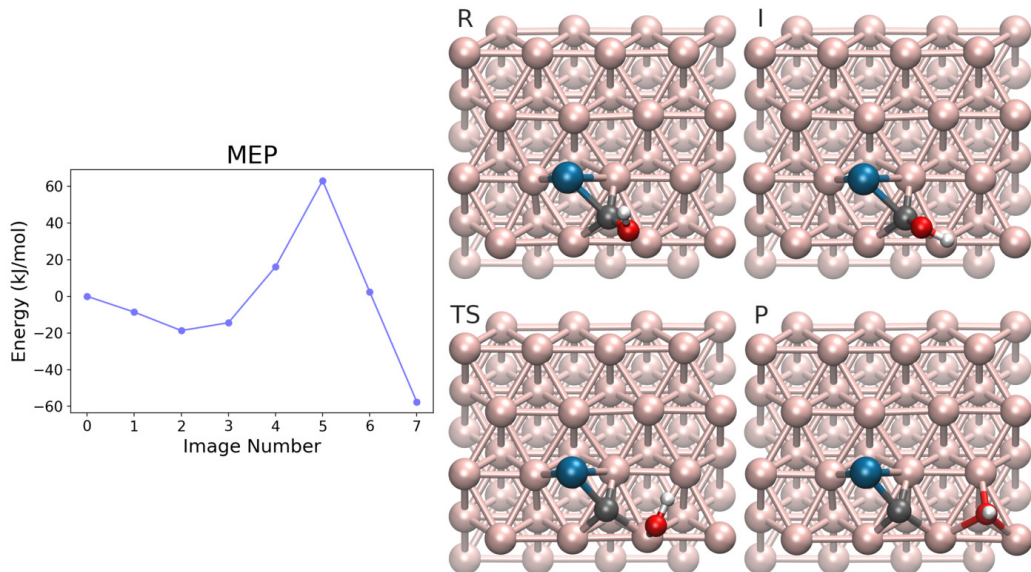


Figure 2.50: MEP and geometries of interest of the R21 elementary step: $\text{COH} \longrightarrow \text{C} + \text{OH}$. **R**eactant, image 0; **I**ntermediate, image 2; **TS**, image 5; **P**roduct, image 7. Colors: H white; C black; O red; Ni rose gold; Ru blue.

structures used to determine its transition state were: a reactant in which the CHOH species is placed with the C–O bond parallel to the surface over a bridge site, while the carbon also bonds an HCP Ru; and a product where the CH fragment is over an HCP site, still bonded to the ruthenium that now is on a bridge site, meanwhile the hydroxyl group slipped towards an FCC site near its original position.

The MEP, reported in figure 2.51, is smooth, and the transition state was located next to the reactant at image two. Its geometry shows that the C–O distance increased with respect to the reactant. Moreover, the CH fragment is more centered on the top of its nearest Ni, while OH moved towards a bridged position.

This elementary step is very exothermic with a ΔE_r of -112.1 kJ/mol, while its activation energy is 55.2 kJ/mol.

R23: $\text{CH}_2\text{OH} \longrightarrow \text{CH}_2 + \text{OH}$ This elementary step was investigated using, as reactant, a structure in which the ruthenium atom is on HCP site, bonding the carbon of the CH_2OH species, whose hydroxyl group in turn interacts with a bridge site of the nickel surface. In this structure, the CH_2 group is far from the surface, bridged between Ru and O. In the product

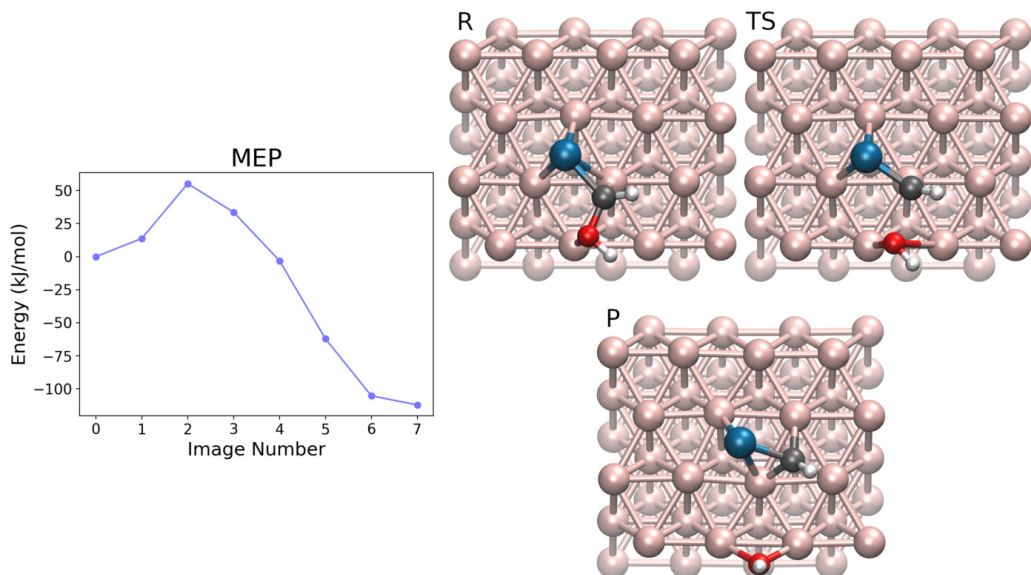


Figure 2.51: MEP and geometries of interest of the R22 elementary step: $\text{CHOH} \longrightarrow \text{CH} + \text{OH}$. **R**eactant, image 0; **TS**, image 2; **P**roduct, image 7. Colors: H white; C black; O red; Ni rose gold; Ru blue.

geometry, instead, the hydroxyl group is now isolated on an FCC site, while the CH_2 fragment, still bonded to Ru, is closer to the surface over a bridge site.

Figure 2.52 shows a mostly smooth MEP that locates the transition state of this reaction at image two. Since its energy is very close to that of the reactant, the two geometries do not differ sensibly. Indeed, the only difference is an elongation of the C–O bond (1.479 Å in the reactant, 1.898 Å in the TS) mostly due to the approaching of the hydroxyl group to the nickel surface.

This strongly exothermic reaction, whose ΔE_r is -112.9 kJ/mol, is accompanied by a small activation energy of 24.2 kJ/mol, showing the instability of the CH_2OH species when it interacts in the described way with the ruthenium decoration.

R24a: $\text{CH}_3\text{OH} \longrightarrow \text{CH}_3 + \text{OH}$ Studying the dissociation of CH_3OH was tricky, probably due to the limited interaction capabilities of this species with its environment: being the carbon fully saturated, only the oxygen can interact effectively. For this reason, two different ways in which this step can occur were investigated. In this paragraph R24a is discussed, which is similar to R21, R22, and R23 in the sense that the alcoholic species dissociates leaving its hydroxyl group on the surface, while the carbon fragment moves

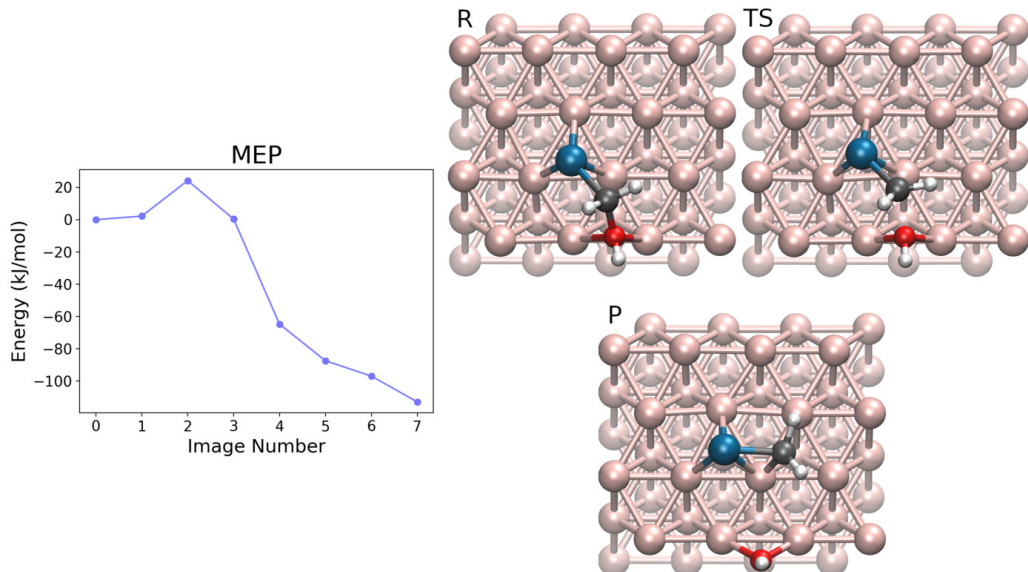


Figure 2.52: MEP and geometries of interest of the R23 elementary step:
 $\text{CH}_2\text{OH} \longrightarrow \text{CH}_2 + \text{OH}$. Reactant, image 0; TS, image 2;
 Product, image 7. Colors: H white; C black; O red; Ni rose gold;
 Ru blue.

to the ruthenium atom. In the reactant structure, CH_3OH is anchored to a top site using its oxygen, with the methyl group slightly oriented towards Ru. In the product geometry, instead, the methyl group is bonded to Ru, leaving the hydroxyl fragment on an FCC site of the surface.

The CI-NEB calculation was performed using six images, but this time the best achievement of the FIRE algorithm was to reach $7.3 \cdot 10^{-3} E_h/\text{\AA}$ on the highest force norm (incidentally, that of the transition state) before starting to diverge. Figure 2.53 shows an abrupt MEP, especially going from images one to two, and from four to five. The transition state is located at image two. It shows an interesting structure in which one hydrogen has been transferred from CH_3 to Ru, thus allowing the now under-saturated carbon to interact with ruthenium. From this point on, the CH_2 fragment will separate from the hydroxyl group, then taking back the third hydrogen. From these considerations, one may imagine that this is not a real elementary step and that one or more reaction intermediates could be involved. The difficulties in this CI-NEB could be due to the small resolution of the elastic band: it is totally possible that using more images would have revealed additional points of interest in the MEP, especially in its steepest regions.

This reaction has an exothermic ΔE_r of -81.7 kJ/mol. Because of the

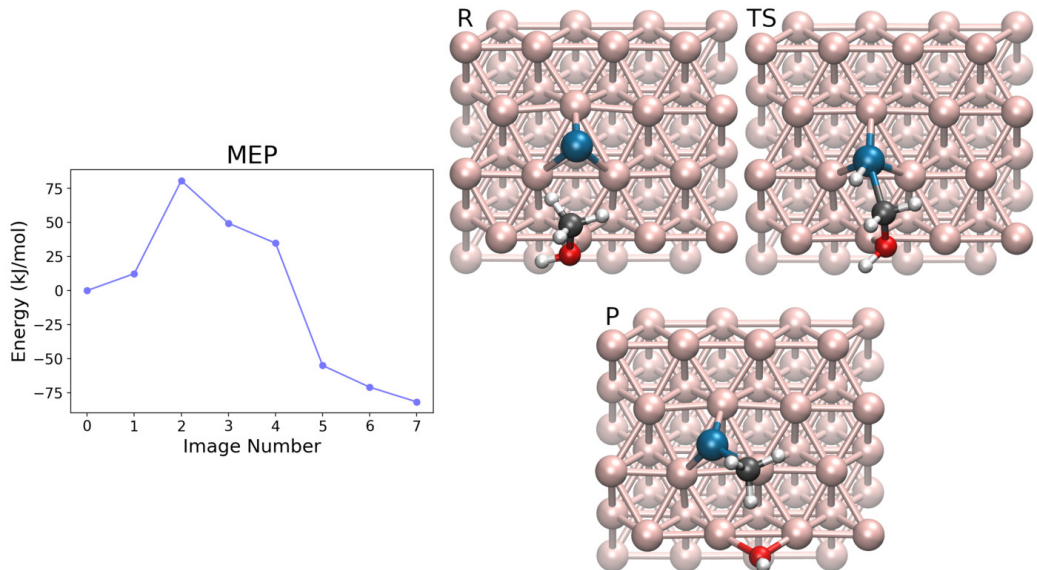


Figure 2.53: MEP and geometries of interest of the R24a elementary step: $\text{CH}_3\text{OH} \longrightarrow \text{CH}_3 + \text{OH}$. Reactant, image 0; TS, image 2; Product, image 7. Colors: H white; C black; O red; Ni rose gold; Ru blue.

difficulties in CI-NEB calculation, however, it was possible to locate the TS only using a looser convergence threshold than the usual one. This means that the determined TS for this elementary step is not as accurate as the others, and so it is the value of 80.7 kJ/mol for the activation energy.

R24b: $\text{CH}_3\text{OH} \longrightarrow \text{CH}_3 + \text{OH}$ Because of the difficulties in R24a, another route was attempted to find the transition state of $\text{CH}_3\text{OH} \longrightarrow \text{CH}_3 + \text{OH}$. This time, instead of placing the methanol molecule over the nickel surface, in the reactant structure it was positioned on top of an HCP Ru, interacting with it through the hydroxyl group. In the product geometry, instead, the ruthenium atom is on a bridge site, interacting with the methyl group on one side, and with the hydroxyl group on the opposite side. Here the two groups are also close to the nickel surface.

The CI-NEB was performed using six images. Optimization of the elastic band was carried with the FIRE algorithm up to the convergence threshold of $4.5 \cdot 10^{-3} E_h/\text{\AA}$. The minimum energy path, reported in figure 2.54, is peaked around image two. An examination of its structure reveals that the methyl group is now closer to Ru (C–Ru distance: 2.385 Å in TS, 3.175 Å in reactant), while also being not completely separated from the hydroxyl

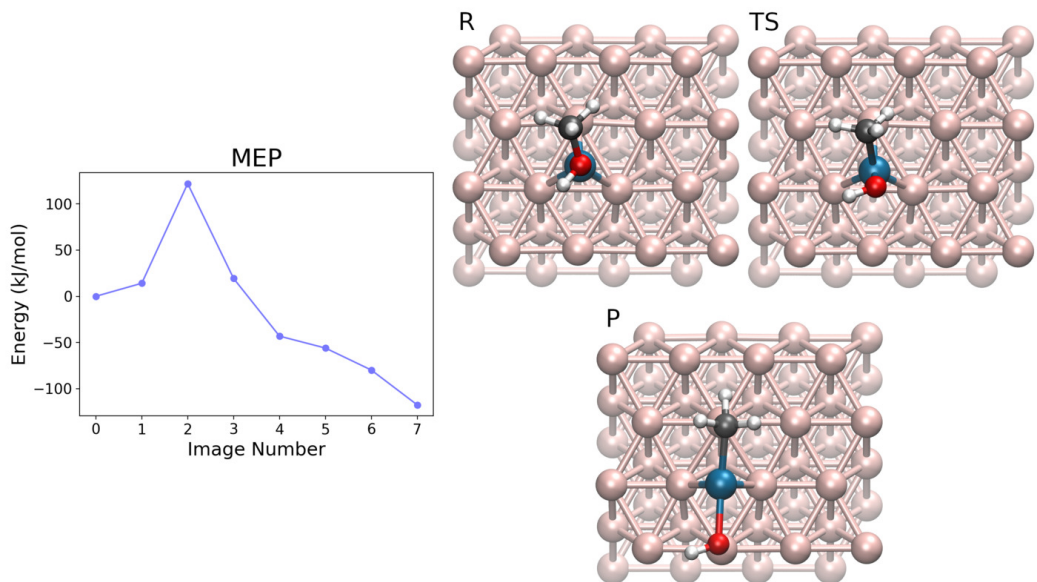


Figure 2.54: MEP and geometries of interest of the R24b elementary step: $\text{CH}_3\text{OH} \longrightarrow \text{CH}_3 + \text{OH}$. Reactant, image 0; TS, image 2; Product, image 7. Colors: H white; C black; O red; Ni rose gold; Ru blue.

group (C–O distance: 1.930 Å in TS, 1.449 Å in reactant).

Using the said structure as reactant and product, this elementary step has a ΔE_r of -117.5 kJ/mol (more exothermic than R24a), while its activation energy is 121.9 kJ/mol.

As a final note, another CI-NEB was attempted to study this reaction, using the same reactant geometry of R24b but a different product structure, in which only the hydroxyl group was bonded to Ru, while the methyl group was adsorbed on the nickel surface. Performing the said calculation showed that there was an intermediate, the optimization of which gave the geometry used as the product of R24b.

R25: C + H → CH The atomic carbon hydrogenation step was investigated preparing, as reactant, a structure where the atomic carbon is on an HCP site bonded to a bridged Ru, while the atomic hydrogen is on the HCP site next to that of the carbon. In the product geometry both Ru and C stays on the same places, while the hydrogen is the only one that changes its position, leaving the nickel surface to bond the carbon.

Figure 2.55 shows a smooth MEP, probably tanks to the high resolution of the elastic band. Images five is the TS, whose geometry shows the hydrogen

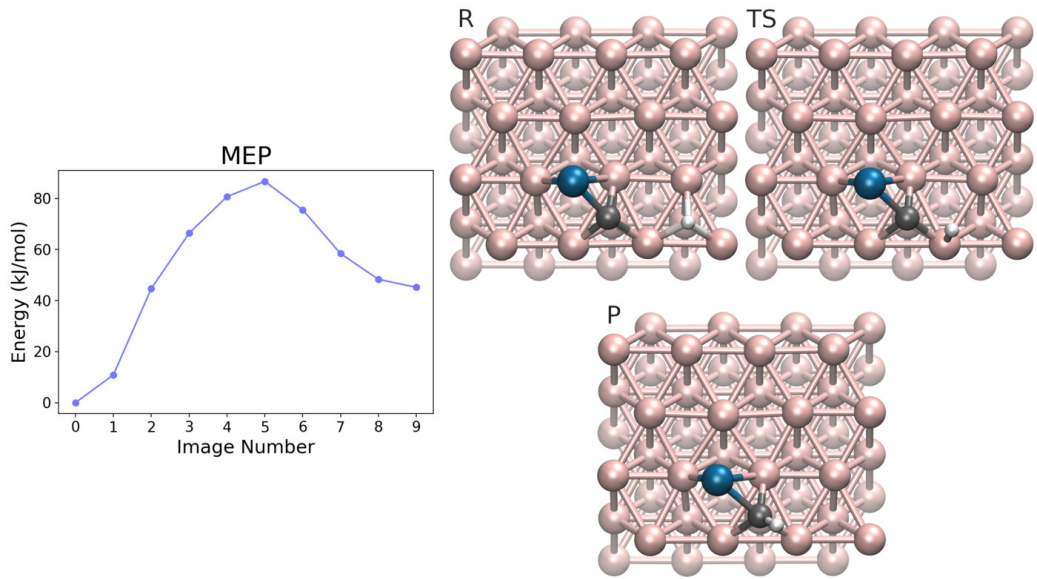


Figure 2.55: MEP and geometries of interest of the R25 elementary step: $\text{C} + \text{H} \longrightarrow \text{CH}$. Reactant, image 0; TS, image 5; Product, image 9. Colors: H white; C black; Ni rose gold; Ru blue.

over the top site that connects the two HCP sites occupied by C and H in the reactant structure.

This is an endothermic elementary step with a ΔE_r of 45.2 kJ/mol, whose activation energy is 86.7 kJ/mol.

R26: $\text{CH} + \text{H} \longrightarrow \text{CH}_2$ The reactant geometry prepared to study this elementary step, has the CH fragment on an HCP site bonded to the near bridged Ru, the atomic hydrogen being on an adjacent HCP site. In the product structure, instead, the CH_2 group is on a bridge site still bonded to the ruthenium atom that slipped on the nearest HCP site.

Figure 2.56 shows a smooth MEP, in which appear both a transition state at image five, and a labile intermediate at image seven. In the TS the atomic hydrogen is approaching CH, leaving its original HCP position for something in between a top and an FCC site. Regarding the reaction intermediate, it has Ru on the same bridge site as in the reactant structure, and CH_2 on a bridge site that is not the same one of the product: this Ru– CH_2 complex will very easily shift on the surface, reaching the final conformation of the product.

This elementary step has a ΔE_r of 73.3 kJ/mol, while its activation energy being 96.3 kJ/mol. This imply a very low energy barrier for the backward

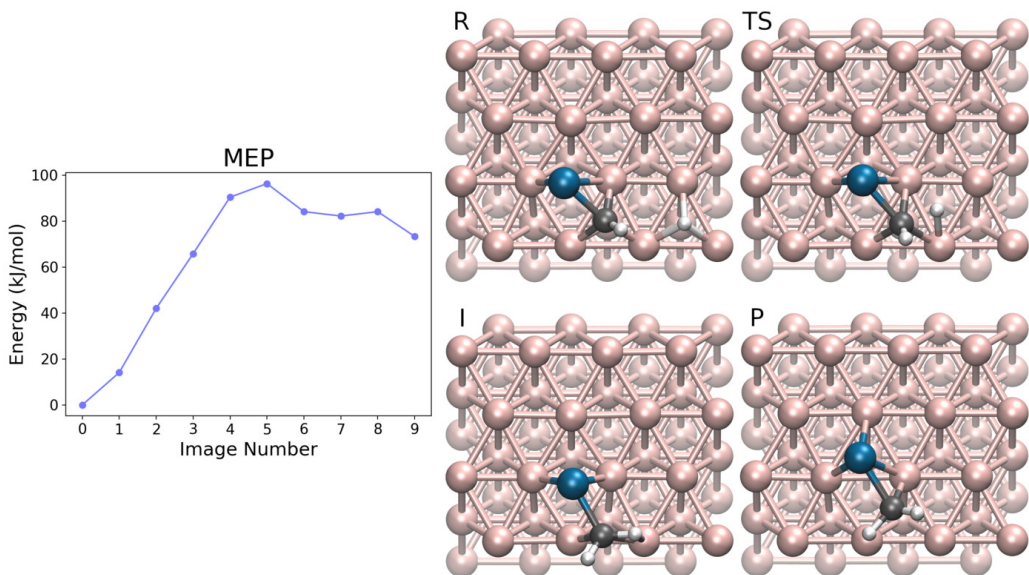


Figure 2.56: MEP and geometries of interest of the R26 elementary step: $\text{CH} + \text{H} \longrightarrow \text{CH}_2$. **R**eactant, image 0; **TS**, image 5; **I**ntermediate, image 7; **P**roduct, image 9. Colors: H white; C black; Ni rose gold; Ru blue.

process, i.e. the CH_2 dehydrogenation.

R27a: $\text{CH}_2 + \text{H} \longrightarrow \text{CH}_3$ The first attempt to study the hydrogenation of CH_2 was made using an atomic hydrogen adsorbed over an FCC site of the nickel surface. The other elements of the reactant structure are the Ru atom on a bridge site that bonds the near CH_2 group, the carbon of which is placed over an FCC site. In the product structure, instead, the methyl group is simply bonded to an HCP Ru, slightly leaned towards the surface.

The transition state was located using a slightly looser threshold of $3.5 \cdot 10^{-3} E_h/\text{\AA}$ on all force norms. As shown in figure 2.57, the MEP has a peak at image three (TS), and a very shallow intermediate at image four. The TS geometry shows that the atomic H migrated to the HCP site below the CH_2 group. The intermediate structure is very similar to that of TS, but here H is closer to C than to the nickel surface. From here two events, namely a slight rotation of the just formed methyl group and the migration of Ru towards the HCP site, will move the hydrogen further away from the surface, thus reaching the energy minimum given by the product.

The ΔE_r for this elementary step is 56.5 kJ/mol, and its low activation energy of 74.9 kJ/mol implies a that the backward dehydrogenation process

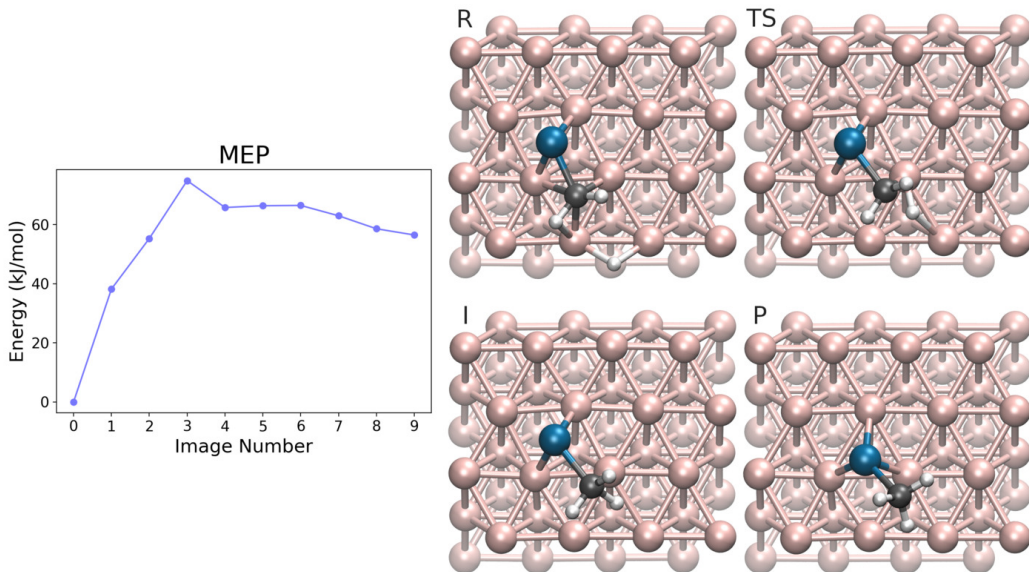


Figure 2.57: MEP and geometries of interest of the R27a elementary step: $\text{CH}_2 + \text{H} \longrightarrow \text{CH}_3$. **R**eactant, image 0; **TS**, image 3; **I**ntermediate, image 4; **P**roduct, image 9. Colors: H white; C black; Ni rose gold; Ru blue.

is favored.

R27b: $\text{CH}_2 + \text{H} \longrightarrow \text{CH}_3$ The R27b step presents an alternative way in which this hydrogenation could happen, i.e. the pivoting of H over Ru to bond the CH_2 group from above. In the reactant structure there is a bridged Ru that interacts with an HCP CH_2 on one side, and with a top H on the other. In the product structure, instead, the methyl group is bonded to Ru, which in turn migrated towards the nearest HCP site.

Figure 2.58 shows a jagged MEP (mainly in its first half), in which there are three maxima at images one, three and five, and two reaction intermediates at images two and four. The last part of the MEP is, instead, flat, with images seven, eight and nine having virtually the same energy: they only differ for a rotation of the methyl group. Despite the high resolution of the elastic band, the eight images were badly distributed during the optimization process since there is a low image density (i.e. two adjacent images differ too much due to the high displacements that the nuclei undergo) in the involved region (the jagged one), whereas too many of them are wasted on different methyl conformation at the end of the band near the product.

The aforementioned figure shows the intermediate at image two, in which

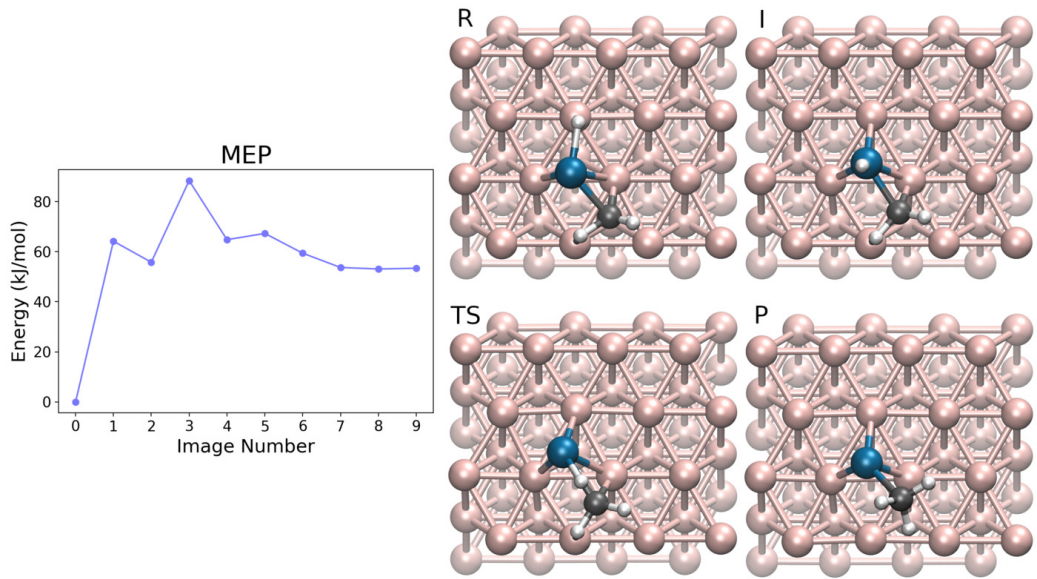


Figure 2.58: MEP and geometries of interest of the R27b elementary step:
 $\text{CH}_2 + \text{H} \longrightarrow \text{CH}_3$. **R**eactant, image 0; **I**ntermediate, image 2;
TS, image 3; **P**roduct, image 9. Colors: H white; C black; Ni rose gold; Ru blue.

the atomic hydrogen migrated on top of Ru. The highest transition state of image three, in which the same atomic hydrogen began its descent towards the CH_2 group, is also reported. In comparison to their positions in the reactant structure, in the TS Ru moved towards the HCP site, dragging the CH_2 group that moved from an HCP to a bridge site.

With a ΔE_r of 53.4 kJ/mol the reaction is endothermic, its activation energy being 88.4 kJ/mol with respect to the TS of image three. Compared to R27a, the Ru-pivoted hydrogenation has a slightly higher activation energy.

R28: $\text{CH}_3 + \text{H} \longrightarrow \text{CH}_4$ The final elementary step that needs to be studied is the hydrogenation that gives a methane molecule. For this one was used a reactant structure in which the methyl group was on top of an HCP Ru (Ru–C distance being 2.043 Å), while the atomic hydrogen is on a top site also bonded with Ru. The product structure has, more simply, a methane molecule above Ru, at a Ru–C distance of 2.752 Å.

The MEP of figure 2.59 shows a peak at image five, the transition state, and a reaction intermediate at image eight, just before the product. In the TS structure, the methyl group is closer to the nickel surface, just above the atomic hydrogen. Here the Ru–C distance is 2.174 Å, and it is notewor-

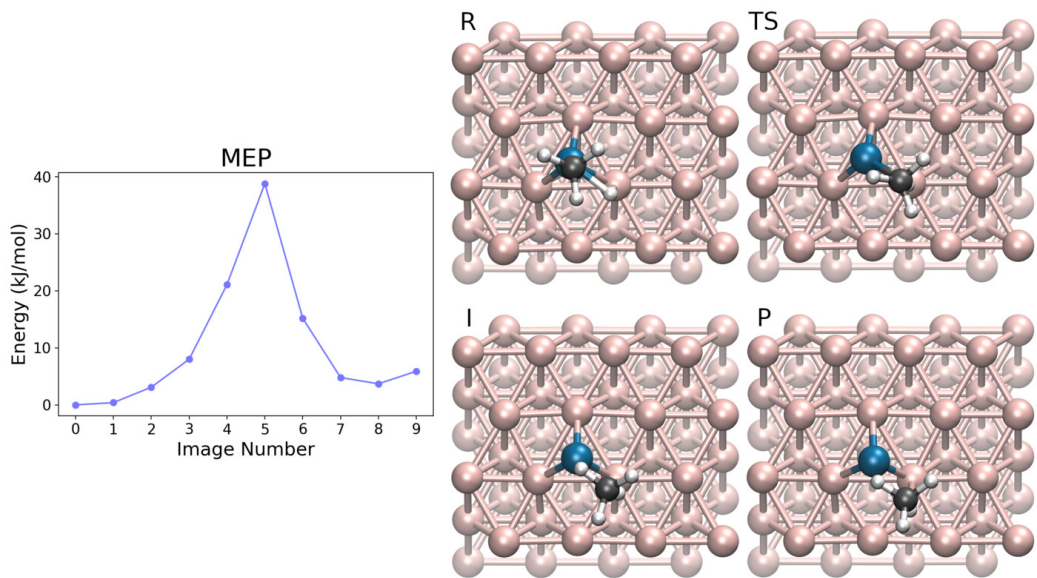


Figure 2.59: MEP and geometries of interest of the R28 elementary step: $\text{CH}_3 + \text{H} \longrightarrow \text{CH}_4$. **R**, Reactant, image 0; **TS**, image 5; **I**, Intermediate, image 8; **P**, Product, image 9. Colors: H white; C black; Ni rose gold; Ru blue.

thy to say that all the three original hydrogens of the methyl group point upwards as in the reactant geometry, just as if the methane molecule was already formed (considering the fourth H below C). The reaction intermediate, instead, differs from the product only for the position of the methane molecule.

The ΔE_r of 3.7 kJ/mol was computed using the absolute energy of the intermediate instead of that of the product, the activation energy being 38.8 kJ/mol.

2.6 CO₂ Methanation on Fe-Decorated Ni (111)

In this Fe-decorated system, just like as in the Ru-decorated one, the 13th elementary step, CH₃O + H → CH₃OH, is missing due to the difficulties encountered in the CI-NEB. The usual 16 chemical species were investigated, for a total of 27 elementary steps labeled from 1 to 28 to match the ones in the section about the pristine nickel surface. Table 2.5 reports a summary of the obtained ΔE_r and E_a , while a discussion of each elementary step follows.

F01: CO₂ → CO + O As always, the first elementary step is the carbon dioxide dissociation, here on the Fe-decorated nickel (111) surface. The two structures used to locate the transition state were: as reactant, a very distorted CO₂ molecule that interacts with a bridged Fe through one oxygen, while the other one is on a bridge site; as product, a CO molecule adsorbed on an HCP site through its carbon, whose oxygen interacts with the near Fe, whereas the atomic oxygen is on the closest HCP site.

The transition state is located at image three of the minimum energy path, reported in figure 2.60. TS structure shows a just dissociated oxygen on the same HCP site it will occupy in the product, whereas the CO fragment has its carbon over a bridge site while maintaining the Fe–O interaction.

This exothermic elementary step has a ΔE_r of -48.8 kJ/mol and an activation energy of 78.8 kJ/mol. As a final note, the reactant structure described in this paragraph differs from that of R01. Despite it has been tried to use a starting structure in which both oxygens were placed near the nickel surface also for this Fe-decorated system, during the optimization process CO₂ changes its orientation, finally reaching the vertical conformation here reported.

F02: CO₂ + H → COOH To study the CO₂ hydrogenation that gives the COOH species, it was used a reactant structure in which Fe is on an HCP site, interacting with an oxygen of CO₂. This latter species interacts with the nickel surface through the carbon (on a bridge site) and the other oxygen (near a top site). Finally, the atomic hydrogen is on an FCC site not too far away from C. Regarding the product structure, the iron atom is still on the same HCP site, but now it is closer to C rather than O. The hydrogen, instead, is now bonded to an oxygen, and the resulting hydroxyl group is raised from the surface.

As shown in figure 2.61, the MEP is very stepped in the first part and has a peaked shape around image three, the transition state. The TS geometry is similar to that of the product, e.g. the oxygen that was bonded to Fe in

Table 2.5: Elementary steps on Fe-decorated Ni (111) surface. All energies expressed in kJ/mol.

Code	Elem. Step	ΔE_r	$E_{a\rightarrow}$	$E_{a\leftarrow}$
F01	$\text{CO}_2 \longrightarrow \text{CO} + \text{O}$	-48.8	78.8	127.7
F02	$\text{CO}_2 + \text{H} \longrightarrow \text{COOH}$	116.8	161.9	45.1
F03	$\text{CO}_2 + \text{H} \longrightarrow \text{CHOO}$	46.9	87.1	40.2
F04	$\text{CHOO} \longrightarrow \text{CHO} + \text{O}$	28.0	95.3	67.2
F05	$\text{COOH} \longrightarrow \text{COH} + \text{O}$	19.1	98.5	79.4
F06	$\text{COOH} \longrightarrow \text{CO} + \text{OH}$	-139.8	43.5	183.2
F07	$\text{CO} + \text{H} \longrightarrow \text{CHO}$	134.7	137.4	2.7
F08	$\text{CHO} + \text{H} \longrightarrow \text{CH}_2\text{O}$	31.8	52.6	20.8
F09	$\text{CH}_2\text{O} + \text{H} \longrightarrow \text{CH}_3\text{O}$	8.1	88.5	80.4
F10	$\text{CO} + \text{H} \longrightarrow \text{COH}$	166.9	209.2	42.2
F11	$\text{CHO} + \text{H} \longrightarrow \text{CHOH}$	112.8	141.9	29.1
F12	$\text{CH}_2\text{O} + \text{H} \longrightarrow \text{CH}_2\text{OH}$	73.9	112.9	39.0
F14	$\text{CO} \longrightarrow \text{C} + \text{O}$	82.3	212.3	130.0
F15	$\text{CHO} \longrightarrow \text{CH} + \text{O}$	-60.3	73.6	133.8
F16	$\text{CH}_2\text{O} \longrightarrow \text{CH}_2 + \text{O}$	-47.7	64.0	111.7
F17	$\text{CH}_3\text{O} \longrightarrow \text{CH}_3 + \text{O}$	-49.2	156.6	205.8
F18	$\text{COH} + \text{H} \longrightarrow \text{CHOH}$	89.6	99.7	10.1
F19	$\text{CHOH} + \text{H} \longrightarrow \text{CH}_2\text{OH}$	50.1	76.5	26.5
F20a	$\text{CH}_2\text{OH} + \text{H} \longrightarrow \text{CH}_3\text{OH}$	26.7	87.5	60.7
F20b	$\text{CH}_2\text{OH} + \text{H} \longrightarrow \text{CH}_3\text{OH}$	27.1	73.5	46.4
F21	$\text{COH} \longrightarrow \text{C} + \text{OH}$	-17.8	95.7	113.5
F22	$\text{CHOH} \longrightarrow \text{CH} + \text{OH}$	-125.7	10.7	136.4
F23	$\text{CH}_2\text{OH} \longrightarrow \text{CH}_2 + \text{OH}$	-118.4	51.2	169.6
F24	$\text{CH}_3\text{OH} \longrightarrow \text{CH}_3 + \text{OH}$	-105.6	119.9	225.5
F25	$\text{C} + \text{H} \longrightarrow \text{CH}$	21.4	82.2	60.8
F26	$\text{CH} + \text{H} \longrightarrow \text{CH}_2$	59.2	85.5	26.2
F27	$\text{CH}_2 + \text{H} \longrightarrow \text{CH}_3$	42.6	88.5	45.9
F28	$\text{CH}_3 + \text{H} \longrightarrow \text{CH}_4$	29.3	75.8	46.5

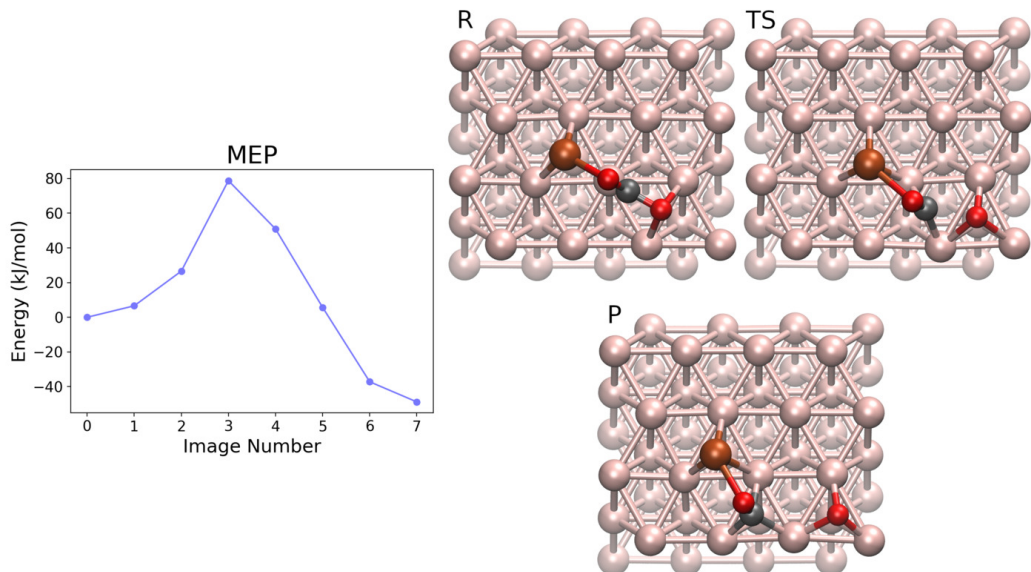


Figure 2.60: MEP and geometries of interest of the F01 elementary step: $\text{CO}_2 \longrightarrow \text{CO} + \text{O}$. Reactant, image 0; TS, image 3; Product, image 7. Colors: C black; O red; Ni rose gold; Fe dark orange.

the reactant here is on a bridge site (as it is in the product). The hydrogen, instead, is on a bridge site between an HCP site and an oxygen. Using only six images for this calculation did not allow to appreciate a reaction intermediate (that is likely to exist) in the first part of the MEP, due to the hydrogen hopping from the initial FCC to an HCP site.

With a ΔE_r of 116.8 kJ/mol, this elementary step is very endothermic, its associated activation energy being 161.9 kJ/mol.

F03: $\text{CO}_2 + \text{H} \longrightarrow \text{CHO}$ To investigate this elementary step, the chosen reactant structure has the CO_2 molecule adsorbed in a vertical position near Fe, making an O–C–O angle of 122.6° . One of the oxygen interacts strongly with a bridged Fe, while the other is on a bridge site of the nickel surface. The atomic hydrogen is on an FCC site not too far from C. In the product structure, the O–C–O angle is similar in amplitude (130.3°), but where in the reactant C was close to the nickel, here is far away from the surface, since now it is coordinate with an extra hydrogen.

The MEP makes a very drastic step going from image one to two (the TS), and then begins a slow descending. As reported in figure 2.62, in the TS structure the hydrogen is near the carbon, but still very close to the surface. The CO_2 geometry is also different from the reactant since C is beginning its

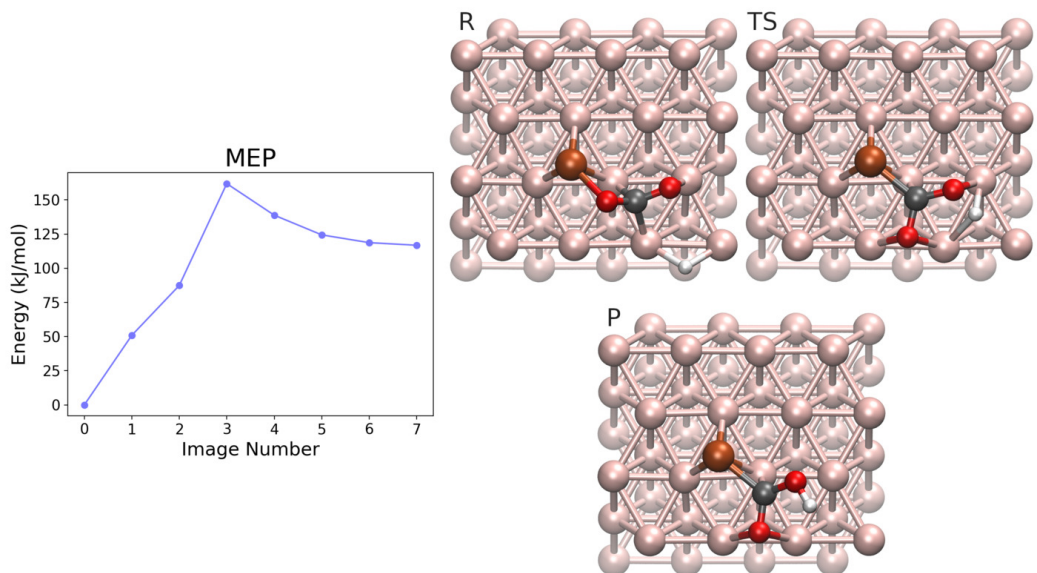


Figure 2.61: MEP and geometries of interest of the F02 elementary step: $\text{CO}_2 + \text{H} \longrightarrow \text{COOH}$. **R**eactant, image 0; **TS**, image 3; **P**roduct, image 7. Colors: H white; C black; O red; Ni rose gold; Fe dark orange.

rotation to move away from the surface.

This elementary step has a moderate ΔE_r of 46.9 kJ/mol, its activation energy being 87.1 kJ/mol.

F04: CHOO \longrightarrow CHO + O To investigate the dissociation of CHOO into CHO and atomic oxygen, the structure of choice for the reactant was exactly the same as the product of F03. The product geometry, on the other hand, has the CHO species interacting with an HCP Fe through the oxygen, and with a top site of the nickel towards the carbon, whereas the atomic oxygen was placed on an FCC site not to far away from the carbon from which it dissociated.

This CI-NEB calculation was also flawless. The MEP, reported in figure 2.63, has a high peak at image three, the second half of the path being smoother than the first. In the TS structure, the geometry of the Fe–CHO complex does not differ from the one it has in the product. The main difference between the two is in the position of the atomic oxygen, that in TS is on the HCP site just next to C, the C–O distance being 1.906 Å (1.267 Å in the reactant).

To this elementary step are associated a ΔE_r of 28.0 kJ/mol, and an activation energy of 95.3 kJ/mol.

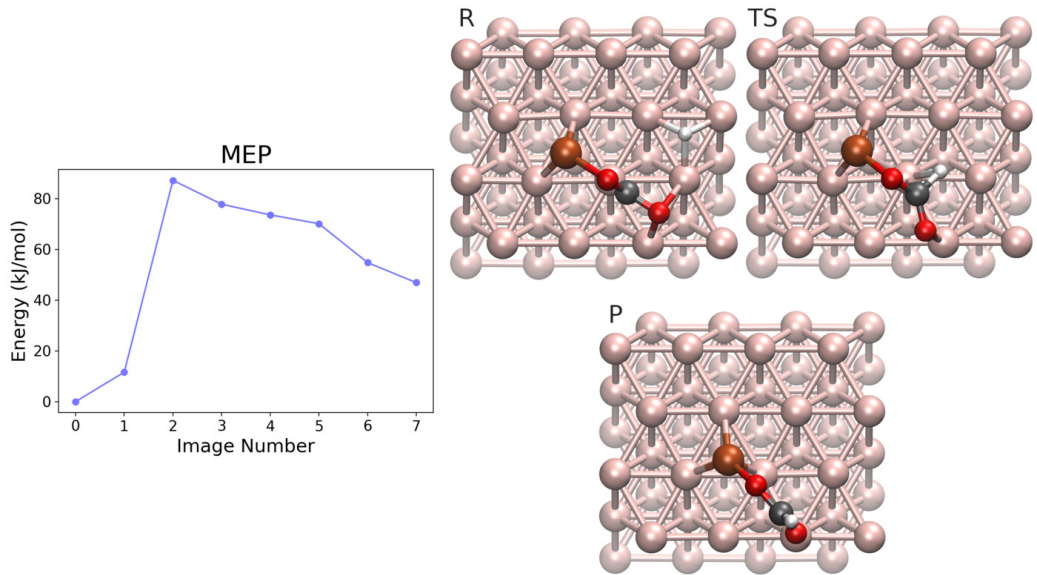


Figure 2.62: MEP and geometries of interest of the F03 elementary step: $\text{CO}_2 + \text{H} \longrightarrow \text{CHO}$. **R**eactant, image 0; **TS**, image 2; **P**roduct, image 7. Colors: H white; C black; O red; Ni rose gold; Fe dark orange.

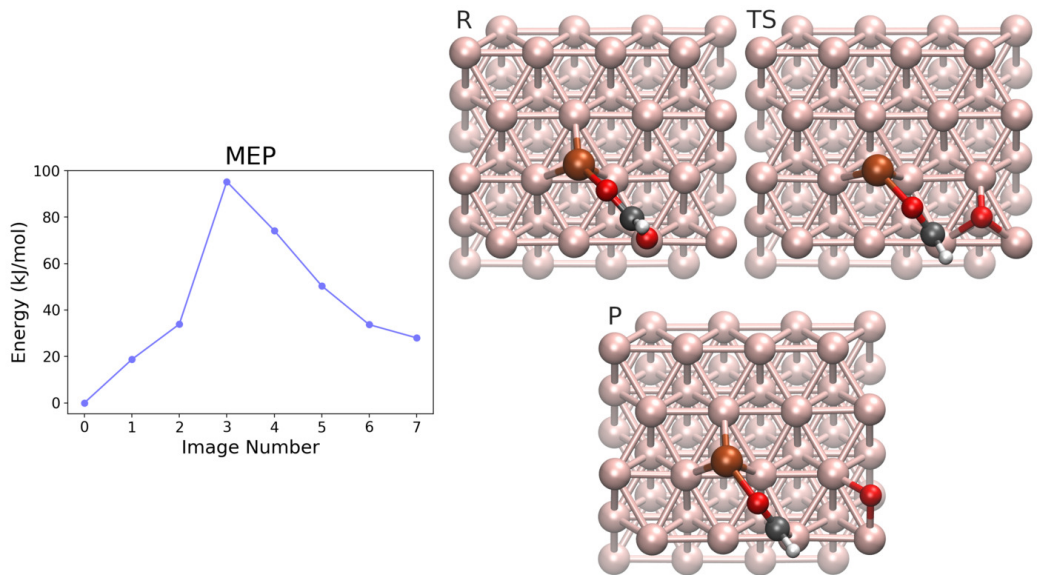


Figure 2.63: MEP and geometries of interest of the F04 elementary step: $\text{CHO} \longrightarrow \text{CHO} + \text{O}$. **R**eactant, image 0; **TS**, image 3; **P**roduct, image 7. Colors: H white; C black; O red; Ni rose gold; Fe dark orange.

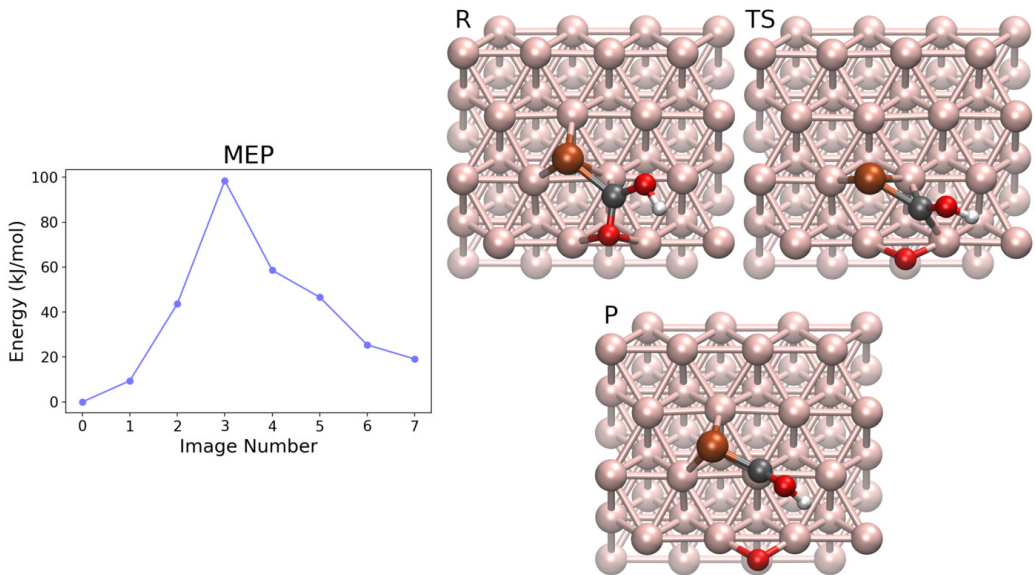


Figure 2.64: MEP and geometries of interest of the F05 elementary step: $\text{COOH} \longrightarrow \text{COH} + \text{O}$. **R**eactant, image 0; **TS**, image 3; **P**roduct, image 7. Colors: H white; C black; O red; Ni rose gold; Fe dark orange.

F05: $\text{COOH} \longrightarrow \text{COH} + \text{O}$ This elementary step was investigated using, as reactant, a structure in which: Fe is on an HCP site, interacting with C; the oxygen of COOH is on a bridge site, while its hydroxyl group is slightly raised with respect to the nickel surface. In the product geometry, instead, Fe is a bit shifted towards the near bridge site, but not completely on top of it; the COH fragment interacts with its carbon with both Fe and a Ni atom (top site). Finally, the atomic oxygen is on an FCC site nearby.

The TS is located at image three, and as can be seen from the MEP (figure 2.64) it has a very high energy compared to both the reactant and product structures. Its geometry shows how the atomic oxygen is already in the FCC site: it is the position of the Fe–COH complex on the surface that differs from both endpoints of the elastic band. The Fe nucleus is on a bridge site, and so it is the carbon of COH: this shift is probably required to push the dissociating oxygen to its final FCC site, thus breaking the C–O bond.

This slightly endothermic reaction has a ΔE_r of 19.1 kJ/mol and an activation energy of 98.5 kJ/mol.

F06: $\text{COOH} \longrightarrow \text{CO} + \text{OH}$ The F06 elementary step is about the dissociation of COOH into CO and OH. The reactant structure chosen to

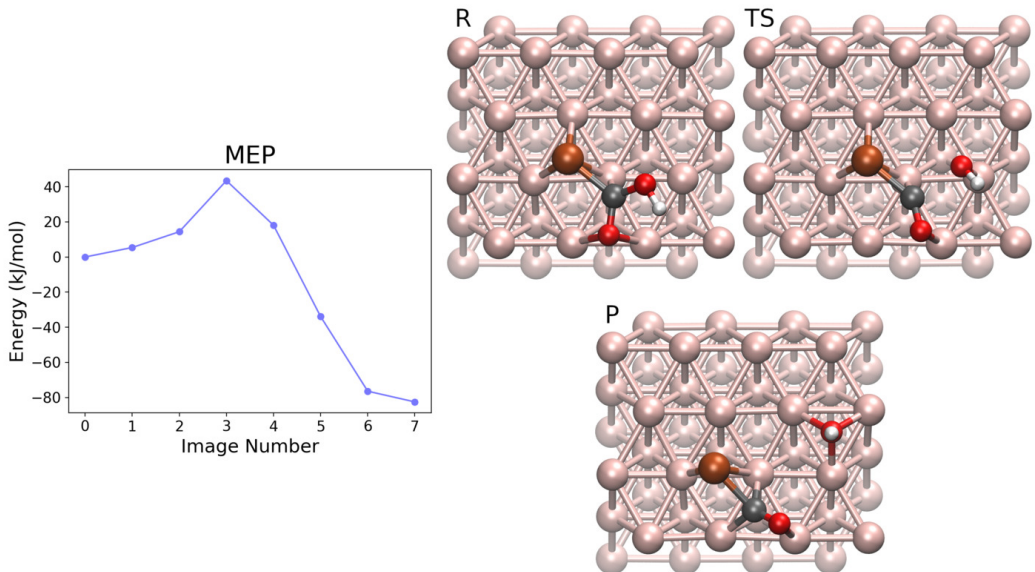


Figure 2.65: MEP and geometries of interest of the F06 elementary step: $\text{COOH} \longrightarrow \text{CO} + \text{OH}$. **R**eactant, image 0; **TS**, image 3; **P**roduct, image 7. Colors: H white; C black; O red; Ni rose gold; Fe dark orange.

determine the TS is the same as that of F05. The product geometry, instead, has the iron atom on a bridge site, bonded to the carbon monoxide through C, whereas the hydroxyl group is on an FCC site not to far away from carbon.

Figure 2.65 reports the MEP and some geometries of interest, one of which being the transition state located at image three. Its structure shows that the hydroxyl group approached the nickel surface, here being almost over a top site. The C–OH distance increased significantly (TS 1.999 Å, reactant 1.385 Å) despite C has not moved noticeably. From this point on, the reaction proceeds with readjustments of both the CO and OH fragments towards more comfortable sites.

Some time after the execution of this CI-NEB, it was found out that the interaction of the CO molecule with Fe through the carbon is not the preferred one, compared with the geometry in which it interacts through the oxygen. Furthermore, performing a CI-NEB between these two conformations shows that the former is not an energy minimum at all, since it is the highest point of the MEP of $\text{CO}_{\text{O@Fe}} \longrightarrow \text{CO}_{\text{C@Fe}}$, that has a ΔE_r of 57.3 kJ/mol. This means that the product used in F06 is not a minimum, and that its energy should be adjusted before computing ΔE_r and activation energy, that then turn out to be -139.8 and 43.5 kJ/mol, respectively.

F07: CO + H → CHO This elementary step is about the hydrogenation of carbon monoxide to give the CHO species. The structure used as reactant has a CO molecule on a HCP site, anchored to the nickel surface through the carbon, while the oxygen is interacting with a nearby HCP Fe. The atomic hydrogen is located on an HCP site adjacent to that of C. In the product structure the Fe–O interaction is maintained, the oxygen, however, is here closer to the surface, so a Ni–O interaction is also present. Finally, the hydrogen is bonded to carbon, which in turn shifted towards a bridge site due to the augmented coordination.

It is difficult to locate at a first glance the TS by looking at the MEP of figure 2.66, since the curve flattens out in its second half. This shows how labile the product structure is, being extremely close in energy to the transition state located at image five. A closer look at its geometry reveals that it is indeed very similar to the product, the only difference being a slight rotation of the whole CHO fragment with respect to the underlying nickel surface.

Both the ΔE_r of 134.7 kJ/mol and the activation energy of 137.4 kJ/mol imply that the backward elementary step, the CHO dissociation, is extremely favored both thermodynamically and kinetically (having a negligible activation energy of 2.7 kJ/mol).

As a final note, the one presented here was not the only CI-NEB attempt for this elementary step. Another one was carried out, but unfortunately it did not converge. During that calculation a reaction intermediate was found, optimized, and the result used as the product structure reported in this paragraph.

F08: CHO + H → CH₂O The F08 step is about the hydrogenation of CHO that gives CH₂O. The reactant and product geometries were specifically chosen to investigate a Fe-pivoted hydrogenation mechanism. For this reason, in the reactant, CHO interacts with an HCP Fe through C while O is on a bridge site, whereas the atomic hydrogen is on a top site, very close to the iron atom. In the product structure, instead, both Fe and O maintain their original position while bonding a CH₂ group that is raised from the nickel surface.

The not smooth MEP, reported in figure 2.67, shows two maxima at images two and five (the latter being the highest TS), and two minima at images three and six. The intermediate at image three (not reported in the figure) has the atomic hydrogen on top of Fe. The TS structure shows the atomic H approaching CH from above. Finally, the intermediate at image six has a very similar structure to the product, but here Fe is shifted towards

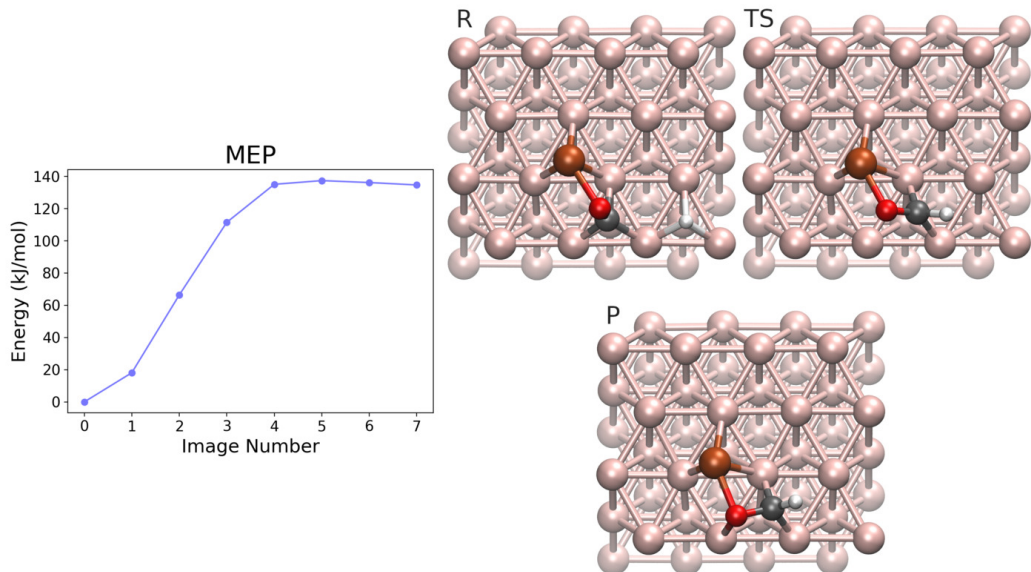


Figure 2.66: MEP and geometries of interest of the F07 elementary step: $\text{CO} + \text{H} \longrightarrow \text{CHO}$. Reactant, image 0; **TS**, image 5; Product, image 7. Colors: H white; C black; O red; Ni rose gold; Fe dark orange.

a bridge site, making the CH_2 group closer to the nickel surface (distances between C and its closest Ni being 1.985 Å and 2.670 Å on image six and seven, respectively) thus producing a stabilizing interaction.

The ΔE_r of 31.8 kJ/mol for this elementary step was computed using the absolute energy of the intermediate at image six instead of that of the product, due to its higher stability. The found activation energy is 52.6 kJ/mol.

F09: $\text{CH}_2\text{O} + \text{H} \longrightarrow \text{CH}_3\text{O}$ The reactant structure used to investigate this elementary step has the CH_2O 's oxygen on an FCC site, while the CH_2 group is far from the surface, bonded to a bridged Fe. The atomic hydrogen is on a top site near Fe, with which it interacts. The product geometry has the isolated Fe atom on an FCC site, whereas the CH_3O species is adsorbed on an HCP site through the oxygen.

The CI-NEB calculation was performed using five images, optimized up to $3.2 \cdot 10^{-3} E_h/\text{\AA}$ on all force norms with the FIRE algorithm. The MEP, reported in figure 2.68, is not smooth, with a big leap between images three (the transition state) and four. The TS geometry is very similar to that of the reactant, the main difference being that the atomic hydrogen is here over Fe, very close to the CH_2 group.

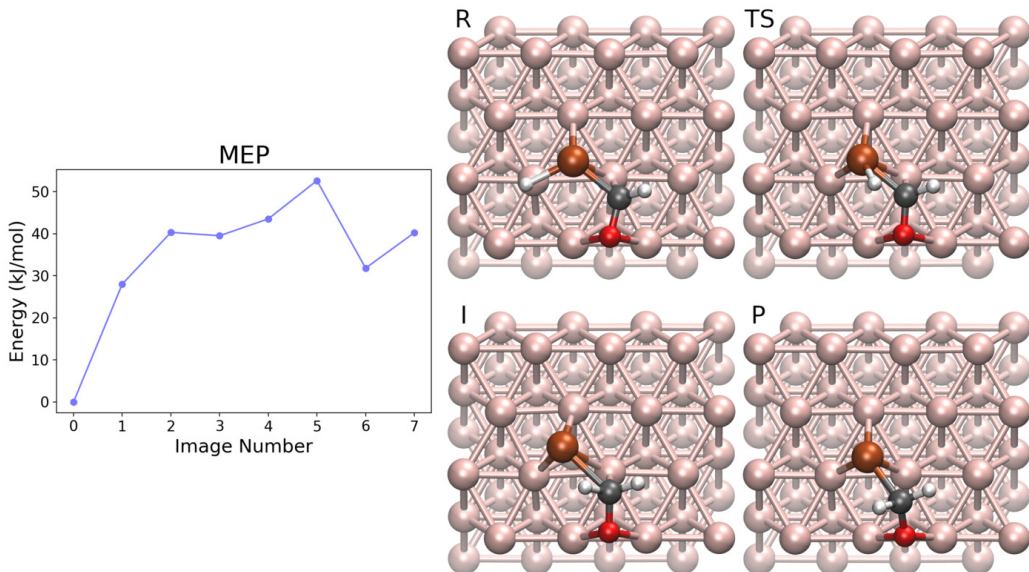


Figure 2.67: MEP and geometries of interest of the F08 elementary step: $\text{CHO} + \text{H} \longrightarrow \text{CH}_2\text{O}$. Reactant, image 0; TS, image 5; Intermediate, image 6; Product, image 7. Colors: H white; C black; O red; Ni rose gold; Fe dark orange.

The ΔE_r and activation energy are 8.1 and 88.5 kJ/mol, respectively. As a final note, another CI-NEB was tried using the same reactant structure here discussed, but with a different product in which Fe was on an HCP site, and the CH_3O species on FCC site. That calculation, however, suffered from severe convergence problems: it was possible to optimize the elastic band only up to $4.3 \cdot 10^{-2} E_h/\text{\AA}$ before all images started to diverge. The MEP of the last iteration shows that the atomic hydrogen leaves its position near Fe for the nickel surface, from which it will subsequently reach the CH_2 group. This shows how a change in the product structure allows to find other reaction paths, in which the hydrogenation does not exploit the Fe atom as a pivot but occurs through the nickel surface. Because the convergence threshold was too loose, the activation energy is not meaningful and hence it is not reported. Nevertheless, even a failed calculation can give some qualitative insights.

F10: $\text{CO} + \text{H} \longrightarrow \text{COH}$ To locate the TS of the hydrogenation of CO on its oxygen, the reactant structure of choice has the carbon monoxide on an HCP site adsorbed through C. The presence of Fe on an HCP site nearby attracts the oxygen, thus the CO molecule is not perfectly perpendicular to

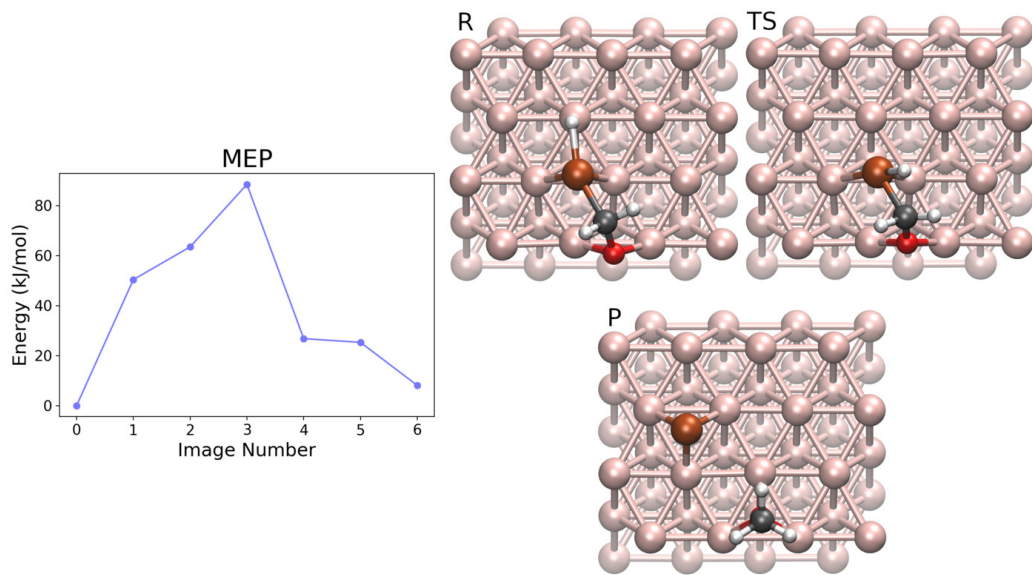


Figure 2.68: MEP and geometries of interest of the F09 elementary step: $\text{CH}_2\text{O} + \text{H} \longrightarrow \text{CH}_3\text{O}$. **R**eactant, image 0; **TS**, image 3; **P**roduct, image 6. Colors: H white; C black; O red; Ni rose gold; Fe dark orange.

the surface. The atomic hydrogen is on an FCC site near CO. The product structure, instead, has the COH fragment on the same HCP site as the starting CO, but here Fe is on a bridge site, mostly interacting with C rather than with O.

The smooth MEP reported in figure 2.69 shows that TS is located at image five. Examining its geometry one can see that O moved away from Fe (that is now on a bridge site), while the atomic hydrogen left the FCC site for a top one, approaching the oxygen.

Due to the high stability of the carbon monoxide species in the reactant, the reaction is strongly endothermic with a ΔE_r of 166.9 kJ/mol, which leads to a very high activation energy of 209.2 kJ/mol. Another reason for the instability of the product geometry compared to that of the reactant is that Fe interacts mostly with C, while this is not the case in the reactant, where Fe is closer to O than to C. This is one of many cases in which the marked preference of Fe towards O occurs, whereas in Ru-decorated systems similar Ru–O interactions were not observed.

F11: $\text{CHO} + \text{H} \longrightarrow \text{CHOH}$ The F11 step is about the hydrogenation of CHO to give the CHOH alcoholic species. The structure used as reactant

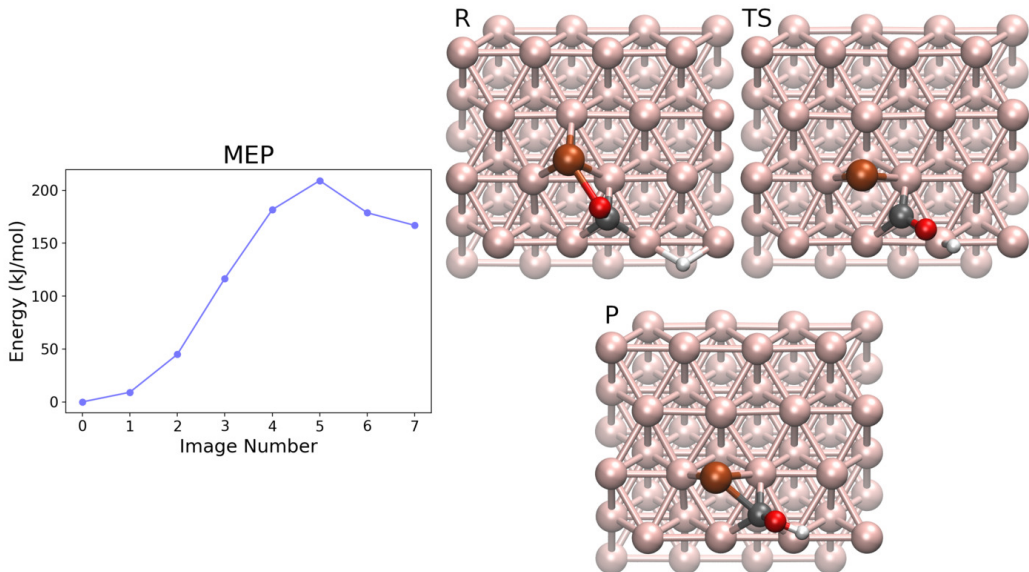


Figure 2.69: MEP and geometries of interest of the F10 elementary step: $\text{CO} + \text{H} \longrightarrow \text{COH}$. Reactant, image 0; **TS**, image 5; Product, image 7. Colors: H white; C black; O red; Ni rose gold; Fe dark orange.

has Fe on an HCP site, interacting with the carbon of CHO, which in turn is on a top site. The oxygen of CHO is on a bridge site, and the atomic H is on a FCC site close to it. In the product geometry the positions of Fe and the CH group do not differ much from the starting ones in the reactant. What changes, instead, is the higher coordination of the oxygen due to the new O–H bond, because of which O leaves its previous bridge site for a top one.

A six images elastic band was optimized using the FIRE algorithm. Due to some convergence difficulties, a looser threshold of $5.1 \cdot 10^{-3} E_h/\text{\AA}$ was used for this calculation. Looking at the MEP of figure 2.70, it is clear that those convergence difficulties were due to an uneven path, in which the most interesting points are an intermediate at image two and the transition state at image five. The structure of the intermediate shows a rotated CHO species in which O is closer to Fe (again, note that this kind of interaction produces a structure that is very stable, more than the reactant itself), where at the same time H hopped from an FCC to an HCP site. On the other hand, the TS structure shows a CHO fragment that is pretty much in the same orientation as in the product, while the atomic hydrogen is on the FCC site just below the oxygen.

Like the previous one, this elementary step is also highly endothermic with a ΔE_r of 112.8 kJ/mol and an associated activation energy of 141.9 kJ/mol.

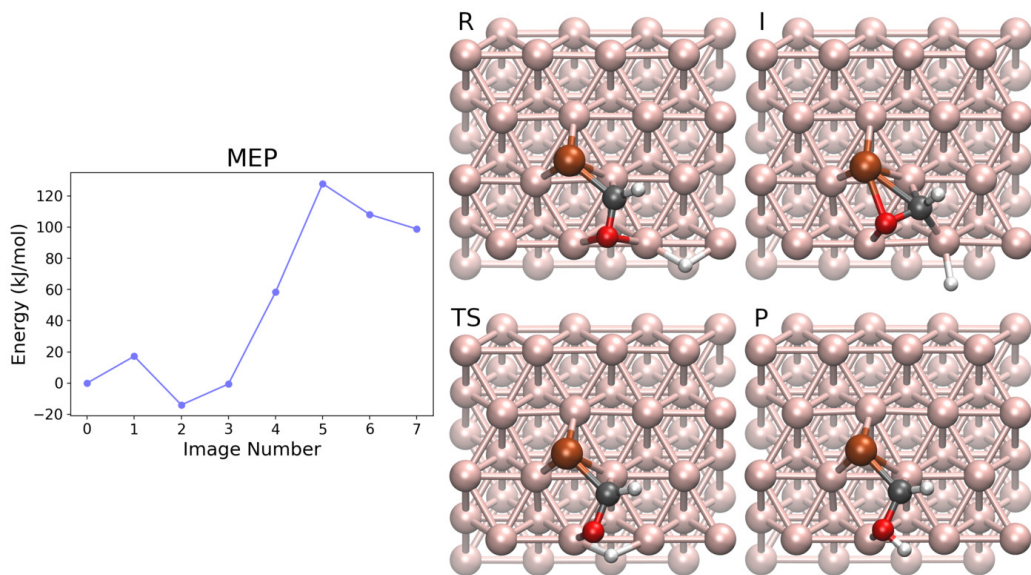


Figure 2.70: MEP and geometries of interest of the F11 elementary step: $\text{CHO} + \text{H} \longrightarrow \text{CHOH}$. **R**eactant, image 0; **I**ntermediate, image 2; **TS**, image 5; **P**roduct, image 7. Colors: H white; C black; O red; Ni rose gold; Fe dark orange.

Both energies were calculated using the absolute energy of the intermediate at image two instead of that of the reactant.

F12: $\text{CH}_2\text{O} + \text{H} \longrightarrow \text{CH}_2\text{OH}$ In this paragraph the hydrogenation of the CH_2O species that gives the CH_2OH alcohol is analyzed. The chosen reactant structure has a Fe atom on an HCP site, the CH_2O fragment is bonded to Fe via C and to a bridge site of the nickel surface through O, and there is an atomic hydrogen on an HCP site near the oxygen. The product geometry is very similar, the only difference being that now the hydrogen is bonded to O, giving an hydroxyl group. Strangely enough, in this optimized structure the oxygen maintains its bridge position, despite its higher coordination with respect to the reactant.

Figure 2.71 shows a MEP peaked around image four, that also presents two reaction intermediates, one just after the reactant at image one, the other one just before the product at image six. Intermediate at image one (not reported in figure) corresponds to the hopping of atomic H from its original HCP site to the FCC site below. TS shows, instead, that the atomic hydrogen is now on another FCC site, the one under the oxygen of CH_2O , which in turn shifted from a bridge to a top site. Here Fe moved a bit

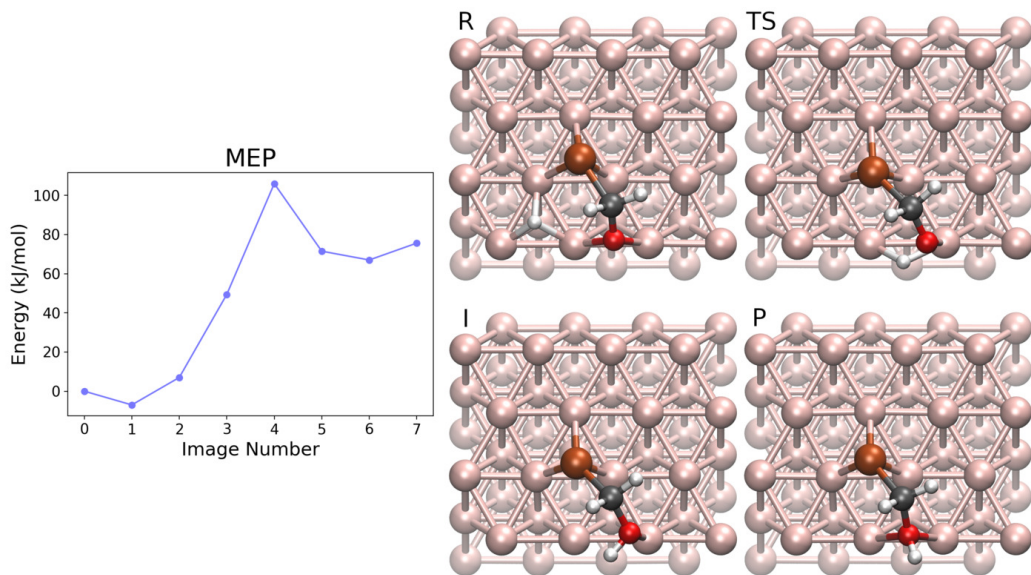


Figure 2.71: MEP and geometries of interest of the F12 elementary step: $\text{CH}_2\text{O} + \text{H} \longrightarrow \text{CH}_2\text{OH}$. Reactant, image 0; TS, image 4; Intermediate, image 6; Product, image 7. Colors: H white; C black; O red; Ni rose gold; Fe dark orange.

towards a bridge position, following the small shift of the CH_2O species. In the intermediate at image six, finally, there is the formation of the CH_2OH species, where the hydroxyl group interact with a top site of the surface.

For this elementary step, both the ΔE_r and activation energy, whose values are 73.9 and 112.9 kJ/mol respectively, were computed using the absolute energies of the intermediates at image one and six instead of, respectively, those of reactant and product.

F14: $\text{CO} \longrightarrow \text{C} + \text{O}$ This paragraph is about the carbon monoxide dissociation. In the structure used as reactant, the carbon of CO is on an HCP site, interacting with a bridged Fe. The oxygen points upward and is far from Fe. In the product structure, the atomic oxygen is on an HCP site next to that of the atomic carbon, which keeps its interaction with Fe.

The minimum energy path, reported in figure 2.72, is peaked around image four. Its geometry shows that the oxygen is closer to the surface than in the reactant, and it occupies a bridge site. The carbon is more centered on the HCP site, and in its displacement it pulled the iron atom, which is here more centered on the bridge site.

For the same reason explained in the paragraph on the F06 step, it was

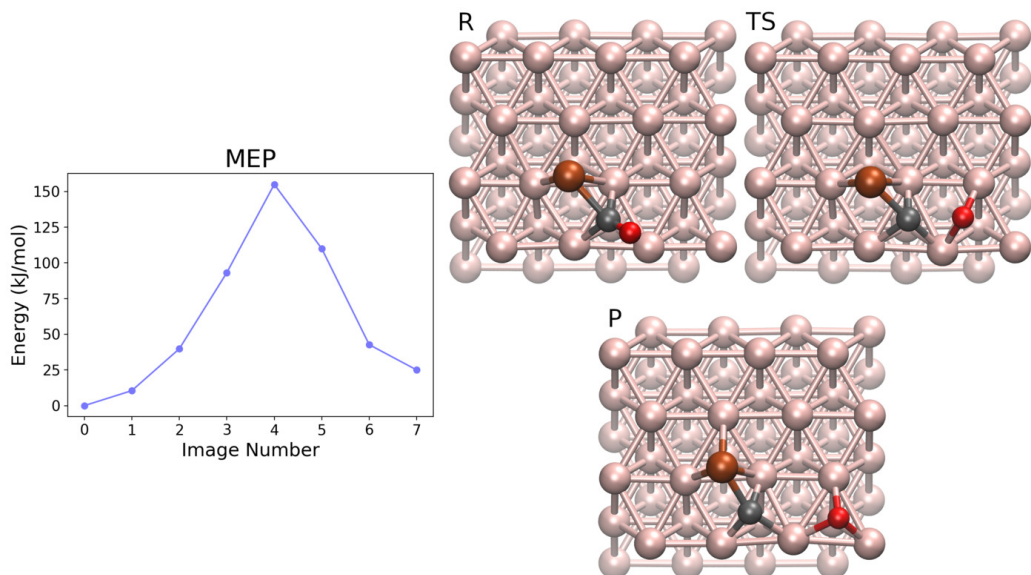


Figure 2.72: MEP and geometries of interest of the F14 elementary step: $\text{CO} \longrightarrow \text{C} + \text{O}$. **R**eactant, image 0; **TS**, image 4; **P**roduct, image 7. Colors: C black; O red; Ni rose gold; Fe dark orange.

later found out that the reactant of F14 is a transition state. Considering its closest minimum (CO that interacts with Fe through the oxygen), the corrected ΔE_r and activation energy for this elementary step are 82.3 and 212.3 kJ/mol, respectively.

F15: $\text{CHO} \longrightarrow \text{CH} + \text{O}$ To investigate this elementary step, two structures were prepared. In the reactant, Fe is on HCP site, while CHO interacts with the catalyst in different ways: C, near a top site, is close to Fe, whereas O is on a bridge site. The product structure, instead, has Fe on a bridge site, interacting with the carbon of CH which is on an HCP site. Finally, the atomic oxygen is on another HCP site, near CH.

Figure 2.73 shows the MEP for this elementary step: it has a peak at image three, the transition state. Despite the absolute energy of TS being closer to that of the reactant, its structure is similar to that of the product because they have in common the positions of both Fe and CH. The difference between the two is the position of the oxygen, that in TS is approaching the near FCC site but is still close enough to C. The MEP also shows a rapid decrease going from image six to seven: it is very likely that the lack of resolution of the elastic band did not catch a transition state in this region due to the oxygen hopping from an FCC (as in image three) to the near HCP

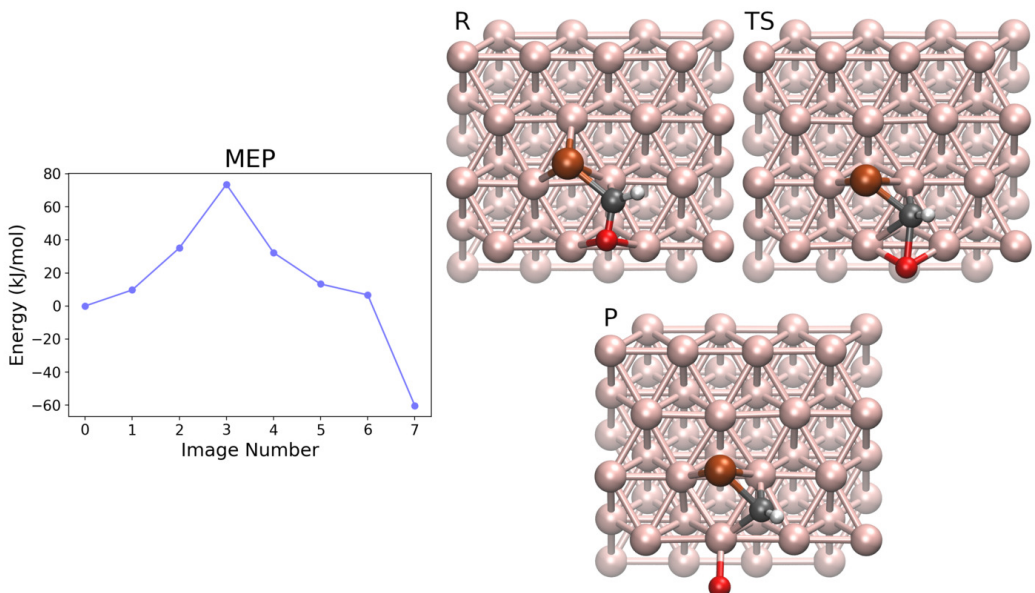


Figure 2.73: MEP and geometries of interest of the F15 elementary step: $\text{CHO} \longrightarrow \text{CH} + \text{O}$. Reactant, image 0; TS, image 3; Product, image 7. Colors: H white; C black; O red; Ni rose gold; Fe dark orange.

site (as in product).

This is an exothermic reaction with an associated ΔE_r of -60.3 kJ/mol, its activation energy being 73.6 kJ/mol.

F16: $\text{CH}_2\text{O} \longrightarrow \text{CH}_2 + \text{O}$ To study the oxygen dissociation from the CH_2O species, the used structures were: as reactant, a CH_2O anchored to the nickel surface through a bridged oxygen, while the CH_2 group (far from the surface) bonds an HCP Fe; as product, Fe is now on a bridge site, interacting with a CH_2 that has its carbon on an FCC site, meanwhile the atomic oxygen found its place on an HCP site nearby.

The search for this TS was not flawless. For this reason an higher resolution elastic band with eight images was employed, and its optimization was performed using FIRE up to the looser threshold of $3.5 \cdot 10^{-3} E_h/\text{\AA}$. The MEP, reported in figure 2.74, shows a reaction intermediate (whose energy is lower than that of the reactant) at image two, and a transition state at image four. In the intermediate Fe is already on a bridge site. Its displacement pulled the CH_2 group, that is now closer to the nickel surface. An examination to the geometry of image four reveals that in TS the CH_2 group interacts more with Fe than with O, as can be deduced from the orientation of the

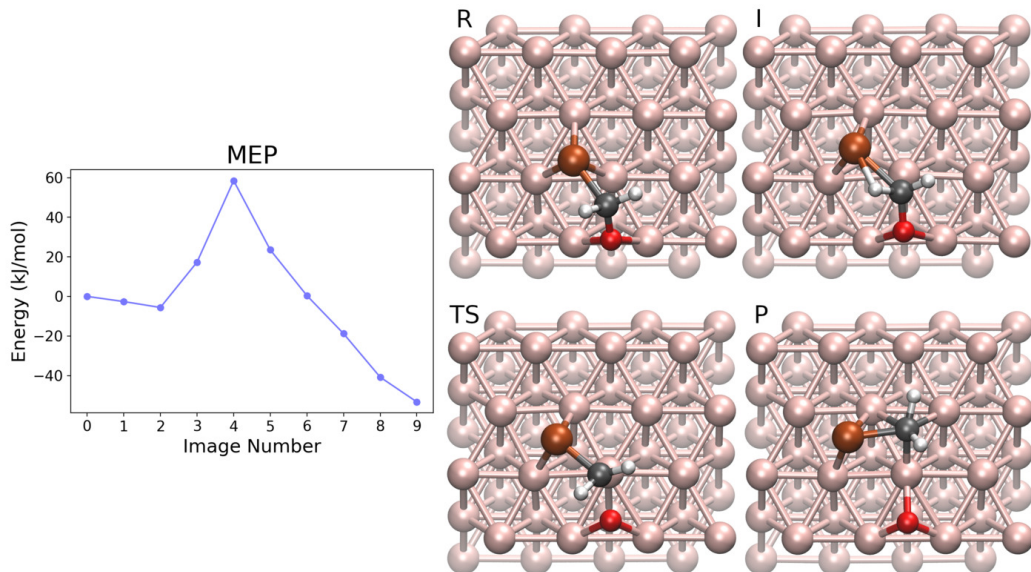


Figure 2.74: MEP and geometries of interest of the F16 elementary step:
 $\text{CH}_2\text{O} \longrightarrow \text{CH}_2 + \text{O}$. **R**eactant, image 0; **I**ntermediate, image 2; **TS**, image 4; **P**roduct, image 9. Colors: H white; C black; O red; Ni rose gold; Fe dark orange.

two hydrogens that point towards the oxygen.

To compute both ΔE_r and activation energy, the absolute energy of the reaction intermediate was used instead of that of the reactant. Their values are, respectively, -47.7 and 64.0 kJ/mol.

F17: $\text{CH}_3\text{O} \longrightarrow \text{CH}_3 + \text{O}$ The F17 elementary step is about the oxygen dissociation of the CH_3O species. To locate the transition state, a structure was used as reactant in which Fe is on an HCP site, whereas CH_3O is on an FCC site through its oxygen, the methyl group pointing up to the void. In the product geometry, instead, the methyl group is bonded to the HCP Fe, while the atomic oxygen remains on its FCC site.

Figure 2.75 shows an unusual MEP since there is not a single well defined peak: the two highest images, very close in energy, give to the MEP its flat top shape. The transition state is located at image three, and a closer look at its geometry shows an isolated methyl group that is “flying” towards Fe. Since it is difficult to see from the top view image, the following C–O distances of 1.430 Å and 2.621 Å, respectively in the reactant and TS structures, should give an insight on the magnitude of what is happening.

Despite the reaction being exothermic, with a ΔE_r of -49.2 kJ/mol, it

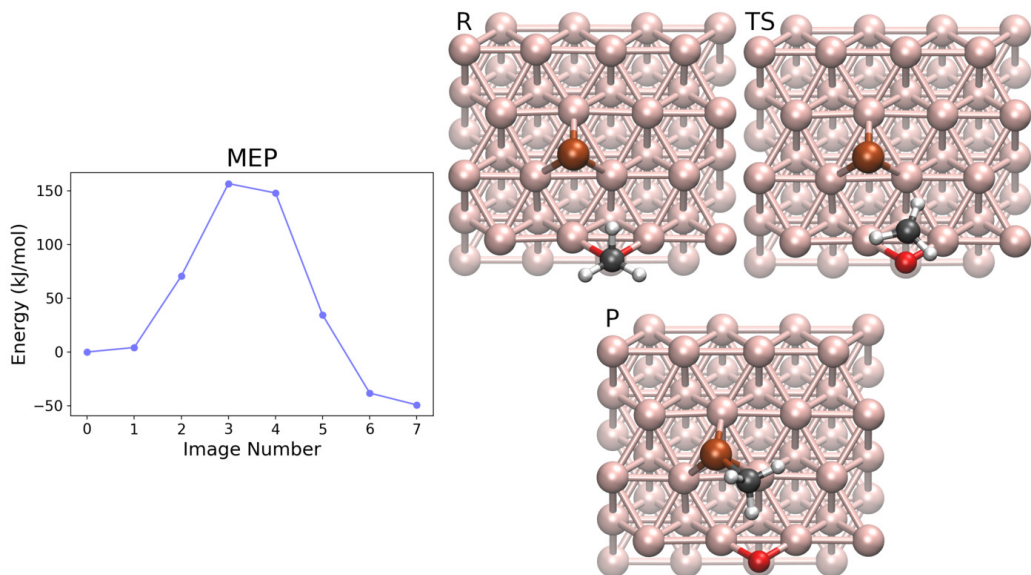


Figure 2.75: MEP and geometries of interest of the F17 elementary step: $\text{CH}_3\text{O} \longrightarrow \text{CH}_3 + \text{O}$. Reactant, image 0; TS, image 3; Product, image 7. Colors: H white; C black; O red; Ni rose gold; Fe dark orange.

requires a remarkable activation energy of 156.6 kJ/mol, due to the high instability of the isolated CH_3 fragment in the transition state.

F18: $\text{COH} + \text{H} \longrightarrow \text{CHOH}$ To investigate the hydrogenation of COH that gives the CHO_H species, the chosen reactant structure has the iron atom on a bridge site that interacts with an FCC carbon belonging to COH, the hydroxyl group of which points upward, far away from the surface. The atomic hydrogen is on an FCC site next to that of C. In the product geometry, Fe maintains its bridge position, C acquires the previously atomic hydrogen, and the newly formed CH moved towards a top site while maintaining its interaction with Fe. The hydroxyl group, finally, is now closer to the surface, with O over a top site.

The MEP, reported in figure 2.76, is one of the strangest found so far. This is because all the images except the reactant have a very similar absolute energy. The transition state is located at image three, while all the subsequent images oscillate back and forth between the TS and product geometries. This is a clear sign that the chosen elastic band was too long, and using less than six images would have worked just as well to locate the transition state. TS structure differs slightly from the product one, the main

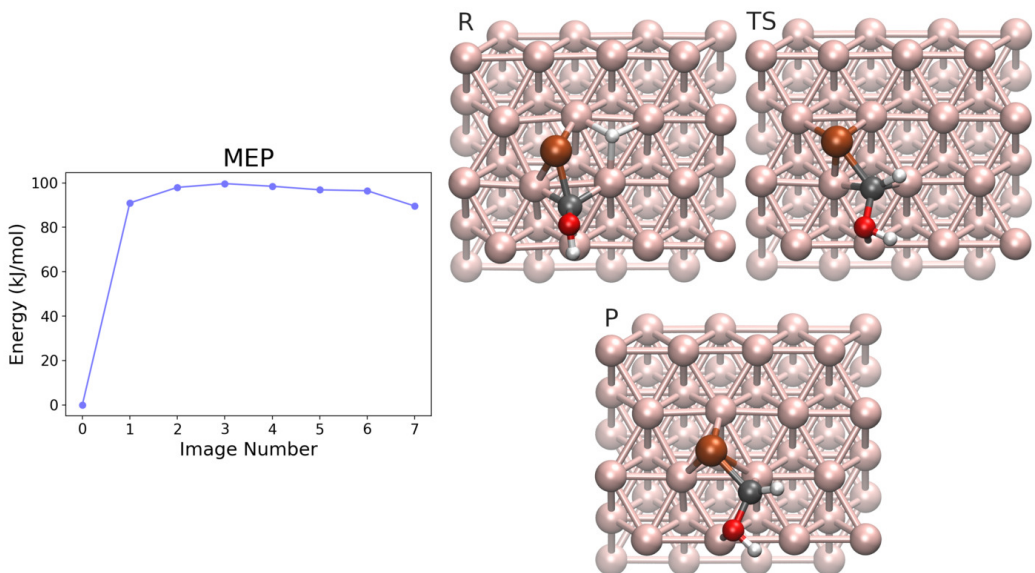


Figure 2.76: MEP and geometries of interest of the F18 elementary step: $\text{COH} + \text{H} \longrightarrow \text{CHOH}$. **R**eactant, image 0; **TS**, image 3; **P**roduct, image 7. Colors: H white; C black; O red; Ni rose gold; Fe dark orange.

differences being the Fe atom on an FCC site (instead of a bridge one), and C on a bridge site (instead of an almost top one).

With a ΔE_r of 89.6 kJ/mol, this elementary step is highly endothermic, the found activation energy being 99.7 kJ/mol. The negligible backward activation energy of 10.1 kJ/mol, along with the thermodynamic instability of the product structure, they both make this elementary step very unlikely to occur.

F19: $\text{CHOH} + \text{H} \longrightarrow \text{CH}_2\text{OH}$ This elementary step is about the hydrogenation of CHOH that gives the CH_2OH species. The chosen geometry for the reactant has an HCP Fe that interact with the carbon of CHOH , in which both CH and OH groups are over two different top sites of the nickel surface. The atomic hydrogen is on an HCP site next to that of Fe. Concerning the product structure, here the CH_2 group of CH_2OH is far from the surface, between an HCP Fe and a bridged oxygen.

The CI-NEB calculation converged with the usual parameters but the MEP, reported in 2.77, is quite jagged: there is a high jump in energy going from image one to two (due to the H hopping from the surface to Fe, not shown in figure), and there is also a reaction intermediate at image six,

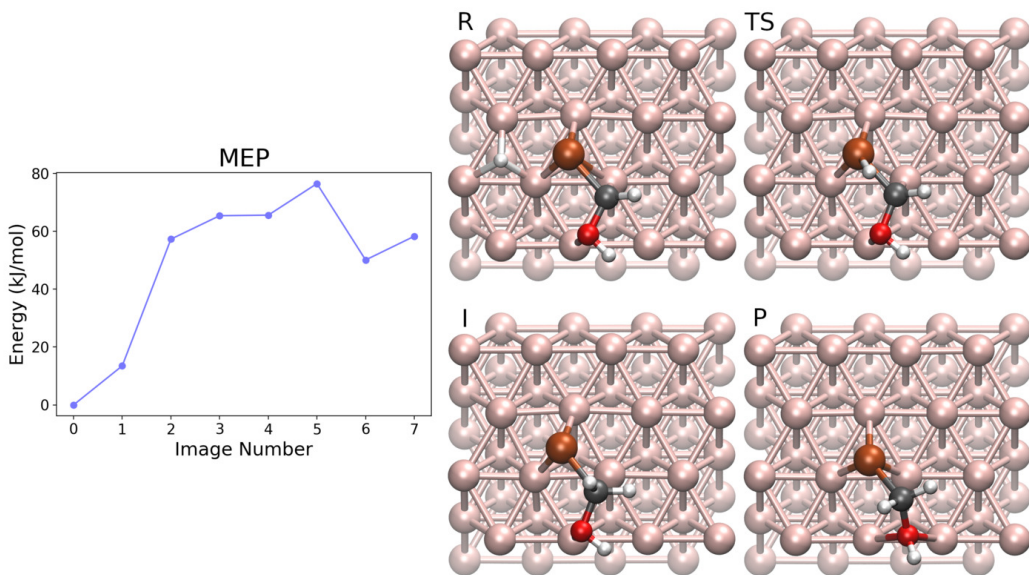


Figure 2.77: MEP and geometries of interest of the F19 elementary step: $\text{CHOH} + \text{H} \longrightarrow \text{CH}_2\text{OH}$. Reactant, image 0; TS, image 5; Intermediate, image 6; Product, image 7. Colors: H white; C black; O red; Ni rose gold; Fe dark orange.

just before the product. The transition state is located at image five, whose structure shows that the atomic hydrogen is over Fe, approaching the carbon from above. The intermediate structure, instead, is another conformation of the CH_2OH species over the surface. Here almost all positions are different from those on the product: Fe is on a bridge site, CH_2 is closer to the nickel surface, and the hydroxyl group is on a top site.

Being the reaction intermediate at image six more stable than the product, its energy was used to compute the ΔE_r of 50.1 kJ/mol. The activation energy for this elementary step is 76.5 kJ/mol.

F20a: $\text{CH}_2\text{OH} + \text{H} \longrightarrow \text{CH}_3\text{OH}$ The reactant chosen to study this further hydrogenation process has Fe on an HCP site, which interacts with the hydroxyl group of CH_2OH , the atomic hydrogen being on an FCC site not too far from CH_2 whose carbon is on a top site. In the product geometry things are not so different regarding Fe and the hydroxyl group, but here the carbon has an additional hydrogen and then moved away from the surface. The distance between C and the nickel immediately below it is 1.922 Å in the reactant and 3.463 Å in the product geometry. As a final note, the structure described here for the product was chosen because of the difficulties that

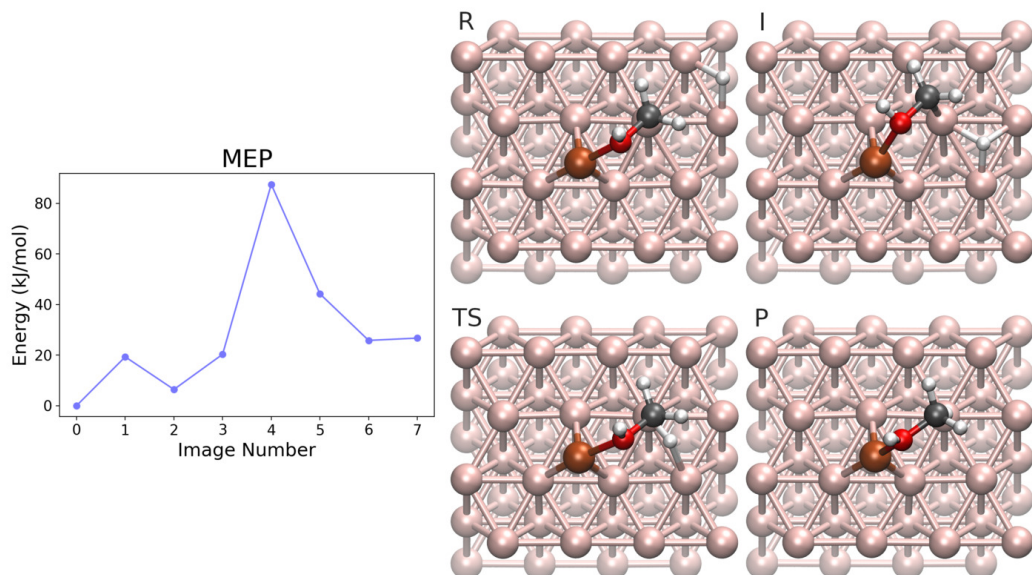


Figure 2.78: MEP and geometries of interest of the F20a elementary step: $\text{CH}_2\text{OH} + \text{H} \longrightarrow \text{CH}_3\text{OH}$. **R**eactant, image 0; **I**ntermediate, image 2; **TS**, image 4; **P**roduct, image 7. Colors: H white; C black; O red; Ni rose gold; Fe dark orange.

arose during the optimization of the CH_3OH species anchored to the nickel surface by means of the hydroxyl group: the alternative was to stick it to Fe.

The CI-NEB calculation required a looser threshold of $3.5 \cdot 10^{-3} E_h/\text{\AA}$ in order to converge a six images elastic band. By looking at the MEP in figure 2.78, it is clear that this was not an easy calculation since the curve resembles a roller coaster. There is an intermediate at image two, whose structure shows that the atomic hydrogen hopped to another FCC site, in order to better approach the CH_2 group. Then, at image four, there is the transition state: here the atomic hydrogen is on a bridge site, midway between the nickel surface and CH_2 . Finally, image six has an energy almost imperceptibly lower than the one of the product: this is an alternative conformation of CH_3OH with a slightly rotated methyl group.

The ΔE_r for this step is 26.7 kJ/mol, while its activation energy is 87.5 kJ/mol.

F20b: $\text{CH}_2\text{OH} + \text{H} \longrightarrow \text{CH}_3\text{OH}$ Another CI-NEB was performed on the same $\text{CH}_2\text{OH} + \text{H} \longrightarrow \text{CH}_3\text{OH}$ elementary step using different starting structures. In F20b, the reactant geometry has the atomic hydrogen close to Fe, while the CH_2OH species is on the nickel surface with both C and O

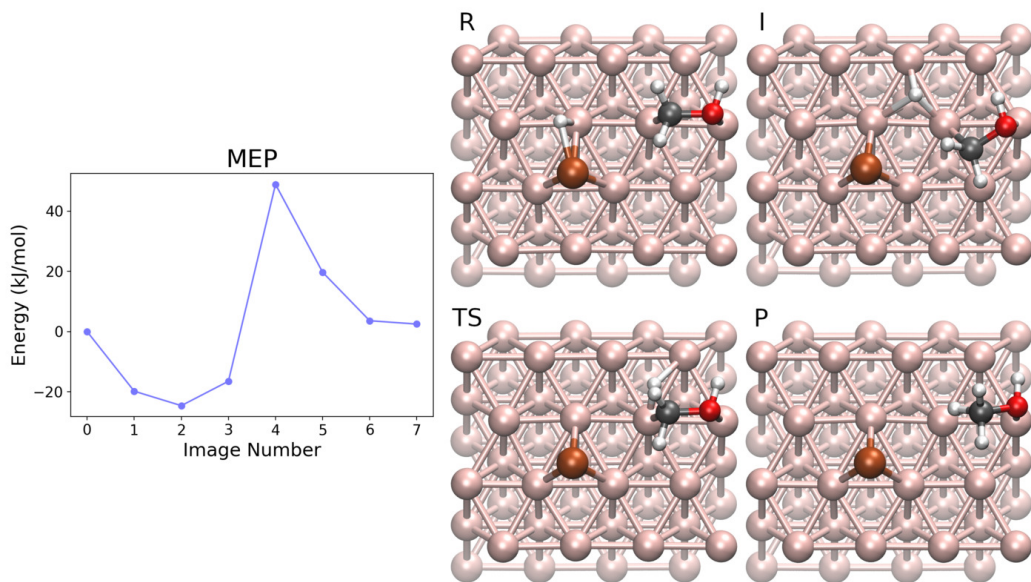


Figure 2.79: MEP and geometries of interest of the F20b elementary step: $\text{CH}_2\text{OH} + \text{H} \longrightarrow \text{CH}_3\text{OH}$. **R**eactant, image 0; **I**ntermediate, image 2; **TS**, image 4; **P**roduct, image 7. Colors: H white; C black; O red; Ni rose gold; Fe dark orange.

over two different top sites. In the product structure, instead, the CH_3OH interacts with the nickel surface only by means of the hydroxyl group whose O is on a top site, while the methyl group points far away from the surface. Here CH_3OH is far enough from Fe to allow the geometry optimization calculation to converge.

The MEP in figure 2.79 shows a reaction intermediate after the reactant at image two, and a peak at image four, the transition state. In the intermediate the atomic hydrogen moved from Fe to an HCP site of nickel (111), while the carbon of CH_2OH shifted from a top to a bridge site in order to accommodate the nearby hydrogen. In the TS, the atomic H hopped to the next FCC site and C came back on its original top site, the final results being that the two are now extremely close.

When studied using this reaction route, this elementary step has a ΔE_r of 27.1 kJ/mol and an activation energy of 73.5 kJ/mol. The former is virtually identical to that of F20a, while the latter is 14.0 kJ/mol smaller, suggesting that this kind of hydrogenation is easier when the CH_2OH species is far from Fe.

F21: $\text{COH} \longrightarrow \text{C} + \text{OH}$ This elementary step is about the dissociation

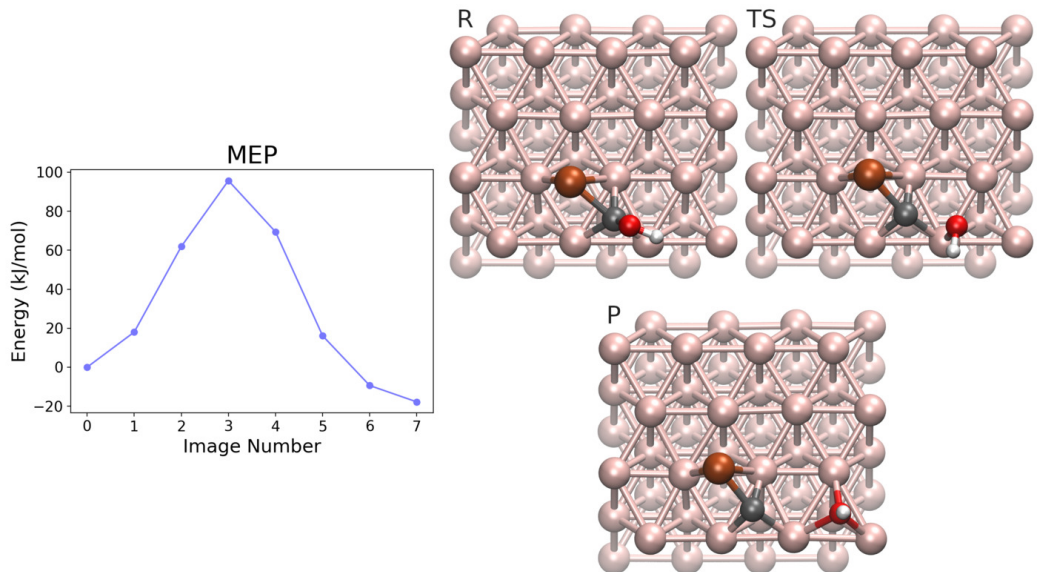


Figure 2.80: MEP and geometries of interest of the F21 elementary step: $\text{COH} \longrightarrow \text{C} + \text{OH}$. **R**eactant, image 0; **TS**, image 3; **P**roduct, image 7. Colors: H white; C black; O red; Ni rose gold; Fe dark orange.

of the COH species into atomic carbon and an hydroxyl group. The reactant structure prepared for the purpose has the iron atom on a bridge site, which interacts with the HCP carbon of COH, whose hydroxyl group in turn points upward far away from the surface. Finally, in the product geometry both Fe and the now atomic C are on the initial sites (bridge and HCP, respectively) while the hydroxyl group is on an HCP site next to that of the carbon.

The MEP for this elementary step is smooth, as shown in figure 2.80. The TS is located at image three: its geometry shows that the hydroxyl group is closer to the nickel surface (more precisely, it is near a top site), whereas the C–O distance increases with respect to the reactant structure (TS 1.999 Å, reactant 1.383 Å).

This elementary has a slightly exothermic ΔE_r of -17.8 kJ/mol, and a relatively high activation energy of 95.7 kJ/mol.

F22: $\text{CHOH} \longrightarrow \text{CH} + \text{OH}$ In this paragraph, the dissociation of CHOH into CH and OH is analyzed. The reactant structure has the CHOH species adsorbed with both C and O on two different top sites, while at the same time C also interacts with an HCP Fe. In the product geometry, on the other hand, the CH fragment is isolated on an FCC site, while the iron

atom moved to a bridge site to better interact with the hydroxyl group that remained on the same top site.

The CI-NEB calculation was not simple to carry out, and the six images elastic band was converged only to the looser threshold of $4.8 \cdot 10^{-3} E_h/\text{\AA}$ using the FIRE optimizer. The minimum energy path, reported in figure 2.81 is unusual, since the first six geometries share similar energies. The transition state is located at image two, while image three is a very labile intermediate. Examining the geometry of the latter, the only difference with respect to the reactant is the position of the CH group, whose carbon moved from a top to a bridge site. In its shift, it moved away from Fe. The TS geometry seems to be exactly in between those of the reactant and of the intermediate at image three: the carbon is midway between the top and the bridge sites, and in its migration it is keeping its interaction with Fe, that in turn is centered on the HCP site. It seems that once the CHO_H species is completely over nickel, as in the reaction intermediate, it can easily dissociate almost without an energy barrier, since the hydroxyl group ends up next to the Fe atom.

Having a ΔE_r of -125.7 kJ/mol, this is elementary step is strongly exothermic. Its is accompanied by an activation energy of 10.7 kJ/mol. These results are very similar to those of the backward F18 step: CHO_H —> COH + H. Apparently, the CHO_H species is extremely unstable when it is found near the Fe atom, and so it tends to dissociate in every possible way.

F23: CH₂OH —> CH₂ + OH The reactant structure chosen to study this elementary step has the CH₂OH species bonded to an HCP Fe through the carbon, while the oxygen is over a bridge site (however it is very faraway from the surface, the distance with the closest Ni being 2.263 Å). Conversely, in the product geometry the hydroxyl group is on the FCC site closest to its previous position, whereas CH₂ is still bonded to Fe but now it is also closer to the nickel surface.

The CI-NEB calculation was quite challenging, and at the end it was possible to converge a six images elastic band up to $5.4 \cdot 10^{-3} E_h/\text{\AA}$ on all force norms using the FIRE algorithm. The MEP shown in figure 2.82 is quite smooth, with just a big leap between images three and four. TS is located at image two, and its structure shows that the hydroxyl group is approaching the bridge site (distance with the closest Ni being 2.059 Å) while also moving away from CH₂.

Despite the strongly exothermic ΔE_r of -118.4 kJ/mol, this elementary step has a moderately high activation energy of 51.2 kJ/mol.

F24: CH₃OH —> CH₃ + OH The dissociation of CH₃OH into methyl

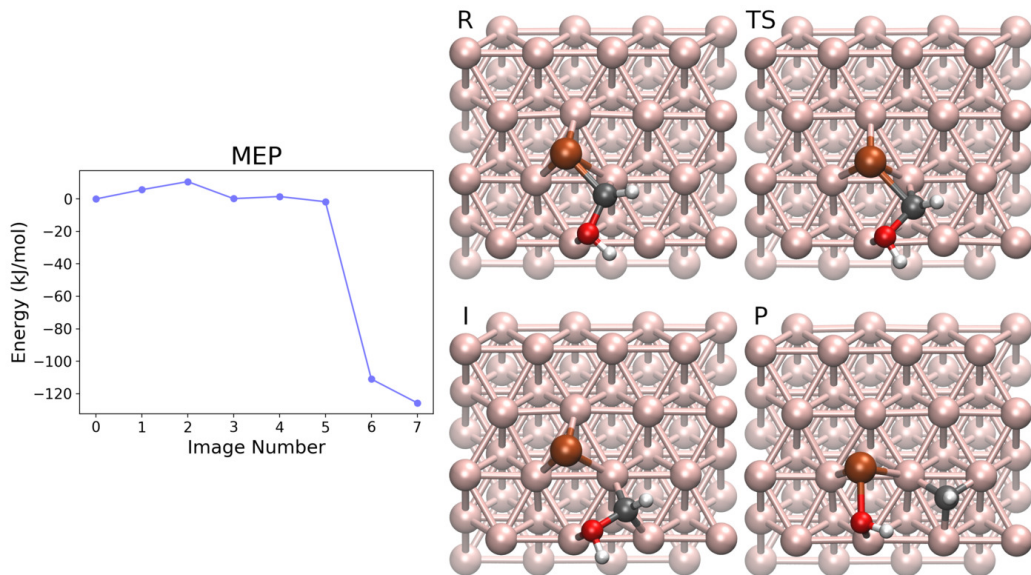


Figure 2.81: **MEP** and geometries of interest of the F22 elementary step:
 $\text{CHOH} \longrightarrow \text{CH} + \text{OH}$. Reactant, image 0; **TS**, image 2;
Intermediate, image 3; **P**roduct, image 7. Colors: H white; C black; O red; Ni rose gold; Fe dark orange.

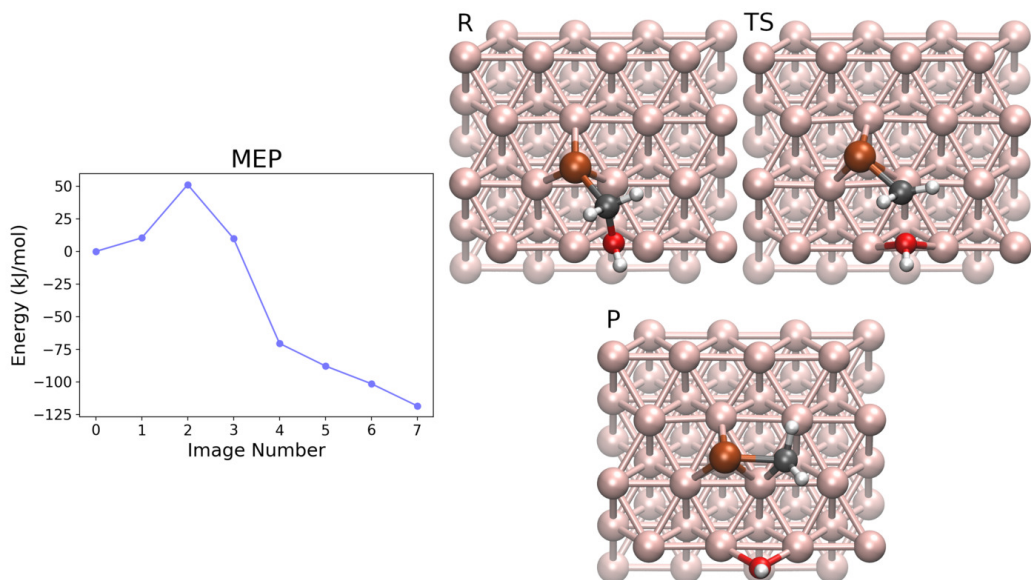


Figure 2.82: **MEP** and geometries of interest of the F23 elementary step:
 $\text{CH}_2\text{OH} \longrightarrow \text{CH}_2 + \text{OH}$. Reactant, image 0; **TS**, image 2;
Product, image 7. Colors: H white; C black; O red; Ni rose gold;
Fe dark orange.

and hydroxyl groups was investigated using, as reactant, a geometry in which the methanol is on top of an HCP Fe, interacting with it through the hydroxyl group. In the product structure CH_3OH split: CH_3 is now on a top site of nickel (111), whereas OH is still bonded on top of Fe.

Surprisingly enough, despite the big displacement of the CH_3 fragment between the reactant and product structures, the CI-NEB calculation succeeded using the standard parameters. In the MEP reported in figure 2.83 there are two images of about the same energy (two and three), giving to the curve that peculiar flat top shape. The transition state is located at image two, furthermore there is a reaction intermediate at image six. The TS geometry shows an isolated methyl group floating around, far from both the nickel surface and the hydroxyl group. The intermediate structure, instead, has the CH_3 group exactly on an FCC site, where one of its hydrogens points to the oxygen of the hydroxyl group. Here OH is still bonded to Fe, but the latter shifted to a bridge site.

To compute the ΔE_r of -105.6 kJ/mol, the absolute energy of the intermediate was used in place of that of the product. The high activation energy for this elementary step is 119.9 kJ/mol, an appropriate value considering the unstable isolated methyl group in the transition state.

It is worth noting that another NEB was tried for this elementary step using a methane molecule near the nickel surface as reactant, and, as product, a methyl group bonded to Fe and a Ni-adsorbed hydroxyl group. This calculation did not converge up to a satisfactory threshold (best was $1.22 \cdot 10^{-2} E_h/\text{\AA}$), and for this reason it will not be presented on a dedicated paragraph. Its energetic, however, is comparable to the one obtained in F24, with a ΔE_r of -109.0 kJ/mol and an activation energy of 117.1 kJ/mol. But, once more, these values must be considered very cautiously because of the not very strict convergence threshold.

F25: $\text{C} + \text{H} \longrightarrow \text{CH}$ To study the hydrogenation of the adsorbed atomic carbon, a structure was chosen as reactant in which C and H are on two bordering HCP sites. Moreover, there is a bridged Fe interacting with the atomic carbon. In the product structure Fe maintains its position on the bridge site near C, while H is now bonded to the HCP carbon.

The fairly simple CI-NEB calculation found a MEP, reported in figure 2.84, that is generally smooth, in which the transition state is located at image four. The TS geometry shows that the atomic hydrogen moved from an HCP to a bridge site, and it is now closer to C.

This elementary step is slightly endothermic, having a ΔE_r of 21.4 kJ/mol, while its activation energy is 82.2 kJ/mol.

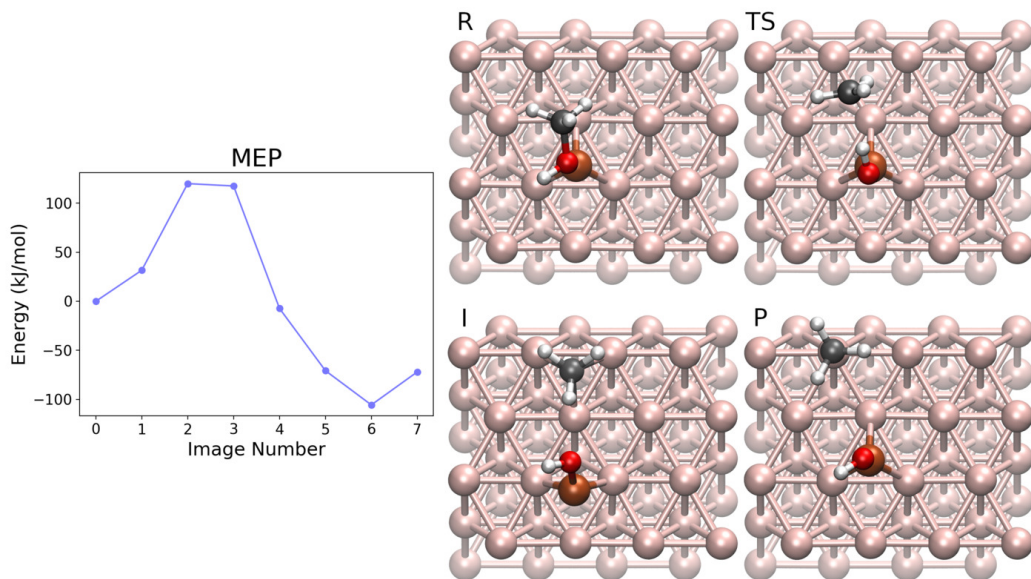


Figure 2.83: MEP and geometries of interest of the F24 elementary step:
 $\text{CH}_3\text{OH} \longrightarrow \text{CH}_3 + \text{OH}$. Reactant, image 0; **TS**, image 2;
 Intermediate, image 6; Product, image 7. Colors: H white; C black; O red; Ni rose gold; Fe dark orange.

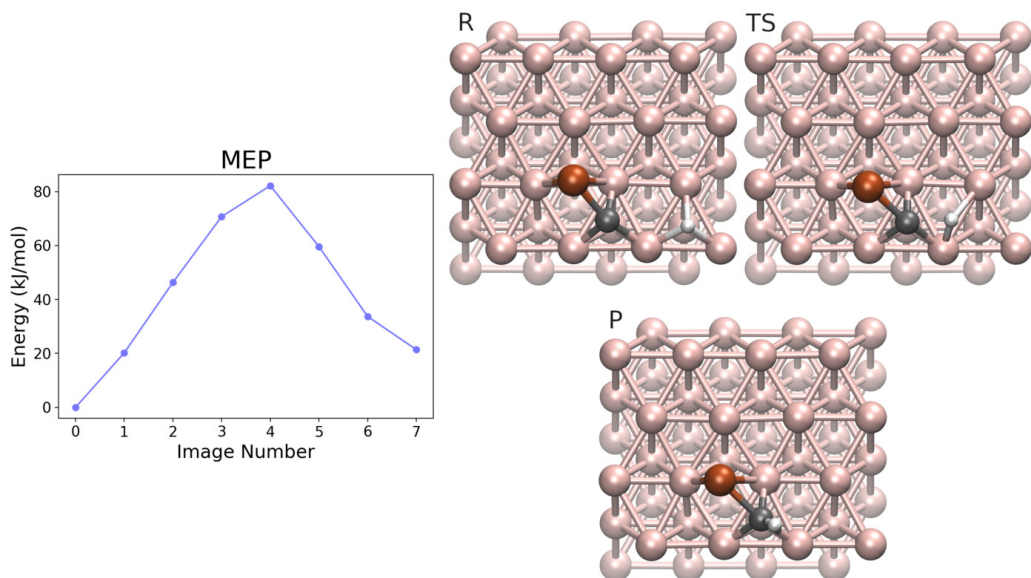


Figure 2.84: MEP and geometries of interest of the F25 elementary step:
 $\text{C} + \text{H} \longrightarrow \text{CH}$. Reactant, image 0; **TS**, image 4; **P**, image 7.
 Colors: H white; C black; Ni rose gold; Fe dark orange.

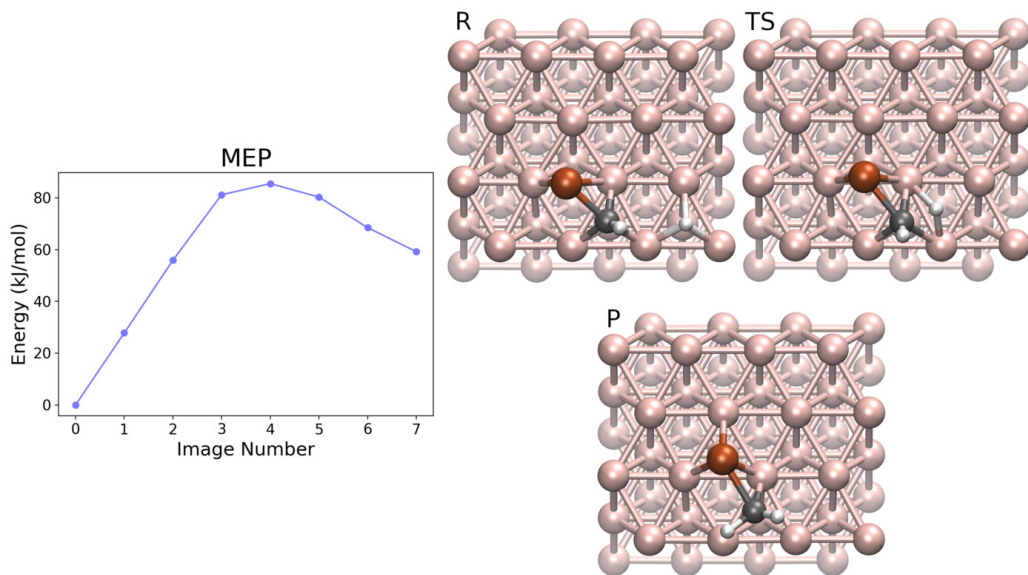


Figure 2.85: MEP and geometries of interest of the F26 elementary step: $\text{CH} + \text{H} \longrightarrow \text{CH}_2$. **R**, Reactant, image 0; **TS**, image 4; **P**, Product, image 7. Colors: H white; C black; Ni rose gold; Fe dark orange.

F26: $\text{CH} + \text{H} \longrightarrow \text{CH}_2$ To investigate the further hydrogenation of CH, in the reactant geometry of choice that chemical species is placed on an HCP site, interacting through the carbon with a bridged Fe, whereas the atomic hydrogen is on another HCP site nearby. In the product structure, instead, the newly formed CH_2 is on the near bridge site, while Fe shifted towards an HCP site.

Like in the previous elementary step, the MEP for this one is smooth and locates the TS at image four, as reported in figure 2.85. Its structure shows that the atomic hydrogen is almost over the bridge site next to C, and that the CH group rotated slightly in order for the carbon to accommodate a second hydrogen. Other than that, both the positions of Fe and C are the same ones as in the reactant structure.

The reaction is moderately endothermic with a ΔE_r of 59.2 kJ/mol. Its activation energy of 85.5 kJ/mol implies a low barrier for the backward reaction.

F27: $\text{CH}_2 + \text{H} \longrightarrow \text{CH}_3$ The next hydrogenation step happens on the CH_2 species and gives a methyl group. The chosen reactant has a slightly off-centered HCP Fe that bonds both a bridged CH_2 fragment and a top atomic hydrogen. This conformation was selected to investigate the Fe-pivoted hy-

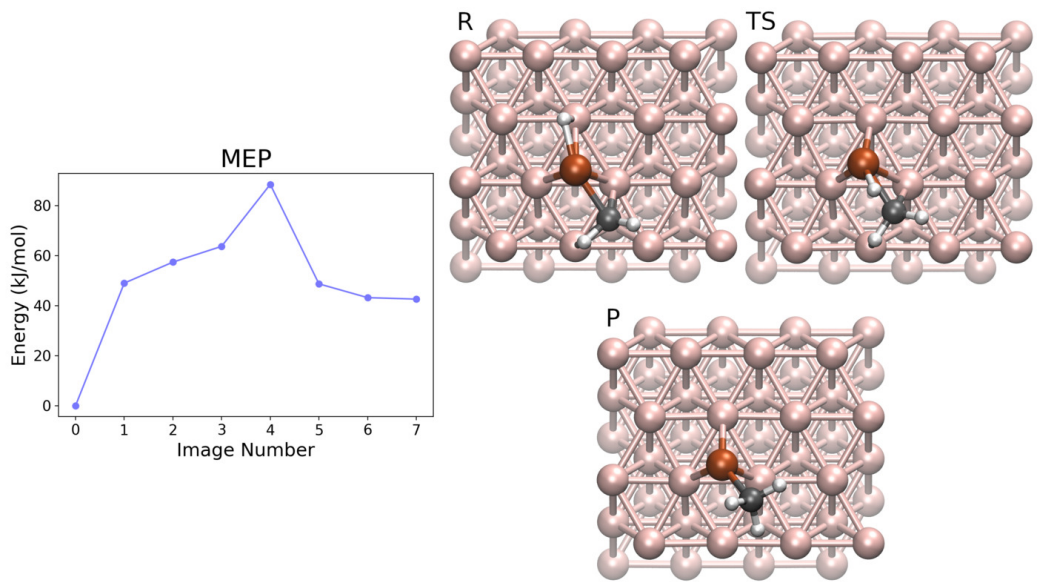


Figure 2.86: MEP and geometries of interest of the F27 elementary step: $\text{CH}_2 + \text{H} \longrightarrow \text{CH}_3$. Reactant, image 0; TS, image 4; Product, image 7. Colors: H white; C black; Ni rose gold; Fe dark orange.

drogenation mechanism. The product structure used as the ending point of the elastic band is very simple: just the same HCP Fe with a methyl group bonded to it.

The MEP, reported in figure 2.86, shows a peak at image four, the reaction transition state. Going from image zero to three, the atomic hydrogen climbs the iron atom, reaching its top. The TS geometry displays that H is now descending towards the carbon, being midway between Fe and C.

The ΔE_r and activation energy associated with this elementary step are 42.6 and 88.5 kJ/mol, respectively.

F28: $\text{CH}_3 + \text{H} \longrightarrow \text{CH}_4$ Finally, F28 investigates the last hydrogenation step required to produce a methane molecule. The reactant structure was prepared with a Fe atom on an HCP site, on top of which there is the methyl group, the C–Fe distance being 1.962 Å. The atomic hydrogen is on another HCP site, next to that of Fe. As product, a geometry was used where Fe is still on the HCP site, and a methane molecule is located above the decorated surface having a very low interaction with that. Here the C–Fe distance is 2.536 Å.

Figure 2.87 shows an uneven MEP, where two big leaps are present between the pairs of images two and three, and five and six. The transition

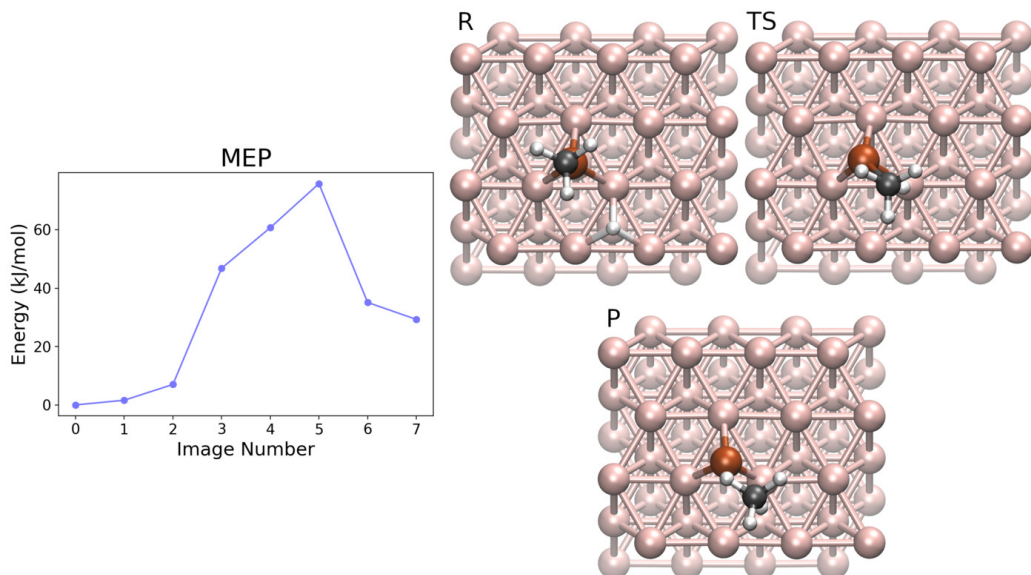


Figure 2.87: MEP and geometries of interest of the F28 elementary step: $\text{CH}_3 + \text{H} \longrightarrow \text{CH}_4$. **R**eactant, image 0; **TS**, image 5; **P**roduct, image 7. Colors: H white; C black; Ni rose gold; Fe dark orange.

state geometry at image five shows that the atomic hydrogen hopped to a top site near its initial HCP position. Also, the methyl group moved over the atomic hydrogen, in order to promote the subsequent hydrogenation. In TS, the C–H distance is 1.596 Å, whereas in the product it is 1.135 Å.

This elementary steps has a slightly endothermic ΔE_r of 29.3 kJ/mol, and an activation energy of 75.8 kJ/mol.

2.7 Influence of an External Electric Field

Twelve elementary steps on both the pristine and Ru-decorated nickel surfaces were also investigated introducing an *external electric field* (EEF) in the electronic structure calculations, in order to inquire its effect on the main structures involved, i.e. reactant, product and transition state. Specifically, these steps are: $\text{CO}_2 \longrightarrow \text{CO} + \text{O}$; $\text{CH}_n\text{O} + \text{H} \longrightarrow \text{CH}_{n+1}\text{O}$ with $n \in [0, 2]$; $\text{CH}_n\text{O} \longrightarrow \text{CH}_n + \text{O}$ with $n \in [0, 3]$; and $\text{CH}_n + \text{H} \longrightarrow \text{CH}_{n+1}$ with $n \in [0, 3]$. The EEF is always perpendicular to the surface, while its module can either be positive or negative depending on whether it is leaving or entering the surface, respectively. The CI-NEB calculations were then repeated for the aforementioned steps, taking care to first re-optimize the reactant and product structures including the EEF. As a side note, a test CI-NEB was performed twice on the same elementary step with different setups: one starting *ex novo* from IDPP interpolation; the other using the optimized image geometries obtained for the same step without EEF. In both cases, the CI-NEB converged to the same MEP, giving the same TS geometry. The difference between the two was the required computational time, largely inferior when the optimized images were used as starting guess: for this reason, this procedure was followed to investigate the remaining steps.

The steps on the pristine surface were investigated mainly using EEFs of +0.3 and -0.3 eV/Å. The results, reported in table 2.6, show that the most affected steps are those of the group $\text{CH}_n\text{O} + \text{H} \longrightarrow \text{CH}_{n+1}\text{O}$. In particular, the $\text{CO} + \text{H} \longrightarrow \text{CHO}$ reaction was studied at additional values of EEF, since it had the strongest response to the external perturbation: going from +1.0 to -1.0 eV/Å, both ΔE_r and $E_{a\rightarrow}$ increase sensibly, while $E_{a\leftarrow}$ slightly decreases. It seems that a negative EEF has a destabilizing effect on the adsorbed CO (where C is closer to the surface), thus improving its reactivity with respect to the carbon hydrogenation. Finally, $\text{CO}_2 \longrightarrow \text{CO} + \text{O}$ seems to be an outlier, since both positive and negative EEFs have the same effect on the reaction energetics.

The experience gained with the previous calculations suggested me to use EEF of -1.0 and +1.0 eV/Å from the very beginning to investigate the steps on the Ru-decorated surface, in order to see more easily the effects on the reaction energetics. The obtained results, reported in table 2.7, show more complex trends compared the previous case. The behavior of the $\text{CO} + \text{H} \longrightarrow \text{CHO}$ step, for example, is reversed since $E_{a\rightarrow}$ decreases going towards negative EEF. The problem is that also $E_{a\leftarrow}$ decreases, thus making the backward reaction effortless under such EEF. Same considerations can be made for $\text{CHO} + \text{H} \longrightarrow \text{CH}_2\text{O}$. In both $\text{CH}_2\text{O} \longrightarrow \text{CH}_2 + \text{O}$ and $\text{CH}_3\text{O} \longrightarrow \text{CH}_3 + \text{O}$ the overall effect of EEF is not easy to interpret, but it seems that

the negative one gives better results both in terms of ΔE_r and of a favorable $E_{a\rightarrow}/E_{a\leftarrow}$ ratio. Moreover, these elementary steps were not affected in the pristine system, probably due to the spatial arrangements of the carbonyl species. Finally, $\text{CH}_3 + \text{H} \longrightarrow \text{CH}_4$ is clearly favored by a positive EEF. In conclusion, considering that some steps prefer a negative EEF, while others are advantaged by a positive one, it is not possible to tell which one is better in this particular catalytic surface without the help of an objective method (such as a kinetic model).

2.8 Enumerating all Reaction Paths

Up to this point, we have 16 different chemical species and a bunch of elementary steps that connect them one another (28 for the pristine nickel surface, 27 for the two decorated ones). In order to discern a reaction mechanism for the methanation process, the first step is to search and enumerate all the possible paths from carbon dioxide to methane. This task is performed employing a software developed by us, called Pathgen. Here is how it works. The whole graph is stored in the program memory as a $n \times n$ square matrix M of boolean values, being n the number of vertices in the graph. The matrix element $M_{i,j}$ is True if there is an edge going from vertex i (v_i) to vertex j (v_j), False otherwise (in graph theory, an edge can be described by an ordered pair of vertices: (v_i, v_j)). Pathgen can work with both directed and undirected graphs: in the latter case M is symmetrical with respect to the main diagonal, thus if a connection between v_i and v_j exists then $M_{i,j} = M_{j,i} = \text{True}$. The graph representing the methanation process of this study is an example of undirected graph since each elementary step can occur in both forward (one step “closer” to methane) or backward (one step “farther” from methane) directions. Moreover, for reasons that will be explained in detail later, which have to do with the explicit treatment of the production of water molecules during the methanation process, it is important to be able to treat some vertices in a special way, as if they belong to a sort of “group”. Pathgen was implemented with the capability to work with graphs in which there are groups of vertices, as well as with regular graphs.

The task of finding all the possible paths is delegated to a single recursive subroutine inside Pathgen: `findPaths`, reported in algorithm 1. There is a single explicit call to `findPaths` inside the main program, whereas all the other ones are performed by the subroutine itself. The arguments required at the time of the first call are: the initial and final vertices v_i and v_f , i.e. the two between which we are interested in all the possible paths that connect them (corresponding to the ones of CO_2 and CH_4 , in this study); two arrays for the

Table 2.6: Elementary steps on pristine Ni (111) surface in the presence of an external electric field (EEF, in eV/Å). All energies expressed in kJ/mol.

Code	Elem. Step	EEF	ΔE_r	$E_{a\rightarrow}$	$E_{a\leftarrow}$
N01	$\text{CO}_2 \longrightarrow \text{CO} + \text{O}$	+0.3	-131.7	30.7	162.4
		0.0	-92.9	48.9	141.8
		-0.3	-131.1	31.4	162.5
N07	$\text{CO} + \text{H} \longrightarrow \text{CHO}$	+1.0	118.8	138.1	19.3
		+0.6	126.3	143.4	17.1
		+0.3	132.2	147.8	15.5
		0.0	138.0	152.4	14.4
		-0.3	143.1	156.8	13.7
		-0.6	148.2	161.7	13.4
N08	$\text{CHO} + \text{H} \longrightarrow \text{CH}_2\text{O}$	-1.0	155.7	168.2	12.5
		+0.3	61.4	81.5	20.1
		0.0	63.6	84.3	20.7
N09	$\text{CH}_2\text{O} + \text{H} \longrightarrow \text{CH}_3\text{O}$	-0.3	65.7	87.4	21.7
		+0.3	38.8	68.1	29.3
		0.0	41.8	71.5	29.7
N14	$\text{CO} \longrightarrow \text{C} + \text{O}$	-0.3	44.0	74.8	30.8
		+1.0	112.2	235.9	123.7
		+0.3	108.5	233.3	124.8
N15	$\text{CHO} \longrightarrow \text{CH} + \text{O}$	0.0	108.2	233.6	125.4
		-0.3	108.6	234.3	125.7
		-1.0	112.5	239.5	127.0
N16	$\text{CH}_2\text{O} \longrightarrow \text{CH}_2 + \text{O}$	+0.3	-51.4	89.0	140.3
		0.0	-52.7	87.7	140.3
		-0.3	-53.5	86.9	140.4
N17	$\text{CH}_3\text{O} \longrightarrow \text{CH}_3 + \text{O}$	+0.3	-41.1	75.6	116.7
		0.0	-42.6	75.6	118.3
		-0.3	-43.7	76.0	119.7
N25	$\text{C} + \text{H} \longrightarrow \text{CH}$	+0.3	-84.8	111.6	196.3
		0.0	-88.2	111.2	199.4
		-0.3	-90.6	111.8	202.4
N26	$\text{CH} + \text{H} \longrightarrow \text{CH}_2$	+0.3	-20.1	82.8	102.9
		0.0	-12.2	87.6	99.9
		-0.3	-8.4	88.8	97.2
N27	$\text{CH}_2 + \text{H} \longrightarrow \text{CH}_3$	+0.3	54.0	72.5	18.5
		0.0	55.8	73.6	17.8
		-0.3	57.6	74.8	17.2
N28	$\text{CH}_3 + \text{H} \longrightarrow \text{CH}_4$	+0.3	19.8	65.1	45.3
		0.0	21.6	66.3	44.7
		-0.3	23.6	67.8	44.3
		+0.3	58.4	101.8	43.5
		0.0	57.3	104.9	47.6
		-0.3	55.5	103.0	47.5

Table 2.7: Elementary steps on Ru-decorated Ni (111) surface in the presence of an external electric field (EEF, in eV/Å). All energies expressed in kJ/mol.

Code	Elem. Step	EEF	ΔE_r	$E_{a\rightarrow}$	$E_{a\leftarrow}$
R01	$\text{CO}_2 \longrightarrow \text{CO} + \text{O}$	+1.0	-90.4	39.6	129.9
		0.0	-91.6	40.6	132.2
		-1.0	-92.9	40.3	133.3
R07	$\text{CO} + \text{H} \longrightarrow \text{CHO}$	+1.0	90.1	141.2	51.2
		0.0	86.8	128.4	41.6
		-1.0	99.5	114.8	15.3
R08	$\text{CHO} + \text{H} \longrightarrow \text{CH}_2\text{O}$	+1.0	58.7	90.9	32.2
		0.0	61.3	78.7	17.5
		-1.0	60.3	64.9	4.7
R09	$\text{CH}_2\text{O} + \text{H} \longrightarrow \text{CH}_3\text{O}$	+1.0	-3.8	87.6	91.4
		0.0	7.4	90.8	83.4
		-1.0	20.1	91.7	71.6
R14	$\text{CO} \longrightarrow \text{C} + \text{O}$	+1.0	11.6	145.5	133.9
		0.0	10.4	144.5	134.1
		-1.0	9.9	144.9	135.1
R15	$\text{CHO} \longrightarrow \text{CH} + \text{O}$	+1.0	-71.1	77.4	148.6
		0.0	-68.8	77.9	146.6
		-1.0	-72.2	79.5	151.7
R16	$\text{CH}_2\text{O} \longrightarrow \text{CH}_2 + \text{O}$	+1.0	-65.0	68.1	133.2
		0.0	-73.2	81.1	154.3
		-1.0	-76.0	49.4	125.4
R17	$\text{CH}_3\text{O} \longrightarrow \text{CH}_3 + \text{O}$	+1.0	-18.3	119.0	137.2
		0.0	-45.4	161.8	207.2
		-1.0	-84.0	133.3	217.2
R25	$\text{C} + \text{H} \longrightarrow \text{CH}$	+1.0	37.7	84.0	46.4
		0.0	45.2	86.7	41.5
		-1.0	52.8	90.3	37.4
R26	$\text{CH} + \text{H} \longrightarrow \text{CH}_2$	+1.0	70.0	93.9	23.9
		0.0	73.3	96.3	23.0
		-1.0	75.0	97.7	22.8
R27b	$\text{CH}_2 + \text{H} \longrightarrow \text{CH}_3$	+1.0	55.8	157.3	101.5
		0.0	53.4	88.4	35.1
		-1.0	17.7	134.1	116.4
R28	$\text{CH}_3 + \text{H} \longrightarrow \text{CH}_4$	+1.0	-27.1	24.3	51.4
		0.0	3.7	38.8	35.1
		-1.0	42.4	68.7	26.3

visited vertices and groups, $visited_v$ and $visited_g$, with all values initialized to False; and an empty string $path$. At the start of its execution, `findPaths` will mark the initial vertex v_i as visited in order to prevent infinite recursion over loop edges. Then it will cycle among all the vertices in the graph. If one or more of the following conditions occur: i) the vertex v_j was visited, ii) the group to which v_j belongs was visited, or iii) there is no edge going from v_i to v_j ; then v_j is discarded and the search continues with the next vertex. If, instead, there is such an edge from v_i to v_j , then there are two possibilities: i) v_j is different from v_f , in this case if the group of v_j is different from the group of v_i , then the latter is marked as visited (since we want to avoid all those unnecessarily long paths that cross over the same group more than once) and `findPaths` is recursively called with the arguments: v_j and v_f as the initial and final vertices, the updated arrays of visited vertices and groups, and a new string obtained by the concatenation of the old sting $path$ and the vertex v_i ; ii) v_j is the same as v_f , in such a case the search ends and the path just found can be added to the list of valid paths.

Two final notes on the previous algorithm: i) it is important to reset the `updated_visitedg` array to the same value of $visited_g$ (line 21) before each recursive call to `findPaths` in order to prevent a very insidious bug whose effect is to drastically reduce the amount of paths found; ii) all the checks about the belonging groups are optional and can be disabled in order to work with more traditional kind of graphs.

If one is interested in the search of all paths between groups of vertices, then the direct application of algorithm 1 to the whole graph is not the best way to proceed. It is better, instead, to perform a preliminary skimming of the possible paths by first executing a search of the paths over groups of vertices. In order to do so, one first need to define in which case two groups of vertices are connected by a *group edge*. The rule is pretty simple: if i) an edge between the ordered pair of vertices (v_i, v_j) exists, and ii) v_i and v_j belong to different groups g_m and g_n ; then a edge between the ordered pair of groups (g_m, g_n) also exists. This way it is possible to build a connectivity matrix for groups, and to use it to search for all paths over groups of vertices: when one of these paths is found, then it is possible to search for all paths on vertices inside it. This step is not as straightforward as it seems, since to put it into action it is first required to build an *ad hoc* connectivity matrix. Such new connectivity matrix is similar to the original one, with two main differences: i) all the connections going to/coming from vertices belonging to groups other than the ones in the group path are turned off; and ii) all edges between vertices that don't belong to two subsequent groups in the group path are also turned off.

Figure 2.88 gives a visual insight of this search inside group paths. The

Algorithm 1 Recursive subroutine findPaths

1: ▷ Arguments:
2: $\leftarrow v_i$; ▷ the initial vertex from where to start the search
3: $\leftarrow v_f$; ▷ the final vertex in which to stop the search
4: $\leftarrow \text{visited}_v$; ▷ boolean array of already visited vertices
5: $\leftarrow \text{visited}_g$; ▷ boolean array of already visited groups
6: $\leftarrow \text{path}$; ▷ string containing all the vertices encountered so far
7:
8: ▷ Body:
9: $\text{updated_visited}_v \leftarrow \text{visited}_v$ with vertex v_i marked as visited;
10: **for** $j = 1$, number of vertices **do**
11: **if** v_j has been visited **then**
12: cycle to the next j ;
13: **end if**
14: **if** group of v_j has been visited **then**
15: cycle to the next j ;
16: **end if**
17: **if** there is an edge from v_i to v_j **then**
18: **if** v_j is the same as v_f **then** ▷ found a complete path
19: add $\text{path} + \text{string}(v_i) + \text{string}(v_f)$ to the found paths;
20: **else** ▷ keep searching along v_j
21: $\text{updated_visited}_g \leftarrow \text{visited}_g$;
22: **if** group of v_j is different from group of v_i **then**
23: $\text{updated_visited}_g \leftarrow \text{visited}_g$ with group of v_i
24: marked as visited;
25: **end if**
26: **call** findPaths with arguments:
27: $v_i \leftarrow v_j$;
28: $v_f \leftarrow v_f$;
29: $\text{visited}_v \leftarrow \text{updated_visited}_v$;
30: $\text{visited}_g \leftarrow \text{updated_visited}_g$;
31: $\text{path} \leftarrow \text{path} + \text{string}(v_i)$;
32: **end if**
33: **end if**
34: **end for**

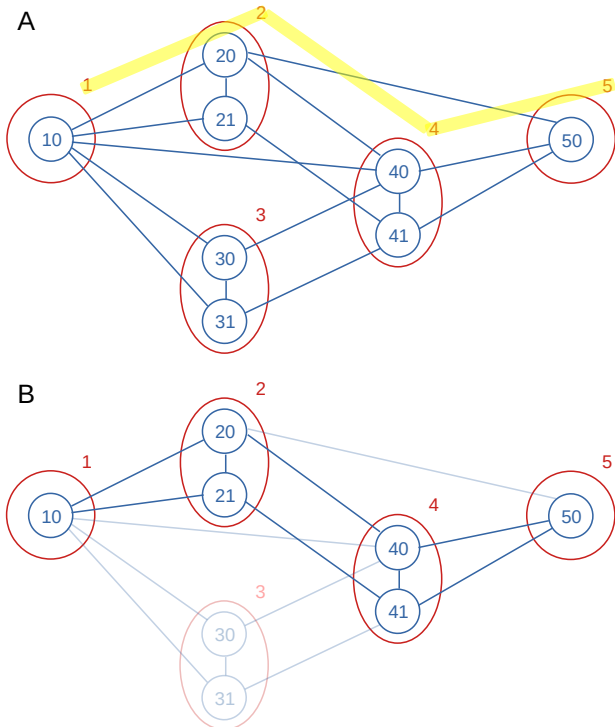


Figure 2.88: Search for all paths on vertices inside a group path: A) full graph with highlight of the group path of interest (1-2-4-5); B) resulting graph in which the irrelevant vertices and edges were dimmed out, used to build and ad hoc connectivity matrix.

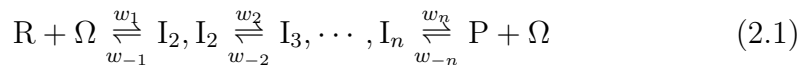
graph in this example is constituted by 8 vertices belonging to 5 different groups and 15 edges, the interest being in paths going from vertex 10 to vertex 50. Instead of searching directly on the full graph (search over vertices), the first step is to identify a group path by searching over groups. Figure 2.88.A shows one of this paths, namely 1-2-4-5. Then one can proceed to eliminate all the vertices and edges that are not directly involved in this path. Figure 2.88.B shows the resulting graph with all the non-interesting objects dimmed out: this simplified graph can then be used to build an ad hoc connectivity matrix for the search over vertices. A detailed description of this procedure is given in algorithm 2, that was designed to maintain connectivity between vertices within a group, and to work with both directed and undirected graphs.

Algorithm 2 Build ad hoc connectivity matrix using paths over groups

```
1:                                                               ▷ Arguments:  
2:  $\leftarrow path_g;$                                          ▷ a path over groups  
3:  $\leftarrow original\_cm;$                                      ▷ original connectivity matrix on vertices  
4:  
5:                                                               ▷ Body:  
6:  $adhoc\_cm \leftarrow False;$   
7: for  $k = 1$ , number of groups in  $path_g - 1$  do  
8:    $g_1 \leftarrow k^{th}$  group in  $path_g$ ;  
9:    $g_2 \leftarrow (k + 1)^{th}$  group in  $path_g$ ;  
10:  for  $i = 1$ , number of vertices do  
11:    for  $j = 1$ , number of vertices do  
12:       $g_i \leftarrow$  group of vertex  $i$ ;  
13:       $g_j \leftarrow$  group of vertex  $j$ ;  
14:      if  $((g_i = g_1) \vee (g_i = g_2)) \wedge ((g_j = g_1) \vee (g_j = g_2))$  then  
15:         $adhoc\_cm(i, j) = original\_cm(i, j)$   
16:      end if  
17:    end for  
18:  end for  
19: end for
```

2.9 The Simplified Christiansen Method

Once all possible paths between the two chemical species of interest were found, the next step is to assess how fast (or probable) each one of them is. In the present study, this is done by applying an approach originally developed in our group based on the algebraic system outlined by Christiansen.[43, 44] Every reaction path is a sequence of consecutive transformations that from $CO_{2(g)}$ (R) goes to $CH_{4(g)}$ (P) passing by a number of intermediate species (I). This can be schematized by the equation



where Ω represents the free catalytic site on the surface, w_1, \dots, w_n are the rates (in s^{-1}) at which a given species transforms in the next one, and w_{-1}, \dots, w_{-n} are the rates at which it goes back to the previous one. These rates are computed using the activation energies found by the CI-NEB calculations, as

$$w = \frac{k_B T}{h} \exp\left(-\frac{E_a}{RT}\right) \quad (2.2)$$

where k_B and h are the Boltzmann and Plank constants, respectively, T is the temperature expressed in kelvin, and R is the gas constant.

To the chemical equation 2.1 is associated the system of kinetic equations

$$\begin{aligned}\theta_1 w_1 - \theta_2 w_{-1} &= s_1 \\ \theta_2 w_2 - \theta_3 w_{-2} &= s_2 \\ &\vdots \\ \theta_n w_n - \theta_1 w_{-n} &= s_n\end{aligned}\tag{2.3}$$

where θ_1 is the molar fraction of the free site, $\theta_2, \dots, \theta_n$ are the molar fractions of the intermediates I_2, \dots, I_n , and s_1, \dots, s_n are the velocities associated to each intermediate step (in s^{-1}). Of course, the molar fractions are related by

$$\sum_{i=1}^n \theta_i = 1\tag{2.4}$$

In steady-state condition, all velocities s_1, \dots, s_n become equal to that of the slowest step, let's call it s without subscript

$$s_1 = s_2 = \dots = s_n = s\tag{2.5}$$

equation (2.3) thus become

$$\begin{aligned}\frac{\theta_1}{s} w_1 - \frac{\theta_2}{s} w_{-1} &= 1 \\ \frac{\theta_2}{s} w_2 - \frac{\theta_3}{s} w_{-2} &= 1 \\ &\vdots \\ \frac{\theta_n}{s} w_n - \frac{\theta_1}{s} w_{-n} &= 1\end{aligned}\tag{2.6}$$

that can be written in matrix form as

$$\begin{pmatrix} w_1 & -w_{-1} & 0 & \cdots & 0 \\ 0 & w_2 & -w_{-2} & \cdots & 0 \\ 0 & 0 & w_3 & \cdots & 0 \\ \vdots & \vdots & \vdots & \ddots & \vdots \\ -w_{-n} & 0 & 0 & \cdots & w_n \end{pmatrix} \begin{pmatrix} \theta_1/s \\ \theta_2/s \\ \theta_3/s \\ \vdots \\ \theta_n/s \end{pmatrix} = \begin{pmatrix} 1 \\ 1 \\ 1 \\ \vdots \\ 1 \end{pmatrix}\tag{2.7}$$

Instead of solving the linear system of equations, in its original work Christiansen suggested to build the so called *partition matrix*, a tool that is more convenient for this task and also has a mnemonic form that make

it easy to work with. This is undoubtedly helpful if one tries to solve the system using pencil and paper, but some problems arise if this strategy is implemented as is in a computer code, due to the finite precision by which calculators can represent real numbers in memory. For instance, if there are too many steps involved in a given mechanism, being each element of the partition matrix a product of exponentials (the w), the result can very easily exceed the maximum value allowed (e.g. if double precision is used in Fortran 2008, then the only representable numbers are those with an exponent between -308 and 308). For this reason, in the actual implementation of the Simplified Christiansen Method (SCM) used in this study, the system in eq. (2.7) is solved directly using the `dgesv()` subroutine of the `lapack` linear algebra library in order to get all the unknown variables θ_i/s . Then using the normalization of θ_i , eq. (2.4), and dividing both sides for s , one gets

$$\sum_{i=1}^n \frac{\theta_i}{s} = \frac{1}{s} \implies s = \left(\sum_{i=1}^n \frac{\theta_i}{s} \right)^{-1} \quad (2.8)$$

where all the members θ_i/s inside the sum are known. Now that both s and all θ_i/s are known, a simple multiplication will give the values of θ_i .

All of this is performed for each possible path by which CO_2 ends up in CH_4 . Having the reaction rates (s_i) associated to all the found paths P , one can compute their selectivity (σ_i) as

$$\sigma_i = \frac{s_i}{\sum_j^P s_j} \quad (2.9)$$

This value can be used to obtain information about the global reaction rate (s^g) of the process, as

$$s^g = \sum_i^P s_i \sigma_i \quad (2.10)$$

Moreover, the global molar fraction of each species i involved (θ_i^g) can similarly be computed as

$$\theta_i^g = \sum_j^P \theta_i^j \sigma_j \quad (2.11)$$

where θ_i^j is the molar fraction of the species i in the reaction path j .

2.10 Searching the Best Reaction Path

The theoretical framework just discussed can be applied to the CO_2 methanation problem to get an insight about the intrinsic meaning of all the found

activation energies. Starting from the pristine nickel surface, a graph similar to that of figure 2.2 was used, where the 16 chemical species are the vertices, and the 28 elementary steps are undirected edges, so that the findPaths algorithm can travel them in both directions. This way, a total of 1122 different reaction paths were found to connect CO₂ to CH₄, each of which was tested with the SCM method in the range of temperatures from 400 K to 1400 K, at steps of 100 K. The same analysis was performed for the two decorated systems. The graphs associated with them have 16 vertices and 27 undirected edges. The missing connection between the CH₃O and CH₃OH species reduces the amount of paths between CO₂ and CH₄ to 618.

Table 2.8 reports the global reaction rates (s^g) obtained for the three surfaces at different temperatures. These data can be used to fit the Arrhenius equation, that in logarithmic form shows the linear dependence of $\ln s^g$ on the inverse of the temperature

$$s^g = A \exp\left(-\frac{E_{app}}{RT}\right) \implies \ln s^g = \ln A - \frac{E_{app}}{RT} \quad (2.12)$$

where E_{app} is the apparent activation energy. The fitting procedure returns values of: 1) $E_{app} = 157.5 \pm 0.7$ kJ/mol, $A = 28.6 \pm 0.1$ s⁻¹ for the methanation process on the pristine nickel (111) surface; 2) $E_{app} = 143.6 \pm 0.4$ kJ/mol, $A = 30.22 \pm 0.07$ s⁻¹ on the Ru-decorated surface; and 3) $E_{app} = 178.8 \pm 0.2$ kJ/mol, $A = 30.05 \pm 0.04$ s⁻¹ on the Fe-decorated surface. These numbers show that the activity of the investigated systems to the methanation reaction decrease in the order: Ru-decorated > pristine Ni (111) > Fe-decorated. Moreover, the difference of ~ 35 kJ/mol between Ru and Fe shows that the nature of the decoration plays a central role, therefore the activity difference with the pristine surface is not only due to the geometric defect created by the presence of a further atom on the surface.

Sorting the reaction mechanisms by speed, some general trends can be observed: i) at 400 K, the first mechanism of each catalyst model is more than two orders of magnitude faster than the second one; ii) increasing the temperature decreases the speed differences between the top mechanisms, making them competitive with respect to the first one; and iii) the order in which the mechanisms are ranked depends on temperature, i.e. each mechanism can gain or lose positions at different temperatures (even if, in the investigated range of temperatures, the fastest mechanism maintains its top place in the ranking).

Table 2.9 reports the top mechanisms on the three surfaces at 900 K, since this is a common temperature at which many experimental tests on similar catalysts are performed.[45, 46, 47, 48, 49] Six and four mechanisms are reported for the Ru- and Fe-decorated systems respectively, since the

Table 2.8: Global reaction rates (s^g) obtained with the SCM method at different temperatures (T), for the three nickel surfaces investigated. T expressed in K, s^g in s^{-1} .

T	s^g		
	Prist.	Ru-dec.	Fe-dec.
400	5.4903E-09	2.1115E-06	4.7799E-11
500	9.4923E-05	1.3086E-02	2.3621E-06
600	5.9366E-02	4.3989E+00	3.1665E-03
700	5.5138E+00	2.7709E+02	5.3838E-01
800	1.5599E+02	6.0992E+03	2.5146E+01
900	2.0236E+03	6.6433E+04	4.9575E+02
1000	1.5465E+04	4.4160E+05	5.3362E+03
1100	8.1634E+04	2.0483E+06	3.6932E+04
1200	3.2970E+05	7.2503E+06	1.8326E+05
1300	1.0884E+06	2.0843E+07	7.0314E+05
1400	3.0662E+06	5.0877E+07	2.2021E+06

ones after those are more than 100 times slower than the respective first one. For the pristine surface, however, the top mechanisms are closer in speed, and become more than 100 times slower with respect to the first one starting from the 12th. For convenience, it was chosen to report only the first eight. Observing these fastest mechanisms one notices that: i) in no cases CO_2 dissociates directly into carbon monoxide, moreover, CO never appears as a reaction intermediate (this is probably due to the fact that every elementary step that from CO gives another species has always, without any exception, a forward activation energy way higher than the backward one); ii) on the decorated systems, all mechanisms except one involve the $\text{CO}_2 + \text{H} \longrightarrow \text{CHOO}$ step, whereas on the pristine surface this is the case only for four of them, the other half prefers to pass through $\text{CO}_2 + \text{H} \longrightarrow \text{COOH}$; iii) there are two out of eight mechanisms on the pristine surface that involve atomic carbon as an intermediate, whereas in the Fe-decorated system they are two out of four, while in the Ru-decorated there are none.

These points seem to suggest that the Fe-decorated nickel (111) surface may not be a good catalyst for the methanation reaction due to the formation of atomic carbon and its potential accretion near Fe, being this its favorite site according to the CI-NEB that addressed the $\text{C}/\text{Fe} \longrightarrow \text{C}/\text{Ni}$ migration process. Moreover, this is also the system with the higher E_{app} . Exactly the same considerations, but in the opposite way, can be made for the Ru-decorated system, that shows a better activity to the CO_2 methanation process than the pristine nickel surface both in terms of a lower E_{app}

and a limited production of the inconvenient atomic carbon.

Explicit Treatment of the Formation of Water Molecules

When CO_2 reacts in a large excess of H_2 , carbon is not the only species that is reduced: there is also oxygen. The overall reaction is in fact $\text{CO}_2 + 4 \text{H}_2 \longrightarrow \text{CH}_4 + 2 \text{H}_2\text{O}$. In this study it was tried to explicitly take into account the production of water and its desorption, just like it is done for methane. It should be noted, however, that the results reported in this section are not definitive as it is not yet clear whether such a model is plausible. Therefore, the following discussion should be taken with a pinch of salt.

All the surface chemical species involved in the elementary steps of the methanation process reported in this study always contain a carbon atom and a variable number of hydrogen and oxygen atoms. The latter, in particular, can range from zero to two. As an example, let's start with a CO_2 molecule adsorbed on nickel: all the oxygen atoms are bound to the main species, thus there is no oxygen dissociated on the surface in any form (atomic, hydroxyl group or H_2O molecule). Suppose now that the species dissociates into $\text{CO} + \text{O}$. The main species (CO) contains only one oxygen, hence the other one must be somewhere on the surface. Finally, a species like CH_3 lost both of its two original oxygen atoms, which are therefore somewhere on the surface. These adsorbed oxygen can react with hydrogen atoms, giving hydroxyl groups and then water. As a final note, the O_2 formation reaction was not considered for two reasons: i) in the working conditions there is a strong excess of hydrogen, so it is likely that O mostly meets H rather than another atom of its kind; ii) the oxygen hopping has an activation energy about four times higher than that of hydrogen, so the first species is less mobile on the surface.

Oxygen can therefore be seen as a kind of “background” species with respect to the “main” species, i.e. those containing carbon. In order to formalize this argument, the notation shown in table 2.10 was used, in which every possible background is listed and numbered so to have a quickly reference to them. Accordingly, the main species containing two oxygen atoms have only one possible background (0), those containing one have three (1, 4, 16), and those without oxygen have six possible backgrounds (2, 5, 8, 17, 20, 32). Another way to tell this is that there are three different sets of backgrounds. Inside each set, the backgrounds are connected within each other in the way reported in figure 2.89 (given that the water formation on the nickel surface starting from atomic hydrogen and oxygen is a reversible process).

Table 2.9: Main reaction mechanisms for the methanation process on the three catalyst models at 900 K, sorted by decreasing speed.

Pristine Ni (111)
1) $\text{CO}_2 \rightarrow \text{COOH} \rightarrow \text{COH} \rightarrow \text{CHO} \rightarrow \text{CH}_2\text{O} \rightarrow \text{CH}_2 \rightarrow \text{CH}_3 \rightarrow \text{CH}_4$
2) $\text{CO}_2 \rightarrow \text{CHOO} \rightarrow \text{CHO} \rightarrow \text{CH} \rightarrow \text{CHOH} \rightarrow \text{CH}_2\text{OH} \rightarrow \text{CH}_2\text{O} \rightarrow \text{CH}_2 \rightarrow \text{CH}_3 \rightarrow \text{CH}_4$
3) $\text{CO}_2 \rightarrow \text{COOH} \rightarrow \text{COH} \rightarrow \text{CHOH} \rightarrow \text{CHO} \rightarrow \text{CH} \rightarrow \text{CH}_2 \rightarrow \text{CH}_3 \rightarrow \text{CH}_4$
4) $\text{CO}_2 \rightarrow \text{CHOO} \rightarrow \text{CHO} \rightarrow \text{CH} \rightarrow \text{CH}_2 \rightarrow \text{CH}_3 \rightarrow \text{CH}_4$
5) $\text{CO}_2 \rightarrow \text{COOH} \rightarrow \text{COH} \rightarrow \text{C} \rightarrow \text{CH} \rightarrow \text{CHOH} \rightarrow \text{CHO} \rightarrow \text{CH}_2\text{O} \rightarrow \text{CH}_2 \rightarrow \text{CH}_3 \rightarrow \text{CH}_4$
6) $\text{CO}_2 \rightarrow \text{CHOO} \rightarrow \text{CHO} \rightarrow \text{CH}_2\text{O} \rightarrow \text{CH}_2 \rightarrow \text{CH}_3 \rightarrow \text{CH}_4$
7) $\text{CO}_2 \rightarrow \text{CHOO} \rightarrow \text{CHO} \rightarrow \text{CH} \rightarrow \text{C} \rightarrow \text{COH} \rightarrow \text{CHOH} \rightarrow \text{CH}_2\text{OH} \rightarrow \text{CH}_2\text{O} \rightarrow \text{CH}_2 \rightarrow \text{CH}_3 \rightarrow \text{CH}_4$
8) $\text{CO}_2 \rightarrow \text{COOH} \rightarrow \text{COH} \rightarrow \text{CHOH} \rightarrow \text{CH}_2\text{OH} \rightarrow \text{CH}_2\text{O} \rightarrow \text{CH}_2 \rightarrow \text{CH}_3 \rightarrow \text{CH}_4$
Ru-decorated Ni (111)
1) $\text{CO}_2 \rightarrow \text{CHOO} \rightarrow \text{CHO} \rightarrow \text{CH}_2\text{O} \rightarrow \text{CH}_2 \rightarrow \text{CH}_3 \rightarrow \text{CH}_4$
2) $\text{CO}_2 \rightarrow \text{CHOO} \rightarrow \text{CHO} \rightarrow \text{CH}_2\text{O} \rightarrow \text{CH}_2\text{OH} \rightarrow \text{CH}_2 \rightarrow \text{CH}_3 \rightarrow \text{CH}_4$
3) $\text{CO}_2 \rightarrow \text{CHOO} \rightarrow \text{CHO} \rightarrow \text{CH} \rightarrow \text{CH}_2 \rightarrow \text{CH}_3 \rightarrow \text{CH}_4$
4) $\text{CO}_2 \rightarrow \text{CHOO} \rightarrow \text{CHO} \rightarrow \text{CH}_2\text{O} \rightarrow \text{CH}_2\text{OH} \rightarrow \text{CHOH} \rightarrow \text{CH} \rightarrow \text{CH}_2 \rightarrow \text{CH}_3 \rightarrow \text{CH}_4$
5) $\text{CO}_2 \rightarrow \text{CHOO} \rightarrow \text{CHO} \rightarrow \text{CHOH} \rightarrow \text{CH} \rightarrow \text{CH}_2 \rightarrow \text{CH}_3 \rightarrow \text{CH}_4$
6) $\text{CO}_2 \rightarrow \text{COOH} \rightarrow \text{COH} \rightarrow \text{CHOH} \rightarrow \text{CHO} \rightarrow \text{CH} \rightarrow \text{CH}_2 \rightarrow \text{CH}_3 \rightarrow \text{CH}_4$
Fe-decorated Ni (111)
1) $\text{CO}_2 \rightarrow \text{CHOO} \rightarrow \text{CHO} \rightarrow \text{CH}_2\text{O} \rightarrow \text{CH}_2 \rightarrow \text{CH}_3 \rightarrow \text{CH}_4$
2) $\text{CO}_2 \rightarrow \text{CHOO} \rightarrow \text{CHO} \rightarrow \text{CH} \rightarrow \text{CH}_2 \rightarrow \text{CH}_3 \rightarrow \text{CH}_4$
3) $\text{CO}_2 \rightarrow \text{CHOO} \rightarrow \text{CHO} \rightarrow \text{CH} \rightarrow \text{C} \rightarrow \text{COH} \rightarrow \text{CHOH} \rightarrow \text{CH}_2\text{OH} \rightarrow \text{CH}_2\text{O} \rightarrow \text{CH}_2 \rightarrow \text{CH}_3 \rightarrow \text{CH}_4$
4) $\text{CO}_2 \rightarrow \text{CHOO} \rightarrow \text{CHO} \rightarrow \text{CH} \rightarrow \text{C} \rightarrow \text{COH} \rightarrow \text{CHOH} \rightarrow \text{CH}_2\text{OH} \rightarrow \text{CH}_2 \rightarrow \text{CH}_3 \rightarrow \text{CH}_4$

Table 2.10: Numbering convention for the background oxygen. N_O is the number of oxygen atoms on the nickel surface. A zero in the column of any chemical species states that it is not present in the background, conversely a one indicates that it is. The Dec column reports the decimal value of the binary string associated with the background species.

N_O	2 H ₂ O	H ₂ O	2 OH	OH	2 O	O	Dec
0	0	0	0	0	0	0	0
1	0	0	0	0	0	1	1
1	0	0	0	1	0	0	4
1	0	1	0	0	0	0	16
2	0	0	0	0	1	0	2
2	0	0	0	1	0	1	5
2	0	0	1	0	0	0	8
2	0	1	0	0	0	1	17
2	0	1	0	1	0	0	20
2	1	0	0	0	0	0	32

Before moving on, there are some things that need to be defined when considering the background species: i) an elementary step between two main species that have the same amount of oxygen does not involve a change in the background; ii) conversely, an elementary step between two main species that do not have the same amount of oxygen does involve a change in the background; and iii) water can irreversibly desorb since in flow conditions the produced water is constantly replaced by new reactant, thus implying that some transitions from a background to another are irreversible. Figure 2.89 reports the rules associated to these points.

Thus, with the additional consideration that the water desorption process is irreversible, main species containing two oxygen atoms have only one possible background, species with one oxygen have four, while those without oxygen have ten possible backgrounds. This way, it is possible to draw a graph like the one shown in figure 2.90, where the main species are intended as groups of vertices, each of which corresponding to a pair (main species, background). It should be noted that, in this graph, the steps associated with the desorption of a water molecule are indicated with an arrow since they are directed edges: this way, the findPaths algorithm can follow them in the correct direction. The goal is to go from CO₂(0) to CH₄(0), i.e. a methane molecule with no oxygen in the background since it leaved in the form of water. The search for the paths is performed by using the version of Pathgen that works with groups of vertices (following the rules outlined in

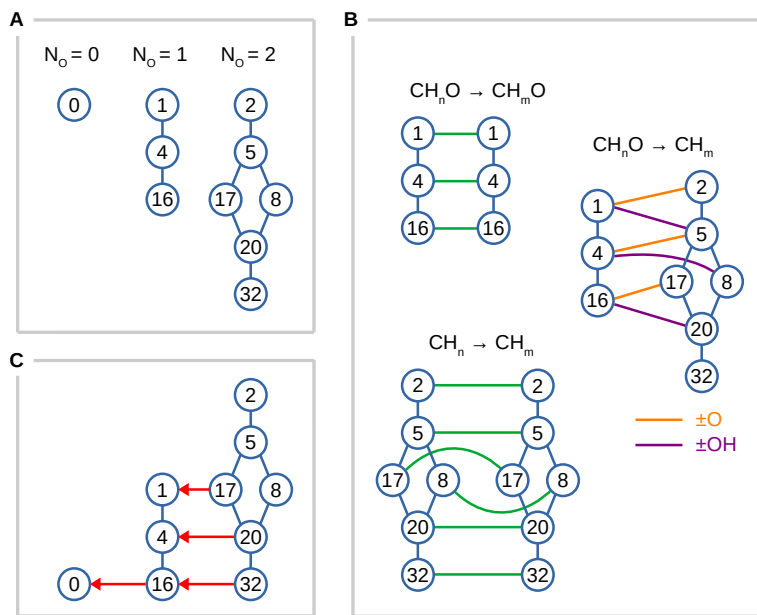


Figure 2.89: Rules to connect: A) backgrounds within each set; B) two main species having same/different backgrounds; C) different sets of backgrounds due to irreversible water desorption.

the previous section).

The resulting calculation was really intensive: the graph, composed of 85 vertices and 202 edges, contains more than 31 billion paths on the vertices, divided in 1122 paths on the groups (i.e. paths on the main species). An SCM was carried out for each of them, and the results grouped so that each one contributed to the correct mechanism (i.e. path on the groups). Once this investigation was concluded, it was observed that: i) at 900 K the fastest mechanisms are very close one another, to the point that starting from the 116th in the ranking, mechanisms are more than 100 times slower than the first one; ii) s^g at 900 K is about two orders of magnitude smaller than that obtained without the explicit treatment of background species; iii) E_{app} is ~ 15 kJ/mol higher than the one obtained without backgrounds; iv) the fastest mechanism at 900 K ($\text{CO}_2 \longrightarrow \text{COOH} \longrightarrow \text{COH} \longrightarrow \text{C} \longrightarrow \text{CH} \longrightarrow \text{CHOH} \longrightarrow \text{CH}_2\text{OH} \longrightarrow \text{CH}_2\text{O} \longrightarrow \text{CH}_2 \longrightarrow \text{CH}_3 \longrightarrow \text{CH}_4$) is not among the fastest ones obtained when the methanation process is investigated without the background species, moreover it involves atomic carbon.

2.11 Conclusion

In this chapter, the elementary steps involved in the CO_2 methanation process were presented. These were investigated on three different catalytic surfaces, reporting the results of the CI-NEB calculations performed through the Empathes package. This way, a knowledge of both the structures and the energies of the involved transition states was acquired, thus obtaining a list of activation energies that have been later used within a kinetic model. Some other processes were also investigated, such as: 1) the hopping of H, C, and O atoms on the surface; 2) the migrations of the H, C, CH, CH_2 and CH_3 species from the decoration (both Ru and Fe) to the pristine nickel surface; and 3) the two consecutive steps involved in the formation of water: $\text{O} + \text{H} \longrightarrow \text{OH}$ and $\text{OH} + \text{H} \longrightarrow \text{H}_2\text{O}$. This last point is important because water is produced in the methanation process $\text{CO}_2 + 4 \text{H}_2 \longrightarrow \text{CH}_4 + 2 \text{H}_2\text{O}$, especially when this is performed in an environment rich in H_2 .

Some elementary steps on pristine and Ru-decorated nickel surfaces were also investigated applying an external electric field (EEF), thus probing what chemical species are mostly affected by this perturbation, and how it influences the reaction energetic in terms of both ΔE_r and activation energy. The observed trend was that the oxygen-containing species have an higher response to the external electric field, showing a greater variation of the energetic values going from negative to positive EEFs. On the other hand,

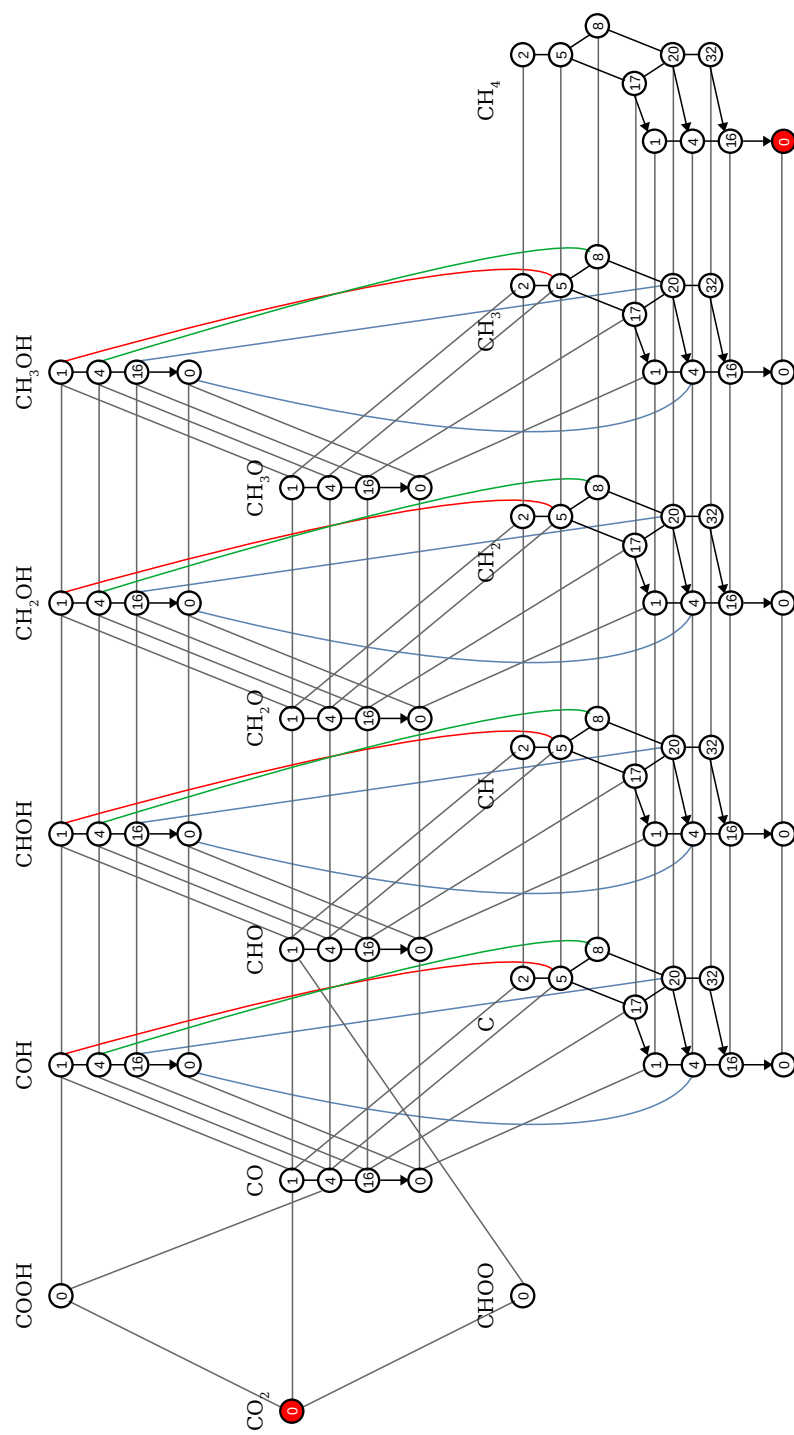


Figure 2.90: Graph used for the methanation process with background species. Paths searched from $\text{CO}_2(0)$ to $\text{CH}_4(0)$. Colored edges are used only to facilitate viewing.

those species constituted only by carbon and hydrogen atoms are mostly not affected by an EEF, being both ΔE_r and activation energy very similar to the ones obtained without it. This can easily be explained in terms of polarity: the larger the electric dipole moment of a species, the stronger its interaction with an external electric field. In particular, one of the most sensitive steps was found to be $\text{CO} + \text{H} \longrightarrow \text{CHO}$, in which a positive EEF decreases the activation energy of the forward reaction while increasing that of the backward reaction.

The computed activation energies were used in the kinetic model given by the Simplified Christiansen Method (SCM) in order to obtain the apparent activation energy for the methanation process on the three tested catalysts. This method, however, was not meant to work with such an intricate network of chemical species and elementary steps like the one presented here: it needs a linear path that goes from reactant to product, in which there can be any number of intermediates. For this reason, it was first necessary to search all the possible paths that connect CO_2 to CH_4 , and then to analyze them individually through SCM. These single results were finally combined to get the global reaction rate of the process. By executing many SCM analysis at different temperatures, one gets a series of reaction rates that can be used to fit the Arrhenius equation, thus obtaining the apparent activation energy for each catalyst model. Despite it is not simple to compare these values with the experimental ones (since the former are obtained using a series of computational methods, namely DFT, CI-NEB and SCM, each of them bringing its assumptions and hence approximations), they can still be compared with each other: this shows that the Ru-decorated system is more active to the methanation process than the pristine surface, which in turn behaves better than the Fe-decorated one. It is worth noting, however, that the decorated systems are very “stiff” since in this computational model all elementary steps occur next to the decoration, while in a real world scenario it is absolutely possible that some steps take place next to the decoration, while others may happen on the nickel (111) portion of the catalyst. If considered, these additional degrees of freedom may have the effect to reduce the apparent activation energy of the decorated systems. This could be an idea for further investigations on this subject.

Chapter 3

Halloysite Carbon-Coating

3.1 Introduction

3.1.1 Li–O₂ Batteries

Since their first appearance in 1996 [50], the Li–O₂ batteries have received an ever increasing interest by the scientific community due to their high theoretical energy density, that makes them suitable for intensive applications such as electric vehicles. There are, however, some technical difficulties that must be solved before these systems can be applied in real life devices. One should overcome, for instance: low power density, high charge overpotentials, and low stability to charge-discharge cycles.

A Li–O₂ device has a lithium metal anode, a liquid or solid state electrolyte, and a cathode, that is a more complex device composed by a supporting material and an active material. The cathodic active material are the O₂ molecules, that are found in the atmosphere and must travel through the supporting material to come into contact with the electrolyte. The supporting material should then be porous, to let O₂ to diffuse, and catalytic, since it must be suitable for both the oxygen reduction reaction (ORR) occurring in the discharge phase, and for the oxygen evolution reaction (OER), occurring during recharge. The main product of the discharge reaction is Li₂O₂, but other lithium oxides, such as LiO₂ and Li₃O₄, have been reported in the literature [51]. When the cathode is fully covered in Li₂O₂ the spontaneous ORR stops, and the battery is completely discharged.

One of the most studied problem is how to effectively remove Li₂O₂ from the cathode surface. Since Li₂O₂ is a non conductive material, large agglomerates imply high overpotentials to revert them, hence a low electric efficiency. It is known that Li₂O₂ morphology is highly correlated to the ease of its decomposition. The two predominant forms [52, 53] of the this oxide

are micrometric size toroids (that grow toward the solution), and nanofilms (that grow on the cathode surface). While the latter are easy to remove (especially if thinner than 10 nm), the former are generally tougher, hence undesirable.

Tailoring the cathode properties in order to achieve the desired Li_2O_2 morphology is one of the most studied aspect of the Li– O_2 batteries. Among the investigated materials there are: natural and doped (N, B) graphene [54]; Co nanoparticles anchored on porous carbon nanosheets [55]; BC_3 and NC_3 nanosheets [56]; Co_9S_8 , a material similar to an agave plant with an high specific surface area [57]; Co_4N nanorod on carbon nanofibers [58]; N-doped nanocages [52]; N-doped carbon nanofibers, coated with TiO_2 , which in turn is covered with Ru nanoparticles [59]; cracked carbon sub-micron tubes, decorated with Au nanoparticles in the inner wall [60]; RuO_2 on carbon nanotubes (CNTs) [53]; CNTs decorated with Pd, Pt, Ru and Au nanoparticles inside and outside the nanotube lumen [61].

A particularly attractive idea, reported in some of the cited articles, is to delimit an area where Li_2O_2 can grow. This is done using chemical structures that have cavities, such as the aforementioned carbon nanotubes.

3.1.2 HNTs Applied to Electrochemical Systems

Halloysite is a 1:1 aluminosilicate and its crystal structure can be described as a layer composed by two building blocks: SiO_4 tetrahedra and AlO_6 octahedra, with stoichiometric formula $\text{Al}_2\text{Si}_2\text{O}_5(\text{OH})_4 \cdot 2\text{H}_2\text{O}$. It is a clay mineral belonging to the kaolinite group, occurring in nature with platy, spheroidal, or hollow tubular shape. The dominant morphology is the multi-walled tubular one (HNT), with sizes between 500 and 1000 nm in length and 15-100 nm in inner diameter. A spiral-like structure could be clearly imaged by electron microscopy experiments [62, 63]. Thanks to its peculiar shape, halloysite is considered a promising entrapment system for the loading, the storage, and the controlled release of several species [64, 65]. Moreover, these clay materials are economically viable and environmentally friendly and, for this reason, competitive with other tubular systems as carbon, polymeric, metal, or metal oxide nanotubes.

Halloysite has an intriguing structure for the purpose of confinement, but unfortunately it is not conductive. There are, however, some reported applications of HNTs to electrochemical systems. As cathodes, HNTs are used predominantly in Li–S cells, where they are firstly made conductive (towards a procedure of adsorption of an organic precursor followed by a pyrolysis), and then applied on top of the cathode in order to catch and trap lithium polysulfides nanoparticles [66, 67, 68, 69]. In other studies, they are

used as solid polymer electrolytes [70, 71] and gel polymer electrolytes [72], and as membranes [73].

There are then several studies in which HNTs are used as templates (and sometimes they are not even removed) to: form N-doped carbon nanotubes [74], grow porous carbon nanoparticle used in Li-ion [75], grow MoS₂ used in Zn-ion [76]. Other times HNTs are simply selectively functionalized and then used [77, 78]. Therefore their use in electrochemical systems does not seem impossible.

3.1.3 Purpose of the Study

From current knowledge, there are no reports in the scientific literature about the application of HNT-based material to Li-O₂ batteries. HNTs have the general advantage of being inexpensive and eco-friendly, furthermore their internal structure could prove extremely useful to confine Li₂O₂, if it could be exploited.

As reported in many works, HNTs can be made conductive after the adsorption of organic molecules followed by pyrolysis [66, 67, 68, 69]. The choice of the organic precursor has an influence on the final coating material, which can be a mere or doped carbon film. In the latter case, the hetero atoms could offer a better nucleation site than the carbon one, potentially affecting the growth mechanism of Li₂O₂.

It is in this context that this investigation develops. There is a significant amount of preliminary work that must be accomplished to answer the question about the suitability of HNTs as a cathode material for Li-O₂ cells. The first step is the investigation of the carbon-coating process of HNTs, since there is a lack of computational studies on this subject. The coating can happen, at least in principle, on both the inner and outer surfaces. Structures of HNTs covered on the inner wall with a carbon layer can be used to demonstrate if lithium oxides are more likely to grow here or inside a clean halloysite nanotube; while HNTs carbon-coated on the outer wall can give insights about the development of electrical conductor behavior. The carbon-coating phenomenon can be explored in, at least, the following ways:

- Sequential adsorption of carbon atoms, to simulate an amorphous carbon coating.
- Adsorption of aromatic compounds, like benzene molecules and graphene fragments, to simulate a structured carbon coating.

The carbon-coating of the outer halloysite surface, the silicic layer, was chosen as the subject of this investigation. This is commonly performed

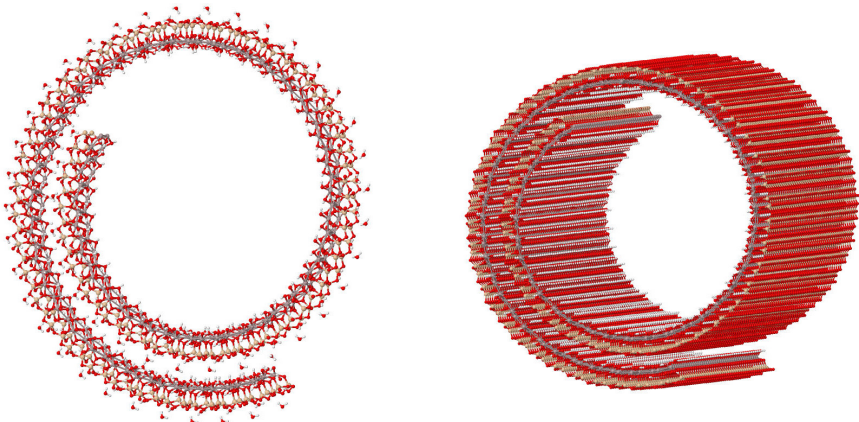


Figure 3.1: The unit cell for a HNT model with one-third overlapping arms (left) and a portion of the corresponding nanotube (right).

experimentally, but the details at the atomic scale, about what is really happening and how, are missing. Such a study is therefore aimed to bring insights about the structure of carbon-coated HNTs and their behavior as conductors. Considering the public interest due to their applicability as electrodes, this study is the preliminary step required to investigate their suitability in specific electrochemical systems, such as the Li–O₂ cell where they have not been applied so far. Halloysite would be a good candidate as cathode material if, thanks to its nanotubular structure, it could address the growth of the discharge products inside its lumen only.

3.2 Computational Details

The program of choice for this investigation was Gaussian 16. The chemical systems were studied using the Density Functional Theory, with M06L exchange-correlation functional [79] and SVP basis set.[80] The Density Fit technique was used in order to save computational time on coulomb bielectronic integrals; the auxiliary basis functions used for this purpose were automatically generated by Gaussian 16 starting from those of the main basis set. All structures were optimized in the singlet spin multiplicity. Finally, due to the system size the calculations of vibrational frequencies (useful for determining if the optimized molecular geometry was a real minimum on the potential energy surface, a transition state, or something else) were not performed.

The model of an halloysite nanotube of 5 nm in diameter, reported in figure 3.1, was obtained by replicating along the tube axis a spiral supercell built and relaxed as described in the paper by Ferrante et al.[81] In this process, the experimental value of 5.2 Å was applied along the repeating direction. This model was already used in some computational studies in our group.[82, 83, 84]

Three different models of halloysite surfaces were derived from a portion of the arm of the spiral nanotube model previously discussed, these are: pristine (258 atoms), substituted (264 atoms), and Si-vacant (261 atoms). The substituted surface of halloysite can be obtained via hydroxyl substitution in alkaline solution; if this process is further performed, it can cause the complete elimination of a $\text{Si}(\text{OH})_4$ molecule, which is the origin of the Si-vacant surface considered in this study. Since halloysite is a nanotube, the said structures are slightly curved: this characteristic has been preserved maintaining the most external H and O nuclei fixed in their position during geometry optimizations. One can be confident that this stratagem does not affect the general conclusions of the investigation, since local deformations on inner or outer surfaces of the nanotube should not distort its whole geometry sensibly. Figure 3.2 shows the three silicic HNT surfaces considered in this study; the convention adopted in this work for the top view is that the lower aluminum layer protrudes on the left side.

In order to model the carbon-coating process (experimentally performed in an high temperature, carbon-rich environment), the carbon atoms were added one at the time, near specific sites of the halloysite surface. The general working method was: i) take a surface with n C atoms, with $n = 0, 1, \dots$, ii) add a new C atom on interesting sites, iii) optimize all the geometries obtained in the previous step, iv) select the more stable geometry of the batch as the starting point for the next carbon atom, v) repeat. At each iteration of the working cycle, for all three HNT surface models, there are six halloysite sites on top of which a carbon atom is always put. These are the six most central silicon atoms (enumerated in figure 3.3), the only exception being the Si-vacant surface, in which one of these starting structures has the carbon on top of the vacancy. Moreover, additional sites are also taken into account if they seem promising candidates to host carbon.

In order to lighten the following sections, an appropriate notation is now introduced to indicate the studied structures. Each optimized structure is stated by a string of characters, such as this one: P4C03. The first character “P” denotes the starting HNT surface and so it can have three different values: P, S, or V for pristine, substituted and Si-vacant, respectively. The next two characters “4C” state how many carbon atoms where added to the original structure (four in this example). Finally, the last two characters

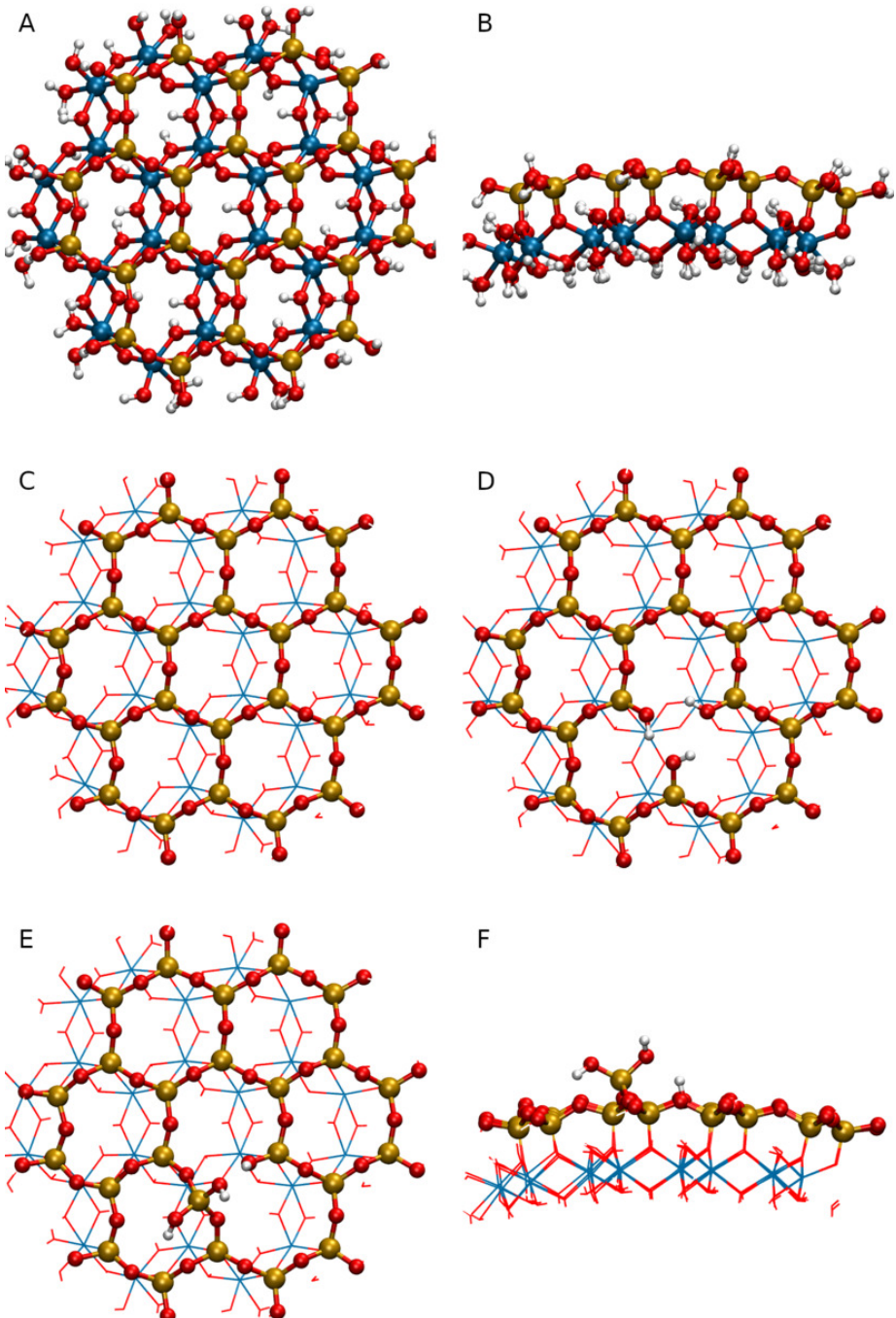


Figure 3.2: Models of HNT surface. A,B) pristine, top and side view; C) pristine, Si-layer; D) Si-vacant, Si-layer; E,F) substituted, Si-layer, top and side view. Colors: H white; O red; Al blue; Si gold.

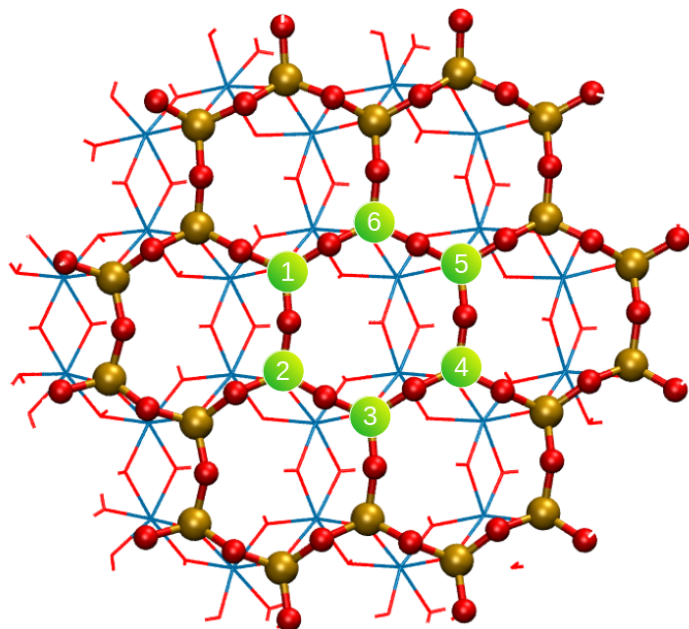


Figure 3.3: The six sites where a new carbon atom is always put. This image shows the pristine HNT surface, but the same numbering order is also used for the other two surfaces. Colors: H white; O red; Al blue; Si gold.

“03” identify the structure itself: when the number is in the inclusive range 01,...,06 it means that the un-optimized geometry had the last-added carbon on top of the corresponding silicon of figure 3.3; while for numbers greater than 06 there is not a general rule, so a description of the starting geometry before optimization will always be provided.

3.3 Pristine Halloysite Surface

In this section, all the investigated structures obtained from the pristine halloysite surface model, covered with up to ten carbon atoms, are discussed. Tables A.1, A.2 and A.3, in the appendix, report the final energy and a quick recap comment for each of them.

1st Carbon When choosing where to place the first carbon atom on the pristine HNT surface, there are some considerations that can be done. If the curvature of the model was not taken into account, then all Si atoms would be symmetry equivalents. Let’s now consider the three oxygen atoms bonded to each Si: by joining them with imaginary lines, a triangle is obtained. If a C atom is then positioned not exactly on top of Si, but rather slightly in the direction of one of the sides of the said triangle, then we get three different structures that are not symmetry equivalents (due to the staggered aluminum layer below). Following these considerations, only four different structures were chosen for this investigation. These are: P1C06, where C is exactly on top of Si6; P1C01, with a carbon on top of Si1, slightly moved towards the center of the HNT model; P1C03, that has a C atom on top of Si3, slightly moved towards the center of the surface; and P1C05, where C is on top of Si5, once again slightly moved towards the center of the structure.

The four optimized geometries thus obtained are very similar: in all cases, the added carbon atom snags between a silicon and an oxygen, breaking a Si–O bond, and forming two new bonds: Si–C and C–O. This kind of intercalation is a common behavior that in this investigation has been observed whenever the carbon is next to a non-defective site of the halloysite (in all three pristine, substituted, and Si-vacant models). The P1C03 structure is the most stable of the batch, whereas P1C01 has a slightly higher absolute energy: 12.2 kJ/mol more with respect to P1C03. On P1C03, carbon and oxygen form a bridge between two Si nuclei on the HNT surface; whereas on P1C01, the carbon points to an hydroxyl group of the aluminum layer below the surface, as explicitly shown in figure 3.4. Being so similar in energy despite the different carbon orientation, both P1C03 and P1C01 were used as starting geometries to investigate the preferred placement of a second

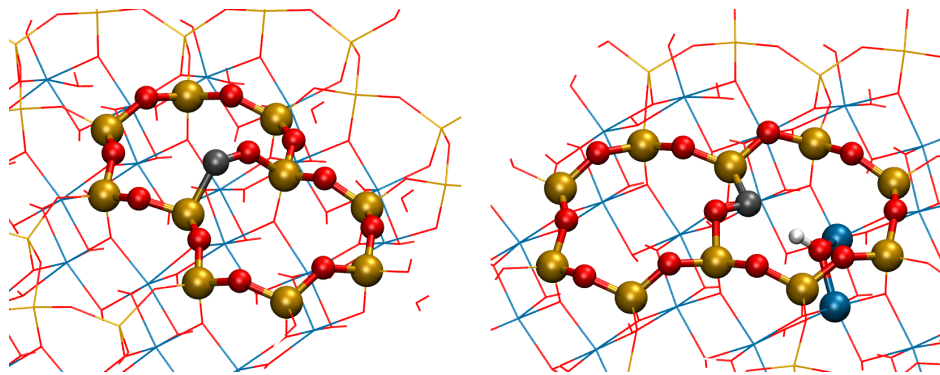


Figure 3.4: Optimized geometries of P1C03 (left) and P1C01 (right). Colors: H white; C black; O red; Al blue; Si gold.

carbon atom (this being the only exception to the working method presented previously).

2nd Carbon A total of twelve structures with a second carbon atom where prepared, six from both P1C03 and P1C01. They are named, respectively, from P2C31 to P2C36, and from P2C11 to P2C16, where the first digit after the “P2C” prefix refers to the starting geometry they were generated from (3 for P1C03, 1 for P1C01), and the last digit indicates in which position the additional carbon atom was placed (as in figure 3.3).

After optimization, P2C32 turned out to be the most stable structure among the twelve, while P2C13 was the most stable among those generated from P1C01, being 56.2 kJ/mol higher than P2C32. As figure 3.5 shows, they have similar geometries: in both cases the two carbon atoms are bonded together and with an oxygen, forming a three-atoms bridge between two adjacent Si on the HNT surface. In P2C32 this bridge is straight, whereas in P2C13 it is at an angle. Because of its lower total energy, P2C32 was chosen as the starting geometry in which to add a third carbon atom. Sorting these twelve structures by increasing energy, all the first six on the list have the two carbon atoms bonded together, while in the last six they are far apart. Furthermore, the energy differences with respect to the most stable structure are also thrilling: P2C11, the sixth in the ranking, is 226.9 kJ/mol above P2C32; while the last six positions detach on average for an outstanding ~ 600 kJ/mol.

3rd Carbon The third carbon atom was placed on seven different sites of the P2C32 structure. Other than the usual ones from P3C01 to P3C06, there is P3C07 in which the additional carbon is above the other two in a

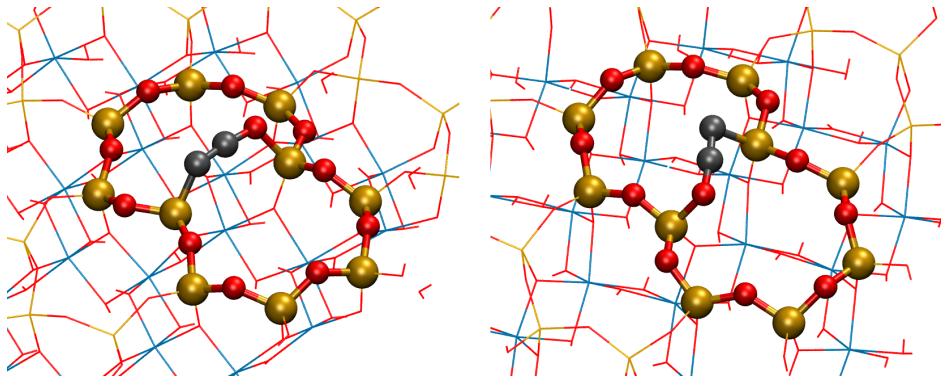


Figure 3.5: Optimized geometries of P2C32 (left) and P2C13 (right). Colors: H white; C black; O red; Al blue; Si gold.

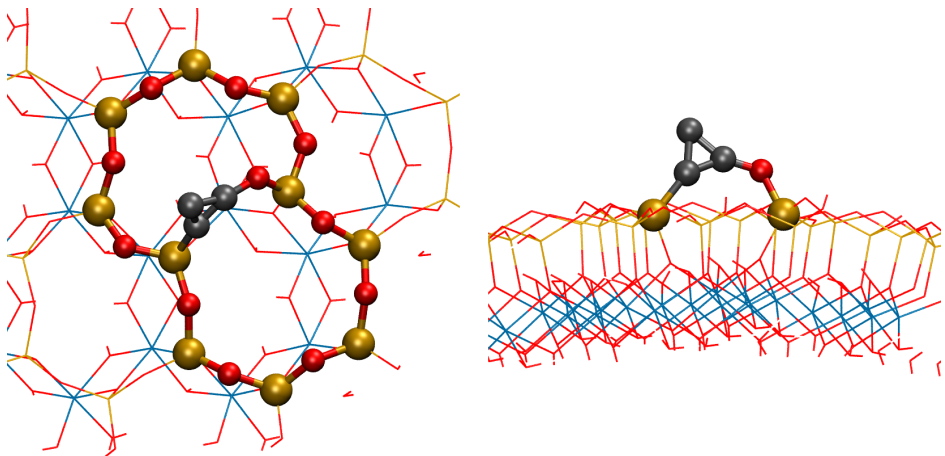


Figure 3.6: Optimized geometry of P3C07, top and side views. Colors: H white; C black; O red; Al blue; Si gold.

triangular fashion.

Once all the structures were optimized, P3C07 was found to be the most stable. Its final geometry, reported in figure 3.6, does not differ much from the initial guess, since the original triangular carbon ring is maintained. Both the second and third most stable structures, respectively P3C04 (85.9 kJ/mol higher than P3C07) and P3C03, have the third carbon bonded to the first two, in the shape of a triangular ring the former, and of a straight line the latter. Then there are P3C05, P3C06, and P3C01, in which the third carbon atom is on a clean part of the surface, not directly connected to the others. Lastly there is P3C02, in which C snagged between a Si and an O on the surface like in the three previous structures, but unlike them here the carbon is also closer to the other two.

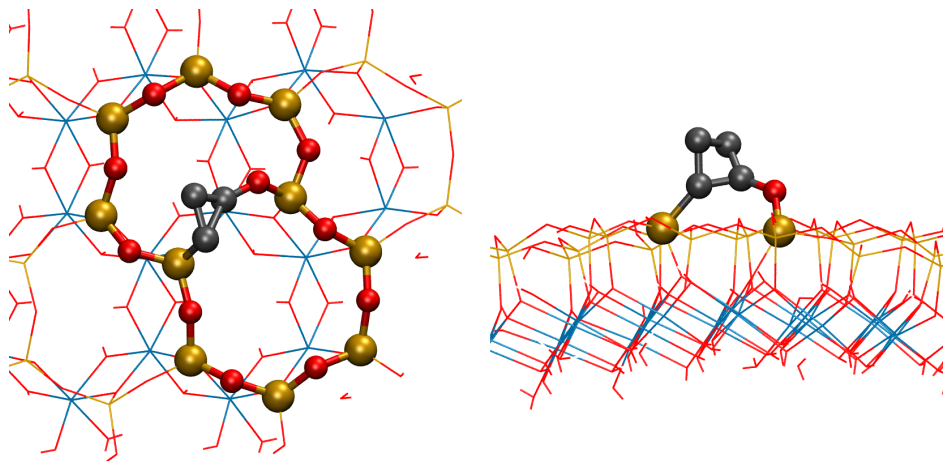


Figure 3.7: Optimized geometry of P4C03, top and side views. Colors: H white; C black; O red; Al blue; Si gold.

4th Carbon Starting from the most stable geometry of the previous paragraph, P3C07, the fourth carbon was added, thus preparing eight different guess geometries for optimization. Other than the notorious six from P4C01 to P4C06, there are: P4C07, with the additional carbon placed on the top vertex of the carbon triangle; and P4C08, where it was added on the side of that carbon structure.

Optimization of these starting geometries shows that the one obtained from P4C03 is the most stable. As reported in figure 3.7, its structure presents a square of carbon atoms (not appreciable from the top view) anchored to the HNT surface in two points, namely to an oxygen and a silicon. Optimization of both P4C07 and P4C08 gave back virtually the same result: a structure very similar to the initial guess of P4C07, with the new carbon bonded to a vertex of the carbon triangle. With equal merit, these structures are second in the ranking at 17.3 kJ/mol more than the first place. In third and fourth position there are P4C04 and P4C02, respectively. In the former the fourth carbon is near the other three, but it does not make a direct bond with them. The P4C02 optimized structure, however, has the four carbon atoms bonded together, furthermore the new C also makes a bond with Si2. This kind of interaction, however, is probably very weak due to the fact that Si2 forms five bonds. Finally, the three least stable geometries, in order P4C05, P4C06, and P4C01, are those where the fourth carbon is far away from the other three, making a Si–C–O bond with the HNT surface.

5th Carbon The fifth carbon was added on the P4C03 structure. Nine different structures were prepared for optimization, they are: from P5C01 to

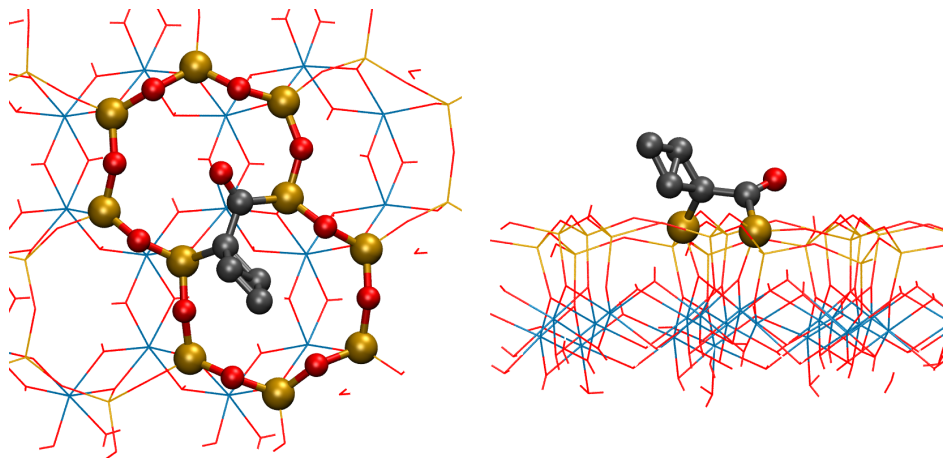


Figure 3.8: Optimized geometry of P5C04, top and side views. Colors: H white; C black; O red; Al blue; Si gold.

P5C06, the additional carbon was placed on top of the most central silicon atoms; in P5C07 it was positioned next to a vertex of the preexisting carbon square; in P5C08 it was placed over the face of the square; and, finally, in P5C09 the fifth carbon was positioned next to a side of the square, close to the anchoring oxygen.

Sorting the optimized structures by increasing total energy points out that P5C04 is the most stable. Its geometry, reported in figure 3.8, shows that the fifth carbon, originally on top of Si4, rips off the near oxygen from its silicon, and then bonds directly to the preexisting carbon structure. As a final result, two carbon atoms anchor the HNT surface through Si3 and Si4. Next, the starting geometries of P5C02 and P5C07 both fell in the same minimum of the potential energy surface. Their optimized structure, that is 65.5 kJ/mol less stable than P5C04, shows that the fifth carbon rests on a side of the original carbon square. In order of increasing energy there are: P5C09, P5C08, and P5C03, that have all five carbon atoms bonded together; and P5C05, P5C06, and P5C01, in which the fifth carbon is near a clean portion of the HNT surface.

6th Carbon Using P5C04 as starting point, the sixth carbon atom was added in nine different sites: from P6C01 to P6C06 it was placed above the corresponding Si; on P6C07 the new carbon was over a vertex of the original carbon square; in P6C08 it was put above the square face; and finally in P6C09 it was bonded to the protruding oxygen atom.

The results obtained from geometry optimizations state that P6C04 is the most stable structure. Here, as shown in figure 3.9, all six carbon atoms are

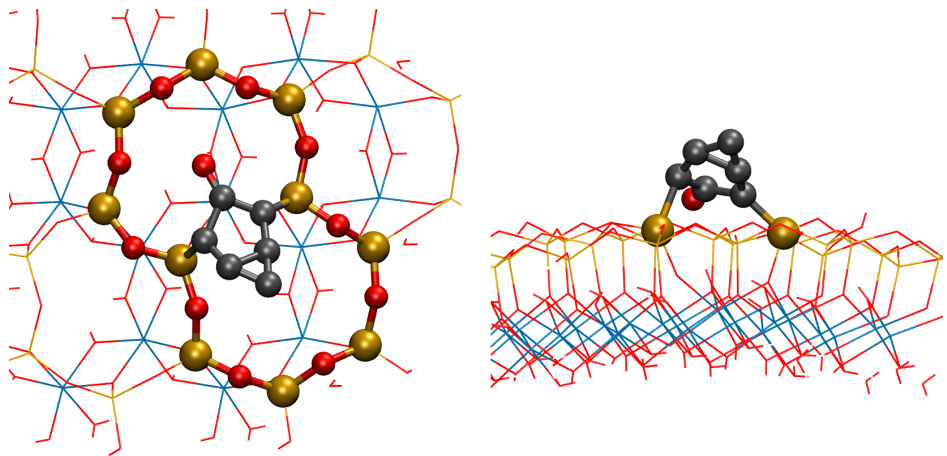


Figure 3.9: Optimized geometry of P6C04, top and side views. Colors: H white; C black; O red; Al blue; Si gold.

bonded together, forming two fused rings. Moreover, two carbons anchor the HNT surface on Si3 and Si4, while another one is bonded to a oxygen (the one originally bridged between the said silicon atoms). Structure P6C07 got the second place for stability, placing itself 143.7 kJ/mol higher than P6C04. Then, sorted by increasing energy, there are: P6C03, P6C02, P6C08, and P6C09, in which the sixth carbon is either directly bonded to the preexisting ones, or very close to them; and P6C05, P6C06, and P6C01, in which it is on a clean part of the HNT surface.

7th Carbon Also in this case, nine structures were prepared starting from P6C04. The geometries named from P7C01 to P7C06 were built in the usual way; in P7C07, C is bonded to the oxygen of the existing carbon structure; P7C08 has the additional carbon on top of the others; and finally, in P7C09, it was placed above the five-membered carbon ring.

The optimization process found the same energy minimum for both P7C04 and P7C03. The resulting geometry, reported in figure 3.10, shows that the seven carbon atoms are bonded contiguously: there is still a five membered ring (like in P6C04), but here it is a single carbon that anchors the surface on both Si3 and Si4. The other two carbon atoms are bonded to two different sides of the main ring, while the oxygen is still bonded to a vertex of it. At 35.3 kJ/mol more, the second place for stability goes to P7C08, whose optimization found once again a structure where all carbon atoms are bonded together. The third place is atypical, since it belongs to P7C05, the starting geometry of which generally ends up in the last positions. As usual, the seventh carbon in P7C05 performed an intercalation between Si and O

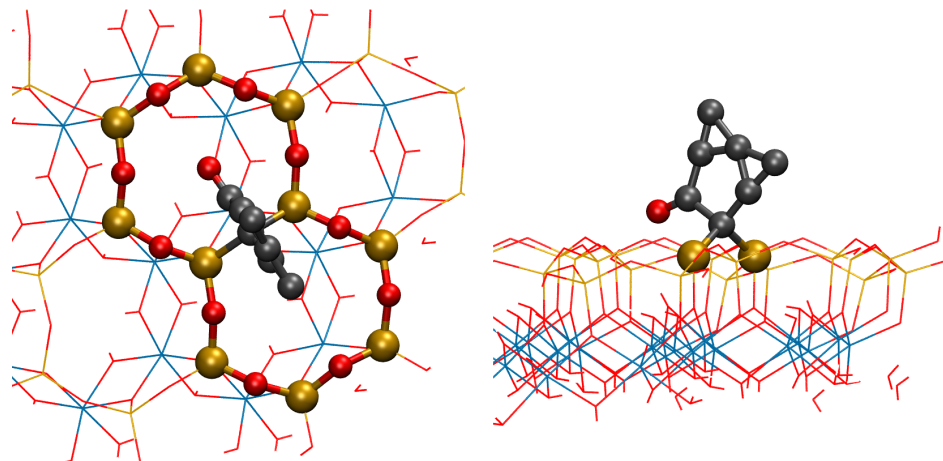


Figure 3.10: Optimized geometry of P7C04, top and side views. Colors: H white; C black; O red; Al blue; Si gold.

on the HNT surface, but this time it also bonded the preexisting carbon structure, thus acting as a further anchoring point. Then P7C09, P7C02, and P7C07 follow, where the additional carbon bonds the others generating multiple rings; and P7C06 and P7C01 in which it is on the clean part of the surface, far away from the others.

8th Carbon Using P7C04 as a basis, eleven structures were prepared inserting an additional carbon atom. As usual, from P8C01 to P8C06 the new carbon was placed on the six central sites; in P8C07 it was bonded to the oxygen; while in P8C08 and P8C09 it was placed on two different sites over the carbon structure; and finally in P8C10 and P8C11 the additional carbon was positioned above both faces of the five-membered carbon ring.

Optimizations show that the most stable structure, by a large amount, is the one obtained from P8C09. Unfortunately, here all eight carbon atoms are bonded one after another in a straight line perpendicular to the HNT surface, extending towards the void. Such a structure is not realistic. Moreover, it presented many difficulties during the optimization process. For these reasons, it has been discarded, and the next on the list, namely P8C08, has been chosen as the most stable of the batch. Its structure, reported in figure 3.11, shows a central six-membered carbon ring that bonds the HNT surface through a single vertex, whose adjacent carbon still keeps its oxygen. The remaining two carbon atoms are bonded to two different sides of the main ring.

The second place is earned by P8C03, at only 13.3 kJ/mol more, followed by P8C04, P8C11 and P8C10. In all four structures the carbon atoms are

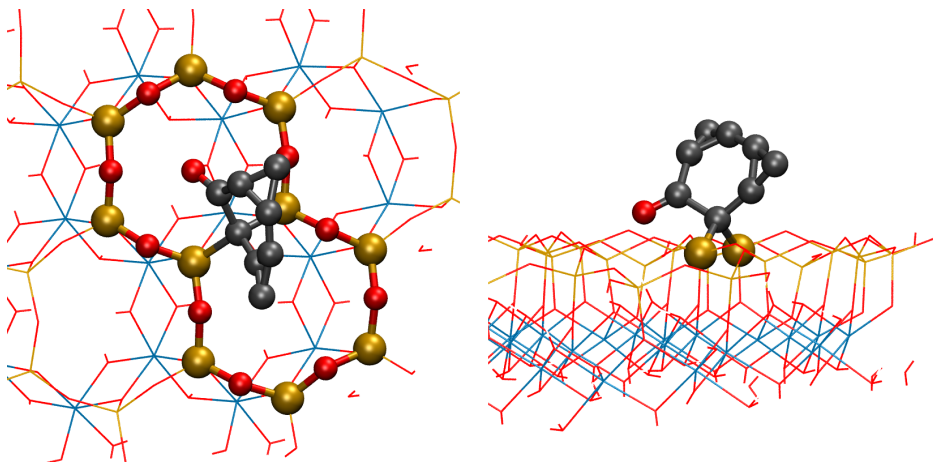


Figure 3.11: Optimized geometry of P8C08, top and side views. Colors: H white; C black; O red; Al blue; Si gold.

bonded together, generating fused rings. Moreover, it is appropriate to note that P8C10 and P8C11, despite starting with the eighth carbon on opposite faces of the main ring, both fell on the same energy minimum after optimization. Follow: P8C07, in which the additional C stays bonded to O; and P8C06, P8C02, P8C05 and P8C01, in this order, where the new C is on the clean part of the surface. It is noteworthy that, in P8C02, the eighth carbon also bonds the others, thus acting as further anchoring point for the agglomerate.

9th Carbon Starting from P8C08, ten structures were prepared adding a further carbon. Geometries named from P9C01 to P9C06 are built in the usual way; in P9C07, the new atom was placed over the top side of the main ring; while in P9C08, it is above its face; P9C09 has the additional carbon placed next to the oxygen; while in P9C10 it is bonded to another carbon that does not belong to the main ring.

The most stable geometry among all was the one obtained from P9C04, reported in figure 3.12, in which the optimization process altered substantially the initial guess. Here a seven-membered ring arises, in which two carbon atoms bond one silicon each (Si3 and Si4). Moreover, the main ring is still bonded to an oxygen (on a vertex) and two carbon atoms (on two different sides). Next there is P9C09 at 135.5 kJ/mol higher, where a CO molecule is produced. Four structures follow in which all nine carbon atoms are bonded together: P9C10, P9C07, P9C03 and P9C08. Finally, there are the geometries where the last added carbon is on the clean part of the surface, far away from the others, in order P9C06, P9C05, P9C02 and P9C01.

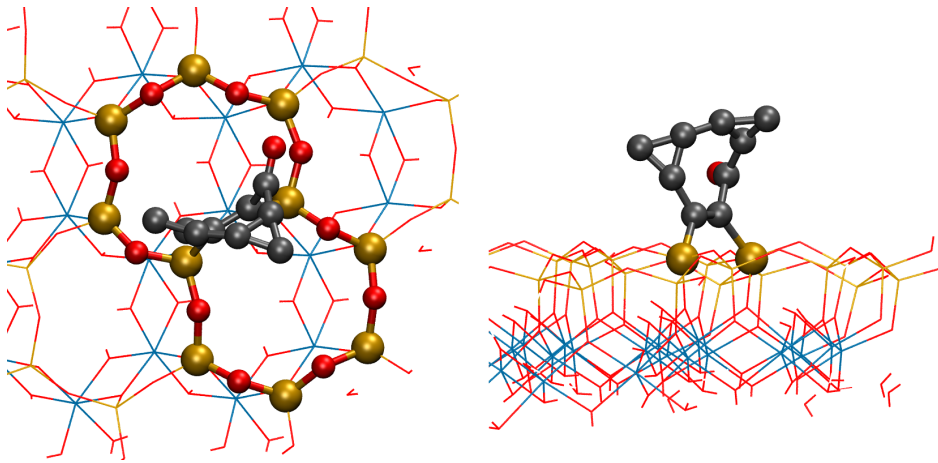


Figure 3.12: Optimized geometry of P9C04, top and side views. Colors: H white; C black; O red; Al blue; Si gold.

10th Carbon The tenth and last carbon was added to the P9C04 structure, generating a total of ten initial guesses. As usual, the geometries from P10C01 to P10C06 have the additional carbon over the six most central Si. In P10C07 it was placed on a ring side, the one farther from the HNT surface. In both P10C08 and P10C09, the tenth carbon was positioned in the center of the seven-membered ring, respectively in the top and lower halves; while in P10C10 it was next to the oxygen.

The most stable structure of the batch after optimization resulted to be P10C08. Its geometry, reported in figure 3.13, presents an elongated nine-membered carbon ring that bonds: an oxygen (on a vertex), a carbon (on a side), and the HNT surface on two different Si atoms. The second place for stability belongs to P10C07 (at 94.2 kJ/mol higher), followed by P10C03 and P10C09, all of the three having the ten carbon atoms directly bonded. Then there are P10C05 and P10C10, in which there is the formation of a CO molecule. The four last position are taken by P10C04 and P10C02, in which all carbon atoms are directly bonded forming multiple fused rings; and lastly P10C06 and P10C01, where the tenth carbon is on a clean part of the surface.

3.4 Substituted Halloysite Surface

In this section, all the investigated structures obtained from the substituted halloysite surface model, covered with up to ten carbon atoms, are discussed. Tables A.4, A.5 and A.6, in the appendix, report the final energy and a quick

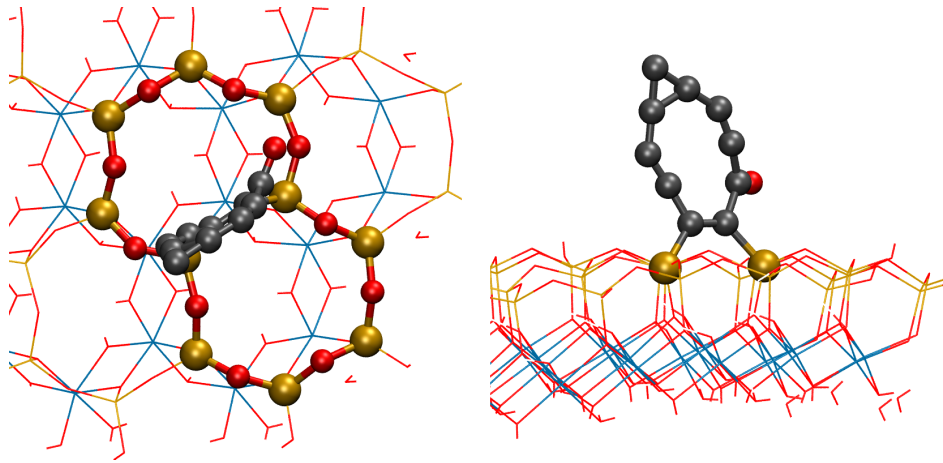


Figure 3.13: Optimized geometry of P10C08, top and side views. Colors: H white; C black; O red; Al blue; Si gold.

recap comment for each of them.

1st Carbon On the substituted HNT surface, eight different sites were investigated while looking for the preferred position of the first carbon atom. Structure from S1C01 to S1C06 are the ones where the guessed starting position of carbon is on top of the six most central silicons of the surface. S1C03 needs a special attention since Si3 is the defective one, bonded with two hydroxyl groups: in this case the carbon was initially put on top of Si3, between the two hydroxyl groups. In S1C07, the first carbon was placed at bond distance to the oxygen of the most central hydroxyl group. Similarly, in S1C08, the carbon was bonded to the oxygen of the most peripheral hydroxyl group. Both S1C07 and S1C08 were chosen for investigation because of the different orientation of the two hydrogens of the hydroxyl groups, that made the final positions of the carbon atom slightly different in the two case. Moreover, the carbon in S1C07 is closest to the defective portion of the surface than the one in S1C08.

Once all starting geometries were optimized, the most stable one turned out to be S1C02. Its structure, reported in figure 3.14, shows how the carbon subverted the original substituted HNT structure, putting itself between Si2 and Si3 in place of the oxygen, that in turn is now bonded exclusively to the carbon. The second in the ranking is S1C07, being only 5.2 kJ/mol higher than the first one, in which C leaves its initial position to bond the hydroxyl group on Si4. Then, in order of decreasing stability, there are: S1C03, S1C04, and S1C08, in which the carbon is somewhere around the defective site; and finally S1C06, S1C05, and S1C01, in which it is on a clean part of the surface.

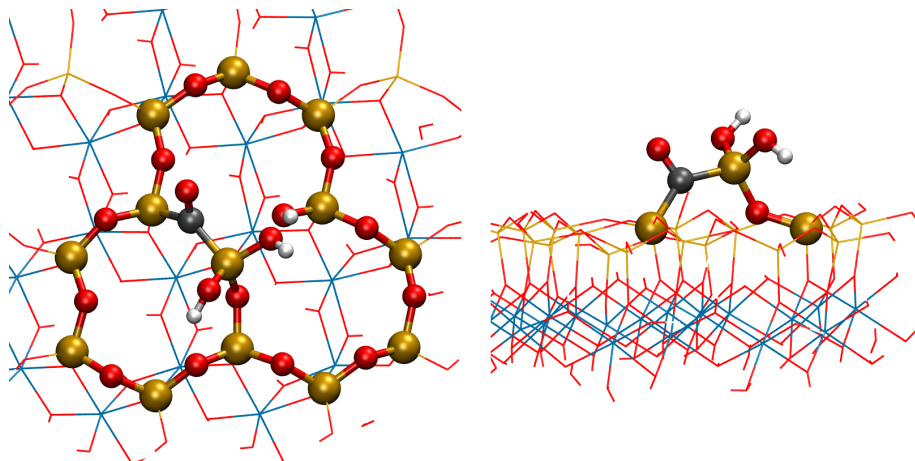


Figure 3.14: Optimized geometry of S1C02, top and side views. Colors: H white; C black; O red; Al blue; Si gold.

2nd Carbon Using the optimized S1C02 as the starting geometry, the second carbon atom was added on seven different sites. As always, from S2C01 to S2C06, there are the structures where the new carbon is put on top of the most internal silicons, while S2C07 starts with the carbon bonded to the oxygen of the hydroxyl group of Si3, the one nearest to the defect.

It is just this structure, the S2C07, that turns out to be the most stable after optimization. The resulting geometry, reported in figure 3.15, needs a short discussion because many things happened. The second carbon, originally put near the oxygen of the hydroxyl group, does three things: 1) it snatches the hydroxyl group from Si3; 2) it bonds the oxygen belonging to the near carbonyl; and 3) it also steals the hydrogen once belonged to the hydroxyl group of Si4. As a consequence of this turmoil, Si3 is now lacking one of its ligand, while an oxygen of Si4 is unsaturated: this is the perfect condition so that Si3 and Si4 can bond together by means of an oxygen. This way, a Si–O–Si link on the HNT surface has been reestablished. This does not mean, however, that Si3 is placed here in the same way as it would have been on a pristine surface: the main difference is that the bond with the underlying aluminum layer is now hindered by the fact that the linking oxygen is saturated by an hydrogen. As a result, Si3 slightly protrudes above the surface. Another way of seeing/describing this same geometry is as a formic acid molecule bonded to the unsaturated carbon on the HNT surface.

The second most stable structure is S2C02, being 36.4 kJ/mol higher. Here two carbon atoms and an oxygen are bonded together to form a small cycle. Then there are S2C04 and S2C03, where on the former the new carbon is near the defect, while on the latter both carbon atoms are bonded to

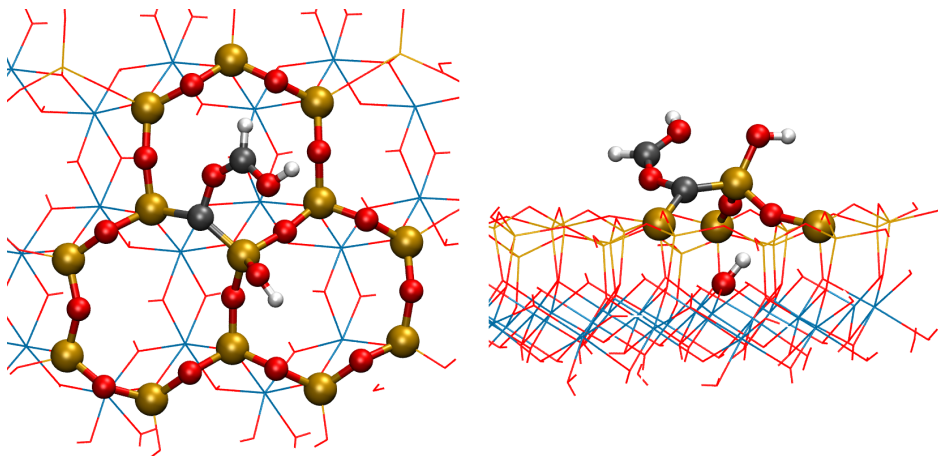


Figure 3.15: Optimized geometry of S2C07, top and side views. Colors: H white; C black; O red; Al blue; Si gold.

the same silicon. Finally, the least stable structures are S1C05, S1C06, and S1C01, where the second carbon is near a non-defective portion of the surface.

3rd Carbon The best position for the third carbon was investigated starting from the most stable structure of the previous batch of calculations: S2C07. Seven different geometries were prepared: from S3C01 to S3C06, the new carbon atom was added over the usual central sites; while on S3C07 it was placed over the carbon belonging to the formic acid.

Once all geometries were optimized, the most stable was found to be S3C02. However, a closer inspection of its final structure shows that the formic acid molecule (the one seen on S2C07) detached from the surface, being now simply adsorbed on it. The other two carbon atoms are bonded together, and they form a bridge between Si2 and Si3. Due to the loss of carbon in the form of formic acid, this was not chosen as the starting geometry in which to add the fourth carbon.

At 53.8 kJ/mol higher, the second most stable structure is S3C07. After optimization, S3C07 shows the formation of a small carbon compound, as reported in figure 3.16. Here all three carbon atoms are bonded together, and alongside with an oxygen they form a four-membered heterocycle. One of the carbon atoms serves as an anchoring point to the HNT surface, bonding both Si2 and Si3; another carbon is bonded to an hydroxyl group; while the last one has an hydrogen. This structure was chosen as the starting point for exploring the preferred position of the fourth carbon.

Finally, sorted by increasing energy there are: S3C04, S3C01, S3C03, and S3C06 (optimization on S3C05 did not converge). S3C04 has some anchoring

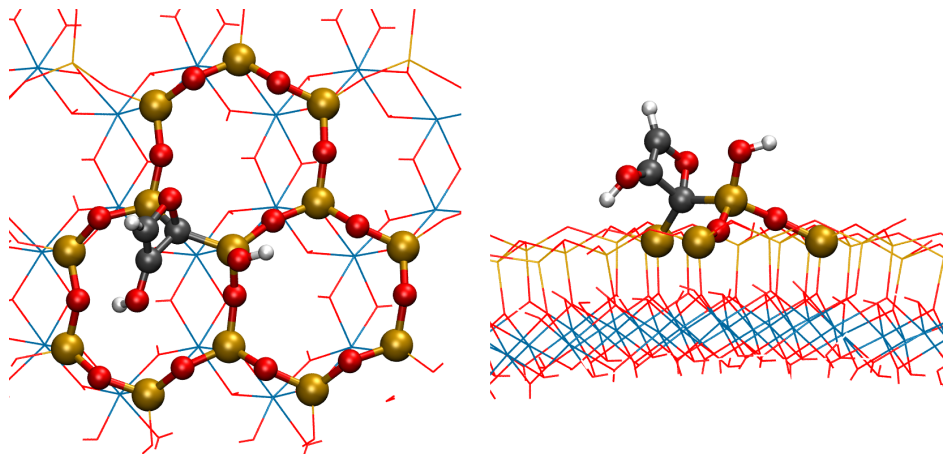


Figure 3.16: Optimized geometry of S3C07, top and side views. Colors: H white; C black; O red; Al blue; Si gold.

points, and the three carbon atoms form a six-membered heterocycle with two oxygens and a silicon. Similarly, on S3C01 there is a seven-membered heterocycle with two oxygens and two silicons. On S3C03 all carbon atoms are close one another, but not directly bonded. Finally, on S3C06 the third carbon is far away from the others, on a clean portion of the surface.

4th Carbon Starting from S3C07, seven different position were investigated to determine where the fourth carbon atom prefers to stay. As usual, geometries from S4C01 to S4C06 have the new carbon over the most internal silicons. In S4C07, however, the additional carbon was placed near the heterocyclic oxygen.

After performing all optimizations, the geometry obtained from S4C02 was the most stable. Its structure, reported in figure 3.17, shows that the new carbon, originally on top of Si2, place itself between the Si-anchoring carbon and its previous neighbor, the heterocyclic oxygen. Overall, the resulting structure is pretty similar to the starting one, S3C07, just with one more carbon atom constituting the ring.

The second place for stability is owned by S4C03, being only 21.1 kJ/mol more. Also in this case, all four carbon atoms are bonded together. Moreover, the newly added carbon snatches the hydroxyl group from Si3, while maintaining its bond with this silicon. Despite the additional anchoring point of this carbonaceous structure to the HNT surface, this optimized geometry is thermodynamically disadvantaged with respect to S4C02. Next there are S4C07 and S4C04, in both of which the fourth carbon is near the defect but not directly bonded to the other carbon atoms; and finally S4C06, S4C05,

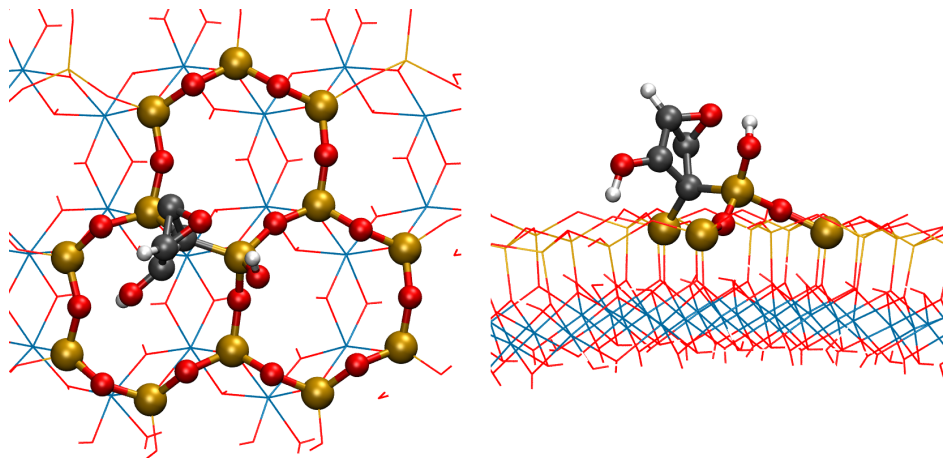


Figure 3.17: Optimized geometry of S4C02, top and side views. Colors: H white; C black; O red; Al blue; Si gold.

and S4C01, where the new carbon is near the non-defective portion of the surface.

5th Carbon The best position for the fifth carbon atom was searched starting from seven different geometries based on S4C02. Those from S5C01 to S5C06 are the usual ones, the exceptions being S5C02 and S5C03, in which the additional carbon could not be placed precisely above the relative silicons because of the steric hindrance. Lastly, in S5C07 the new carbon was added on top of the existing carbonaceous structure, near both the oxygen and a carbon (the one bonded to an hydrogen).

Once all optimizations were completed, the structure S5C03 was found to be the most stable. Figure 3.18 shows how much the final geometry of S5C03 differs from its initial guess, since many things happened in the process. The additional carbon, originally on Si3, moved away from that silicon while bonding its oxygen. In the meantime, the carbon takes the hydrogen previously belonged to the hydroxyl group of Si3, and the oxygen that once was on the carbonaceous structure. As a result, a molecular fragment similar to formic acid (without the acidic hydrogen) is now bonded to Si3.

Being 55.3 kJ/mol less stable, S5C07 takes the second place. During its optimization, however, a carbon monoxide molecule detaches from the rest of the structure. Next, both S5C01 and S5C02 end up in the same energy minimum, sharing the third place for stability; in their resulting geometry all carbon atoms are directly bonded. Finally there are S5C04, where the fifth carbon is near the defect but is not bonded with the carbonaceous structure; and S5C06 and S5C05, where the new carbon is on the clean part of the

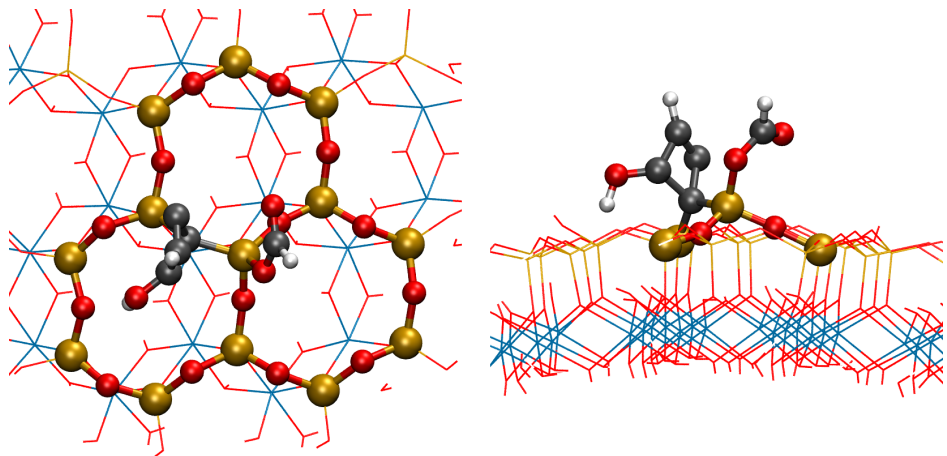


Figure 3.18: Optimized geometry of S5C03, top and side views. Colors: H white; C black; O red; Al blue; Si gold.

surface.

6th Carbon Starting from S5C03, the sixth carbon was added in eight different position. From S6C01 to S6C06 it was placed on top of the central silicons; in S6C07 the carbon was positioned over the unsaturated oxygen of the quasi-formic acid portion; and in S6C08 it was put near the less coordinated carbon of the four-membered ring.

The calculations show that the optimized geometry obtained from S6C02 is the most stable. As represented in figure 3.19, the sixth carbon (originally placed on top of Si2) finds its favorite place in the carbon ring, effectively becoming its fifth member. The next most stable geometries are S6C08 (at 33.5 kJ/mol more than the first one), and S6C03: the former has the additional carbon bonded to the existing carbon ring, while in the latter it is bonded to the quasi-formic acid molecule. In S6C08 the optimized geometry does not differ to much from the initial guess: the new carbon has the effect to flatten the carbon ring to which it is bonded. In S6C03, instead, C moves from Si3 to the quasi-formic acid molecule, revolutionizing its structure. The final result is the formation of a quasi-glyoxal molecule (the smallest dialdehyde) in which an hydrogen is missing: for this reason it can bond the HNT surface on Si3 via the under-coordinated carbon.

Then, in order of increasing energy, there are: S6C07, in which a carbon monoxide molecule forms and then floats around above the surface; S6C04, where the new carbon is bonded to the quasi-formic acid; and S6C06, S6C05 and S6C01, in which the sixth carbon is on the clean portion of the surface, far away from the defect.

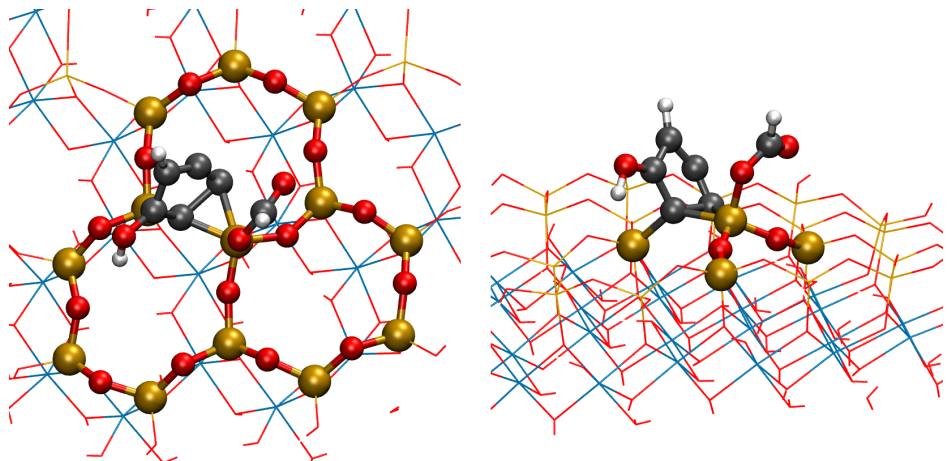


Figure 3.19: Optimized geometry of S6C02, top and side views. Colors: H white; C black; O red; Al blue; Si gold.

7th Carbon An additional carbon atom was placed on seven different sites of S6C02. The structures named from S7C01 to S7C06 are built in the usual way, while in S7C07 the new atom was placed as a bridge between the five-membered carbon ring and the oxygen of the quasi-formic acid fragment.

After optimization, the most stable structure turned out to be S7C04, but since here there is the formation of a CO molecule floating above the HNT surface, this structure has been excluded from further investigation. Then there is S7C02, in which the 7th carbon finds its place on the preexisting ring, giving rise to the structure reported in figure 3.20. Next for stability, at an energy of 18.7 kJ/mol higher, there is S7C07, in which the new carbon is on a side of the original five-membered ring. At a distance higher than 150 kJ/mol, S7C06 and S7C03 follow, in both of which the additional carbon is bonded to the original ring. Finally, the last two positions are taken by S7C05 and S7C01, where the seventh carbon is on a clean part of the HNT surface.

8th Carbon Starting from S7C02, nine structures were prepared and then investigated. The geometries named from S8C01 to S8C06 have the eighth carbon over the usual central sites; in S8C07, C is bonded to the free oxygen of the quasi-formic acid fragment; S8C08 has the new carbon bonded to a vertex of the main ring; and finally, in S8C09, the additional carbon was placed at the center of the ring, slightly above its plane.

The most stable structure after optimization was found to be S8C08, in which the additional atom is bonded to the preexisting carbon ring. Its geometry, reported in figure 3.21, is not easy to describe: there is a five-

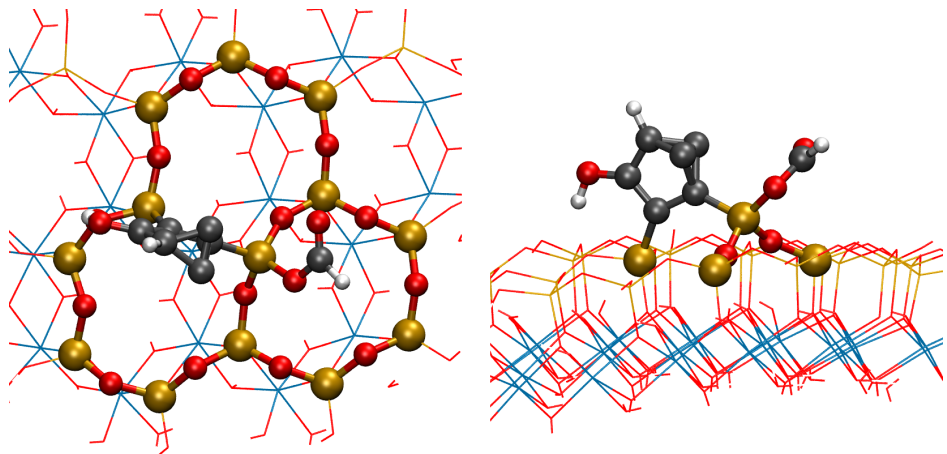


Figure 3.20: Optimized geometry of S7C02, top and side views. Colors: H white; C black; O red; Al blue; Si gold.

membered carbon ring with a “double” vertex (just as in S7C02), which in turn bonds the eighth carbon. The second place in order of stability is taken by S8C02, at only 9.2 kJ/mol more. Its structure, just like those of S8C03 and S8C09 (the next in the ranking), presents the additional carbon directly bonded to the others. Then there is S8C07, in which a CO molecule is formed; and lastly, at ~ 300 kJ/mol from the most stable, there are S8C04, S8C06, S8C05 and S8C01, where the new C is far away from the others, on a clean portion of the surface.

9th Carbon The next carbon was added to nine different sites of S8C08. From S9C01 to S9C06, the ninth carbon was placed over the usual central silicones. In S9C07 it was bonded to the highest carbon of the preexisting structure, while in S9C08 it was positioned at one side of the main carbon ring. Finally, in S9C09, the additional C was bonded to the free oxygen of the quasi-formic acid fragment.

After the optimization of all these structures, S9C08 turned out to be the most stable. Its geometry, reported in figure 3.22, is fundamentally different from the initial guess: here the three-dimensionality of the carbon aggregate is lost in exchange of two planar, fused rings (6- and 4-membered) that share a single side. The smaller ring anchors the surface through two Si atoms, while the bigger one is saturated in two adjacent vertices by an hydroxyl group and an hydrogen. This is a very stable structure, especially in comparison with S9C09, which takes the second place at 84.6 kJ/mol higher. However, in S9C09 there is the formation of a carbon monoxide molecule, and this generally has an highly stabilizing effect on the structure. Accordingly, it

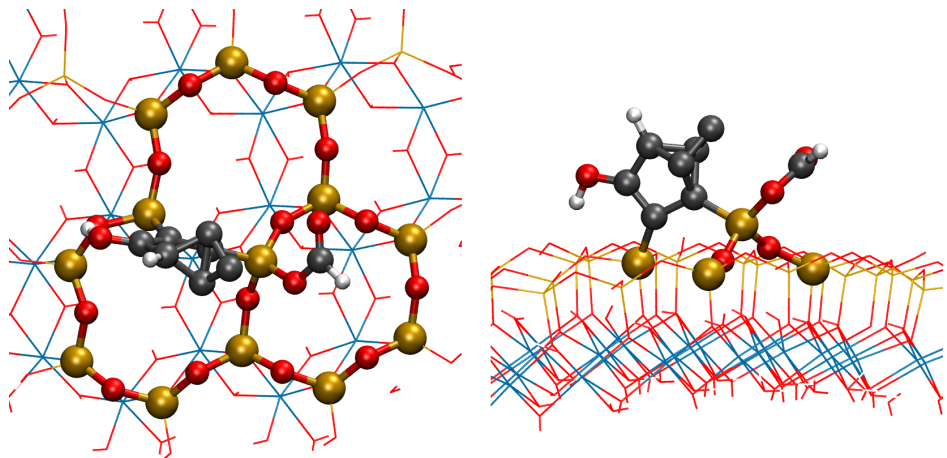


Figure 3.21: Optimized geometry of S8C08, top and side views. Colors: H white; C black; O red; Al blue; Si gold.

would be better to compare the absolute energy of S9C08 with that of S9C07, the third in ranking. The latter is still a “valid” structure, since all atoms are bonded in a single molecular fragment, but the energy difference with the most stable structure is a remarkable 192.0 kJ/mol.

The S9C03 and S9C02 structures follow in order of stability, where in both cases the ninth C is bonded to the preexisting carbon agglomerate forming some fused rings. The last part of the ranking is reserved to S9C06, S9C04, S9C01 and S9C05 in this order, where the additional carbon is on a clean part of the surface in all cases.

10th Carbon Starting from the S9C08 structure, the tenth and last carbon was added in ten different sites. Structures named from S10C01 to S10C06 are prepared in the usual way. In S10C07 the additional carbon was placed over a side of the six-membered carbon ring. In both S10C08 and S10C09, it was positioned at the two opposite faces of the bigger ring. Finally, in S10C10, C was bonded to the free oxygen of the quasi-formic acid fragment.

The first three positions in terms of stability belong to S10C07, S10C03 and S10C02, respectively. These have very similar absolute energies, the difference between third and first place being only 31.5 kJ/mol. In all cases, in the optimized geometries the 10th C is bonded to the preexisting carbon structure. In particular, the geometry of S10C07 (figure 3.23) does not depart too much from the initial guess, and the tenth carbon makes only minor adjustments on the side of the ring. Next on the list is S10C08, where the tenth carbon is bonded to the bigger carbon fragment; it is followed by S10C10, in which a CO molecule detaches from the rest. Then, with similar energies,

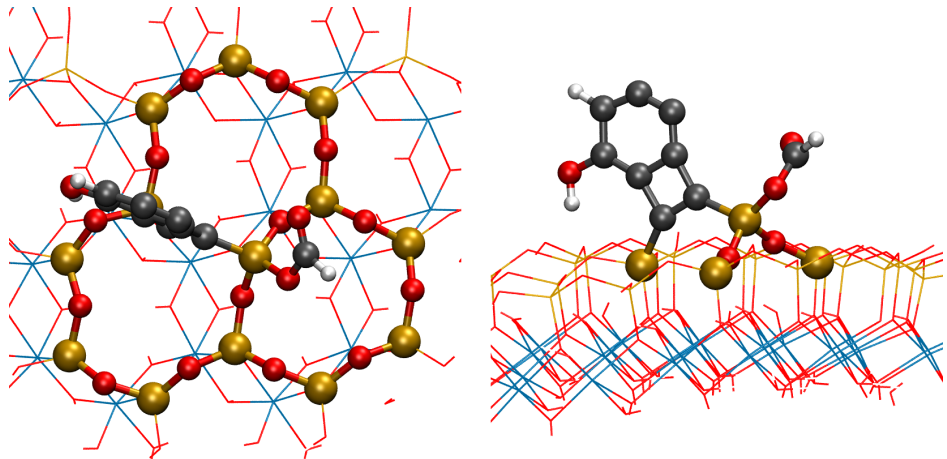


Figure 3.22: Optimized geometry of S9C08, top and side views. Colors: H white; C black; O red; Al blue; Si gold.

there are S10C09 and S10C04: in the former the additional carbon stands with the others forming some fused rings, while in the latter it is bonded to the HNT surface close to the defective site. Finally there are S10C06, S10C05 and S10C01, where the supplementary C is on a clean part of the HNT surface.

3.5 Si-vacant Halloysite Surface

In this section, all the investigated structures obtained from the Si-vacant halloysite surface model, covered with up to ten carbon atoms, are discussed. Tables A.7, A.8 and A.9, in the appendix, report the final energy and a quick recap comment for each of them.

1st Carbon This new series of calculations is based on the defective halloysite model in which the silicon Si3 is missing. In order to inquire its favorite position, the first carbon atom was positioned on six different sites, this guess geometries being named from V1C01 to V1C06. Naming convention is the same as previous sections, the only exception being V1C03, in which “03” no more means “over Si3”, but “over the missing silicon”.

Once all optimizations were performed, the most stable structure resulted to be V1C03, represented in figure 3.24. This is the one with the carbon nearest to the defect. Similarly to what has been seen on the substituted surface with the first carbon, even in this HNT model the preference of the unsaturated carbon for the defective site is confirmed. During optimization

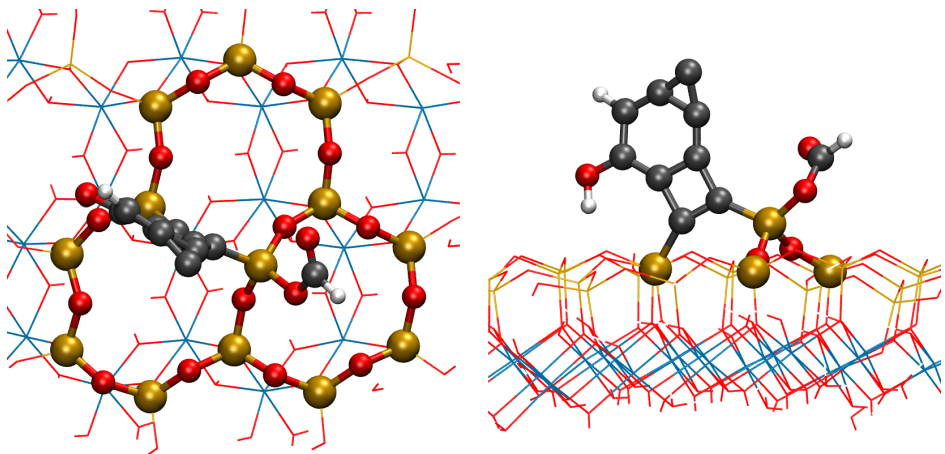


Figure 3.23: Optimized geometry of S10C07, top and side views. Colors: H white; C black; O red; Al blue; Si gold.

the carbon takes an hydrogen from a nearby hydroxyl group, bonding to its oxygen.

The second most stable structure is V1C04, with an absolute energy 45.0 kJ/mol higher than the first one. V1C04 is followed by V1C02, both of them having the carbon near the surface defect; while in the remaining three geometries the carbon is on the clean part of the HNT surface, its interaction being an intercalation between a silicon and an oxygen.

2nd Carbon Starting from V1C03, six different positions were also tried for the second carbon, named from V2C01 to V2C06. After optimization, the geometry obtained from V2C03 was found to be the most stable. The starting guess for this structure was with the second carbon placed on the defective site, beside the two hydroxyl groups and the preexisting carbon. Optimization shows, however, that the guess was not close to the optimal position, since the new carbon prefers to bond the first one directly, stealing its hydrogen in the process. In the final geometry of V2C03, reported in figure 3.25, the newly added carbon is the one farther from the surface.

At 62.1 kJ/mol higher, V2C02 is the second most stable structure. Even in V2C02 the two carbon atoms are directly bonded, but the second one is also bonded to the HNT surface. Strangely enough, though, this doubly-anchored carbon structure is less stable than V2C03. Then there are, in order, V2C05, V2C06, and V2C01, in which for all of them the new carbon is on a clean portion of the surface. Finally, optimization of V2C04 failed, but the energy related to the last performed optimization step is between the ones of V2C02 and V2C05, again confirming the trend for which the most

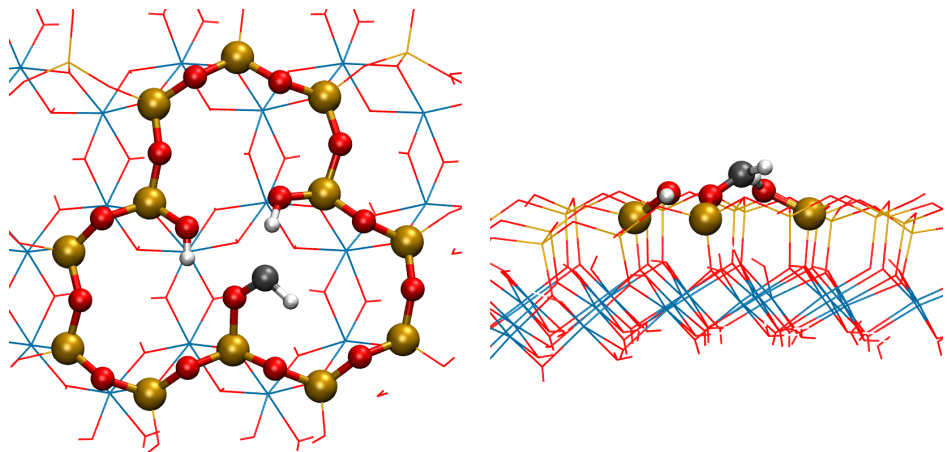


Figure 3.24: Optimized geometry of V1C03, top and side views. Colors: H white; C black; O red; Al blue; Si gold.

stable geometries are those where carbon atoms are close together.

3rd Carbon To further the investigation, a third carbon atom was placed in seven different sites of V2C03, the starting geometry for this step. Of these resulting geometries, the ones from V3C01 to V3C06 are those with the carbon over the usual sites, while in V3C07 the guessed position for it is near the two preexisting carbon atoms, in a triangular fashion.

The optimized structures obtained from V3C03 and V3C07 ended up in the same minimum of the potential energy surface, thus sharing the first position for the most stable geometry. As reported in figure 3.26, the three carbon atoms are bonded together forming a triangular structure, which in turn is anchored to an oxygen near the defect of the HNT surface.

Second place is achieved by V3C02, that with its additional 299.1 kJ/mol in absolute energy is well spaced from the first two. Then, with a similar energy, V3C04 follows. Both of these two geometries have the third carbon near the defect (bonded to Si2 and Si4, respectively), but not directly bonded to the preexisting carbon atoms. Finally, by increasing energy there are V3C05, V3C06, and V3C01, in which the new carbon is far away from the defect.

4th Carbon Using the V3C03 structure as starting point, a total of eight different places for the next carbon were probed. The resulting structures named from V4C01 to V4C06 are those with the fourth carbon over the central silicons, whereas in V4C07 and V4C08 the new atom was placed, respectively, near a side and a vertex of the triangular carbon structure.

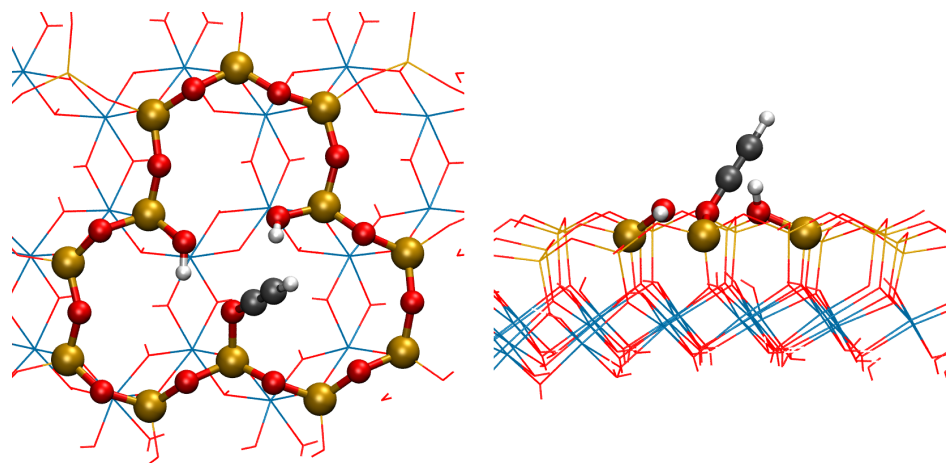


Figure 3.25: Optimized geometry of V₂C₀₃, top and side views. Colors: H white; C black; O red; Al blue; Si gold.

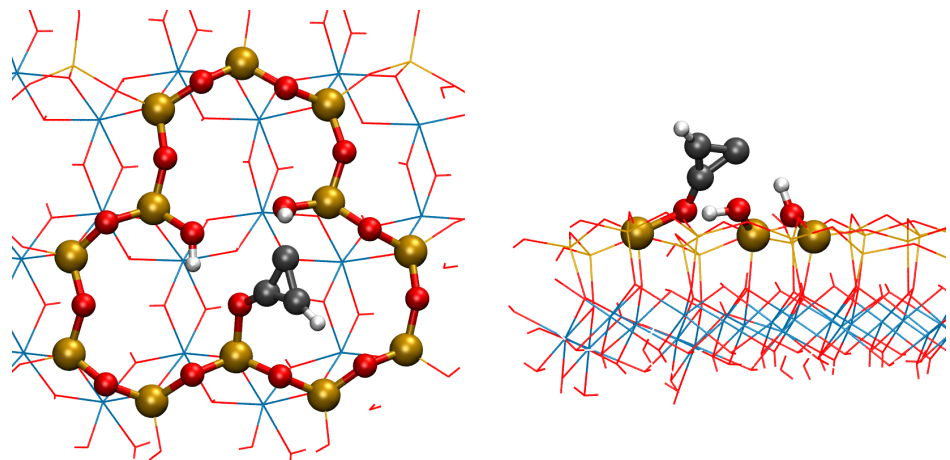


Figure 3.26: Optimized geometry of V₃C₀₃, top and side views. Colors: H white; C black; O red; Al blue; Si gold.

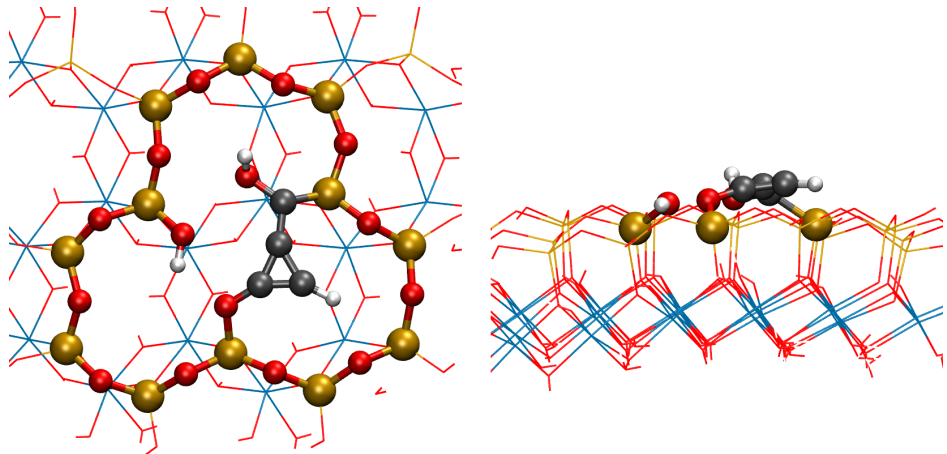


Figure 3.27: Optimized geometry of V4C04, top and side views. Colors: H white; C black; O red; Al blue; Si gold.

The optimized geometry of the most stable structure, namely V4C04, shows a change to the trend seen so far. As reported in figure 3.27, the resulting carbonaceous aggregate has all carbon atoms bonded together (as expected from the most stable one), but this time it lays flat over the defective site, unlike the other smaller structures that protrude vertically toward the void. This is accomplished thanks to the fourth carbon that, originally placed over Si4, bonds both the hydroxyl group and the preexisting triangular carbon structure, acting as a further anchoring point.

The second most stable structure is V4C07 at 145.8 kJ/mol higher. The optimized structure is not so different from the starting guess, as a result there is a quadrilateral structure of carbon atoms bonded to the surface through a single anchoring point. Similar case for V4C08, third in the standings, where the optimized structure is similar to the guessed one, thus having four carbon atoms bonded together and a single anchoring point to the HNT surface. Then there are V4C03 and V4C02, on which the fourth carbon is near the defect but not directly bonded to the other three; and finally V4C05, V4C06, and V4C01, where the new carbon is in a pristine portion of the surface, far away from the defect.

5th Carbon Starting from the most stable structure of the previous paragraph, the fifth carbon atom was placed in eight different sites in order to evaluate the thermodynamically favorite geometry. The six structures named from V5C01 to V5C06 are the usual ones, while V5C07 starts with the new atom over the most central carbon of the preexisting agglomerate, and finally V5C08 has its additional carbon bonded to both the agglomerate and Si4.

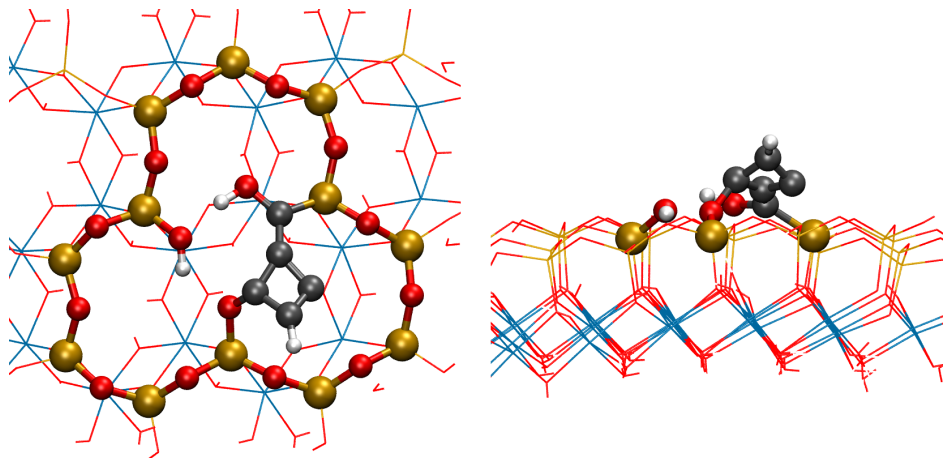


Figure 3.28: Optimized geometry of V5C08, top and side views. Colors: H white; C black; O red; Al blue; Si gold.

The optimized geometry obtained from V5C08 is the most stable. As figure 3.28 shows, the new carbon moves away from Si4 towards the triangular carbon structure, opening it and becoming the fourth member of the newly created ring. From the side view perspective it is easy to see that this structure is less flat on the surface than the previous one, slightly pointing towards the void.

At 39.0 kJ/mol more, V5C04 takes the second place for stability; V5C03 and V5C07 follow. All these three structures have the five carbon atoms bonded together, in particular V5C07 is the only one in which the carbonaceous structure resembles a cluster, i.e. it has a three-dimensionality that differs from all the carbon rings and chains seen so far. Last places are earned by, in order, V5C02, where the new carbon is near the defect but not directly bonded to the others; and V5C06, V5C05, and V5C01, in which it is on a pristine portion of the surface.

6th Carbon Starting from V5C08, seven different positions were taken into account while searching for the preferred position of the sixth carbon. Other than the usual six geometries from V6C01 to V6C06, structure V6C07 starts with the new carbon over the face of the four membered carbon ring. It is precisely this structure that gives the most stable geometry of the batch, after that all optimizations were performed. The result of the calculation, shown in figure 3.29, is that the sixth carbon prefers to join the ring rather than stay on its top, thus becoming its fifth member. Also in this case, the side view of the structure shows that the growing agglomerate points towards the void rather than stay flat on the surface.

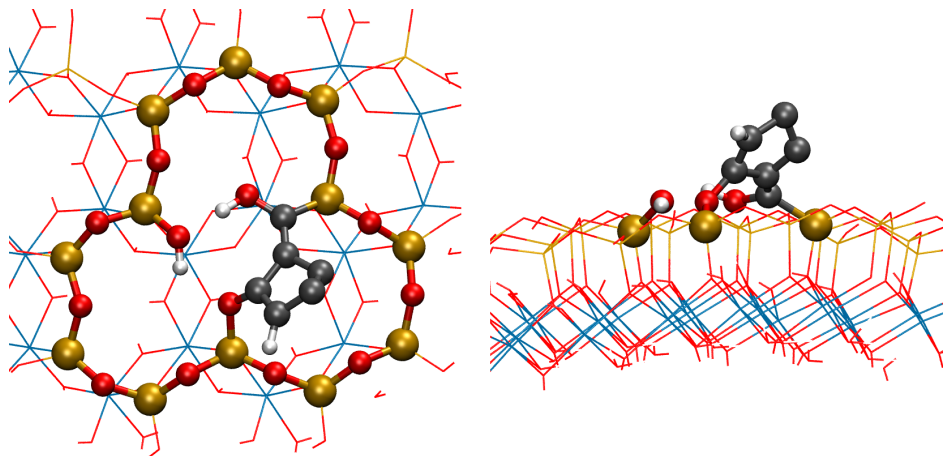


Figure 3.29: Optimized geometry of V6C07, top and side views. Colors: H white; C black; O red; Al blue; Si gold.

V6C02 is the second most stable structure being 79.2 kJ/mol higher than V6C07. Different things happen during this optimization: i) the new carbon, starting on top of Si2, steals the hydroxyl group from silicon, and ii) it bonds the oxygen of the nearby hydroxyl group (the one belonging to the carbon agglomerate) while at the same time taking its hydrogen. The resulting geometry has thus three anchoring point: this could be the reason for its high stability, despite the fact that not all six carbon atoms are directly bonded.

Then there are V6C03 and V6C04, in which all carbon atoms are bonded together, the former forming a five-membered carbon ring, while the latter forms a four-membered one. Finally, in V6C06, V6C05, and V6C01, the sixth carbon is near a non-defective portion of the surface, and the carbon performs its intercalation between a silicon and an oxygen, as it always does in this situation.

7th Carbon Using the most stable structure with six carbon atoms, the preferred site for the seventh one was searched using eight guessed starting positions. From V7C01 to V7C06 there are the ones with the new atom above the most central silicon, in V7C07 the seventh carbon is bonded to one of the two less saturated carbon of the ring, while in V7C08 it is bonded to the other less saturated one.

After the usual optimizations, the V7C04 geometry shows up to be the most stable. Here the new carbon, originally on top of Si4, moved towards the carbonaceous structure, interacting with it so strongly to become the sixth member of the carbon ring, as showed in figure 3.30. Even this structure

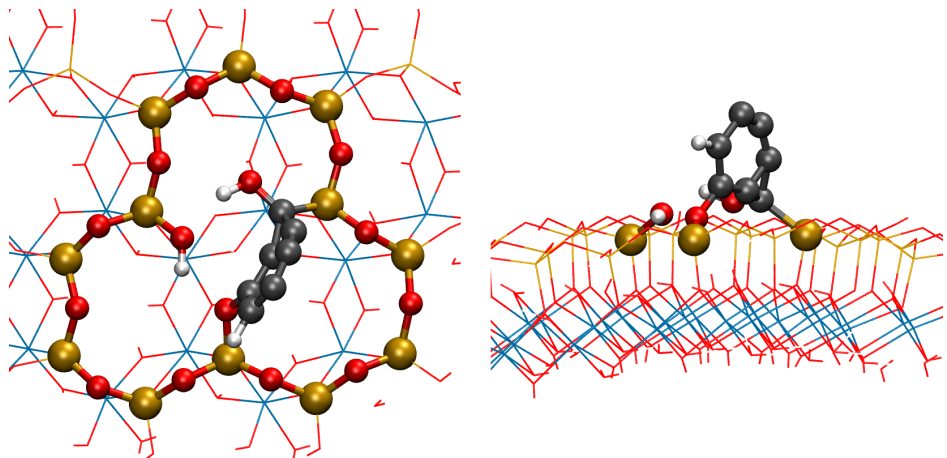


Figure 3.30: Optimized geometry of V7C04, top and side views. Colors: H white; C black; O red; Al blue; Si gold.

follows the trend started with the addition of the fifth carbon since, as the side view shows, the carbonaceous structure keeps growing vertically.

At just 19.9 kJ/mol higher there is V7C07, followed by V7C08. In both cases the new carbon, originally placed near an unsaturated carbon of the ring, moves towards one of the sides of the latter (the same for both structures, thus explaining the small difference in energy between the two). Also in V7C03 all carbon atoms are bonded together, forming a three-dimensional cluster structure. In V7C02, instead, something similar to what has been seen for V6C02 happens: the seventh carbon remains on top of Si2, steals its hydroxyl group and also bonds the oxygen of the hydroxyl group of the carbonaceous structure. Again, the resulting carbon agglomerate has three anchoring points to the HNT surface, but unlikely the case of V6C02, this time its energy is way higher (315.3 kJ/mol) than the most stable structure. Last positions are earned by V7C06, V7C05, and V7C01, in which the new carbon is near a pristine portion of the surface, far away from the others.

8th Carbon In order to assess the best position for a further carbon, eight different geometries were prepared starting from V7C04. Other than the usual six from V8C01 to V8C06, there are: V8C07, in which the new carbon was placed on a side of the carbon ring (the one farthest from the surface); and V8C08, in which the new atom was on the ring face.

Once optimizations were concluded, the geometry obtained from V8C07 resulted to be the most stable among all. The final structure, reported in figure 3.31, is not so different from the initial guess: there was a slight adjustment of the overall carbonaceous structure, but the eighth carbon did

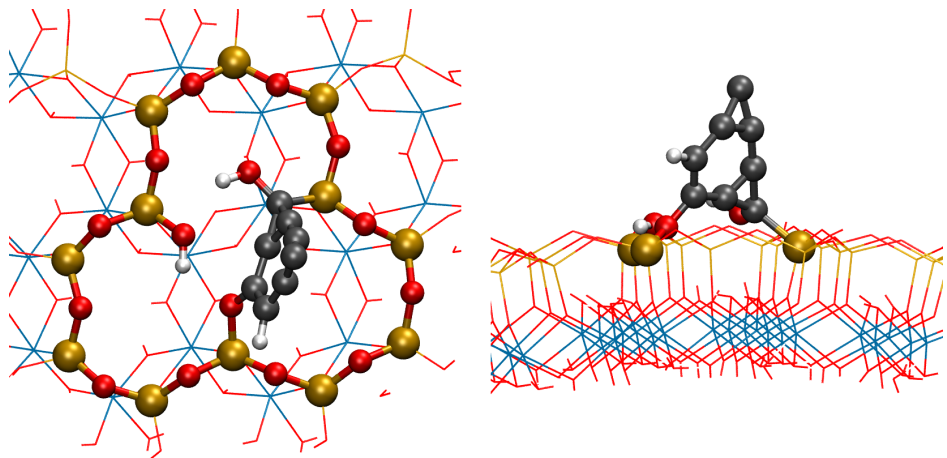


Figure 3.31: Optimized geometry of V8C07, top and side views. Colors: H white; C black; O red; Al blue; Si gold.

not move from its original position on the side of the ring. As a result, the agglomerate keeps growing in height.

Structure V8C08 takes the second place, being only 9.5 kJ/mol less stable than the first one. Here the optimization algorithm moved the eighth carbon from its initial position over the face of the carbon ring towards the ring itself, the final result being a bigger, seven-membered ring. The next three structures, as always in order of increasing energies, are: V8C04, V8C02, and V8C03. Both V8C04 and V8C03 have all eight carbon atoms bonded together, whereas V8C02 is the exception, since here the eighth carbon is only bonded to Si2 but, unlike the V6C02 and V7C02 cases, it does not link to the carbonaceous agglomerate. Despite this, V8C02 is still more stable than V8C03, in which all carbon atoms are close together. Finally, V8C05, V8C06, and V8C01 are the geometries where the new carbon is near a pristine part of the surface.

9th Carbon Using structure V8C07 as the starting point, the preferred position for the ninth carbon atom was searched starting from ten different guessed sites. As always there are the geometries from V9C01 to V9C06, with the new carbon over each of the most central silicons; in V9C07 the supplementary atom was added over the barest side of the carbon ring; V9C08 has the ninth carbon over the face of the ring, whereas in V9C09 it is also over the ring face, but on the opposite side; and finally in V9C10 the new carbon was placed in the highest place possible: on top of the carbon farthest from the HNT surface.

Performing all optimizations shows that the structure obtained from V9C07

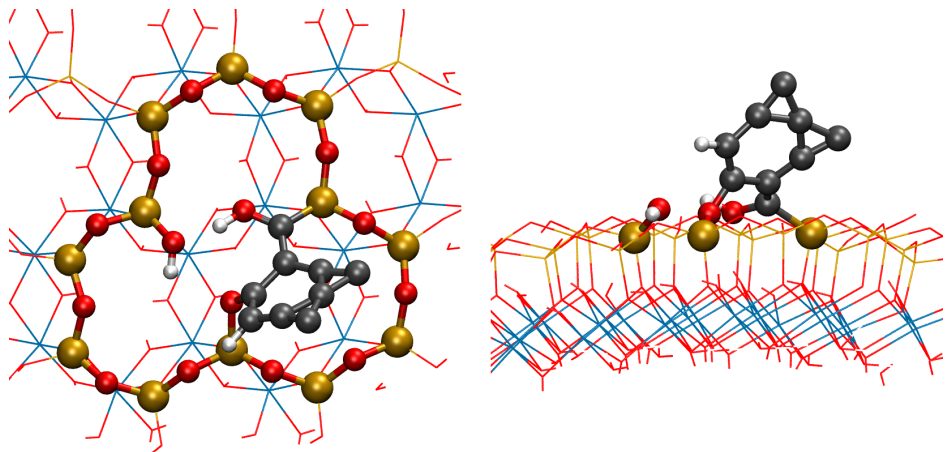


Figure 3.32: Optimized geometry of V9C07, top and side views. Colors: H white; C black; O red; Al blue; Si gold.

is the most stable. In the optimized geometry, reported in figure 3.32, the new carbon did not move from its original position and continues to stick to that side of the carbon ring. There is, however, a general rearrangement of the whole agglomerate: in particular the carbon that bonds Si4 is now bonded to the ring from a single vertex (and no more from a side, as in V8C07). As a consequence, the carbon ring is now less stiff, and the newly acquired freedom lets it bend slightly towards the HNT surface (as can be guessed from the top view of this structure).

The second place for stability belongs to V9C04 with its 62.9 kJ/mol more, in which the new carbon ends up sticking to the agglomerate. Then there is V9C10, whose geometry does not differ much from the original guess. V9C08 and V9C09 follow, where in the latter there is the formation of an agglomerate that resembles the portion of a dome. V9C03 is the last structure of the series in which all carbon atoms are bonded together. Finally there are: V9C02, with the new carbon near the defect but far from the agglomerate; and V9C05, V9C06, and V9C01, where the new atom is on the pristine portion of the surface.

10th Carbon The tenth and final carbon was placed in ten different sites of V9C07. The resulting structures named from V10C01 to V10C06 are those with the new carbon placed over the five most central silicones and the vacancy; in V10C07 the additional atom is over the carbon bonded to Si4; V10C08 has it above the face of the carbon ring; finally in V10C09 the tenth carbon is on top of the carbonaceous structure, far away from the surface; whereas in V10C10 it is still on top, but closer to the hydrogen.

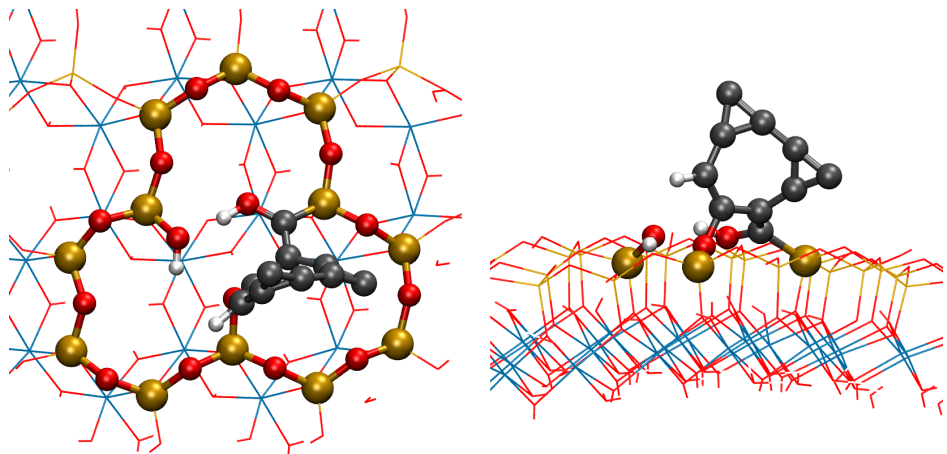


Figure 3.33: Optimized geometry of V10C10, top and side views. Colors: H white; C black; O red; Al blue; Si gold.

Optimizations find that the final geometry of V10C10, reported in figure 3.33, is the most stable among all. The tenth carbon, initially bonded to the six-membered ring, between another carbon and an hydrogen, in the optimized structure is still outside of the ring but its presence allowed to the nearest carbon to enter the ring structure, that hence became seven-membered.

V10C04 is the next more stable structure, at only 5.3 kJ/mol higher. Its optimized geometry has a lot of interconnected carbon rings, the main difference with V10C10 being the absence of a seven-membered ring (the main ring here has still six members). Then follow, in order, V10C09, V10C07, and V10C08. Same story here: all ten carbon are bonded together, forming many interconnected rings. Then there are V10C02 and V10C03. The former does not have all ten carbon atoms directly bonded, but the tenth is instead connected to the main carbonaceous structure through a bridge oxygen. It is a kind of an exception, since despite its connectivity it still has a lower energy than V10C03, which instead has all carbon atoms directly bonded. Finally the less stable structures are, in order, V10C06, V10C05, and V10C01, in which the new carbon is near a pristine portion of the surface.

3.6 Density of States Analysis

Once collected all the optimized carbon-coated halloysite structures, they have been grouped by both number of carbon atoms and surface model, for a total of 33 groups: from zero to ten atoms, in three different surfaces. In

each group, only the most stable and “valid” structure has been selected, where the term valid means that no dissociation occurred (e.g CO formation). These 33 structures have then been further investigated by population analysis of molecular orbitals. Figures 3.34, 3.35 and 3.36 show the *density of states* (DOS) and the *projected density of states* of carbon atoms (PDOS) for the most stable structures in the pristine, substituted and Si-vacant HNT surfaces, respectively.

All three surfaces without carbon atoms, in their ground state, exhibit the HOMO in the range -6.0/-5.9 eV, and the LUMO in the range 0.6/0.8 eV, with a resulting band gap of 6.5/6.8 eV. By looking at the DOS, the observed behavior is that, as the number of surface carbon atoms grows, there is a general increase of molecular orbitals (both occupied and unoccupied) within the original halloysite band gap. In most cases, these MOs are made up almost entirely of carbon basis functions, with few exceptions such as P5C and S1C: this can be interpreted as a proximity effect of the carbon, that pushes some halloysite atoms out of their comfort zone (in terms of electronic structure, not spatial position).

3.7 Conclusion

The focus of this study was the outer layer of HNTs, in order to shed light on both the growth mechanism of carbon aggregates, and the acquisition of electrical conductor behavior by the whole system. A total of 247 different geometries were optimized on all three models of halloysite surface. The observed trend is, in all cases, that carbon atoms prefer to agglomerate rather than be scattered on the halloysite surface. This means that, once a nucleation site is formed (by intercalation of C between Si and O), each additional carbon tends to place itself close to it by thermodynamic preference. A nice example is V4C04: it has all four carbon atoms arranged in such a way that they cover the Si vacancy. They are flat on the HNT surface, anchoring it in two different sites. But then, by adding more carbon to that structure, the aggregate grows up vertically without making any further bond to the surface rather than the original two. Since this investigation stops at ten carbon atoms, it is not known what happens next, but two reasonable hypothesis can be made. First one, this aggregate keeps growing up to a critical dimension that, once reached, causes a collapse of the carbon cluster towards the HNT surface, thus creating further anchoring points. Second one, in a real system under pyrolysis conditions and with a lot of carbon ready available, it is possible that many different small carbon aggregates can grow on the HNT surface not too far away from each other, and that after a certain dimension

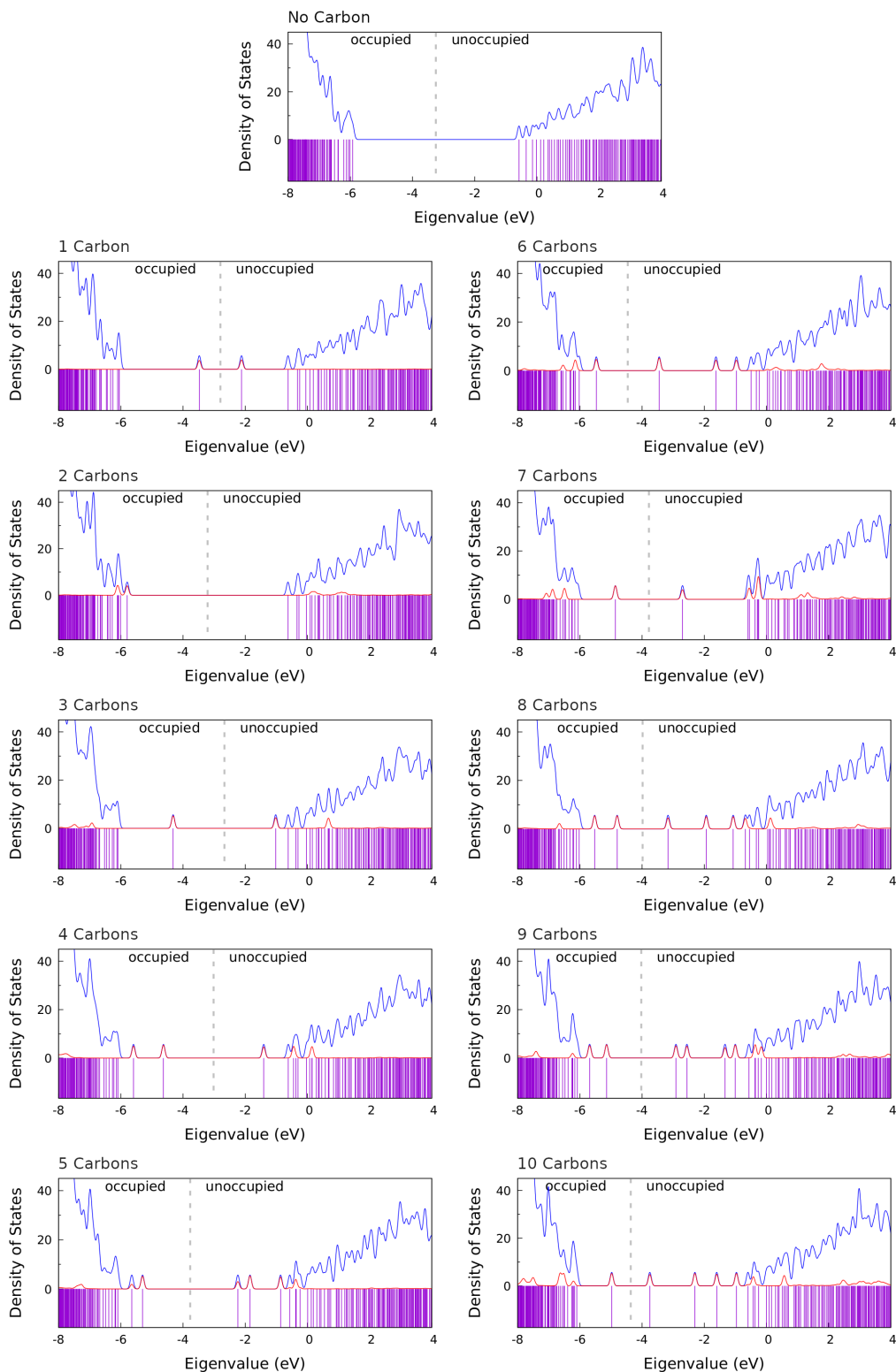


Figure 3.34: DOS (blue) & carbon PDOS (red) of pristine HNT.

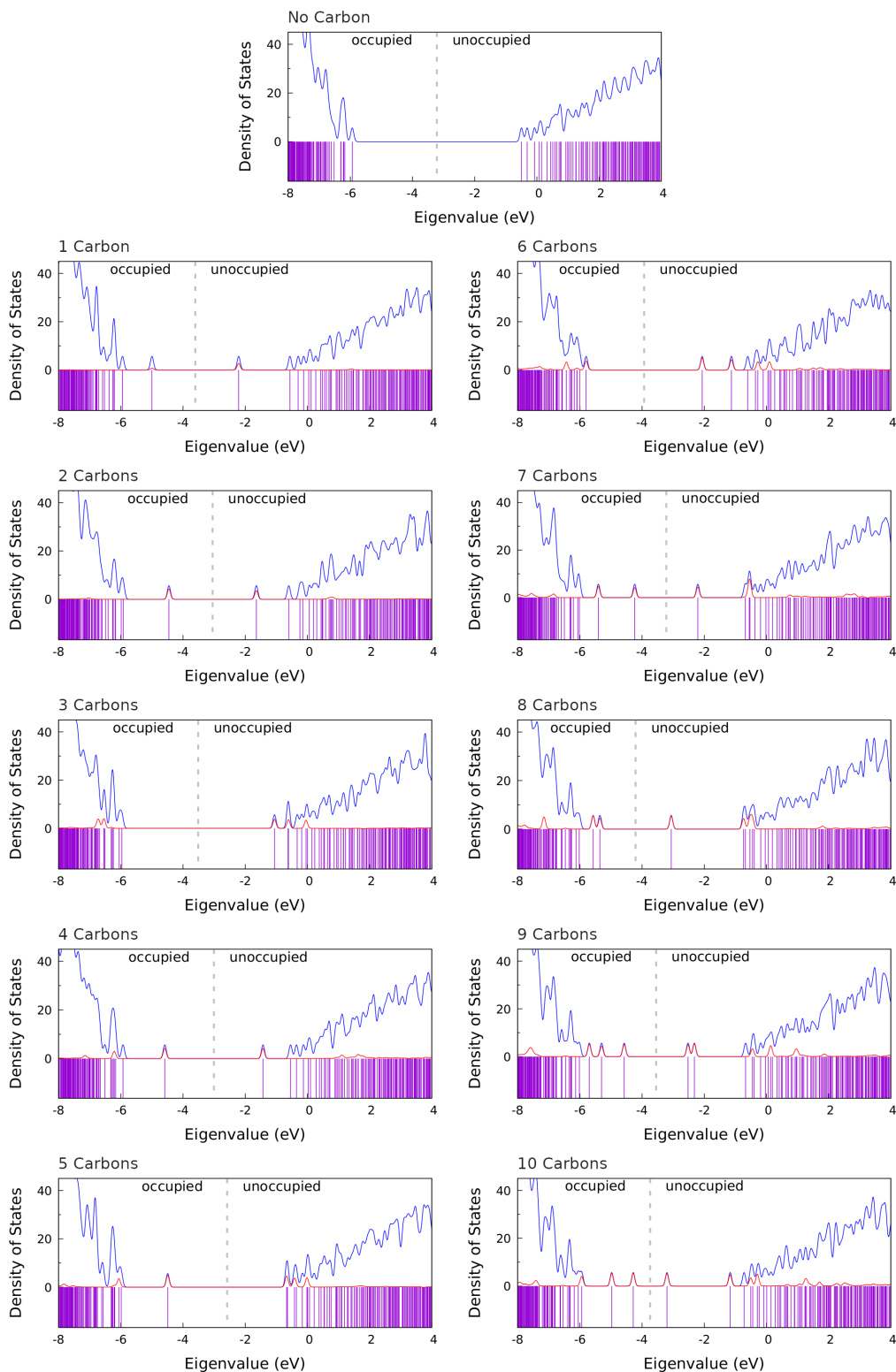


Figure 3.35: DOS (blue) & carbon PDOS (red) of substituted HNT.

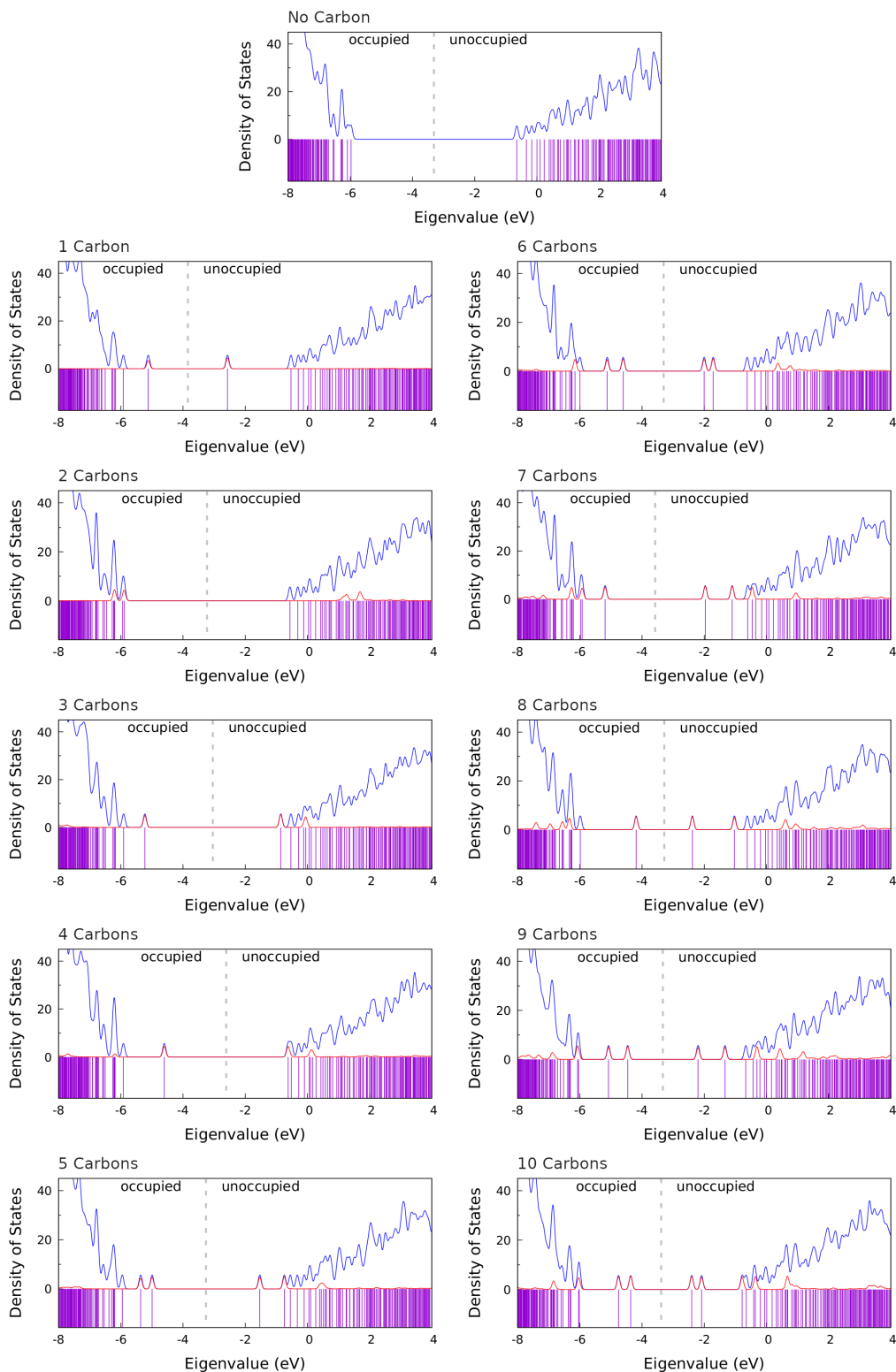


Figure 3.36: DOS (blue) & carbon PDOS (red) of Si-vacant HNT.

is reached they fuse together.

Another comment can be made about the CO formation that occurs in some calculations. This mostly happens when, in the incremental building approach of this study, an additional carbon is put next to an oxygen, which in turn is bonded only to the carbon aggregate. In these cases, geometry optimizations show that the new carbon rips off the oxygen from the aggregate, thus forming the very stable CO species. This suggest that obtaining carbonaceous structures doped with oxygen could be a difficult task due to the low tendency of CO (which is almost certainly produced) to react.

The coating of the selected halloysite models using up to ten carbon atoms is not enough to observe a complete coverage of the band gap, but still it shows the appearance of sparse electronic states separated from one another, exactly in the region of interest. The overall effect is the reduction of the energy gap between HOMO and LUMO, who themselves remain separated by the valence and conduction bands, respectively. These local accretions of carbon aggregates dope the structure, bringing the occupied and unoccupied electronic levels closer together, and making the material more semiconductor-like. Likely enough, a dozen of carbon atoms are not sufficient to demonstrate that the material becomes a conductor. They give, however, a clear qualitative indication that they contribute to the creation of new electronic states exactly within the halloysite band gap, possibly bridging it once an appropriate coverage level is reached. This is in agreement with the experimental results, and paves the way to further investigations.

3.8 Acknowledgment

Part of this work on halloysite carbon-coating has been performed under the Project HPC-EUROPA3 (INFRAIA-2016-1-730897), with the support of the EC Research Innovation Action under the H2020 Programme; in particular, the author gratefully acknowledges the support of Dr. Miguel Pruneda of the Catalan Institute of Nanoscience and Nanotechnology (ICN2), and the computer resources and technical support provided by the Barcelona Supercomputing Center (BSC).

Afterwords

In this work, CO₂ methanation on the three different nickel-based catalysts was investigated by adopting an innovative approach, as for the first time the transition states were found by means of a software (namely Siesta) that computes electronic structures using pseudo atomic orbitals (PAO), whereas similar works in the literature make exclusive use of plane waves (typically VASP). This was possible thanks to the development of a software, Empathes, capable of identifying the transition states through the CI-NEB method, interfacing with Siesta for the calculations of electronic structures. The other point of novelty consists on the catalysts themselves, since Ru- and Fe-decorated systems were studied as single atom catalysts (SACs).

Clearly, what investigated in this study is a great simplification compared to the real system, both because computationally, at this level of theory, it is only possible to study single molecular events rather than systems made up of a multitude of interacting particles; and because we have focused exclusively on the (111) surface of nickel, whereas in the real system the metal likely exhibits more than one face. To broaden the study, a way could be to investigate the methanation process also on other major surfaces, e.g. (100), in order to see how the preferred reaction mechanism changes. Finally, the results obtained on the various surfaces should be combined in a way that takes into account how nickel naturally exposes its faces, thus obtaining a description of this phenomenon that is qualitatively closer to experimental observations.

The carbon-coating process on the silicic surface of halloysite was investigated using an ab-initio approach, building the carbon structures by adding one atom at a time, and selecting the starting geometry each time on the sole basis of thermodynamic stability. This approach differs greatly from the one generally reported in those articles with a strong experimental focus, in which the narrow computational investigation generally gets rid of the question by placing a layer of graphene over the material of interest. There is no reason, indeed, to believe that the carbon layer formed following a pyrolysis or chemical vapor deposition process is structurally ordered like graphene, a

fact supported by many authors who explicitly state that it is amorphous. In this study, three different halloysite surfaces were covered with up to ten carbon atoms each. It has been observed that in any case carbons tend to stick together forming multi-ring structures (or more rarely clusters), rather than lying apart interacting only with superficial Si and O. Furthermore, a DOS analysis reveals how the halloysite band gap generally gets populated by electronic states as the number of carbons on the surface increases: these energy levels are almost entirely due to carbon, as demonstrated by the corresponding PDOS.

This study demonstrated how carbon tends to form agglomerates on the silicic layer of halloysite, and that although these do not have an ordered structure like that of graphene, there is still a thickening of electronic states exactly in the halloysite band gap, a property related to electronic conductivity. It is likely that, by adding more and more carbon atoms to the surface, a complete connection between the valence and conduction bands will be achieved. Based on the acquired knowledge, further investigations could be carried out regarding the applicability of this composite material within electrochemical cells. In particular, regarding Li–O₂ cells, the formation of lithium oxides (the discharge products) on both the aluminum and silicic surfaces of halloysite (both with and without a covering carbon layer) could be studied in order to determine if the material is suitable for this technological application.

Appendix A

Tables

Table A.1: Optimized structures of the pristine HNT surface containing from 1 to 4 carbon atoms. ΔE (kJ/mol) are computed with respect to the most stable structure of each series.

Structure	ΔE	Note
P1C03	0.0	C on the clean part
P1C01	12.2	C on the clean part
P1C05	33.4	C on the clean part
P1C06	37.1	C on the clean part
P2C32	0.0	2 carbons bonded together
P2C33	2.1	2 carbons bonded together
P2C13	56.2	2 carbons bonded together
P2C16	89.4	2 carbons bonded together
P2C34	198.6	2 carbons bonded together
P2C11	226.9	2 carbons bonded together
P2C15	564.2	2nd C on the clean part
P2C31	569.1	2nd C on the clean part
P2C36	597.1	2nd C on the clean part
P2C35	600.4	2nd C on the clean part
P2C12	604.7	2nd C on the clean part
P2C14	609.8	2nd C on the clean part
P3C07	0.0	3 carbons bonded together (ring)
P3C04	85.9	3 carbons bonded together (ring)
P3C03	141.2	3 carbons bonded together (line)
P3C05	345.8	3rd C on the clean part
P3C06	356.0	3rd C on the clean part
P3C01	399.7	3rd C on the clean part
P3C02	423.2	3rd C near the others, bonded to HNT
P4C03	0.0	4 carbons bonded together (ring)
P4C08	17.3	4 carbons bonded together (ring)
P4C07	17.3	4 carbons bonded together (ring)
P4C04	111.9	4th C bonded to the others through O
P4C02	116.2	4 carbons bonded together (ring)
P4C05	281.3	4th C on the clean part
P4C06	291.7	4th C on the clean part
P4C01	329.7	4th C on the clean part

Table A.2: Optimized structures of the pristine HNT surface containing from 5 to 7 carbon atoms. ΔE (kJ/mol) are computed with respect to the most stable structure of each series.

Structure	ΔE	Note
P5C04	0.0	5 carbons bonded together (ring)
P5C02	65.5	5 carbons bonded together (ring)
P5C07	65.5	5 carbons bonded together (ring)
P5C09	67.7	5 carbons bonded together (ring)
P5CB1	90.6	5 carbons bonded together (ring)
P5C08	95.2	5 carbons bonded together (cluster)
P5C03	133.4	5 carbons bonded together (ring)
P5C05	439.4	5th C near the defect
P5C06	455.4	5th C on the clean part
P5C01	494.5	5th C on the clean part
P6C04	0.0	6 carbons bonded together (fused rings)
P6C07	143.7	6 carbons bonded together (fused rings)
P6C03	157.2	6 carbons bonded together (fused rings)
P6C02	264.7	6th C near the others
P6C08	284.1	6 carbons bonded together (cluster)
P6C09	313.5	6th C bonded to the others through O
P6C05	417.2	6th C on the clean part
P6C06	428.6	6th C on the clean part
P6C01	469.4	6th C on the clean part
P7C04	0.0	7 carbons bonded together (fused rings)
P7C03	0.1	7 carbons bonded together (same as pr-7C003b)
P7C08	35.3	7 carbons bonded together (fused rings)
P7C05	143.2	7th C bonded to both HNT and the other carbons
P7C09	186.2	7 carbons bonded together (fused rings)
P7C02	190.6	7 carbons bonded together (fused rings)
P7C07	373.7	7 carbons bonded together (fused rings)
P7C06	504.1	7th C on the clean part
P7C01	564.5	7th C on the clean part

Table A.3: Optimized structures of the pristine HNT surface containing from 8 to 10 carbon atoms. ΔE (kJ/mol) are computed with respect to the most stable structure of each series.

Structure	ΔE	Note
P8C09	0.0	All carbons in a straight line (not useful)
P8C08	411.9	8 carbons bonded together (fused rings)
P8C03	425.2	8 carbons bonded together (fused rings)
P8C04	428.7	8 carbons bonded together (fused rings)
P8C11	526.7	8 carbons bonded together (fused rings)
P8C10	526.7	8 carbons bonded together (same as pr-8C010a)
P8C07	769.5	8th C bonded to the others through O
P8C06	803.3	8th C on the clean part
P8C02	816.5	8th C bonded to both HNT and the other carbons
P8C05	828.2	8th C on the clean part
P8C01	860.8	8th C on the clean part
P9C04	0.0	9 carbons bonded together (fused rings)
P9C09	135.5	CO formation, floating above the surface
P9C10	148.5	9 carbons bonded together (fused rings)
P9C07	172.4	9 carbons bonded together (fused rings)
P9C03	179.0	9 carbons bonded together (fused rings)
P9C08	315.3	9 carbons bonded together (fused rings)
P9C06	459.1	9th C on the clean part
P9C05	494.3	9th C on the clean part
P9C02	508.4	9th C on the clean part
P9C01	523.9	9th C on the clean part
P10C08	0.0	10 carbons bonded together (elongated ring)
P10C07	94.2	10 carbons bonded together (fused rings)
P10C03	113.5	10 carbons bonded together (fused rings)
P10C09	120.6	10 carbons bonded together (fused rings)
P10C05	148.8	CO formation, floating above the surface
P10C10	164.9	CO formation, floating above the surface
P10C04	216.3	10 carbons bonded together (fused rings)
P10C02	245.9	10 carbons bonded together (fused rings)
P10C06	524.0	10th C on the clean part
P10C01	556.1	10th C on the clean part

Table A.4: Optimized structures of the substituted HNT surface containing from 1 to 4 carbon atoms. ΔE (kJ/mol) are computed with respect to the most stable structure of each series.

Structure	ΔE	Note
S1C02	0.0	C near the defective part
S1C07	5.2	C near the defective part
S1C03	74.8	C near the defective part
S1C04	154.6	C near the defective part
S1C08	170.3	C near the defective part
S1C06	170.4	C on the clean part
S1C05	171.3	C on the clean part
S1C01	178.8	C on the clean part
S2C07	0.0	2nd C bonded to the first through O
S2C02	36.4	2 carbons bonded together (C-C-O ring)
S2C04	189.6	2nd C neat the defective part
S2C03	234.9	2nd C near the defective part
S2C05	328.3	2nd C on the clean part
S2C06	329.3	2nd C on the clean part
S2C01	352.8	2nd C on the clean part
S3C02	0.0	formic acid formation, adsorbed on the surface (not useful)
S3C07	53.8	3 carbons bonded together (ring)
S3C04	310.0	3 carbons close to each other
S3C01	517.5	3 carbons close to each other
S3C03	535.7	3 carbons close to each other
S3C06	631.2	3rd C on the clean part
S4C02	0.0	4 carbons bonded together
S4C03	21.1	4 carbons bonded together
S4C07	61.7	4th C bonded to the others through O
S4C04	271.3	4th C near the defect
S4C06	327.2	4th C on the clean part
S4C05	340.0	4th C on the clean part
S4C01	344.7	4th C on the clean part

Table A.5: Optimized structures of the substituted HNT surface containing from 5 to 7 carbon atoms. ΔE (kJ/mol) are computed with respect to the most stable structure of each series.

Structure	ΔE	Note
S5C03	0.0	5th C in a quasi formic acid molecule (missing one H)
S5C07	55.3	CO formation, floating above the surface
S5C01	112.9	5th C bonded to the others through O
S5C02	112.9	5th C bonded to the others through O (same as s1-5C000b)
S5C04	534.0	5th C near the defect
S5C06	610.7	5th C on the clean part
S5C05	628.3	5th C on the clean part
S6C02	0.0	6th C bonded to other 4 carbons (ring)
S6C08	33.5	6th C bonded to other 4 carbons (ring)
S6C03	108.9	6th C bonded to the quasi formic acid
S6C07	114.7	CO formation, floating above the surface
S6C04	340.5	6th C bonded to the quasi-formic acid through O
S6C06	417.0	6th C on the clean part
S6C05	430.7	6th C on the clean part
S6C01	433.2	6th C on the clean part
S7C04	0.0	CO formation, floating above the surface
S7C02	222.3	7th C bonded to other 5 carbons (fused rings)
S7C07	241.0	7th C bonded to other 5 carbons (fused rings)
S7C06	376.2	7th C bonded to other 5 carbons (ring)
S7C03	487.6	7th C bonded to other 5 carbons (fused rings)
S7C05	783.0	7th C on the clean part
S7C01	800.7	7th C on the clean part

Table A.6: Optimized structures of the substituted HNT surface containing from 8 to 10 carbon atoms. ΔE (kJ/mol) are computed with respect to the most stable structure of each series.

Structure	ΔE	Note
S8C08	0.0	8th C bonded to other 6 carbons (fused rings)
S8C02	9.2	8th C bonded to other 6 carbons (fused rings)
S8C03	40.8	8th C bonded to other 6 carbons (fused rings)
S8C09	126.9	8th C bonded to other 6 carbons (cluster)
S8C07	180.4	CO formation, floating above the surface
S8C04	292.7	8th C on the clean part
S8C06	297.6	8th C on the clean part
S8C05	312.4	8th C on the clean part
S8C01	313.1	8th C on the clean part
S9C08	0.0	9th C bonded to other 7 carbons (fused rings)
S9C09	84.6	CO formation, floating above the surface
S9C07	192.0	9th C bonded to other 7 carbons (fused rings)
S9C03	194.8	9th C bonded to other 7 carbons (fused rings)
S9C02	388.7	9th C bonded to other 7 carbons (fused rings)
S9C06	674.7	9th C on the clean part
S9C04	677.8	9th C on the clean part
S9C01	688.5	9th C on the clean part
S9C05	689.9	9th C on the clean part
S10C07	0.0	10th C bonded to other 8 carbons (fused rings)
S10C03	4.5	10th C bonded to other 8 carbons (fused rings)
S10C02	31.5	10th C bonded to other 8 carbons (fused rings)
S10C08	250.2	10th C bonded to other 8 carbons (fused rings)
S10C10	328.8	CO formation, floating above the surface
S10C09	330.8	10th C bonded to other 8 carbons (fused rings)
S10C04	363.2	10th C near the defect
S10C06	448.6	10th C on the clean part
S10C05	460.4	10th C on the clean part
S10C01	469.2	10th C on the clean part

Table A.7: Optimized structures of the Si-vacant HNT surface containing from 1 to 4 carbon atoms. ΔE (kJ/mol) are computed with respect to the most stable structure of each series.

Structure	ΔE	Note
V1C03	0.0	C near the defective part
V1C04	45.0	C near the defective part
V1C02	88.7	C near the defective part
V1C05	203.4	C on the clean part
V1C01	205.9	C on the clean part
V1C06	229.8	C on the clean part
V2C03	0.0	2 carbons bonded together
V2C02	62.1	2 carbons bonded together
V2C05	596.5	2nd C on the clean part
V2C06	600.0	2nd C on the clean part
V2C01	630.2	2nd C on the clean part
V3C03	0.0	3 carbons bonded together (ring)
V3C07	0.0	3 carbons bonded together (ring)
V3C02	299.1	3rd C near the defect
V3C04	303.5	3rd C near the defect
V3C05	411.7	3rd C on the clean part
V3C06	414.3	3rd C on the clean part
V3C01	423.6	3rd C on the clean part
V4C04	0.0	4 carbons bonded together (ring)
V4C07	145.8	4 carbons bonded together (ring)
V4C08	161.6	4 carbons bonded together (ring)
V4C03	280.6	4th C near the defect
V4C02	368.6	4th C near the defect
V4C05	443.0	4th C on the clean part
V4C06	450.2	4th C on the clean part
V4C01	477.8	4th C on the clean part

Table A.8: Optimized structures of the Si-vacant HNT surface containing from 5 to 7 carbon atoms. ΔE (kJ/mol) are computed with respect to the most stable structure of each series.

Structure	ΔE	Note
V5C08	0.0	5 carbons bonded together (ring)
V5C04	39.0	5 carbons bonded together (ring)
V5C03	55.6	5 carbons bonded together (ring)
V5C07	208.3	5 carbons bonded together (ring)
V5C02	328.3	5th C near the defect
V5C06	415.6	5th C on the clean part
V5C05	421.6	5th C on the clean part
V5C01	449.7	5th C on the clean part
V6C07	0.0	6 carbons bonded together (ring)
V6C02	79.2	6th C bonded to the others through O
V6C03	92.4	6 carbons bonded together (ring)
V6C04	188.4	6 carbons bonded together (ring)
V6C06	365.1	6th C on the clean part
V6C05	370.4	6th C on the clean part
V6C01	395.1	6th C on the clean part
V7C04	0.0	7 carbons bonded together (fused rings)
V7C07	19.9	7 carbons bonded together (fused rings)
V7C08	23.8	7 carbons bonded together (fused rings)
V7C03	168.5	7 carbons bonded together (cluster)
V7C02	315.3	7th C bonded to the others through O
V7C06	574.7	7th C on the clean part
V7C05	581.4	7th C on the clean part
V7C01	602.8	7th C on the clean part

Table A.9: Optimized structures of the Si-vacant HNT surface containing from 8 to 10 carbon atoms. ΔE (kJ/mol) are computed with respect to the most stable structure of each series.

Structure	ΔE	Note
V8C07	0.0	8 carbons bonded together (fused rings)
V8C08	9.5	8 carbons bonded together (fused rings, similar to e1-8C006a)
V8C04	69.8	8 carbons bonded together (fused rings)
V8C02	333.6	8th C bonded to both HNT and the other carbons
V8C03	359.2	8 carbons bonded together (fused rings)
V8C05	436.7	8th C on the clean part
V8C06	439.7	8th C on the clean part
V8C01	470.2	8th C on the clean part
V9C07	0.0	9 carbons bonded together (fused rings)
V9C04	62.9	9 carbons bonded together (fused rings)
V9C10	69.3	9 carbons bonded together (fused rings)
V9C08	146.1	9 carbons bonded together (fused rings)
V9C09	149.8	9 carbons bonded together (fused rings)
V9C03	276.3	9 carbons bonded together (fused rings)
V9C02	309.3	9th C near the defect
V9C05	403.0	9th C on the clean part
V9C06	409.1	9th C on the clean part
V9C01	437.6	9th C on the clean part
V10C10	0.0	10 carbons bonded together (fused rings)
V10C04	5.3	10 carbons bonded together (fused rings)
V10C09	21.8	10 carbons bonded together (fused rings)
V10C07	44.2	10 carbons bonded together (fused rings)
V10C08	162.5	10 carbons bonded together (fused rings)
V10C02	164.9	10th C bonded to the others through O
V10C03	172.8	10 carbons bonded together (fused rings)
V10C06	443.2	10th C on the clean part
V10C05	454.0	10th C on the clean part
V10C01	465.8	10th C on the clean part

Appendix B

Listings

Listing B.1: Input file for Gaussian, built by Empathes

```
1|%nproc=2
1|%mem=2GB
1|#p b3lyp/cc-pvdz
E|#scf(conver=8)
E|#scf(maxcycle=64)
E|#force test
E|
2|gaussian title
2|
2|0 1
E|O      0.000000    0.000000    0.000000
E|C     -1.209277    0.000000    0.000000
E|H     -1.896357    0.876338    0.000000
E|H     -1.558378   -1.162947    0.000000
E|
```

Listing B.2: Input file for Siesta, built by Empathes

```
1|SystemName lblneb
1|SystemLabel lblneb
1|NumberOfAtoms      4
1|AtomicCoordinatesFormat    Ang
1|%block AtomicCoordinatesAndAtomicSpecies
E|      0.000000      0.000000      0.000000  1
E|     -1.207081      0.000000      0.000000  2
E|     -1.868949      0.896768      0.000000  3
E|     -1.615736     -1.120896      0.000000  3
2|%endblock AtomicCoordinatesAndAtomicSpecies
2|NumberOfSpecies      3
2|%block ChemicalSpeciesLabel
2| 1 8 O
2| 2 6 C
2| 3 1 H
2|%endblock ChemicalSpeciesLabel
2|PAO.EnergyShift      0.005 Ry
2|PAO.SoftDefault      true
2|PAO.BasisType        split
2|PAO.BasisSize        DZP
2|LatticeConstant      1.0 Ang
2|%block LatticeParameters
2|30.0 30.0 30.0 90.0 90.0 90.0
2|%endblock LatticeParameters
2|xc.functional        GGA
2|xc.authors          PBE
2|SpinPolarized       true
2|MeshCutoff          450 Ry
2|DM.UseSaveDM        true
2|SolutionMethod      diagon
2|MD.TypeOfRun        CG
2|MD.NumCGsteps       0
E|DM.Tolerance        1.00E-04
E|MaxSCFIterations    64
E|WriteForces         true
```

Listing B.3: Empathes input to perform NEB/Gaussian

```
#START
4
O      0.000000    0.000000    0.000000
C     -1.203990   -0.000000    0.000000
H     -1.805419    0.945297    0.000000
H     -1.805419   -0.945297    0.000000

#END
4
O      0.000000    0.000000    0.000000
C     -1.317837   -0.000000    0.000000
H     -1.542714    1.108433    0.000000
H      0.296335   -0.928935    0.000000

#STARTENERGY -114.507640701
#ENDENERGY -114.423707780

#OPTCYCLE -1
#OPTCONV 1.0E-3
#IDPP
#IMAGES 6
#CLIMBING 1

#PESPROGRAM gaussian
#PESEXEC g09

#PESINPUTTEMPLATE 1
%nproc=2
%mem=2GB
#p b3lyp/cc-pvdz
#ENDPESINPUTTEMPLATE

#PESINPUTTEMPLATE 2
gaussian title

0 1
#ENDPESINPUTTEMPLATE
```

Listing B.4: Empathes input to perform NEB/Siesta

```

#START
4
O      0.013513    0.000000   -0.000000   1
C     -1.204755   -0.000000    0.000000   2
H     -1.811774    0.966861   0.000000   3
H     -1.811774   -0.966861   0.000000   3

#END
4
O      0.005787   -0.000049    0.000000   1
C     -1.330060   -0.009745    0.000000   2
H     -1.547582    1.125306   0.000000   3
H      0.307075   -0.936793   0.000000   3

#STARTENERGY -643.692226
#ENDENERGY   -641.312969

#OPTCYCLE -1
#OPTCONV 1.0E-3
#IDPP
#IMAGES 6
#CLIMBING 1

#PESPROGRAM siesta
#PESEXEC siesta_psml
#PESPROC 16
#SCFCYCLE 200
#AUXINPUTFILES 1 *.psml
#AUXOUTPUTFILES 1 *.DM

#PESINPUTTEMPLATE 1
SystemName  lblneb
SystemLabel lblneb
NumberOfAtoms        4
AtomicCoordinatesFormat    Ang
%block AtomicCoordinatesAndAtomicSpecies
#ENDPESINPUTTEMPLATE

#PESINPUTTEMPLATE 2
%endblock AtomicCoordinatesAndAtomicSpecies
NumberOfSpecies        3
%block ChemicalSpeciesLabel
1  8  O
2  6  C
3  1  H
%endblock ChemicalSpeciesLabel
PAO.EnergyShift      0.005 Ry
PAO.SoftDefault       true

```

```
PAO.BasisType      split
PAO.BasisSize      DZP
LatticeConstant    1.0 Ang
%block LatticeParameters
30.0 30.0 30.0 90.0 90.0 90.0
%endblock LatticeParameters
xc.functional      GGA
xc.authors         PBE
SpinPolarized      true
MeshCutoff          450 Ry
DM.UseSaveDM       true
SolutionMethod     diagon
MD.TypeOfRun        CG
MD.NumCGsteps      0
#ENDPESINPUTTEMPLATE
```

Listing B.5: Empathes input to restart an interrupted calculation

```
#GEOMETRIESFILE geometries.in

#STARTENERGY -114.507640701
#ENDENERGY -114.423707780

#OPTCYCLE -1
#OPTCONV 1.0E-3
#CLIMBING 1
#CLIMBINGQUICKSTART

#PESPROGRAM gaussian
#PESEXEC g09

#PESINPUTTEMPLATE 1
%nproc=2
%mem=2GB
#p b3lyp/cc-pvdz
#ENDPESINPUTTEMPLATE

#PESINPUTTEMPLATE 2
gaussian title

0 1
#ENDPESINPUTTEMPLATE
```

Appendix C

H₂ Transformations on Graphene Supported Palladium Cluster

Article

H₂ Transformations on Graphene Supported Palladium Cluster: DFT-MD Simulations and NEB Calculations

Francesco Ferrante *¹, Antonio Prestianni¹ , Marco Bertini¹  and Dario Duca¹

Dipartimento di Fisica e Chimica “Emilio Segrè”, Università degli Studi di Palermo, Viale delle Scienze Ed. 17, 90128 Palermo, Italy; antonio.prestianni@unipa.it (A.P.); marco.bertini@unipa.it (M.B.); dario.duca@unipa.it (D.D.)

* Correspondence: francesco.ferrante@unipa.it; Tel.: +39-091-23897979

Received: 19 October 2020; Accepted: 10 November 2020; Published: 12 November 2020



Abstract: Molecular dynamics simulations based on density functional theory were employed to investigate the fate of a hydrogen molecule shot with different kinetic energy toward a hydrogenated palladium cluster anchored on the vacant site of a defective graphene sheet. Hits resulting in H₂ adsorption occur until the cluster is fully saturated. The influence of H content over Pd with respect to atomic hydrogen spillover onto graphene was investigated. Calculated energy barriers of ca. 1.6 eV for H-spillover suggest that the investigated Pd/graphene system is a good candidate for hydrogen storage.

Keywords: hydrogen reaction; supported metal catalysts; hydrogenation elementary events; spillover; DFT

1. Introduction

Molecular hydrogen is fundamental for a large number of catalytic processes, involving chemical and petrochemical conversions of industrial interest. Included in these, ammonia and methanol syntheses, hydroformylation and Fischer-Tropsch reactions as well as catalytic reforming, hydrotreating (hydrodesulfurization), hydrocracking and either hydrogenation or dehydrogenation of hydrocarbons, oils and fats have to be mentioned [1]. Among the catalytic transformations involving hydrogen, a significant amount of important catalysts contains supported transition metals [2].

Recently, sp²-like carbonaceous species, i.e., styrene derivatives, pristine or defective graphene along with carbon nanotubes and graphitic materials, have increased significantly in attractiveness as catalytic material [3–7] and, specifically, as supports [8–13].

One of the key phenomena concerning the hydrogen involvement is clearly its interaction with the supported metal systems [1]. Therefore, the understanding at atomistic level of the mechanisms involving the interaction of hydrogen with such systems represents a substantial target in catalysis [14–24]. Typical elementary events considered as critical in investigating the surface dynamic phenomena are both the physical and chemical molecular H₂ sorption as well as the subsequent fragmentation/recombination, migration and desorption of any surface hydrogen species [1,14–21].

A lot of information has been acquired both by experimental and theoretical studies [14–26], but the analysis of the causes, which dynamically originate the local surface coverage, is still poor [24,27]. In this context, as an example, hydrogen spillover is simply defined as the migration of H atoms to the support from the metal particles, following the dissociative adsorption of H₂ molecule on the metallic sites [28]. However, the spillover mechanism, with the complementary reverse spillover, are still far from being fully understood and further investigations are needed to reach the whole grasp of these phenomena.

From a theoretical point of view, Density Functional Theory (DFT) was employed to compute the energy barrier characterizing the hydrogen migration through the Pt_4 , Pd_6 and Pd_{13} clusters' sites and from these to the graphene surface. In all the evaluated cases, the computed energy barriers were 2.0–2.7 eV [29–32], suggesting that the hydrogen spillover is mostly an energetically hard process. Rangel et al. [33], studying the hydrogen fragmentation, migration and diffusion on one Pd_4 cluster supported on defective graphene, however, observed that the dissociation of the molecular H_2 on the Pd clusters could already occur overcoming energy barriers lower than 0.6 eV and found that the atomic hydrogen migration from the metal to the support occurred overcoming energy barrier values equal to 0.8 eV (on pyridinic defects) and just 0.5 eV (on pyrrolic defects). As a consequence, it was possible to infer that hydrogen fragmentation and migration in these systems might occur almost spontaneously even at room temperature [33].

Studying the energies of sequential H_2 molecules adsorption on Pd clusters at DFT level, Ramos-Castillo et al. [34] suggested that one Pd_4 cluster is able to coordinate several H_2 molecules by shaping H_2 molecular complexes. In this case, the maximum number of H_2 molecules for one Pd_4 cluster supported on graphene resulted equal to four. Conversely, Ebrahimi et al. [35] employed a series of accurate Molecular Dynamics (MD) simulations to characterize the phenomena involved in the H_2 adsorption on graphene nanoribbons, thus observing that the deformation of the graphene structure is closely related to the hydrogen surface coverage.

Recently, Prestianni et al. [24], in an article from now on referred as paper I, introduced a new, quite simple, approach in which the H_2 molecules were addressed “as projectiles” on a supported metal crystallite, namely on a Pd_4 cluster supported on graphene. At lower values of the H_2 kinetic energies, it was observed that the molecular sticking, hence the cluster site hitting was ruled by steering effects imputable to the Pd cluster, which easily reoriented the incoming H_2 molecule to the metallic surface sites, and in this way prompting the fragmentation thus atomic adsorption. Sticking decreased at higher molecular kinetic energies and it appeared that very fast molecules were able to acquire a kind of elusiveness toward the metallic surface which, because of this, was not able to steer and adsorb them.

To add new insights useful to unravel phenomena related to: (i) the surface ruling and hitting of H_2 molecules on metal sites of both pristine and already adsorbed clusters; (ii) the sticking and fragmentation and/or diffusion of atomic hydrogen; and (iii) the existence of spillover and reverse-spillover phenomena, the simple theoretical protocol described in I was mostly employed in the simulations reported in the following.

By these, the individual surface events on a very basic system—taking into consideration the collision of H_2 molecules on a supported fragment, shaped in a periodic system characterized by one unit formed by a (pristine or hydrogen preadsorbed) Pd_4 cluster placed on a C_{47} graphene model—were visually evaluated, by employing DFT Molecular Dynamics.

In details, the modeling routine implied the analysis of the local rearrangements following the single collisions of H_2 molecules with a $[2\text{mH}+(n-m)\text{H}_2]/\text{Pd}_4/\text{C}_{47}$ supported fragment, being $n+m=0-5$. Hence, the effects of the fragment hydrogen coverage as well as the starting speed and the orientation of the H_2 molecule were right correlated to the structural, mechanistic and energetic local changes induced on the same $[2\text{mH}+(n-m)\text{H}_2]/\text{Pd}_4/\text{C}_{47}$ supported fragments.

2. Results and Discussion

The model in this work is the same already used for the preliminary investigations reported in I. Briefly, the studied system is a tetrahedral Pd_4 cluster anchored on the vancancy of a defective graphene sheet, simulated by a periodic system with a supercell of 47 carbon atoms, with cell vector (12.78, 9.84, 30.00 Å); the projectiles are H_2 molecules having predefined kinetic energies, k_e , of 0.005, 0.01, 0.015 and 0.1 eV. In paper I it is evidenced that the hitting of H_2 on $\text{Pd}_4/\text{C}_{47}$ results in fragmentation only for the lowest values of projectile kinetic energy; the H_2 molecule is adsorbed for $k_e = 0.015$ eV and it bounces at the higher energies. This behavior was ascribed to an energetic balance

between the projectile k_e and its interaction energy with the cluster. In agreement with the steering mechanism proposed by Gross and Scheffler [36], low kinetic energy projectiles can undergo more easily to a process of steering and reorienting, which could promote their activation and fragmentation. On the other hand, when the second hitting was considered, i.e., H_2 shot either on $\text{H}_2\text{Pd}_4/\text{C}_{47}$ or on $2\text{HPd}_4/\text{C}_{47}$, it was revealed how the presence of already adsorbed species on the cluster affects the fate of the incoming molecule. In particular, it was evident that, due to repulsive effects from the preadsorbed not-dissociated H_2 , steering effects occur at higher projectile kinetic energies.

The target from which the investigation here reported starts is the system where one H_2 molecule is adsorbed atop the Pd(1) atom (with Pd–H distances of 1.853 and 1.887 Å, and H–H bond length equal to 0.849 Å), one H atom is located on the Pd(1)Pd(3) edge (being 1.887 and 1.738 the H–Pd(1) and H–Pd(3) distances, respectively) and another H atom on the Pd(1)Pd(4) edge (with H–Pd(1) and H–Pd(4) equal to 1.862 and 1.724 Å) of a Pd_4 tetrahedron anchored on defective graphene (see Figure 1 for atoms numbering). To simplify the discussion, the following notation is used throughout: (i) H_2^n is a hydrogen molecule adsorbed on the Pd(n) site of Pd_4 ; (ii) $\text{H}^{n_1[n_2][n_3]}$ is a H atom $\mu^1[\mu^2][\mu^3]$ -bonded to the Pd(n_1)[Pd(n_2)][Pd(n_3)] site(s) of the cluster; and (iii) the $\text{Pd}_4/\text{C}_{47}$ cluster/graphene support is implied. With this notation, the target system above is indicated as $\text{H}_2^1\text{H}^{13}\text{H}^{14}$. Clearly, μ^1 , μ^2 and μ^3 hydrogen atoms are characterized by 1, 2 and 3 apices, respectively. Furthermore, it is worth investigating the effect of H_2 adsorption on the Pd_4 configuration with respect to the graphene defect. The C atoms defining the defect contour in C_{47} are labeled with letters ranging from *a* to *l* (Figure 1), and the anchoring of Pd_4 can be defined by the bonds occurring between the Pd centers of the cluster and those C atoms. Thus, in the $\text{H}_2^1\text{H}^{13}\text{H}^{14}$ system, Pd(2) is bonded to the contour atoms *e* and *i* (Pd–C = 1.989 and 2.002 Å), Pd(3) is bonded to the contour atom *c* (Pd–C = 2.383 Å) and Pd(4) to *a* and *l* (Pd–C = 2.258 and 2.424 Å); the shorthand notation (2*e**i**3**c**4**al*) will be used for this anchoring configuration. For comparison, the one in $\text{Pd}_4/\text{C}_{47}$, without adsorbed hydrogen, is (2*a**e**i**3**b**c**4**al*), with Pd–C distances equal to 1.937, 2.017, 2.053 Å (2*a**e**i*), 2.523, 2.396, 2.536 Å (3*b**c*) and 2.027, 2.218 Å (4*al*), so that in our initial target some bonds between the cluster and the graphene sheet are elongated/broken.

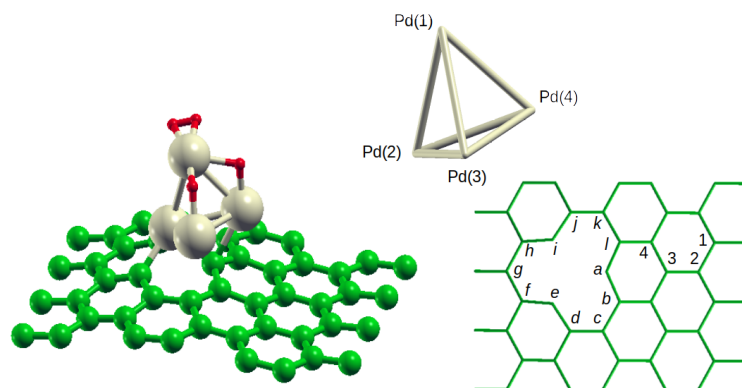


Figure 1. The optimized structure of the $[2\text{H}+\text{H}_2]/\text{Pd}_4/\text{C}_{47}$ system used as initial target for the molecular dynamics simulation of H_2 hitting, along with the atomic labels for the Pd_4 cluster and the graphene sheet that are used throughout.

2.1. Hitting of H_2 on the Hydrogenated Pd_4 Cluster

H₂ on $\text{H}_2^1\text{H}^{13}\text{H}^{14}$: The hitting of H_2 on the $\text{H}_2^1\text{H}^{13}\text{H}^{12}$ system results in adsorption on Pd(4) if the projectile kinetic energy is 0.01 or 0.015 eV; this gives raise to the $\text{H}_2^1\text{H}_2^4\text{H}^{13}\text{H}^{14}$ system, of which, in the following, NVT equilibration is analyzed. In this system, the anchoring configuration of Pd_4 on the graphene defect slightly changes, becoming now (2*e**i**3**b**c**4**a*). At lower energy, 0.005 eV, the H_2 molecule interacts with the cluster but cannot bind to it, hence it steps away. At higher energy, 0.1 eV, the projectile undergoes a sort of reflection: it hits the cluster after 97 fs from the beginning

of simulation and its interaction with Pd(1) lasts only 22 fs, and then it goes rotating in the direction opposite to the incoming one.

H₂ on H₂¹H₂⁴H¹³H¹³⁴: After NVT equilibration, the H₂¹H₂⁴H¹³H¹³⁴ system maintains its configuration. Every simulation of H₂ hitting, beginning with a different projectile initial orientation, invariably resulted in a H₂ molecule adsorbed on the cluster. At k_e = 0.005 eV, the projectile bounces on Pd(3), turns around the cluster and interacts with it in proximity of Pd(4). The palladium cluster, after the hitting, is anchored on graphene only through the Pd(2) and Pd(3) centers. Following equilibration, the H₂ molecule (former the projectile) locates between Pd(1) and Pd(4), and the cluster adopts a (2aei3d4a) position with respect to the defect. Essentially the same result is obtained at k_e = 0.01 eV, even if in this case the projectile firstly interacts with Pd(1), and also at k_e = 0.015 eV, where following the hit H₂ weakly interacts with Pd(3) and only after equilibration it shifts on the Pd(1)–Pd(4) edge. Finally, at k_e = 0.1 eV, the H₂ molecule adsorbs on Pd(1) after bouncing on Pd(3) and again moves to the Pd(1)–Pd(4) edge after NVT. It is then clear that the result of the H₂ hitting on H₂¹H₂⁴H¹³H¹³⁴ is the new system H₂¹⁽⁴⁾H₂⁴H¹²H¹³⁴, where the apex 1(4) underlines that the H₂ molecule is adsorbed atop Pd(1) but one of its atoms interact also with Pd(4). Presumably, this occurrence is observed because both Pd(1) and Pd(4) are already occupied by another H₂ molecule in atop position. Some snapshots of these simulations are collected in Figure 2.

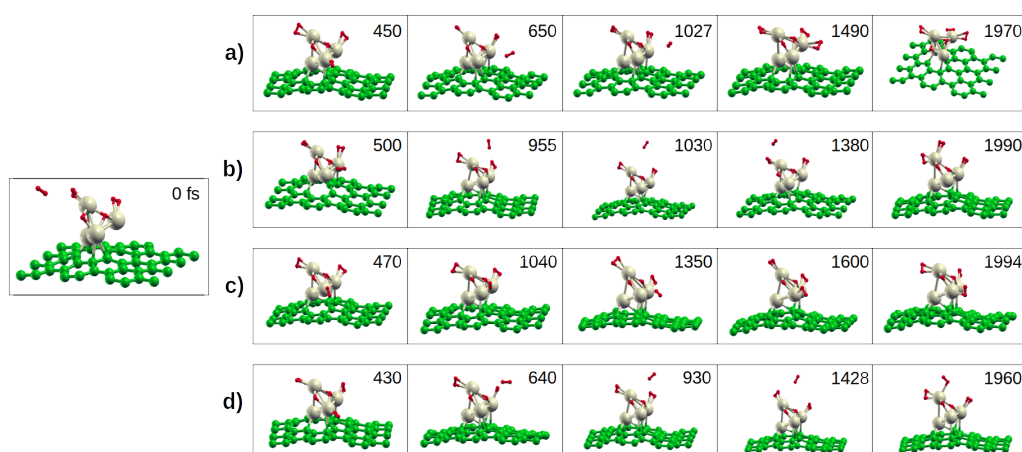


Figure 2. Snapshots from the molecular dynamics simulations of H₂ hitting on the H₂¹H₂⁴H¹³H¹³⁴ system, with initial kinetic energy equal to: (a) 0.005; (b) 0.01; (c) 0.015; and (d) 0.1 eV. The first snapshot is common to all simulations and simulation time is reported in fs.

H₂ on H₂¹⁽⁴⁾H₂⁴H¹²H¹³⁴: In the H₂¹⁽⁴⁾H₂⁴H¹²H¹³⁴ system, only the Pd(3) position is free to adsorb another H₂ molecule, being Pd(2) the main site that anchors the Pd₄ cluster to graphene. As a matter of fact, the adsorption on Pd(3) is just what happens when a k_e = 0.005 eV H₂ projectile is shot on the target, giving rise to a seemingly hydrogen-saturated H₂¹⁽⁴⁾H₂³H₂⁴H¹³H¹³⁴ palladium cluster, with this one in (2aei4a) configuration with respect to the defect arrangement (see Figure 3).

At higher energy (0.01, 0.015 and 0.1 eV), only almost perfect reflections occur. In this case, we also investigated the effect of very high energy particles, namely 0.5 and 1 eV, to see if spillover would take place. Instead, the high energy H₂ always causes the desorption of molecules from the cluster. In particular, the k_e = 0.5 eV projectile adsorbs on Pd(1), substituting itself to the two H₂ molecules locating atop it, which at once desorb, while in the k_e = 1 eV case the projectile reflects and one H₂ from Pd(1) moves away from the cluster.

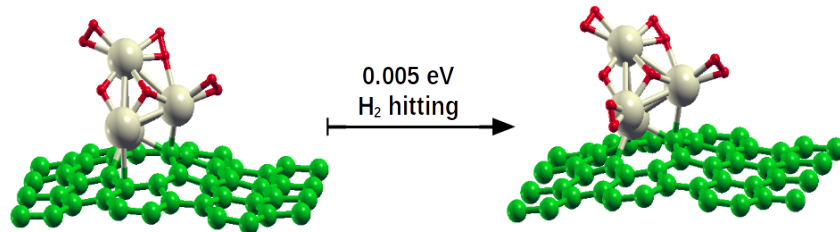


Figure 3. The $\text{H}_2^1\text{H}_2^{1(4)}\text{H}_2^4\text{H}^{13}\text{H}^{134}$ system as results from NVT equilibration (left) and the whole hydrogen saturated Pd_4 cluster anchored on defective graphene (right), obtained from the $k_e = 0.005$ eV simulation.

2.2. Hydrogen Hopping to Graphene

The hopping of one hydrogen atom from the Pd_4 cluster to position C(4) of C_{47} (see Figure 1), as well as the diffusion of H along the $4 \rightarrow 3 \rightarrow 2 \rightarrow 1$ path in the graphene sheet, was investigated by means of NEB calculations. To evaluate the effect on the hopping due to the presence of hydrogen adsorbed on the cluster, the $\text{H}^{124}\text{H}^{134}$, $\text{H}_2^1\text{H}^{13}\text{H}^{14}$ and $\text{H}_2^1\text{H}_2^{1(4)}\text{H}_2^3\text{H}^{13}\text{H}^{134}$ systems (from now on indicated as R1, R2 and R3, respectively) were selected. The first of these systems has only one H_2 molecule fragmented on the palladium cluster while the second is just the starting target system of the molecular dynamics simulations. The third system is similar to the result of hydrogen hitting on $\text{H}_2^1\text{H}_2^4\text{H}^{13}\text{H}^{134}$, but with the adsorbed H_2 molecule shifted from $\text{Pd}(4)$ to $\text{Pd}(3)$; this was necessary because $\text{H}_2^1\text{H}_2^{1(4)}\text{H}_2^4\text{H}^{13}\text{H}^{134}$ does not show any fragmented H atom that could hop onto graphene in any direction coherent to our sheet model. The change is legitimated by the fact that the result of hitting by MD simulations on a given $\text{H-Pd}_4/\text{C}_{47}$ system is to be considered only as one among a multitude of possible outcomes of the real hydrogen hitting, and the adsorption of H_2 on $\text{Pd}(3)$ instead of $\text{Pd}(4)$ can surely be included amid these outcomes. Further, with this choice, in all of the three systems the H-hopping could occur with somehow the same sequence of steps: the breaking of $\text{H-Pd}(1)$ bond, the revolution around $\text{Pd}(4)$, the breaking of $\text{H-Pd}(4)$ bond and the formation of $\text{H-C}(4)$. As a matter of fact, this allows to compare the hopping energetics in the three systems. In the final products the configuration of hydrogen species on the Pd_4 cluster slightly changes, giving rise to the systems $\text{H}^{13}\text{H}^{\text{C}(4)}$, $\text{H}_2^1\text{H}^{134}\text{H}^{\text{C}(4)}$ and $\text{H}_2^1\text{H}_2^3\text{H}^{14}\text{H}^{134}\text{H}^{\text{C}(4)}$, whose energies show that the spillover reactions always occurs with high endoergicity. Here, the apex $\text{C}(4)$ underlines the displacement of the corresponding H atom from the cluster to the graphene site indexed as 4 (see Figure 1), where it binds at a distance of 1.13–1.14 Å.

The results of the NEB calculations from reactants to products are collected in Figure 4. As can be noticed, no matter the starting system, a metastable intermediate locates along the hopping path, where an H atom is located atop the $\text{Pd}(4)$ center; the energy of the transition state from the reactant to this intermediate species slightly exceeds 65 kJ mol⁻¹ in the least favorable case, but is always only a few kJ mol⁻¹ above the energy of the intermediate itself. The step from intermediate to product would occur by overcoming an energy barrier of 104.3, 103.2 and 98.4 kJ mol⁻¹ for the paths starting from R1, R2 and R3, respectively. This would suggest that the presence of hydrogen species on the Pd_4 cluster has only a small influence on the H-hopping. On the other hand, the intermediate-to-product step only reflects the energetics of $\text{H-Pd}(4)$ bond breaking, while the effect of other H-species on the cluster should be better characterized by taking into account the highest energy barrier with respect to the reactant. If this is done, the difference between the three systems is clearly magnified, indicating that, even if the activation toward H-hopping is always quite difficult, the energy barrier sensibly decreases when the number of H-species on the cluster increases. As a matter of fact, the intermediate can be seen as a small ripple in the minimum energy path from reactant to product and it is possible to think

that, in order for the hopping to occur, the reactant has to acquire all in one the energy to overcome the largest barrier.

In the present whole saturated $\text{H}_2^1\text{H}_2^{1(4)}\text{H}_2^3\text{H}_2^4\text{H}^{13}\text{H}^{134}$ system, there is no hydrogen atoms that could spillover to graphene. In this case the possibility of a H-induced hopping was investigated. The H^{134} atom could substitute a H atom of H_2^4 , which in turn let migrate the other of its H atom onto the graphene surface. In more details, the investigated pathway, represented schematically in Figure 5, shows the essentially barrierless formation of two intermediate species, $\text{H}_2^1\text{H}_2^1\text{H}_2^3\text{H}_2^4\text{H}^{13}\text{H}^{14}$ and $\text{H}_2^1\text{H}_2^1\text{H}_2^3\text{H}_2^4\text{H}^{13}\text{H}^4$, and an energy barrier of $169.8 \text{ kJ mol}^{-1}$, to end up with the $\text{H}_2^1\text{H}_2^1\text{H}_2^3\text{H}_2^4\text{H}^{13}\text{H}^{\text{C}(4)}$ final product. This last is $140.9 \text{ kJ mol}^{-1}$ less stable than the initial reactant; the higher calculated endoergicity, with respect to the other spillover products, is presumably due to the fact that in this case, if the net process is considered, the H atom hopped on graphene was removed from a stable μ^3 position. Hence, it is possible to argue that for the same reason the energy barrier for this process is the highest of all the investigated ones, which suggests that H-spillover from a fully-saturated palladium cluster could be more difficult due to a necessary rearrangement of the hydrogen atomic species that need to get a right constellation, close to the receiving carbonaceous surface.

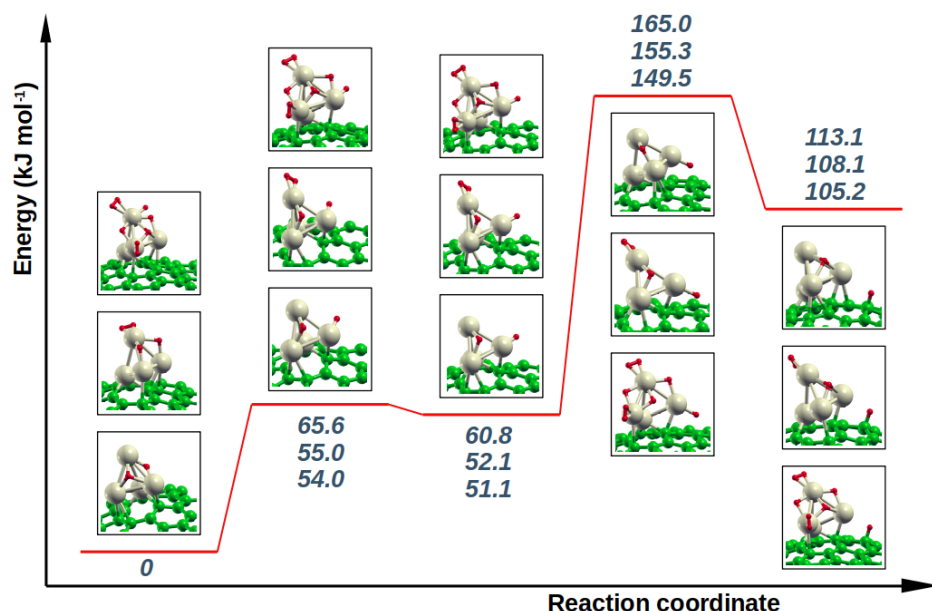


Figure 4. The graph collects the NEB minimum energy paths for the H-hopping to graphene starting from the $\text{H}^{13}\text{H}^{14}$, $\text{H}_2^1\text{H}^{13}\text{H}^{14}$ and $\text{H}_2^1\text{H}_2^{1(4)}\text{H}_2^3\text{H}_2^4\text{H}^{13}\text{H}^{134}$ systems. The energy values (referred to the corresponding reactant and expressed in kJ mol^{-1}) are listed in the order top to bottom for the three cases, respectively. The Pd(4)-H and H-C(4) distances involving the hopping hydrogen in the transition states are 1.703 , 1.616 \AA ; 1.797 , 1.524 \AA ; and 1.715 , 1.562 \AA for the three investigated cases, respectively.

Finally, NEB calculations were performed to investigate the ease of diffusion of hydrogen atom far away from the anchored cluster, i.e., the hydrogen hopping along the $4 \rightarrow 3 \rightarrow 2 \rightarrow 1$ path of graphene (see Figure 1). This was done by considering the spillover product $\text{H}_2^1\text{H}^{134}\text{H}^{\text{C}(4)}$ as representative, which has energy of $108.1 \text{ kJ mol}^{-1}$ higher than the R2 reactant. The results, reported in Table 1, show that not all C position in C_{47} are equivalent, as could be reasonably expected since the bonding of one H atom on graphene site causes a curvature of the sheet, and the ease with which this occurs depends on the position with respect to the defect. Indeed, in the present case, the properties of the graphene curvature are also heavily affected by the palladium cluster anchored on the defect and by the size of

the model used. The same arguments apply to the energies of the transition states for the shifting from one C position to the next, whose trend reflects somehow the stability of the corresponding product and is quantified around $100 \pm 15 \text{ kJ mol}^{-1}$.

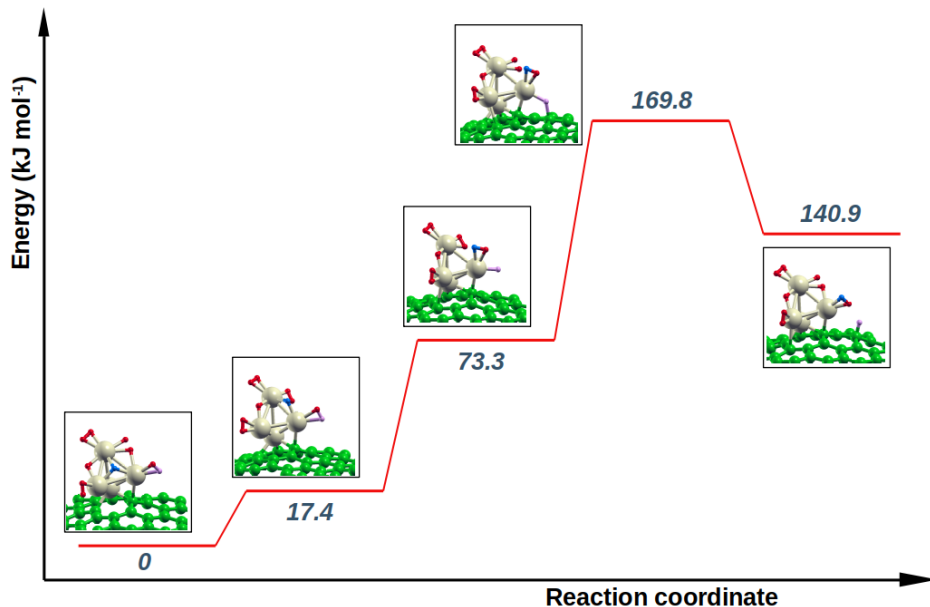


Figure 5. The NEB minimum energy pathway for the process in which hydrogen atoms in the completely saturated Pd_4 cluster rearrange to give H-spillover. The involved H atoms are represented with different colors (blue and pink, instead of red) for clarity. The $\text{Pd}(4)-\text{H}$ and $\text{H}-\text{C}(4)$ distances involving the hopping hydrogen in the transition state are 1.842 and 1.491 \AA .

Table 1. The relative stability of the $\text{H}_2^1\text{H}^{134}\text{H}^{\text{C}(x)}$ systems (ΔE), with the H atom in the x position along the $4 \rightarrow 3 \rightarrow 2 \rightarrow 1$ path, and the energy barriers, E_b , for the H-shift from one position to the one which follows.

System	$\Delta E \text{ (kJ mol}^{-1})$	$E_b \text{ (kJ mol}^{-1})$
$\text{H}_2^1\text{H}^{134}\text{H}^{\text{C}(4)}$	0	92.6
$\text{H}_2^1\text{H}^{134}\text{H}^{\text{C}(3)}$	+7.8	85.0
$\text{H}_2^1\text{H}^{134}\text{H}^{\text{C}(2)}$	-19.2	116.1
$\text{H}_2^1\text{H}^{134}\text{H}^{\text{C}(1)}$	+34.3	—

3. Models and Computational Details

Molecular dynamics simulations were performed within the density functional theory framework by using the SIESTA approach as implemented in the homonym code, version 4.2.1 [37]. The employed relativistic norm-conserving Troullier–Martins pseudopotentials and the double zeta plus polarization quality numerical basis sets, on which the SIESTA method is based, were generated and tested as described elsewhere [13]. The PBE exchange-correlation functional in the spin-polarized form was chosen for all calculations, along with a $4 \times 4 \times 1$ sampling of the Monkhorst-Pack grid and a value of 450 Ry for the mesh cutoff.

The algorithm devised to simulate the hitting of H_2 on the target can be summarized as follows. Start with the optimized geometry of $\text{Pd}_4/\text{C}_{47}$ (the $\text{H}_2^1\text{H}^{13}\text{H}^{14}$ system, in the present work) and perform a 10 ps MD simulation (timestep of 0.5 fs) in the NVT (298 K) ensemble. (A) Once the system is equilibrated, take the atomic positions, velocities and forces of the last snapshot and add to the

system a H_2 molecule with the following characteristics: the first H atom is placed at a distance of 7 Å from the center of mass (CM) of the palladium cluster, with a given angle with respect to the normal to surface; the second H atom is located in the same direction at a distance of 0.75 Å from the first; the velocity vectors of each H atom have magnitudes according to the initial kinetic energy of the projectile and are oriented toward the CM of Pd_4 ; and, finally, the forces acting on the two H centers can be safely assumed to be negligible (hence set to zero) due to the distance of H_2 from the target. Restart the MD simulation for a duration of 2 ps, now using the NVE ensemble in order to not redistribute the energy possessed by the projectile, and analyze the product of the hitting. Do this for projectiles having initial kinetic energies of 0.005, 0.01, 0.015 and 0.1 eV. Since the aim is to investigate the adsorption and/or the fragmentation of H_2 on $\text{Pd}_4/\text{C}_{47}$, the simulations ended with simple reflection or bouncing of the projectile were discarded, while those ended with an effective hitting, i.e., an incipient sticking, were retained, analyzed and then subjected to equilibration in the NVT ensemble for 10 ps. The same procedure is repeated starting from (A) to simulate the hitting of a new H_2 molecule and continue to shoot H_2 until no effective hit occurs, i.e., the Pd_4 cluster appears to be H-saturated.

Hopping of hydrogen species from the metal cluster to the graphene surface sites (spillover) was studied by means of a home-made code, which implements the Climbing Image Nudged Elastic Band method (CI-NEB) [38,39] and is interfaced with the SIESTA program. Reactants and products were fully optimized by SIESTA periodic calculations and NEB images were generated using the image depending pair potential [40]. Every NEB calculation used 13 images connected each other by dynamic springs and a convergence threshold of $3 \times 10^{-3} \text{ E}_h/\text{\AA}$ on the norm of atomic forces was employed.

4. Conclusions

DFT-based molecular dynamics simulations show that a small palladium cluster anchored on a defective site of graphene can be saturated with hydrogen by means of a flux of low-energy H_2 molecules. Cluster H-saturation is reached when five hydrogen molecules are adsorbed/fragmented, taking into account that some cluster sites are not available for the interaction with H_2 . In fact, even if the cluster anchoring configuration slightly changes and/or weakens according to the degree of H-adsorption, one face of the cluster is always firmly interacting with the graphene defect region. As the number of hydrogen species on palladium increases, the energy barrier that rules the H-spillover onto graphene slightly decreases. H-spillover remains an onerous process, which is not surprising given the high endoergicity of the reaction, but the present results indicate that, in the here investigated system, a small palladium cluster on defective graphene, the energy barriers are reduced by 0.5–1.0 eV with respect to other systems (excluding of course those where H-spillover occurs toward a graphene defect). This appears true also if the spillover requires some sort of redistribution/rearrangement of atomic hydrogen on the cluster.

Finally, by considering the whole web of the different pathways presented in this study, straightforwardly it emerges that the reverse-spillover (i.e., hopping from graphene to Pd_4 , rearrangement of hydrogen species on the cluster, and formation and desorption of H_2) is supposed to be an easy process, when occurring on the graphene-anchored palladium clusters. This should encourage experimental investigations to deeper probe this kind of systems, hence to give them a chance as reversible hydrogen storage device.

Author Contributions: Conceptualization, D.D., A.P. and F.F.; methodology, F.F.; software, M.B.; validation, D.D., F.F. and A.P.; formal analysis, F.F.; investigation, A.P., F.F. and M.B.; resources, D.D.; data curation, F.F. and M.B.; writing—original draft preparation, F.F. and D.D.; writing—review and editing, F.F. and D.D.; supervision, D.D.; project administration, D.D.; and funding acquisition, D.D. All authors have read and agreed to the published version of the manuscript.

Funding: This research received no external funding.

Conflicts of Interest: The authors declare no conflict of interest.

References

1. Paál, Z.; Mennon, P. Hydrogen Effects in Metal Catalysts. *Catal. Rev. Sci. Eng.* **1983**, *25*, 229–324. [[CrossRef](#)]
2. Cervený, L. (Ed.) *Catalytic Hydrogenation in "Studies in Surface Science and Catalysis"*, 1 ed.; Elsevier Science Ltd.: Amsterdam, The Netherlands, 1986; Volume 27.
3. Ferrante, F.; Lo Celso, F.; Duca, D. Construction and Characterization of Models of Hypercrosslinked Polystyrene. *Colloid Polym. Sci.* **2012**, *290*, 1443–1450. [[CrossRef](#)]
4. Cortese, R.; Ferrante, F.; Roggan, S.; Duca, D. N-Doped Carbon Networks: Alternative Materials Tracing New Routes for Activating Molecular Hydrogen. *Chem. Eur. J.* **2015**, *21*, 3806–3814. [[CrossRef](#)]
5. Navalón, S.; Herance, J.; Álvaro, M.; García, H. General Aspects in the Use of Graphenes in Catalysis. *Mater. Horiz.* **2018**, *5*, 363–378. [[CrossRef](#)]
6. Wang, C.; Astruc, D. Recent Developments of Metallic Nanoparticle-Graphene Nanocatalysts. *Prog. Mater. Sci.* **2018**, *94*, 306–383. [[CrossRef](#)]
7. Palmisano, G.; Casiraghi, C.; Dionysiou, D.D.; Ohno, T.; Pintar, A.; Xu, Y.J. Graphitic Materials in Photo(Electro)Catalysis. *Catal. Today* **2018**, *315*, 1. [[CrossRef](#)]
8. Duca, D.; Ferrante, F.; La Manna, G. Theoretical Study of Palladium Cluster Structures on Carbonaceous Supports. *J. Chem. Phys. C* **2007**, *111*, 5402–5408. [[CrossRef](#)]
9. Yang, Y.; Chiang, K.; Burke, N. Porous Carbon-Supported Catalysts for Energy and Environmental Applications: a Short Review. *Catal. Today* **2011**, *178*, 197–205. [[CrossRef](#)]
10. Prestianni, A.; Ferrante, F.; Sulman, M.; Duca, D. DFT Investigation on the Nucleation and Growth of Small Palladium Clusters on a Hypercrosslinked Polystyrene Matrix. *J. Chem. Phys. C* **2014**, *118*, 21006–21013. [[CrossRef](#)]
11. Julkapli, N.; Bagheri, S. Graphene Supported Heterogeneous Catalysts: an Overview. *Int. J. Hydrogen Energy* **2015**, *40*, 948–979. [[CrossRef](#)]
12. Blandez, J.; Esteve-Adell, I.; Primo, A.; Alvaro, M.; García, H. Nickel Nanoparticles Supported on Graphene as Catalysts for Aldehyde Hydrosilylation. *J. Mol. Catal. A Chem.* **2016**, *412*, 13–19. [[CrossRef](#)]
13. Ferrante, F.; Prestianni, A.; Cortese, R.; Schimmenti, R.; Duca, D. Density Functional Theory Investigation on the Nucleation of Homo- and Heteronuclear Metal Clusters on Defective Graphene. *J. Phys. Chem. C* **2016**, *120*, 12022–12031. [[CrossRef](#)]
14. Duca, D.; Botár, L.; Vidóczy, T. Monte Carlo Simulations of Ethylene Hydrogenation on Pt Catalysts. *J. Catal.* **1996**, *162*, 260–267. [[CrossRef](#)]
15. Duca, D.; Baranyai, P.; Vidóczy, T. A Monte Carlo Model for the Hydrogenation of Ethylene on Pt Catalysts. *J. Comput. Chem.* **1998**, *19*, 396–403. [[CrossRef](#)]
16. Duca, D.; La Manna, G.; Russo, M.R. Computational Studies on Surface Reaction Mechanisms: Ethylene Hydrogenation on Platinum Catalysts. *Phys. Chem. Chem. Phys.* **1999**, *1*, 1375–1382. [[CrossRef](#)]
17. Duca, D.; La Manna, G.; Varga, Zs.; Vidóczy, T. Hydrogenation of Acetylene–Ethylene Mixtures on Pd Catalysts: Study of the Surface Mechanism by Computational Approaches. Metal Dispersion and Activity of the Catalyst. *Theor. Chem. Acc.* **2000**, *104*, 302–311. [[CrossRef](#)]
18. Duca, D.; Barone, G.; Varga, Zs. Hydrogenation of Acetylene–Ethylene Mixtures on Pd catalysts: Computational Study on the Surface Mechanism and on the Influence of the Carbonaceous Deposits. *Catal. Lett.* **2001**, *72*, 17–23. [[CrossRef](#)]
19. Duca, D.; Barone, G.; Varga, Zs.; La Manna, G. Hydrogenation of Light Hydrocarbons on Palladium: Theoretical Study of the Local Surface Arrangements. *J. Mol. Struct. (THEOCHEM)* **2001**, *542*, 207–214. [[CrossRef](#)]
20. Barone, G.; Duca, D. Hydrogenation of 2,4-dinitrotoluene on Pd/C Catalysts: Computational Study on the Influence of the Steric Hindrance of the Surface Species and of the Metal Dispersion on the Reaction Mechanism. *J. Catal.* **2002**, *211*, 296–307. [[CrossRef](#)]
21. D’Anna, V.; Duca, D.; Ferrante, F.; La Manna, G. DFT Studies on Catalytic Properties of Isolated and Carbon Nanotube Supported Pd₉ Cluster – I: Adsorption, Fragmentation and Diffusion of Hydrogen. *Phys. Chem. Chem. Phys.* **2009**, *11*, 4077–4083. [[CrossRef](#)]
22. Ferrante, F.; Prestianni, A.; Duca, D. Computational Investigation of Alkynols and Alkyndiols Hydrogenation on a Palladium Cluster. *J. Phys. Chem. C* **2014**, *118*, 551–558. [[CrossRef](#)]

23. Prestianni, A.; Crespo-Quesada, M.; Cortese, R.; Ferrante, F.; Kiwi-Minsker, L.; Duca, D. Structure Sensitivity of 2-Methyl-3-butyn-2-ol Hydrogenation on Pd: Computational and Experimental Modeling. *J. Phys. Chem. C* **2014**, *118*, 3119–3128. [[CrossRef](#)]
24. Prestianni, A.; Ferrante, F.; Duca, D. H₂ Hitting on Graphene Supported Palladium Cluster: Molecular Dynamics Simulations. *Theor. Chem. Acc.* **2017**, *136*, 1. [[CrossRef](#)]
25. Mushrif, S.H.; Rey, A.D.; Peslherbe, G.H. Energetics and Dynamics of Hydrogen Adsorption, Desorption and Migration on a Carbon-Supported Palladium Cluster. *J. Mater. Chem.* **2010**, *20*, 10503–10510. [[CrossRef](#)]
26. Seo, D.H.; Shin, H.; Kang, K.; Kim, H.; Han, S.S. First-Principles Design of Hydrogen Dissociation Catalysts Based on Isoelectronic Metal Solid Solutions. *J. Phys. Chem. Lett.* **2014**, *5*, 1819–1824. [[CrossRef](#)]
27. Lopez, N.; Łodziana, Z.; Illas, F.; Salmeron, M. When Langmuir Is Too Simple: H₂ Dissociation on Pd(111) at High Coverage. *Phys. Rev. Lett.* **2004**, *93*, 146103. [[CrossRef](#)]
28. Prins, R. Hydrogen Spillover. Facts and Fiction. *Chem. Rev.* **2012**, *112*, 2714–2738. [[CrossRef](#)]
29. Psogogiannakis, G.M.; Froudakis, G.E. DFT Study of the Hydrogen Spillover Mechanism on Pt-Doped Graphite. *J. Phys. Chem. C* **2009**, *113*, 14908–14915. [[CrossRef](#)]
30. Wu, H.Y.; Fan, X.; Kuo, J.L.; Deng, W.Q. DFT Study of Hydrogen Storage by Spillover on Graphene with Boron Substitution. *J. Phys. Chem. C* **2011**, *115*, 9241–9249. [[CrossRef](#)]
31. Juarez-Mosqueda, R.; Mavrandonakis, A.; Kuc, A.B.; Pettersson, L.G.M.; Heine, T. Theoretical Analysis of Hydrogen Spillover Mechanism on Carbon Nanotubes. *Front. Chem.* **2015**, *3*, 2. [[CrossRef](#)]
32. Blanco-Rey, M.; Juaristi, J.I.; Alducin, M.; López, M.J.; Alonso, J.A. Is Spillover Relevant for Hydrogen Adsorption and Storage in Porous Carbons Doped with Palladium Nanoparticles? *J. Phys. Chem. C* **2016**, *120*, 17357–17364. [[CrossRef](#)]
33. Rangel, E.; Sansores, E.; Vallejo, E.; Hernández-Hernández, A.; López-Pérez, P.A. Study of the Interplay Between N-Graphene Defects and Small Pd Clusters for Enhanced Hydrogen Storage via a Spill-Over Mechanism. *Phys. Chem. Chem. Phys.* **2016**, *18*, 33158–33170. [[CrossRef](#)] [[PubMed](#)]
34. Ramos-Castillo, C.; Reveles, J.; Zope, R.; de Coss, R. Palladium Clusters Supported on Graphene Monovacancies for Hydrogen Storage. *J. Phys. Chem. C* **2015**, *119*, 8402–8409. [[CrossRef](#)]
35. Ebrahimi, S.; Montazeri, A.; Rafii-Tabar, H. Molecular Dynamics Study of a New Mechanism for Ripple Formation on Graphene Nanoribbons at Very Low Temperatures Based on H₂ Physisorption. *Solid State Commun.* **2013**, *159*, 84–87. [[CrossRef](#)]
36. Gross, A.; Scheffler, M. *Ab initio* Quantum and Molecular Dynamics of the Dissociative Adsorption of Hydrogen on Pd(100). *Phys. Rev. B* **1998**, *57*, 2493–2506. [[CrossRef](#)]
37. Soler, J.M.; Artacho, E.; Gale, J.D.; García, A.; Junquera, J.; Ordejón, P.; Sánchez-Portal, D. The SIESTA Method for Ab Initio Order-N Materials Simulation. *J. Phys. Condens. Matter* **2002**, *14*, 2745. [[CrossRef](#)]
38. Henkelman, G.; Jónsson, H. Improved Tangent Estimate in the Nudged Elastic Band Method for Finding Minimum Energy Paths and Saddle Points. *J. Chem. Phys.* **2000**, *113*, 9978. [[CrossRef](#)]
39. Henkelman, G.; Uberuaga, B.P.; Jónsson, H. A Climbing Image Nudged Elastic Band Method for Finding Saddle Points and Minimum Energy Paths. *J. Chem. Phys.* **2000**, *113*, 9901. [[CrossRef](#)]
40. Smidstrup, S.; Pedersen, A.; Stokbro, K.; Jónsson, H. Improved Initial Guess for Minimum Energy Path Calculations. *J. Chem. Phys.* **2014**, *140*, 214106. [[CrossRef](#)]

Publisher's Note: MDPI stays neutral with regard to jurisdictional claims in published maps and institutional affiliations.



© 2020 by the authors. Licensee MDPI, Basel, Switzerland. This article is an open access article distributed under the terms and conditions of the Creative Commons Attribution (CC BY) license (<http://creativecommons.org/licenses/by/4.0/>).

Bibliography

- [1] Georg Kresse and Jürgen Furthmüller. Efficient iterative schemes for ab initio total-energy calculations using a plane-wave basis set. *Physical review B*, 54(16):11169, 1996.
- [2] M. J. Frisch, G. W. Trucks, H. B. Schlegel, G. E. Scuseria, M. A. Robb, J. R. Cheeseman, G. Scalmani, V. Barone, B. Mennucci, G. A. Petersson, H. Nakatsuji, M. Caricato, X. Li, H. P. Hratchian, A. F. Izmaylov, J. Bloino, G. Zheng, J. L. Sonnenberg, M. Hada, M. Ehara, K. Toyota, R. Fukuda, J. Hasegawa, M. Ishida, T. Nakajima, Y. Honda, O. Kitao, H. Nakai, T. Vreven, J. A. Montgomery, Jr., J. E. Peralta, F. Ogliaro, M. Bearpark, J. J. Heyd, E. Brothers, K. N. Kudin, V. N. Staroverov, R. Kobayashi, J. Normand, K. Raghavachari, A. Rendell, J. C. Burant, S. S. Iyengar, J. Tomasi, M. Cossi, N. Rega, J. M. Millam, M. Klene, J. E. Knox, J. B. Cross, V. Bakken, C. Adamo, J. Jaramillo, R. Gomperts, R. E. Stratmann, O. Yazyev, A. J. Austin, R. Cammi, C. Pomelli, J. W. Ochterski, R. L. Martin, K. Morokuma, V. G. Zakrzewski, G. A. Voth, P. Salvador, J. J. Dannenberg, S. Dapprich, A. D. Daniels, O. Farkas, J. B. Foresman, J. V. Ortiz, J. Cioslowski, and D. J. Fox. Gaussian~09, Revision A.01, 2009. Gaussian Inc. Wallingford CT.
- [3] M. J. Frisch, G. W. Trucks, H. B. Schlegel, G. E. Scuseria, M. A. Robb, J. R. Cheeseman, G. Scalmani, V. Barone, G. A. Petersson, H. Nakatsuji, X. Li, M. Caricato, A. V. Marenich, J. Bloino, B. G. Janesko, R. Gomperts, B. Mennucci, H. P. Hratchian, J. V. Ortiz, A. F. Izmaylov, J. L. Sonnenberg, D. Williams-Young, F. Ding, F. Lipparini, F. Egidi, J. Goings, B. Peng, A. Petrone, T. Henderson, D. Ranasinghe, V. G. Zakrzewski, J. Gao, N. Rega, G. Zheng, W. Liang, M. Hada, M. Ehara, K. Toyota, R. Fukuda, J. Hasegawa, M. Ishida, T. Nakajima, Y. Honda, O. Kitao, H. Nakai, T. Vreven, K. Throssell, J. A. Montgomery, Jr., J. E. Peralta, F. Ogliaro, M. J. Bearpark, J. J. Heyd, E. N. Brothers, K. N. Kudin, V. N. Staroverov, T. A. Keith, R. Kobayashi, J. Normand, K. Raghavachari, A. P. Rendell, J. C. Burant, S. S. Iyengar, J. Tomasi,

M. Cossi, J. M. Millam, M. Klene, C. Adamo, R. Cammi, J. W. Ochterski, R. L. Martin, K. Morokuma, O. Farkas, J. B. Foresman, and D. J. Fox. Gaussian~16 Revision C.01, 2016. Gaussian Inc. Wallingford CT.

- [4] José M Soler, Emilio Artacho, Julian D Gale, Alberto García, Javier Junquera, Pablo Ordejón, and Daniel Sánchez-Portal. The siesta method for ab initio order-n materials simulation. *Journal of Physics: Condensed Matter*, 14(11):2745, 2002.
- [5] Graeme Henkelman and Hannes Jónsson. Improved tangent estimate in the nudged elastic band method for finding minimum energy paths and saddle points. *The Journal of chemical physics*, 113(22):9978–9985, 2000.
- [6] Graeme Henkelman, Blas P Uberuaga, and Hannes Jónsson. A climbing image nudged elastic band method for finding saddle points and minimum energy paths. *The Journal of chemical physics*, 113(22):9901–9904, 2000.
- [7] Søren Smidstrup, Andreas Pedersen, Kurt Stokbro, and Hannes Jónsson. Improved initial guess for minimum energy path calculations. *The Journal of chemical physics*, 140(21):214106, 2014.
- [8] Message Passing Interface Forum. *MPI: A Message-Passing Interface Standard, Version 3.1*. 2015. <https://www.mpi-forum.org/>.
- [9] Erik Bitzek, Pekka Koskinen, Franz Gähler, Michael Moseler, and Peter Gumbsch. Structural relaxation made simple. *Physical review letters*, 97(17):170201, 2006.
- [10] Julien Guénolé, Wolfram G. Nöhring, Aviral Vaid, Frédéric Houllé, Zhuocheng Xie, Aruna Prakash, and Erik Bitzek. Assessment and optimization of the fast inertial relaxation engine (fire) for energy minimization in atomistic simulations and its implementation in lammps. *Computational Materials Science*, 175:109584, 2020.
- [11] Jorge Nocedal and Stephen J Wright. *Numerical optimization*. Springer, 1999.
- [12] Daniel Sheppard, Rye Terrell, and Graeme Henkelman. Optimization methods for finding minimum energy paths. *The Journal of Chemical Physics*, 128(13):134106, 2008.

- [13] JD Barr, AJ Bell, F Ferrante, G La Manna, JL Mundy, CM Timperley, MJ Waters, and P Watts. Fragmentations and reactions of some isotopically labelled dimethyl methyl phosphono and trimethyl phosphoro thiolates and thionates studied by electrospray ionisation ion trap mass spectrometry. *International Journal of Mass Spectrometry*, 244(1):29–40, 2005.
- [14] Marco Bertini, Francesco Ferrante, and Dario Duca. Empathes: A general code for nudged elastic band transition states search. *Computer Physics Communications*, 271:108224, 2022.
- [15] Francesco Ferrante, Antonio Prestianni, Marco Bertini, and Dario Duca. H₂ transformations on graphene supported palladium cluster: DFT-MD simulations and NEB calculations. *Catalysts*, 10(11), 2020.
- [16] Kristian Stangeland, Dori Kalai, Hailong Li, and Zhixin Yu. CO₂ methanation: The effect of catalysts and reaction conditions. *Energy Procedia*, 105:2022–2027, 2017. 8th International Conference on Applied Energy, ICAE2016, 8-11 October 2016, Beijing, China.
- [17] Chalachew Mebrahtu, Florian Krebs, Salvatore Abate, Siglinda Perathoner, Gabriele Centi, and Regina Palkovits. Chapter 5 - CO₂ methanation: Principles and challenges. In Stefania Albonetti, Siglinda Perathoner, and Elsje Alessandra Quadrelli, editors, *Horizons in Sustainable Industrial Chemistry and Catalysis*, volume 178 of *Studies in Surface Science and Catalysis*, pages 85–103. Elsevier, 2019.
- [18] J Hu, K P Brooks, J D Holladay, D T Howe, and T M Simon. Catalyst development for microchannel reactors for martian in situ propellant production. *Catal. Today*, 125:103–110, 2007.
- [19] Ryan Lacdao Arevalo, Susan Meñez Aspera, Mary Clare Sison Escaño, Hiroshi Nakanishi, and Hideaki Kasai. Ru-catalyzed steam methane reforming: Mechanistic study from first principles calculations. *ACS omega*, 2(4):1295–1301, 2017.
- [20] I M Ciobica, F Frechard, R A Van Santen, A W Kleyn, and J Hafner. A dft study of transition states for c- h activation on the ru (0001) surface. *The Journal of Physical Chemistry B*, 104(14):3364–3369, 2000.
- [21] Sharan Shetty, APJ Jansen, and Rutger A van Santen. Methane formation on corrugated ru surfaces. *The Journal of Physical Chemistry C*, 114(51):22630–22635, 2010.

- [22] Pieter W van Grootel, Rutger A van Santen, and Emiel JM Hensen. Methane dissociation on high and low indices rh surfaces. *The Journal of Physical Chemistry C*, 115(26):13027–13034, 2011.
- [23] X. Zhang, W-J Sun, and W Chu. Effect of glow discharge plasma treatment on the performance of Ni/SiO₂ catalyst in CO₂ methanation. *J. Fuel Chem. Technol.*, 41:96–101, 2013.
- [24] Ryan Lacdao Arevalo, Susan Meñez Aspera, Mary Clare Sison Escaño, Hiroshi Nakanishi, and Hideaki Kasai. Tuning methane decomposition on stepped ni surface: The role of subsurface atoms in catalyst design. *Scientific reports*, 7(1):1–8, 2017.
- [25] Daniel Schmider, Lubow Maier, and Olaf Deutschmann. Reaction kinetics of co and CO₂ methanation over nickel. *Industrial & Engineering Chemistry Research*, 60(16):5792–5805, 2021.
- [26] Sergio López-Rodríguez, Arantxa Davó-Quiñonero, Esther Bailón-García, Dolores Lozano-Castelló, Facundo C Herrera, Eric Pellegrin, Carlos Escudero, Max García-Melchor, and Agustín Bueno-López. Elucidating the role of the metal catalyst and oxide support in the ru/CeO₂-catalyzed CO₂ methanation mechanism. *The Journal of Physical Chemistry C*, 125(46):25533–25544, 2021.
- [27] José LC Fajín, José RB Gomes, and M Natália DS Cordeiro. Mechanistic study of carbon monoxide methanation over pure and rhodium-or ruthenium-doped nickel catalysts. *The Journal of Physical Chemistry C*, 119(29):16537–16551, 2015.
- [28] Charlotte Vogt, Matteo Monai, Ellen B Sterk, Jonas Palle, Angela EM Melcherts, Bart Zijlstra, Esther Groeneveld, Peter H Berben, Jelle M Boereboom, Emiel JM Hensen, et al. Understanding carbon dioxide activation and carbon–carbon coupling over nickel. *Nature communications*, 10(1):1–10, 2019.
- [29] Xu Zhang and Zhen Zhou. Perspective on theoretical models for CO₂ electrochemical reduction. *The Journal of Physical Chemistry C*, 126(8):3820–3829, 2022.
- [30] Shiru Lin, Chong Teng, and Junwei Lucas Bao. CO₂ adsorptions on d-block-metal-doped nickel nanoparticles: Unexpected adsorption configurations predicted by machine intelligence. *The Journal of Physical Chemistry C*, 125(36):19839–19846, 2021.

- [31] Rufang Zhao and Yang Wang. High-performance single-atom catalysts for co oxidation: the importance of hydrogen bonds and adsorption strength of the reactant. *The Journal of Physical Chemistry C*, 125(29):15987–15993, 2021.
- [32] Tianfu Liu, Guoxiong Wang, and Xinhe Bao. Electrochemical co₂ reduction reaction on 3d transition metal single-atom catalysts supported on graphdiyne: a dft study. *The Journal of Physical Chemistry C*, 125(47):26013–26020, 2021.
- [33] Caroline R Kwawu, Albert Aniagyei, Destiny Konadu, Elliot Menkah, and Richard Tia. First-principles dft insights into the mechanisms of co₂ reduction to co on fe (100)-ni bimetals. *Theoretical Chemistry Accounts*, 141(3):1–7, 2022.
- [34] Manuel J. Louwerse and Gadi Rothenberg. Transferable basis sets of numerical atomic orbitals. *Phys. Rev. B*, 85:035108, Jan 2012.
- [35] Bhawna Bhatia and David S Sholl. Chemisorption and diffusion of hydrogen on surface and subsurface sites of flat and stepped nickel surfaces. *The Journal of chemical physics*, 122(20):204707, 2005.
- [36] Yunhai Bai, Demetrios Kirvassilis, Lang Xu, and Manos Mavrikakis. Atomic and molecular adsorption on ni (111). *Surface Science*, 679:240–253, 2019.
- [37] Fanglin Che, Jake T Gray, Su Ha, and Jean-Sabin McEwen. Improving ni catalysts using electric fields: a dft and experimental study of the methane steam reforming reaction. *ACS Catalysis*, 7(1):551–562, 2017.
- [38] Sheng-Guang Wang, Dong-Bo Cao, Yong-Wang Li, Jianguo Wang, and Haijun Jiao. Co₂ reforming of ch₄ on ni (111): a density functional theory calculation. *The Journal of Physical Chemistry B*, 110(20):9976–9983, 2006.
- [39] Sheng-Guang Wang, Dong-Bo Cao, Yong-Wang Li, Jianguo Wang, and Haijun Jiao. Chemisorption of co₂ on nickel surfaces. *The Journal of Physical Chemistry B*, 109(40):18956–18963, 2005.
- [40] Ernst D German and Moshe Sheintuch. Predicting ch₄ dissociation kinetics on metals: trends, sticking coefficients, h tunneling, and kinetic isotope effect. *The Journal of Physical Chemistry C*, 117(44):22811–22826, 2013.

- [41] Ernst D German, Olga Nekhamkina, Oleg Temkin, and Moshe Sheintuch. H tunneling effects on sequential dissociation of methane over ni (111) and the overall rate of methane reforming. *The Journal of Physical Chemistry C*, 119(17):9260–9273, 2015.
- [42] Ernst D German and Moshe Sheintuch. Methane steam reforming rates over pt, rh and ni (111) accounting for h tunneling and for metal lattice vibrations. *Surface Science*, 656:126–139, 2017.
- [43] Laura Gueci, Francesco Ferrante, Antonio Prestianni, Francesco Arena, and Dario Duca. Structural, energetic and kinetic database of catalytic reactions: Benzyl alcohol to benzaldehyde oxidation on mnox clusters. *Data in brief*, 38:107369, 2021.
- [44] J.A. Christiansen. The elucidation of reaction mechanisms by the method of intermediates in quasi-stationary concentrations. 5:311–353, 1953.
- [45] Qingyuan Bi, Xieyi Huang, Guoheng Yin, Tianyuan Chen, Xianlong Du, Jun Cai, Jing Xu, Zhi Liu, Yifan Han, and Fuqiang Huang. Cooperative catalysis of nickel and nickel oxide for efficient reduction of co2 to ch4. *ChemCatChem*, 11(4):1295–1302, 2019.
- [46] Mun-Sing Fan, Ahmad Zuhairi Abdullah, and Subhash Bhatia. Utilization of greenhouse gases through dry reforming: Screening of nickel-based bimetallic catalysts and kinetic studies. *ChemSusChem*, 4(11):1643–1653, 2011.
- [47] Ignacio Iglesias, Adrián Quindimil, Fernando Marino, Unai De-La-Torre, and Juan R González-Velasco. Zr promotion effect in co2 methanation over ceria supported nickel catalysts. *international journal of hydrogen energy*, 44(3):1710–1719, 2019.
- [48] Xueying Wen, Leilei Xu, Mindong Chen, Yiyu Shi, Chufei Lv, Yan Cui, Xianyun Wu, Ge Cheng, Cai-E Wu, Zhichao Miao, et al. Exploring the influence of nickel precursors on constructing efficient ni-based co2 methanation catalysts assisted with in-situ technologies. *Applied Catalysis B: Environmental*, 297:120486, 2021.
- [49] Tengfei Zhang and Qing Liu. Lanthanum-modified mcf-derived nickel phyllosilicate catalyst for enhanced co2 methanation: a comprehensive study. *ACS applied materials & interfaces*, 12(17):19587–19600, 2020.

- [50] KM Abraham and Z Jiang. A polymer electrolyte-based rechargeable lithium/oxygen battery. *Journal of the Electrochemical Society*, 143(1):1, 1996.
- [51] Wugang Fan, Beizhou Wang, Xiangxin Guo, Xiangyang Kong, and Jianjun Liu. Nanosize stabilized Li-deficient $\text{Li}_{2-x}\text{O}_2$ through cathode architecture for high performance $\text{Li}-\text{O}_2$ batteries. *Nano Energy*, 27:577–586, 2016.
- [52] Zhiyang Lyu, Lijun Yang, Yanping Luan, Xiao Renshaw Wang, Liangjun Wang, Zehua Hu, Junpeng Lu, Shuning Xiao, Feng Zhang, Xizhang Wang, et al. Effect of oxygen adsorbability on the control of Li_2O_2 growth in $\text{Li}-\text{O}_2$ batteries: Implications for cathode catalyst design. *Nano Energy*, 36:68–75, 2017.
- [53] Ji-Jing Xu, Zhi-Wen Chang, Ying Wang, Da-Peng Liu, Yu Zhang, and Xin-Bo Zhang. Cathode surface-induced, solvation-mediated, micrometer-sized Li_2O_2 cycling for $\text{Li}-\text{O}_2$ batteries. *Advanced Materials*, 28(43):9620–9628, 2016.
- [54] Katarina A Novčić, Ana S Dobrota, Milena Petković, Börje Johansson, Natalia V Skorodumova, Slavko V Mentus, and Igor A Pašti. Theoretical analysis of doped graphene as cathode catalyst in $\text{Li}-\text{O}_2$ and $\text{Na}-\text{O}_2$ batteries—the impact of the computational scheme. *Electrochimica Acta*, 354:136735, 2020.
- [55] Yanjie Zhai, Jun Wang, Qiang Gao, Yuqi Fan, Chuanxin Hou, Yue Hou, Hu Liu, Qian Shao, Shide Wu, Lanling Zhao, et al. Highly efficient cobalt nanoparticles anchored porous N-doped carbon nanosheets electrocatalysts for $\text{Li}-\text{O}_2$ batteries. *Journal of Catalysis*, 377:534–542, 2019.
- [56] Fangfang Zheng, Huilong Dong, Yujin Ji, and Youyong Li. Computational study on catalytic performance of BC_3 and NC_3 nanosheets as cathode electrocatalysts for nonaqueous $\text{Li}-\text{O}_2$ batteries. *Journal of Power Sources*, 436:226845, 2019.
- [57] Xiaodong Lin, Ruming Yuan, Senrong Cai, Youhong Jiang, Jie Lei, San-Gui Liu, Qi-Hui Wu, Hong-Gang Liao, Mingsen Zheng, and Quanfeng Dong. An open-structured matrix as oxygen cathode with high catalytic activity and large Li_2O_2 accommodations for lithium–oxygen batteries. *Advanced Energy Materials*, 8(18):1800089, 2018.

- [58] Ki Ro Yoon, Kihyun Shin, Jiwon Park, Su-Ho Cho, Chanhoon Kim, Ji-Won Jung, Jun Young Cheong, Hye Ryung Byon, Hyuk Mo Lee, and Il-Doo Kim. Brush-like cobalt nitride anchored carbon nanofiber membrane: current collector-catalyst integrated cathode for long cycle Li–O₂ batteries. *ACS nano*, 12(1):128–139, 2018.
- [59] Jingbo Yang, Hongwei Mi, Shan Luo, Yongliang Li, Peixin Zhang, Libo Deng, Lingna Sun, and Xiangzhong Ren. Atomic layer deposition of TiO₂ on nitrogen-doped carbon nanofibers supported Ru nanoparticles for flexible Li–O₂ battery: A combined dft and experimental study. *Journal of Power Sources*, 368:88–96, 2017.
- [60] Fangfang Tu, Junping Hu, Jian Xie, Gaoshao Cao, Shichao Zhang, Shengyuan A Yang, Xinbing Zhao, and Hui Ying Yang. Au-decorated cracked carbon tube arrays as binder-free catalytic cathode enabling guided Li₂O₂ inner growth for high-performance Li–O₂ batteries. *Advanced Functional Materials*, 26(42):7725–7732, 2016.
- [61] Xin Huang, Hong Yu, Huiteng Tan, Jixin Zhu, Wenyu Zhang, Chengyuan Wang, Jun Zhang, Yuxi Wang, Yunbo Lv, Zhi Zeng, et al. Carbon nanotube-encapsulated noble metal nanoparticle hybrid as a cathode material for Li-oxygen batteries. *Advanced Functional Materials*, 24(41):6516–6523, 2014.
- [62] E Abdullayev, A Joshi, W Wei, Y Zhao, and Y Lvov. Enlargement of halloysite clay nanotube lumen by selective etching of aluminum oxide. *ACS nano*, 6:7216–7226, 2012.
- [63] Y Lvov and E Abdullayev. Functional polymer-clay nanotube composites with sustained release of chemical agents. *Progr. Polym. Sci.*, 38:1690–1719, 2013.
- [64] G Cavallaro, D I Donato, G Lazzara, and S Milioto. Films of halloysite nanotubes sandwiched between two layer of bipolimer: From the morphology to the dielectric, thermal, transparency, and wettability properties. *J. Phys. Chem. C*, 115:20491–20498, 2011.
- [65] G Cavallaro, G Lazzara, and S Milioto. Exploiting the colloidal stability and solubilization ability of clay nanotubes/ionic surfactant hybrid nanomaterials. *J. Phys. Chem. C*, 116:21932–21938, 2012.
- [66] Yixian Pei, Yuxin Wang, Yusuf Darraf, An-Yi Chang, Hao Zhao, Xuan Liu, Jianguo Liu, Yuri Lvov, and Shengnian Wang. Confining sulfur par-

- ticles in clay nanotubes with improved cathode performance of lithium–sulfur batteries. *Journal of Power Sources*, 450:227698, 2020.
- [67] Yunyan Wang, Xinbao Wang, Hongqi Ye, and Kai Han. Carbon coated halloysite nanotubes as efficient sulfur host materials for lithium sulfur batteries. *Applied Clay Science*, 179:105172, 2019.
 - [68] Yong Min Kwon, Jihoon Kim, Kuk Young Cho, and Sukeun Yoon. Ion shielding functional separator using halloysite containing a negative functional moiety for stability improvement of Li–S batteries. *Journal of Energy Chemistry*, 60:334–340, 2021.
 - [69] Tian Cen, Yong Zhang, Yanhong Tian, and Xuejun Zhang. Synthesis and electrochemical performance of graphene@halloysite nanotubes/sulfur composites cathode materials for lithium-sulfur batteries. *Materials*, 13(22):5158, 2020.
 - [70] Yue Lin, Xuming Wang, Jin Liu, and Jan D Miller. Natural halloysite nano-clay electrolyte for advanced all-solid-state lithium-sulfur batteries. *Nano Energy*, 31:478–485, 2017.
 - [71] Qinyu Zhu, Xuming Wang, and Jan D Miller. Advanced nanoclay-based nanocomposite solid polymer electrolyte for lithium iron phosphate batteries. *ACS applied materials & interfaces*, 11(9):8954–8960, 2019.
 - [72] Mohammed Khalifa, S Janakiraman, Sudipto Ghosh, A Venimadhav, and S Anandhan. PVDF/halloysite nanocomposite-based non-wovens as gel polymer electrolyte for high safety lithium ion battery. *Polymer Composites*, 40(6):2320–2334, 2019.
 - [73] Liwei Yu, Di Mu, Le Liu, and Jingyu Xi. Bifunctional effects of halloysite nanotubes in vanadium flow battery membrane. *Journal of Membrane Science*, 564:237–246, 2018.
 - [74] Wenjie Liu, Qianxun Ru, Shixiang Zuo, Song Yang, Jie Han, and Chao Yao. Controllable synthesis of nitrogen-doped carbon nanotubes derived from halloysite-templated polyaniline towards nonprecious orr catalysts. *Applied Surface Science*, 469:269–275, 2019.
 - [75] Chandrasekar M Subramaniyam, NR Srinivasan, Zhixin Tai, Hua Kun Liu, John B Goodenough, and Shi Xue Dou. Self-assembled porous carbon microparticles derived from halloysite clay as a lithium battery anode. *Journal of Materials Chemistry A*, 5(16):7345–7354, 2017.

- [76] Yang Yang, Xiuyun Chuan, Jianzhuo Li, Fangfang Liu, and Aijun Li. Synthesis and properties of halloysite templated tubular MoS₂ as cathode material for rechargeable aqueous zn-ion batteries. *Int. J. Electrochem. Sci.*, 15:6052–6059, 2020.
- [77] Vladimir A Vinokurov, Anna V Stavitskaya, Aleksandr P Glotov, Andrei A Novikov, Anna V Zolotukhina, Mikhail S Kotelev, Pawel A Gushchin, Evgenii V Ivanov, Yusuf Darrat, and Yuri M Lvov. Nanoparticles formed onto/into halloysite clay tubules: architectural synthesis and applications. *The Chemical Record*, 18(7-8):858–867, 2018.
- [78] SK Shinde, GS Ghodake, NC Maile, HM Yadav, AD Jagadale, MB Jalak, AA Kadam, Sivalingam Ramesh, C Bathula, and D-Y Kim. Designing of nanoflakes anchored nanotubes-like MnCo₂S₄/halloysite composites for advanced battery like supercapacitor application. *Electrochimica Acta*, 341:135973, 2020.
- [79] Yan Zhao and Donald G. Truhlar. A new local density functional for main-group thermochemistry, transition metal bonding, thermochemical kinetics, and noncovalent interactions. *The Journal of Chemical Physics*, 125(19):194101, 2006.
- [80] Ansgar Schäfer, Hans Horn, and Reinhart Ahlrichs. Fully optimized contracted gaussian basis sets for atoms li to kr. *The Journal of Chemical Physics*, 97(4):2571–2577, 1992.
- [81] F Ferrante, N Armata, and G Lazzara. Modeling of the halloysite spiral nanotube. *The Journal of Physical Chemistry C*, 119(29):16700–16707, 2015.
- [82] F Ferrante, N Armata, G Cavallaro, and G Lazzara. Adsorption studies of molecules on the halloysite surfaces: A computational and experimental investigation. *The Journal of Physical Chemistry C*, 121(5):2951–2958, 2017.
- [83] R Rozza, N Armata, G Lazzara, F Parisi, and F Ferrante. Halloysite nanotubes and metal corrosion inhibitors: a computational and experimental study. *The Journal of Physical Chemistry C*, 97:119–124, 2019.
- [84] R Rozza and F Ferrante. Computational study of water adsorption on halloysite nanotube in different ph environments. *Applied Clay Science*, 190:105589–1–15, 2020.